UAB
Universitat Autònoma de Barcelona

NEW INSIGHTS INTO MANY-PARTICLE BOUND STATES IN QUANTUM FIELD THEORY

Fabio van Dissel

ADVERTIMENT. L'accés als continguts d'aquesta tesi queda condicionat a l'acceptació de les condicions d'ús establertes per la següent llicència Creative Commons: https://creativecommons.org/licenses/?lang=ca

ADVERTENCIA. El acceso a los contenidos de esta tesis queda condicionado a la aceptación de las condiciones de uso establecidas por la siguiente licencia Creative Commons: https://creativecommons.org/licenses/?lang=es

WARNING. The access to the contents of this doctoral thesis it is limited to the acceptance of the use conditions set by the following Creative Commons license: https://creativecommons.org/licenses/?lang=en

NEW INSIGHTS INTO MANY-PARTICLE BOUND STATES IN QUANTUM FIELD THEORY

A thesis presented for the degree of Doctor of Physics by:

Fabio van Dissel

Supervisors: Oriol Pujolàs Boix and Evangelos Sfakianakis

Tutor: Eduard Masso Soler

20th of May 2025

To my grandfather, Lanfranco Emiliani,
who inspired me to look up at the sky and wonder...

Acknowledgements

One sometimes stops to wonder about the virtually infinite amount of diverging paths a human life can take. The thread of fate spreads as an endless web of possibilities as we drift along, pushed by the relentless force of entropy. Where we end up can feel so random, based on a chance encounter or a fleeting thought. Could things have gone differently, or was everything already written in the primordial sky? Whatever the answer to that question is, here we are.

There are many that are deserving of my gratitude, and without whom I would have never written these words. First and foremost, I have to thank my two supervisors. Evangelos for opening the door, and Oriol for guiding me to the end. I also have to thank Eduard, with whom I had the pleasure of teaching *Mecànica Quàntica* to the next generation of physicists. To my other collaborators: George, Mark, Jared, Rodrigo, Wout and Tuan, thank you.

When I moved to Barcelona, over four years ago, I had never realized in what ways growing up in the Netherlands had influenced my personality. It is only through interacting with the diverse group of cultures and nationalities at *IFAE* that I became aware of the extent of my Dutchness. Endless dinner discussions about the merits and intricacies of various national dishes, made my mind wander to the delicious simplicity of chocolate sprinkles on bread. That those dinners could start *at the earliest*, at 21:30, made me think of Henk and Ingrid, who would already be in their bed at that point. The fact that those dinners usually started half an hour after the agreed upon time due to the tardiness of its participants, made me miss the protestant work ethic of my home country.

Despite these (minor) complaints, I want to express how much I value the many wonderful people I bonded with here. Ángel, Calum, Clara, Dounia, Ewan, Francesco Sicily, Gabriel, Jack, Javi, Juan Se, Juanito, Luis, Mathilde, Míriam, Mónica, Ornella, Roger, Sciotti, Silvia and many others deserve mention. Each of these people warrant a separate paragraph in these acknowledgements, but some things are better left unwritten. Although the time will soon come that I will return to my Shire, you have made it so that there is no real going back. *Though I may come to the Shire, it will not seem the same; for I shall not be the same.*

Although returning home after multiple years abroad will feel like a new challenge in itself, I know that I can count on the many people that I left behind to welcome me with open arms. To the *slakkies*; Pol, Jacobus and Daan. To my *jaargenoten*; Timmer, Wietse, Daan, Simon and Daniel. To the others that visited me; Sven, Vincent, Bruno, Kaipo, Bloem and Sander. I look forward to seeing you all soon and reminiscing once again about the days gone by.

An Tamino, ich hoffe, dass du eines Tages diese Arbeit lesen kannst und sie dir genauso viel Freude bereitet wie mir das Finden deiner Flasche vor einigen Jahren. Ich wünsche dir alles Gute für deine zukünftigen Unternehmungen.

As the dispersing strands of life's river slowly converge towards the end of this chapter of my life, it is important to remember the boat on which I navigate the shifting currents. Mama, Papa, Mafalda and the rest of my family, with special mention of my grandmother, *nonna*, you never fail to remind me that the field of physics, despite its universal laws, pales in comparison to the warmth you give me.

Whenever I stop to wonder, and ask myself what could have been, I remind myself of meeting you that chilly Barcelona night. A shining light illuminating the wisdom of my choices, for there's no shadow of a doubt that it was worth it, Jolyn.

Abstract

In this thesis we study various aspects of many-particle bound states in quantum field theories. In bosonic theories many fundamental quanta can occupy the same state, resulting in macroscopic solutions that behave semiclassically on large timescales. If additionally attractive interactions exist between the individual quanta the particles can settle into bound states: localized solutions that are (meta)stable and have well defined properties. We expand and enhance the understanding of these configurations, focusing on real scalar field theories. The thesis is centered around five research works [1–5]. In the first part we give a broad introduction to the topic of many-particle bound states in quantum field theory, focusing on the aspects most relevant to the papers on which this thesis is based. In [1] we construct multi-field oscillons and highlight how these objects form in the early Universe. In [2] we show that multi-field wave dark matter is a viable extension of the popular ULDM paradigm, with better agreement to experimental data in certain areas. In [3] we elucidate the resonant structure of oscillons in the Sine-Gordon model, showing that a tower of long lived excited states exists. In [4] we find a new type of oscillon solution dubbed *soft oscillons*, that contrary to common lore can have arbitrary longevity in gapless theories. Finally, in [5], we assess the accuracy of various approximation schemes used to extend the validity of the semiclassical limit of many-particle bound states.

Contents

I Theoretical introduction **9**

1 Why bound states matter **10**
1.1 In quantum theory . . . 11
1.2 The difference between fermions and bosons . . . 12
1.3 Oscillons, Q-balls and boson stars . . . 14

2 Many-particle states and classical fields **17**
2.1 Revisiting the Bose-Einstein Condensate . . . 17
2.2 The semiclassical limit . . . 19
2.2.1 The coherent state picture . . . 20
2.2.2 Classical nonlinearities and quantum breaktime . . . 21

3 The different types of many-particle bound states **24**
3.1 Compact boson stars . . . 24
3.2 Why we can neglect the curvature of spacetime . . . 26
3.2.1 Oscillons . . . 27
3.3 The nonrelativistic regime . . . 33
3.3.1 Including Newtonian Gravity . . . 35
3.3.2 Nonrelativistic non-topological solitons . . . 36

4 The phenomenology of many-particle bound states **39**
4.1 Oscillons from preheating . . . 39
4.1.1 Oscillon formation . . . 42
4.1.2 Gravitational waves from oscillons . . . 46
4.2 Ultra Light Dark Matter solitons . . . 47
4.2.1 CDM and the problems on small scales . . . 49
4.2.2 Formation of gravitational solitons in ULDM . . . 50
4.2.3 The core-halo relation . . . 53

5 Results and discussion **55**
5.1 Phenomenology of multi-field non-topological solitons . . . 55
5.1.1 Paper 1. Symmetric multi-field oscillons . . . 56
5.1.2 Paper 2. Core and halo properties in multi-field wave dark matter 57
5.2 Discovery and description of new oscillon states . . . 59
5.2.1 Paper 3. Oscillon spectroscopy . . . 59
5.2.2 Paper 4. Soft oscillons . . . 60
5.3 Testing methods of semiclassical backreaction . . . 61
5.3.1 Paper 5. Semiclassical backreaction: a qualitative assessment . . 62
5.4 Concluding remarks . . . 63

II Papers 78

6 Symmetric multi-field oscillons 79

7 Core and halo properties in multi-field wave dark matter 126

8 Oscillon spectroscopy 165

9 Soft oscillons 203

10 Semiclassical backreaction: a qualitative assessment 261

List of publications

This thesis is submitted for assessment in partial fulfillment of the requirements of the PhD in Physics program at the Universitat Autònoma de Barcelona. It consists of a collection of five papers, which are listed below. After an introduction in Part I, the five papers are displayed in Part II. The articles can broadly be divided into three distinct subtopics.

Phenomenology of multi-field non-topological solitons

[1] F. van Dissel and E. I. Sfakianakis, *Symmetric multifield oscillons*, *Physical Review D* **106** (2022)

[2] F. van Dissel, M. P. Hertzberg and J. Shapiro, *Core and halo properties in multi-field wave dark matter*, *Journal of Cosmology and Astroparticle Physics* **2024** (2024) 077

Discovery and description of new oscillon states

[3] F. van Dissel, O. Pujolàs and E. I. Sfakianakis, *Oscillon spectroscopy*, *Journal of High Energy Physics* **2023** (2023)

[4] F. van Dissel and O. Pujolàs, *Soft oscillons*, 2505.00890

Testing methods of semiclassical backreaction

[5] F. van Dissel and G. Zahariade, *Semiclassical backreaction: A qualitative assessment*, *Physical Review D* **111** (2025)

Part I
Theoretical introduction

1 Why bound states matter

Life is suffering. This is one of the four noble truths that was preached by Siddhartha Gautama during the conception of Buddhism. Although the phrase is usually interpreted from a human perspective, its meaning extends to all forms of being. It is doubtful that the Buddha was thinking about nucleons, molecules, or even stars when conceptualizing his philosophy, but chances are that these would prefer to void their existence if given the opportunity. In fact, most physical states evolve in such a way as to reach this ultimate goal. Isolated neutrons decay after about fifteen minutes. Large molecules tend to break down under the right conditions. Stars collapse when their nuclear fuel runs out. As the human experience has taught us, it takes effort to exist, and most physical systems can not provide that conscious struggle.

It helps to stick together. As we might lean on our loved ones for support, so too can interacting states lower each others burden. The 'burden' in the context of physics refers to the energy of the system, and it is therefore not surprising that many physical models with attractive forces contain composite objects that lower the mass of each individual component by adding a negative interaction energy to it. The whole becomes lesser than the sum of its parts. This property allows composites to be the most stable and long-lived configurations in many theories. For this reason *bound states*, as these objects have come to be known, play a central role in our understanding of nature. From the tiniest atom to the largest galactic clusters, bound states are everywhere in our Universe.

The history of human understanding of bound states goes back to the beginnings of natural philosophy itself. In the fourth century BC Aristotle wrote in *Metaphysics* [6] that the Universe consisted of a set of nested, concentric spheres, with our planet at its center. He envisioned that all the celestial bodies observed from earth were confined to perfect circular orbits on these celestial spheres. Ptolemy later developed this into the geocentric model of the Universe, published in *Almagest* [7] in the 2nd century AD. This model would provide the dominant worldview for the next 1400 years. Earlier conceptualizations of bound states can be found in the work of Democritus (circa 460 - 370 BC) who conceived of every substance as a collection of indivisible building blocks he called *atomos* (ancient Greek for "uncuttable") [8]. In his view, everything around us is a bound state, and modern physics agrees with him.

These examples show that the concept of boundedness has always played an important role in the natural sciences. However, it is not until the scientific revolution that a concise mathematical definition of a bound state can be found. In book III of the *principia* [9], Newton calculates at which speeds a projectile can orbit the earth and is consequently be bound to it. This can readily be computed using the concept of energy. A projectile of mass m moving with velocity v at a distance of R from the center of the earth with mass M, has a kinetic and gravitational contribution to its

total energy

$$E = E_g + E_k = -\frac{GMm}{R} + \frac{1}{2}mv^2 \tag{1}$$

In order for the projectile to escape the clutches of the earth its energy must correspond to that of a free object with positive mass and real velocity at spatial infinity. This condition translates into the requirement that $E > 0$, which immediately leads to the famous expression for the escape velocity

$$v_{esc} = \sqrt{\frac{2GM}{R}} \tag{2}$$

Any object orbiting with a speed below this threshold at a distance R from the center of the earth will forever be bounded to it. This simple example highlights an important property of bound states. Namely, bound states exist when attractive interactions, in this case gravity, contribute negative energy to the system, leading to an overall decrease with respect to the free theory. This negative energy can disallow certain asymptotic free states (in this case at spatial infinity), leading to (quasi-)stable composite objects. Over the last century, through the development of quantum theory, it has become clear that not only the macroscopic objects in our solar system are instances of bound states, but that in fact all matter is composed of elementary particles sticking together to lower their collective energy.

1.1 In quantum theory

The discovery of the electron by Joseph Thomson in 1897 and the ensuing discovery of the atomic nucleus in 1911 by Ernest Rutherford showed that matter itself is made out of bound states, albeit of a size much smaller than the orbits of planets in the solar system. As hypothesized by Democritus, some 2000 years earlier, it became clear that everything we interact with in the Universe is made out of a set of fundamental building blocks that were named *atoms* in honor of the ancient Greek philosopher. The boundedness of the fundamental components is enabled by the Coulomb interaction between a positively charged nucleus and a number of negatively charged 'orbiting' electrons. As is the case for planets orbiting the sun, the attractive interaction between positive and negative charges lowers the effective mass of the system. That these type of bound states exist between charged particles might be unsurprising since the Coulomb force and Newton's universal law of gravitation carry the same functional form. This sense of intuition is lost when we add quantum mechanics to the mix.

The foundational experiments of quantum mechanics, performed at the start of the 20th century, showed that the fundamental properties of particles only exist with discrete quantized values. Moreover, particles don't behave as particles at all and are instead best described as waves of probability. In quantum mechanics, the electrons

themselves are not confined to closed orbits. Instead, their probability density is localized near the atomic nucleus. Here probability density refers to the chance of observing the electron in a specific location in space at any given time. This observation immediately leads to the conclusion that only specific configurations for the probability density of the electron are physical. These configurations, called *orbitals*, exist at discrete energies, explaining the spectral lines of atoms. In the quantum world, bound states only exist in certain shapes and sizes.

Strictly speaking, orbitals are bound states of slowly moving particles that don't convert into other particles and whose quantum numbers are conserved over time. By adding relativistic effects to quantum mechanics the framework of quantum field theory was developed. Quantum field theory (QFT) forms the bedrock of modern physics, with exceptional experimental support. Although this framework adds additional decay channels for bound states in the form of number and flavor changing processes, the general ideas remain unchanged. Perhaps the most famous example of a bound state in QFT is positronium, the marriage of an electron and its antiparticle the positron. Positronium decays through the annihilation of its components and QFT is thus required to compute its lifetime. Both the existence and lifetime of positronium have been confirmed experimentally in a multitude of experiments. Measurements of the properties of positronium were a testbed for quantum electrodynamics (QED) in the latter part of the 20th century [10–14], showing once more that bound states form a vital part in both our understanding of nature and our testing of that understanding.

1.2 The difference between fermions and bosons

Positronium is made out of an electron and a positron. Both of these are fermions, particles whose quantum spin number s has a half-integer value. For the electron and positron we have, $s = 1/2$. At a fundamental level, the spin of a particle refers to its transformation properties under spatial rotations. Relativistic spin-1/2 particles, like the electron and positron, are described by the Dirac equation

$$(i\hbar\gamma^\mu\partial_\mu - mc)\,\psi(x) = 0 \tag{3}$$

Where γ^μ are 4×4 matrices that obey the anticommutation relations

$$\{\gamma^\mu, \gamma^\nu\} = 2\eta^{\mu\nu} \tag{4}$$

Solutions of the Dirac equation are four-component vectors called spinors. If one attempts to quantize these objects in terms of creation and annihilation operators, one is led to the conclusion that these also obey anticommutation relations

$$\{\hat{a}_{\vec{k}}, \hat{a}^\dagger_{\vec{q}}\} = (2\pi)^3\delta(\vec{k} - \vec{q}) \tag{5}$$

Where $\hat{a}$ annihilates a fermion to the vacuum and $\hat{a}^\dagger$ creates a fermion from the vacuum. Here, $\delta(x)$ is the Dirac-delta function and $\vec{k}, \vec{q}$ are momenta. This immediately gives us

an important property of fermions. Let's investigate what happens when we attempt to populate two identical fermions in the same quantum state labeled by α

$$|\alpha\alpha\rangle \equiv (\hat{a}_\alpha^\dagger)^2 |0\rangle = -(\hat{a}_\alpha^\dagger)^2 |0\rangle = -|\alpha\alpha\rangle = 0 \tag{6}$$

This state can simply not exist. This is the famous insight summarized in the Pauli exclusion principle:

Identical fermions cannot simultaneously occupy the same quantum state

The hope of finding bound states of many fermions occupying the same state is therefore immediately squashed. This is simply not allowed by the laws of quantum mechanics. This is a pity, as these many-particle states would enhance the study of fundamental physics, as we have seen in the case of positronium. Fortunately, bosons do not have that problem.

Unlike fermions, bosons obey commutation relations, and can therefore occupy the same state. This fact leads to a very interesting phenomena first hypothesized by Satyendra Nath Bose and Albert Einstein in 1925 [15, 16]. They proposed that in the limit of small thermal fluctuations $T \to 0$, a collection of bosons will 'condense' into the collective groundstate of the system. Bose-Einstein condensation was first observed in the lab in 1995, seventy years after the original prediction [17]. The critical temperature T_c below which condensation happens can be estimated by equating the thermal de Broglie wavelength of each boson, to the interparticle separation. Below T_c there is significant overlap between the particles leading to collective behavior. With a gas of single species particles we thus equate

$$\Delta x_{bosons} = n^{-1/d} = \lambda_b = \frac{\hbar}{\sqrt{dmk_bT_c}} \tag{7}$$

Here, n is the number density, d the number of dimensions and m the mass of the individual bosons. We estimate the critical temperature as

$$T_c = \frac{\hbar^2 n^{2/d}}{dmk_b} \tag{8}$$

Note that this temperature also gives an estimate of the velocity of the particles when condensation occurs.

$$\frac{v}{c} \approx \frac{\hbar N}{mL} c \tag{9}$$

Where L is the size of the experimental setup under consideration and N the amount of bosons in the condensate. Taking $L \sim 1$ meter, $N \sim 10^6$ and $m \sim 10^2$ GeV this value becomes

$$\frac{v}{c} \approx 10^{-13} \ll 1 \tag{10}$$

The bosons in the condensate are very nonrelativistic. The collective wavefunction of the condensate is therefore described by the Schrödinger equation. Something particularly interesting happens when there exists a weak attractive interaction between the bosons. It is a good approximation to describe the collective wavefunction with the Gross-Pitaevskii equation in that case

$$i\hbar\dot{\psi}(t,x) = \left[-\frac{\hbar^2}{2m}\nabla^2 + \lambda|\psi(t,x)|^2\right]\psi(t,x) \tag{11}$$

One can find the groundstate of the system by looking for solutions of the time-independent version of this equation. Formally, $\psi(t,x) = e^{-\frac{i\epsilon t}{\hbar}}\Psi(x)$, giving

$$\epsilon\Psi(x) = \left[-\frac{\hbar^2}{2m}\nabla^2 + \lambda|\Psi(x)|^2\right]\Psi(x) \tag{12}$$

In one dimension this equation has an analytic solution. It is

$$\Psi(x) = \frac{N\sqrt{-m\lambda}}{2\hbar}\,\mathrm{sech}\left(\frac{-m\lambda N}{2\hbar^2}x\right) \tag{13}$$

Such that $N = \int dx|\Psi|^2$ represents the total amount of particles. The energy in this state ϵ is given by

$$\epsilon = -\frac{1}{24}\frac{m\lambda^2}{\hbar^2}N^3 \tag{14}$$

The minus sign in front of this expression indicates that this state represents a bound state of N bosons. The relative energy gain due to the attractive interaction is,

$$\frac{|\epsilon|}{E_{free}} = \frac{\epsilon}{mN} = \frac{1}{24}\frac{\lambda^2}{\hbar^2}N^2 \tag{15}$$

The larger the amount of particles in the condensate, the more bound the particles are. This is an explicit example of a many-particle bound state made out of bosons. Since it corresponds to a state with high occupation number, the effects of quantum mechanical fluctuations are suppressed. One of the advantages of bosonic many-particle states is thus that they can be described classically. Although this example focuses on a nonrelativistic bound state with weakly interacting constituents in one dimension, it can be argued that similar objects exist in other limits as well. These show up as classical configurations in nonlinear field theories but they should be thought of as a self-bound state of many interacting bosons. In the last fifty years many of these type of objects have been found with a wide range of applications.

1.3 Oscillons, Q-balls and boson stars

With the understanding that localized, classical field configurations that have a total mass $E \gg m$ correspond to bound states of a large number of bosons, it is worthwhile to search for these solutions. Since they localize many bosons together their

phenomenological effects are much greater than those of the individual quanta. They are therefore ideal testbeds for fundamental physics. The discussion in this thesis will largely be centered around many-particle bound states in (pseudo)scalar field theories. They exist in fields that carry higher spin as well, like vector or tensor fields [18–20], but the vast amount of literature focuses on scalars.

Localized classical field configurations can be split into two categories depending on the origin of their (meta)stability. First, there are *topological solitons*. They owe their stability to the vacuum structure of the theory. When the vacuum is degenerate there is the possibility that the field finds itself in different minima in different regions of space. Topological solitons are the field configurations that interpolate between these regions. Their stability is guaranteed by the boundary conditions of the field. This gives a *topological charge* to the configuration which is conserved within the effective theory. They are characterized by the symmetry group of the vacuum manifold. There are numerous examples of topological solitons and they have found applications in many areas of physics. They include kinks, domain walls, cosmic strings and monopoles.

Second, there are *non-topological solitons*, which as the name suggests don't owe their existence to the topology of the vacuum. Instead they depend on nonlinearities to counteract the dispersive tendencies of free waves. Derrick's theorem showed that these solutions are necessarily nonstationary in three dimensions (or higher) [21]. For that reason, the field configuration is subject to oscillatory motion. They are typically only stable if the theory is endowed with a global symmetry, or if the theory is integrable. Otherwise, they decay through annihilation of multiple bosons within the bound state leading to a (classical) radiation tail. The radiation tail can be very small resulting in lifetimes much larger than the natural timescale of the model m^{-1}. Even when they are not exactly stable we will refer to these solutions as solitons, since their properties are changing slowly. We focus exclusively on non-topological solitons in this thesis, so some historical context is in order.

Arguably the first discovery of a non-topological soliton was made in the context of General Relativity. In two seminal papers [22, 23] from 1968 and 1969 respectively, it was shown that a boson condensate can form gravitationally bound structures, akin to stars. Nowadays, boson stars have found numerous applications in cosmology as potential dark matter candidates [24–30] and sources of gravitational waves [31, 32] and electromagnetic radiation [33]. A few years later, in 1973, stable solitons were found in the Sine-Gordon model [34, 35]. These 'breathers' as they were called, are stable because the Sine-Gordon model is integrable. This property allows the classical field configuration to be quantized in the full QFT picture [36–38]. Breathers only exist in one spatial dimension, and their applications are therefore somewhat limited. In 1985, Sydney Coleman showed that stable non-topological solitons exist in higher dimensions without the need for gravity [39]. In complex scalar field theories with a global

$U(1)$ symmetry, the conserved charge forces certain solutions to remain localized. The charge of these Q-balls counts the total amount of particles in the state.

Sine-Gordon breathers and Q-balls are examples of non-topological solitons that are stable. In generic scalar field theories, that contain no (global) symmetry and are not integrable, these solutions generally don't exist. Classical solutions that decay but have a lifetime much larger than the natural timescale of oscillation of the field can still be of interest. To this end, a new class of bound states were discovered in 1976 by Bogolyubsky and Makhankov in a real scalar field theory with quartic selfinteractions [40, 41]. These localized, oscillating field configurations were found as a general attractor of bubble collapse. They were initially dubbed as pulsons but their subsequent rediscovery by Marcelo Gleiser in the 1990's led to them becoming known by their current name, oscillons [42, 43]. There are very few requirements for the existence of oscillons in a theory, making them the most generic non-topological soliton. They form in many models of the early Universe and their formation is accompanied by a gravitational wave signature that has made them of observational interest in recent years [44–50].

Although many advances have been made in the study of non-topological solitons, most research centers around simple setups with few degrees of freedom. They offer enticing phenomenological tests of physics at the most fundamental scale. From this point of view open questions remain. Many UV-completions of the Standard Model [51–56], as well as the Planck-2018 results [57], favor high energy models with many scalar degrees of freedom. The *String Axiverse* [56], for example, argues that String theory predicts the existence of a plethora of (pseudo)scalar fields in the Universe. We have argued in this chapter that bound states have always played an important role in understanding physics at the most fundamental scale. Finding and understanding the properties of many-particle bound states in realistic models is therefore of vital importance. In this thesis we take a step in this direction, by describing novel states in more realistic models, testing the validity of their classical description, and unraveling the phenomenology of multi-field non-topological solitons.

2 Many-particle states and classical fields

In chapter 1 we alluded to many different types of non-topological solitons. We claimed that these classical field configurations should be understood as bound states of many individual bosons. The aim of this chapter is to make the connection between classical field theory and many-particle bound states in QFT. We will argue that classical configurations correspond to quantum mechanical states at high occupation number.

2.1 Revisiting the Bose-Einstein Condensate

Before discussing relativistic quantum fields, it is useful to briefly revisit Bose-Einstein condensates. As we'll see, they offer an explicit connection between a quantum mechanical and classical description of bosons, and serve as a good analogy for the connection between quantum mechanical and classical fields. The many-particle Hamiltonian of a set of N identical bosons of mass m interacting via contact interactions can be written as,

$$\hat{H} = \sum_{i=1}^{N} \frac{\hat{p_i}^2}{2m} + V_{ext}(\hat{x_i}) + \lambda \sum_{\langle i,j \rangle} \delta(\hat{x_i} - \hat{x_j}) \tag{16}$$

Where $\hat{p_i}, \hat{x_i}$, represent the momentum and position of the ith boson, and $\langle i, j \rangle$ indicates that we take the sum over all pairs of particles. Note that it is virtually impossible to find the $3N$-dimensional eigenstates of (16), especially in the limit that $N \to \infty$. However, we are interested in describing a state that is 'condensed', meaning that the bosons occupy the same state. One can therefore use a *mean field* ansatz, assuming that all the bosons occupy the same single-particle state. The collective wavefunction factorizes,

$$\Psi(t, x_1, x_2, ...x_N) = \prod_{i=1}^{N} \psi(t, x_i) \tag{17}$$

Note that with this ansatz the expectation value for the number density is given by $\langle n(t,x) \rangle = N|\psi(t,x)|^2$. The interaction energy of all the bosons can be computed immediately,

$$\langle \Psi | \, \lambda \sum_{\langle i,j \rangle} \delta(\hat{x_i} - \hat{x_j}) \, | \Psi \rangle = \lambda \, \frac{N\,(N-1)}{2} \int dx \, |\psi|^4 \tag{18}$$

and the Schrödinger equation reduces to a classical equation describing the average particle density in the condensate, the Gross-Pitaevskii equation written in (11), with the redefinition of the collective wavefunction as $\Psi(t,x) = \sqrt{N}\,\psi(t,x)$. For clarity we write it here again,

$$i\hbar\,\dot{\Psi}(t,x) = \left[-\frac{\hbar^2}{2m}\nabla^2 + \tilde{\lambda}|\Psi(t,x)|^2 \right] \Psi(t,x) \tag{19}$$

With $\tilde{\lambda} \approx \lambda\,(1 - 1/N)$. Bose-Einstein condensates thus make an explicit connection between the many-body particle wavefunction and a macroscopic observable, the number density.

The mean field approximation in eq. (17) assumes that all N particles are condensed into the same state. This assumption is accurate for bosons in the limit of vanishing temperature $T \to 0$ and no interactions $\lambda \to 0$, however one generally expects corrections to the Gross-Pitaevskii equation, describing the number density of condensed particles. The question is, how big are these corrections? We can understand this schematically by considering what happens if one of the particles is not in the groundstate condensate but is instead in some exited state $|\alpha\rangle$. The many-particle wavefunction can now be written as,

$$\Psi(t, x_1, x_2, ...x_N) = \frac{1}{\sqrt{N}} \sum_{j=1}^{N} \psi_\alpha(t, x_j) \prod_{i \neq j}^{N} \psi(t, x_i) \tag{20}$$

This will give a correction to the interaction energy of the many-body Hamiltonian,

$$\langle \Psi |\, \lambda \sum_{\langle i,j \rangle} \delta(\hat{x_i} - \hat{x_j})\, |\Psi\rangle = \lambda\, \frac{(N-1)\,(N-2)}{2} \int dx\, |\psi|^4 + \lambda\,(N-1) \int dx |\psi_\alpha|^2 |\psi|^2 \tag{21}$$

The relative correction to the total interaction energy is of $\mathcal{O}(1/N)$. The correction to Gross-Pitaevskii equation describing the number density in the condensate can then be written as,

$$i\hbar\, \dot{\Psi}(t, x) = \left[-\frac{\hbar^2}{2m} \nabla^2 + \tilde{\lambda} |\Psi(t, x)|^2 \right] \Psi(t, x) + \frac{\tilde{\lambda}}{2} \frac{|\Psi_\alpha(t, x)|^2}{N} \Psi(t, x) \tag{22}$$

with $\Psi_\alpha(t, x) = \sqrt{N} \psi_\alpha(t, x)$. In the limit of $N \to \infty$ the condensate is perfectly described within the mean field approximation. With a large number of particles in the condensate, the many-particle wavefunction is described by a classical equation related to the number density (and velocity) in the condensate. Note that this proof is somewhat schematic. See [58–60] for more precise derivations.

Bose-Einstein condensates show that the entire wavefunction of a many-particle system made out of bosons can be described by classical equations of motion, when many bosons occupy the same state. This gives an explicit example for which quantum states describing states of many particles can be described classically. In this thesis we will be interested in relativistic quantum field theories where the particle number is not conserved, so Bose-Einstein condensation does not occur in the same way as it does in quantum mechanics, but it nonetheless serves as a useful analogy. In what follows we'll show that classical limit of these theories can also be thought of as a quantum state at large occupation number.

2.2 The semiclassical limit

We take a general model of a massive real scalar field. We will include the gravitational sector in later discussions. In what follows we set $c = 1$, but keep $\hbar$ explicit as it is essential in understanding semiclassics. The action is written as

$$S = \int d^4x \left[\frac{1}{2}\eta^{\mu\nu}\partial_\mu\phi\partial_\nu\phi - \frac{1}{2}m^2\phi^2 - V_{nl}(\phi) \right]. \tag{23}$$

The nonlinear potential of the scalar $V_{nl}(\phi)$ encodes the self-interactions of the field. It can in principle have any functional form, so to keep our discussion general we simply write

$$V_{nl}(\phi) = \sum_{i=3}^{\infty} \frac{\lambda_n}{n!}\phi^n \tag{24}$$

The action of (23) represents a quantum field theory. The degrees of freedom should therefore be promoted to operators acting on some quantum state. The classical fields correspond to a particular limit of the QFT. They are associated to the lowest order contribution in the semiclassical expansion. We can find classical solutions by looking for an extremum of the action

$$\left.\frac{\delta S[\phi]}{\delta\phi}\right|_{\phi=\phi_c} = 0 \tag{25}$$

Where ϕ_c is the classical field. With this in mind we can perform a functional Taylor expansion of the action around ϕ_c. By virtue of eq. (25) the first order term is 0. We have

$$S[\phi] = S[\phi_c] + 0 + \int \mathrm{d}^4x\, \mathrm{d}^4y\, \eta(x)\, S^2[\phi_c]\, \eta(y) + ..., \tag{26}$$

with the definitions $\eta(x) \equiv \phi_c - \phi(x)$ and $S^2[\phi_c] \equiv \left.\frac{\delta^2 S}{\delta\phi(x)\delta\phi(y)}\right|_{\phi=\phi_c}$ and similarly for higher order terms. The validity of the semiclassical expansion becomes evident if we rescale the variable $\eta(x) \to \hbar^{1/2}\Delta(x)$. The quantum path integral can be written as

$$Z \sim \int \mathcal{D}\phi e^{\frac{i}{\hbar}S[\phi]} \approx e^{\frac{i}{\hbar}S[\phi_c]} \int \mathcal{D}\Delta e^{i\int \mathrm{d}^4x\, \mathrm{d}^4y\, \Delta(x)\, S^2[\phi_c]\, \Delta(y) + \mathcal{O}(\hbar^{1/2})} \tag{27}$$

With this definition it becomes explicit that fluctuations away from ϕ_c scale with powers of $\hbar$. For example, here $\langle \mathcal{T}\eta(x)\eta(y)\rangle \sim \hbar\langle \mathcal{T}\Delta(x)\Delta(y)\rangle = \mathcal{O}(\hbar)$. In the limit of $\hbar \to 0$ we only need to consider the classical path. This simple argument shows how to recover the classical limit, but it is not clear at this point what the conditions are on ϕ_c for fluctuations to be safely ignored. Intuitively, if the classical field is 'small' radiative corrections to the classical dynamics can become important. This is the case for the famous Coleman-Weinberg potential [61]. However, we will argue that for many-particle states quantum fluctuations can be safely ignored.

2.2.1 The coherent state picture

In canonical quantization, the field variables are promoted to operators, while observables are interpreted as the expectation values of operators acting on a quantum state. The classical field is simply the one-point function of the field operator,

$$\phi_c \equiv \langle \hat{\phi} \rangle = \langle \alpha | \, \hat{\phi} \, | \alpha \rangle \tag{28}$$

With this definition, not all states $|\alpha\rangle$ result in a 'classical' evolution of ϕ_c. That is to say, the one-point function isn't typically a solution of the Euler-Lagrange equations. To understand which states are and aren't 'classical', we write the Hamiltonian of the model in (23) in Fourier space. Assuming the model is defined in a cubic box of volume $V = L^3$ with periodic boundary conditions, the system is described by a discrete set of modes,

$$\mathcal{H} = \frac{1}{L^3} \sum_{\vec{n}} \left(\frac{1}{2} \left| \dot{\phi}_{\vec{n}} \right|^2 + \frac{\omega_k^2}{2} \left| \phi_{\vec{n}} \right|^2 \right) + \mathcal{H}_{int} \tag{29}$$

Where $\mathcal{H}$ is the Fourier transform of the nonlinear part of the action and we define $\omega_k^2 = k^2 + m^2$. The wavenumbers are discretized with $\vec{k} = \frac{2\pi}{L} \vec{n}$ and $\vec{n} = (n_x, n_y, n_z) \in \mathbb{Z}^3$. It is straightforward to quantize this theory as the Hamiltonian is now explicitly equivalent to a sum of interacting harmonic oscillators. Of course, this is done in many standard QFT textbooks [62, 63], but we repeat it here to support our reasoning. The linear part of the quantized Hamiltonian can be written as

$$\hat{\mathcal{H}} = \sum_{\vec{n}} \hbar \omega_k \left(\hat{a}_{\vec{n}}^\dagger \hat{a}_{\vec{n}} + \frac{1}{2} \right) = \sum_{\vec{n}} \hbar \omega_k \left(N_{\vec{n}} + \frac{1}{2} \right) \tag{30}$$

At the non-interacting level, each k-mode represents a different quantum harmonic oscillator, and $\hat{N}_{\vec{n}}$ counts the amount of particles in each mode. The noninteracting quantum Hamiltonian (30) contains states whose one-point function solves the classical equations of motion; namely coherent states. A coherent state $|C\rangle$ is an eigenstate of the annihilation operator,

$$\hat{a}_k \, |C\rangle_k = C \, |C\rangle_k \tag{31}$$

Note, in particular that the vacuum is a coherent state ($\phi_c = 0$ is a good classical solution). Under unitary time evolution coherent states remain coherent (bar interactions). The time evolved expression is

$$|C(t)\rangle_k = e^{-i\frac{\omega_k t}{2}} e^{-\frac{|C(0)|^2}{2}} \sum_{i=0}^{\infty} \frac{C(0)^n}{\sqrt{n!}} e^{-in\omega_k t} \, |n\rangle_k \tag{32}$$

It is straightforward to show that the quantity $|C|^2 = \langle \hat{N}_{\vec{n}} \rangle$, the expectation value of the number operator. It counts the average number of particles in the state, and is conserved over time. The wavefunction of the field variable $\psi(\phi_{\vec{n}})$ is a Gaussian whose

width corresponds to the minimal uncertainty allowed by quantum mechanics, and whose mean tracks the classical (linear) equations of motion.

$$\langle\hat{\phi}_{\vec{n}}\rangle = \phi_{\vec{n}}(t=0)e^{-i\omega_k t}, \quad \langle\hat{\phi}^n_{\vec{n}}\rangle = \langle\hat{\phi}_{\vec{n}}\rangle^n + \mathcal{O}(\hbar) \tag{33}$$

Coherent states are the best approximation to classical dynamics within the framework of quantum theory. Unfortunately, the interacting Hamiltonian, $\hat{\mathcal{H}}_{int}$, causes the coherent state to 'break'; in other words (32) isn't a solution of the full nonlinear Schrödinger equation. Even though we can imagine a state that evolves classically, interactions inevitably cause a deviation from the classical path. On the other hand, the interaction terms are also responsible for the existence of the localized classical field configurations that we'll discuss in this thesis. These necessarily require classical nonlinearities to remain bounded. One might therefore think it is inconsistent to include classical nonlinearities while neglecting quantum effects. We will now show that these two effects enter at different orders of the occupation number of the coherent state.

2.2.2 Classical nonlinearities and quantum breaktime

Imagine a classical field that looks like a standing wave with wavenumber $\vec{k}$,

$$\phi(t,\vec{x}) = \phi_0 \cos(\vec{k}\cdot\vec{x})\cos(\omega_k t) \tag{34}$$

The quantum state whose one-point function mimics these dynamics (in the linear theory) is the coherent state that populates the $\vec{k}$ and $-\vec{k}$ modes of the field with an average amount of particles in the volume V

$$N = \frac{\phi_0^2\omega_k V}{2\hbar} = \frac{\phi_0^2}{2\hbar\omega_k^2} \tag{35}$$

while all the other modes are kept in their vacuum (empty) state. Note we have taken the box size to be $V = \omega_k^{-3}$. Now, an important scaling emerges. The field amplitude ϕ_0 and the mode frequency ω_k, are just classical variables that are insensitive to quantum mechanics. The classical limit $\hbar \to 0$ is equivalent to sending the average number of particles $N \to \infty$, while keeping the classical variables fixed. We thus conclude that classical fields correspond to quantum states with a large occupation of particles. Equivalently, we can say that we can ignore quantum effects if the state contains a lot of particles. Equation (35) tells us that this is the case when the amplitude of the classical field is large.

As alluded to, the coherent state is not a solution of the full nonlinear theory. Interactions will induce scatterings (and rescatterings) between the particles in the coherent state. Scattered particles will not in general 'populate' the original coherent state. The initially coherent state will thus necessarily become less coherent over time, until after some point in time the evolution of the one-point function is no longer a

solution of the classical Euler-Lagrange equations. The classical field will no longer be truly classical at this point. The time at which the classical description of the field fails has been dubbed the 'quantum breaktime' in the literature [64, 65]. A sketch of this phenomenon is given in fig. 2. We can estimate the value of the quantum breaktime by computing how long it takes for all the particles in the coherent state to scatter at least once. Taking the potential in (24) and the coherent state representing the classical field in (34), we see that the leading processes are $2 \to 2$ scatterings. The scattering rate is proportional to the dimensionless coupling constant $\hbar\lambda_4 \equiv \alpha$. In a volume $V = \omega_k^{-3}$, the rate at which two particles scatter off each other is given by the rate of the individual process α^2 times the amount of pairs of particles that are available within the volume $\sim N^2$. The total rate of scatterings in the condensate is therefore,

$$\Gamma \approx (\alpha N)^2 \tag{36}$$

The breaktime is estimated to be the time after which order N of such scatterings have taken place,

$$t_{br} \sim \frac{N}{(\alpha N)^2} \tag{37}$$

The quantity $\alpha N = \frac{\phi_0^2 \lambda_4}{2\omega_k^2}$ is called the collective coupling. It doesn't depend on $\hbar$ and is determined entirely by classical variables. It therefore has a fixed value in the semiclassical limit $\hbar \to 0$, and we'll see that it controls the strength of classical nonlinearities. Indeed, the quantum breaktime in (37) goes to infinity in the semiclassical limit $N \to \infty$ and $\alpha N =$ constant. Of course, eq. (37) is but a simple estimate. The actual value of the breaktime depends on the exact background dynamics of the classical background. In particular, if the background is unstable the scaling of the breaktime gan go like $\log(N)$ instead of N. Various methods to extend the validity of the semiclassical approximation have been introduced in the literature [66–74]. Exploring the breaktime of classical variables in these various approximations is the main focus of [5], where we explore this topic in a toy setup with only two (and three) coupled oscillators.

So far we've only discussed states whose one-point function mimic the linear equations of motion. Localized classical field configurations necessarily depend on nonlinearities to exist. But we just concluded that nonlinearities cause a breaking of the classical description. Indeed, our discussion would be more accurate if we were able to construct states whose one-point function obeys the full nonlinear system of equations. Although this should formally be possible, it is usually impossible in practice. One can see that this should be possible however, by inspecting the classical equations of motion,

$$\ddot{\phi} - \nabla^2\phi + m^2\phi + V'_{nl}(\phi) = 0 \tag{38}$$

It is clear that classical nonlinearities become important when $V'_{nl}(\phi) \sim \omega_k^2\phi$. Looking at the quartic term, we see that this happens when the amplitude of oscillation ϕ_0

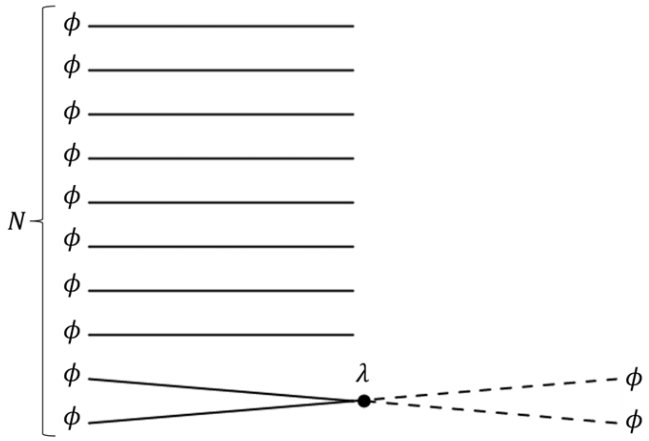

Figure 2: A large occupation number coherent state of N particles will continuously lose particles by quantum scatterings to particles that are not part of the coherent state. After enough time this phenomenon will lead to what is known as *quantum breaking*.

obeys,

$$\lambda_4 \, \phi_0^2 \approx \omega_k^2 \quad \Rightarrow \alpha N \sim 1 \tag{39}$$

So, in other words, classical nonlinearities are controlled by the value of the collective coupling αN. They should therefore be parametrically more important than quantum breaking effects that have an additional $1/N$ suppression. This makes it seem reasonable that classical fields, even considering nonlinearities, correspond to coherent states with large occupation number.

Note that this situation is analogous to the mean-field approximation used to study Bose-Einstein condensates. There, the interaction term in the many-particle Hamiltonian induces corrections to the Gross-Piteavskii equations that scale inversely with the amount of particles in the condensate. The classical equations of motion in a relativistic quantum field theory can also be understood as a mean-field approximation, where we replace nonlinear terms in the Heisenberg equations of motion $\sim \langle \hat{\phi}^n \rangle \approx \langle \hat{\phi} \rangle^n + \mathcal{O}(1/N)$. This is warranted if we are dealing with coherent states, and the classical equations of motion are accurate if $N \gg 1$, just as is the case for a BEC. One can wonder what happens to the initially coherent classical state after the quantum breaktime. It has been argued that a localized quantum remnant can remain for times way beyond the quantum breaktime [75–77].

In the next chapter we will highlight different types of localized classical field configurations, which as we've argued here, are many-particle bound states in the full quantum theory.

3 The different types of many-particle bound states

In the last chapter we arrived at the conclusion that taking the classical limit of a quantum field theory corresponds to considering states with a large occupation of particles. A classical field configuration that localizes energy should therefore be equivalent to a quantum state of many bosons. In this chapter we investigate various types of many-particle bound states by considering localized classical configurations. Again, we focus on a real scalar, minimally coupled to gravity. In the previous discussion we neglected the gravitational sector but we will consider it here as there is no ambiguity in treating it when $\hbar \to 0$. Note that here on out we use natural units $c = 1$ and $\hbar = 1$.

3.1 Compact boson stars

Let's consider the classical action

$$S = \int d^4x\sqrt{-g}\frac{R}{16\pi G} + \int d^4x\sqrt{-g}\left[\frac{1}{2}g^{\mu\nu}\partial_\mu\phi\partial_\nu\phi - \frac{1}{2}m^2\phi^2 - V_{nl}(\phi)\right] \tag{40}$$

The goal will be to find field configurations that are (quasi)stable and concentrate significant energy $E \gg m$ in a localized region of space. In three dimensions static localized configurations are unstable [21] to collapse, so the relevant field configurations have some time dependence (typically an oscillating motion). The full set of equations we need to solve is

$$G_{\mu\nu} = 8\pi G\, T_{\mu\nu} \tag{41}$$

$$-\frac{1}{\sqrt{-g}}\partial_\mu(\sqrt{-g}g^{\mu\nu}\partial_\nu\phi) = m^2\phi + V'_{nl}(\phi) \tag{42}$$

The set of equations (41) and (42) are called the Einstein-Klein-Gordon equations, describing the dynamics of a real scalar in General Relativity. Without specifying $V_{nl}(\phi)$, a localized solution of this set of equations represents the most generic non-topological soliton one can have, made out of real scalar particles. Since the energy-momentum tensor depends quadratically on the field ϕ, one looks for configurations with a time-dependent scalar field $\phi(t, r)$, but a static $T_{\mu\nu}$, such that the spacetime metric is time-independent. Since the lowest energy configurations are expected to be spherically symmetric, one takes the following ansatz for $g_{\mu\nu}$,

$$ds^2 = -A(r)^2dt^2 + B(r)^2dr^2 + r^2d\Omega^2, \tag{43}$$

and for the scalar

$$\phi(t, r) = \Phi_0(r)\cos(\omega t) \tag{44}$$

Unfortunately, these ansatzes do not close the system of EKG-equations (41) and (42). Instead nonlinear terms induce higher harmonics in $\phi \propto \cos(j\omega t)$ with j an integer, that

in turn induce an oscillating metric. These higher harmonics are ultimately responsible for the decay of the solution. Many-particle bound states of real scalars are therefore a tower of harmonics

$$\phi(t,r) = \sum_{j,odd}^{\infty} \phi_j(r)\cos(j\omega t) \tag{45}$$

$$A(t,r) = \sum_{j,even}^{\infty} A_j(r)\cos(j\omega t) \tag{46}$$

$$B(t,r) = \sum_{j,even}^{\infty} B_j(r)\cos(j\omega t) \tag{47}$$

Where we assumed parity in the nonlinear potential $V_{nl}(\phi) = V_{nl}(-\phi)$. By plugging this ansatz into the EKG-equations we can solve for the set of $\{\phi_j, A_j, B_j\}$ numerically. Although the solution isn't asymptotically bounded, and spacetime isn't asymptotically flat, one can show that the series converges quickly. In practice one only needs to solve the system up to some finite value j_{max}. The radiation tail can become so small that the typical lifetime exceeds the age of the Universe by many orders of magnitude. For many purposes these *oscillatons* are stable [78].

This situation is somewhat different than bound structures made out of complex scalar particles. In that case the EKG-equations close exactly. Bound structures in complex scalar fields in general relativity have been studied extensively. Their exact stability is ultimately due to the global $U(1)$ symmetry of complex scalar field theories, which conserves the total amount of particles in the solution. These stable counterparts of the real scalar case are called *boson stars*. They are equivalent to oscillatons with $j_{max} = 1$ in eqs. (45), (46) and (47). Since the radiation tails of oscillatons can be very small, they behave similarly to boson stars. They ultimately share the same phenomenology and impact on cosmology; the nature of the fundamental particles is less important, and the following discussion applies both to complex and real scalar fields.

The properties of boson stars have been mapped. They exist, even when the bosons are free, so $V_{nl}(\phi) = 0$. They are held together by general relativistic effects (later we'll see that similar structures exist in Newtonian gravity). The solutions are labeled by the binding energy of the bosons $\frac{\Delta m}{m} = 1 - \frac{\omega}{m}$, which also controls the oscillation period of the macroscopic configuration. Each ω corresponds to a particular boson star, with a mass M_ω. By decreasing ω the solutions become ever more bound. However, numerical studies show that as $\omega \lesssim 0.8m$, the mass of the star starts has reaches a maximum value. This turnaround point indicates an instability as the bosons will undergo gravitational collapse. Boson stars therefore have a maximum mass

$$M_{Max} = 0.633\, M_{Planck}^2/m \tag{48}$$

Since the radius of boson stars R scales with the Compton wavelength with $R \sim \mathcal{O}(10)m^{-1}$ (found numerically), the compactness of these stars is limited to about $\mathcal{C} = GM/R \sim 0.02$. This is very different from black holes and neutron stars and the most basic boson stars therefore don't 'pose' as compact objects in gravitational wave experiments. However, if there exist repulsive interactions between the bosons, the maximum mass of the star increases. The interaction in essence counteracts the tendency to collapse gravitationally. The size of the repulsive coupling $\lambda > 0$ gives parametric control over the maximum mass that scales with $M_{Max} \sim M^3_{Planck}/m^2\sqrt{\lambda}$. With selfinteractions the maximum compactness of the star is increased to $\mathcal{C} \approx 0.16$, which is closer to the value associated to neutron stars. Boson stars with repulsive interactions can therefore have an impact on gravitational wave astronomy, through binary mergers. Compact boson stars have other interesting phenomenological imprints which we discuss briefly in chapter 4.

The configurations we've talked about so far are (approximate) solutions of the full EKG system of equations. Although they are interesting examples of selfbound bosons in general relativity, one can often simplify the mathematical framework by moving to specific limits of the equations. As we'll show this is in most cases enough to study the phenomenological consequences in cosmology of many-particle bound states. The bound states associated to each distinct limit carry different names, but they are in essence derived from the same action (40).

3.2 Why we can neglect the curvature of spacetime

In many cases that are relevant for cosmology and high energy particle physics, one works in a quantum field theory with a certain range of validity. To be precise, the theory is only valid whenever the energy density is smaller than some scale Λ^4. This scale is typically referred to as the *cutoff* of the effective field theory. This means that the natural scale of the field variable is $\phi \sim \Lambda$. For example the potential of the theory can usually be written as,

$$V(\phi) = \frac{1}{2}m^2\phi^2 + m^2\Lambda^2 V_{nl}\left(\frac{\phi}{\Lambda}\right) \tag{49}$$

with $V_{nl}(x) \sim \mathcal{O}(1)$ and $m < \Lambda$ to ensure the validity of the EFT. The cutoff Λ is usually associated to a symmetry breaking scale that occurred at some point in cosmological history. One therefore typically has that $\Lambda \ll M_{Planck}$. This means that in many scenarios we can neglect the effects of spacetime curvature. In essence, the energy-momentum tensor of the bosonic configuration doesn't lead to significant deviation from a Minkowski background. There is a simple way to see this considering we're interested in bosonic 'lumps' of scalar field, that is to say localized field configurations. The size of such a configuration is usually of order of the Compton wavelength of the field $R \sim m^{-1}$, where m is the mass of the bosonic particle. With the EFT potential

in eq. (49) we can estimate the energy in such a lump,

$$E_{lump} \approx N\Lambda^2/m \tag{50}$$

Where $N \sim \mathcal{O}(1)$, a constant that accounts for the amount of bosons in the bound state. Now, computing the compactness of the lump we see that,

$$\mathcal{C}_{lump} = G\frac{E_{lump}}{R} \approx \left(\frac{\Lambda}{M_{Planck}}\right)^2 \ll 1 \tag{51}$$

The compactness of lumps is therefore negligible. Note that one can certainly have situations where stable lumps exist with $N \gg 1$ in (50), or alternatively $R \ll m^{-1}$, such that the $\mathcal{C} \sim 0.5$. This is what happens for the compact boson stars discussed in the previous section. However, the EFT perspective tells us that these solutions are less likely to form dynamically. With this in mind, it is useful to look for many-particle bound states that are supported solely by selfinteractions in the potential and neglecting the gravitational sector entirely. Bound states in this limit are referred to as *oscillons* [42, 43, 79–88] and play an important role in this thesis. Note that in the limit of very dilute lumps, namely when $\phi \ll \Lambda$, the dominant attractive interaction becomes gravitational again, albeit in the Newtonian regime. Later, we will show that the weak-field limit is actually equivalent to the nonrelativistic limit, which contains interesting bound states in its own right.

3.2.1 Oscillons

To describe oscillons, we can neglect gravitational effects. In essence the r.h.s. of the Einstein equation (41) is approximately equal to zero, and the background metric $g_{\mu\nu} \to \eta_{\mu\nu}$ is Minkowski. In this thesis we will use the mostly negative signature $\eta_{\mu\nu}$. There is only one relevant equation determining the dynamics in this limit, the scalar field e.o.m.

$$\ddot{\phi} - \nabla^2\phi + m^2\phi + V'_{nl}(\phi) = 0 \tag{52}$$

Any localized lump will clearly disperse if $V_{nl}(\phi) = \text{Const}$. Oscillons depend on nonlinear self-interactions to stay localized. A popular method to estimate their properties is to assume an ansatz for the classical field. Oscillons are field configurations that oscillate with some frequency ω, so the most straightforward approach is to assume that to lowest order,

$$\phi_{osc}(t, \vec{x}) = \Phi(\vec{x})\cos(\omega t) \tag{53}$$

where $\Phi(\vec{x})$ is the spatial envelope of the solution. Since the lowest energy configuration of a localized lump is usually spherical, one imposes $\Phi(\vec{x}) = \Phi(r)$ as well. Plugging eq. (53) into eq. (52) and integrating over one period $T = 2\pi/\omega$, we obtain an ODE for the envelope $\Phi(r)$,

$$\partial_r^2\Phi(r) + \frac{2}{r}\partial_r\Phi(r) - (m^2 - \omega^2)\Phi(r) - V'_{eff}(\Phi(r)) = 0 \tag{54}$$

Where the effective potential is defined as

$$V_{eff}(\Phi) = \frac{1}{\pi}\int_0^{2\pi} dt'\, V_{nl}\left(\Phi\cos(t')\right) \tag{55}$$

From the ODE determining the spatial profile (54) we can extract useful information about some basic requirements for the existence of localized oscillons. First, the boundary condition $\Phi(r) \propto \frac{1}{r}e^{-\sqrt{m^2-\omega^2}r}$ as $r \to \infty$ imposes $m > \omega$, such that the oscillon is decaying and therefore bounded. Moreover, one expects that a localized solution has $\partial_r^2\Phi(r)+\frac{2}{r}\partial_r\Phi(r) < 0$ near $r = 0$. It is easy to see that this implies that $V_{nl}(\phi) < \frac{1}{2}m^2\phi^2$ in that region. Attractive selfinteractions are a necessity for oscillons. It is often said that the potential needs to be *shallower than quadratic*, which boils down to the same thing. If these requirements are met, there are a countable infinite set of solutions of eq. (54) for each value of ω, that satisfy a decaying boundary condition at infinity and regularity at the origin. They are labeled by the amount of nodes n in the spatial profile. The study of oscillons with nodes is the focal point of one of the papers that is a part of this thesis [3]. In general the $n = 0$ oscillons have the lowest energy at fixed ω and are therefore the most relevant states.

One can intuitively understand that localized solutions of eq. (54) exist by mapping the equation to that of a classical oscillator. The dynamics are akin to that of a ball dropped in a hilly landscape with zero velocity (regularity at the origin), where one can think of the radial coordinate in (54) as time. A localized decaying solution corresponds to releasing the ball at just the right height for it to stop at the hilltop at $\Phi = 0$. By continuity, it is obvious that these solutions must exist. A sketch of the situation is given in fig. 3.

Oscillons are metastable: lifetime and decay mechanisms

Although the ansatz of eq. (53) is useful to understand some of the characteristics of oscillons, it obviously doesn't tell the whole story. Similar to what happens for the oscillatons mentioned previously, nonlinearities in the potential source higher harmonics that carry away energy from the fundamental mode. To see that this happens just plug in the oscillon ansatz (53) into the scalar e.o.m. (52),

$$\left(\partial_r^2\Phi(r) + \frac{2}{r}\partial_r\Phi(r) - (m^2-\omega^2)\Phi(r) - V'_{eff}(\Phi(r))\right)\cos(\omega t) = h.h. \tag{56}$$

Where $h.h.$ are terms proportional to $\cos(n\omega t)$ with n odd if the potential is even. By construction the l.h.s. of (56) is zero and the higher harmonics therefore act as a source of perturbations $\delta_n \sim \Phi_n(r)\cos(n\omega t)$. These in turn also source additional harmonics and so on. The full oscillon should be described by a tower of harmonics,

$$\phi_{osc}(t,r) = \sum_{n,odd}^{\infty} \Phi_n(r)\cos(n\omega t) \tag{57}$$

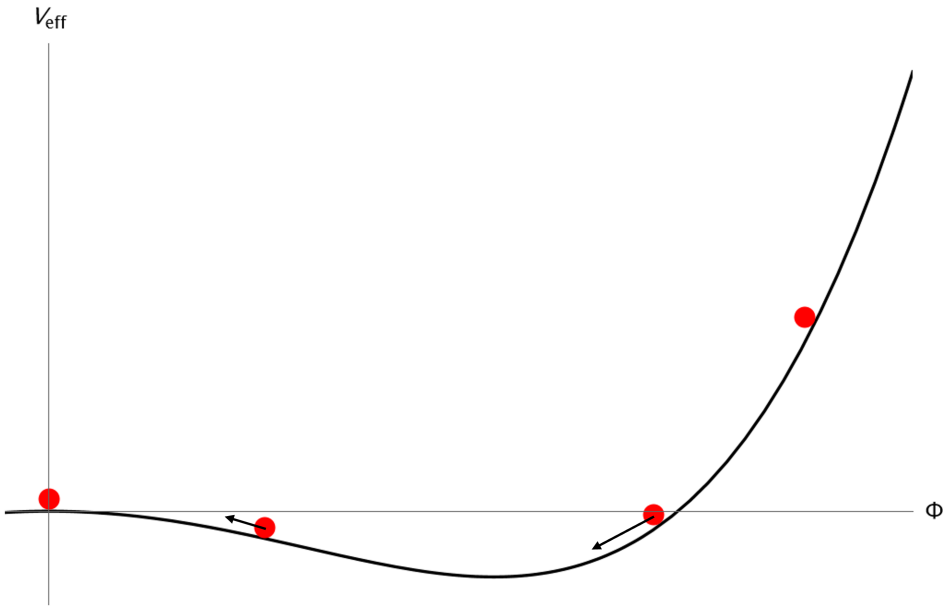

Figure 3: Finding decaying solutions of equation (54) is analogous to releasing a ball in a hilly landscape such that it accelerates and stops exactly at the maximum at $\Phi = 0$. A profile with nodes corresponds to 'overshooting' the maximum but eventually stopping at the hilltop at a later point in 'time'.

Hence, it would seem that the energy of the oscillon is virtually infinite. However, in practice the higher harmonic terms decay quickly enough to avoid this apparent paradox. The fundamental $n = 1$ decaying solution is the dominant mode.

By assuming that $\Phi_1(r) \gg \Phi_{n\geq 3}(r)$ and imposing a maximum harmonic number n_{max} beyond which the sum in eq. (57) is identically 0, we can derive a set of coupled linear ODE's for the modes $\Phi_{n\geq 3}(r)$. The solutions of this set of equations asymptote to $\Phi_n(r) \to e^{-\sqrt{m^2-(n\omega)^2}\, r}$, and for $\omega > m/3$[1] the higher harmonics are therefore radiating modes $\Phi_n(r)\cos(n\omega t) \sim A_n \cos\left(k_n r - \omega_n t\right)/r$, with $k_n = \sqrt{m^2-(n\omega)^2}$, $\omega_n = n\omega$, and A_n the amplitude of the radiating tail. The effect of the higher harmonics is thus to cause energy depletion of the fundamental mode. The set of A_n are determined by solving a linear system of ODE's. Since the equations are linear there are an infinite amount of solutions satisfying the appropriate boundary conditions. One identifies the oscillon with the configurations that minimizes the total energy loss of the solution. Many methods that do this exist in the literature [89–94], one of which is described in our paper [3].

We conclude that an oscillon is only metastable, continuously losing energy through

[1] Almost all oscillons that have been found in the literature obey this constraint. In [4] we describe an oscillon that has $\omega \to 0$, but it is understood in a completely different framework.

classical radiation. Nonetheless, the decay rate can be small leading to extremely long lived oscillons with approximately stable features. Depending on the particulars of the potential under consideration, oscillons have been found with lifetimes between $\mathcal{O}(10^2 - 10^{14})$ oscillation periods [84]. The evolution of an oscillon typically proceeds as follows:

1. A lump of scalar field with size $R \sim m^{-1}$ settles into a coherent oscillating configuration with energy E_ω. The oscillation period is $T = 2\pi/\omega$.

2. The oscillon loses energy at a rate $\dot{E}_\omega$ due to the sourcing of higher harmonics that act as radiation modes.

3. Since the configuration is losing energy it necessarily has to transition to an oscillon with less energy. In practice this means that the oscillon frequency ω increases over time.

4. If no oscillon with smaller energy exists, the configuration quickly dismantles. This process has been dubbed *energetic death* [93] (see text below).

We now describe the main effects that influence this evolution.

Understanding oscillon lifetime and eventual decay

The rate of energy loss of a specific oscillon $\dot{E}_\omega$ will depend on the size of the radiation tails; namely the set of $\{\Phi_{n\geq 3}(r \to \infty)\}$. The exact value of $\dot{E}_\omega$ can depend strongly on the details of the potential. However, there are two generic effects that lower the value of $\dot{E}_\omega$ at specific frequencies ω [93]. These are universal across different models and are worth highlighting in some more detail. Let's focus on the first overtone $\phi_3 \equiv \Phi_3(r)\cos(3\omega t)$, and set all higher harmonics with $n > 3$ identically to zero. This will be enough to illustrate the main points. Assuming $\Phi_1 \gg \Phi_3$, we have a single ODE controlling radiation,

$$\partial_r^2 \Phi_3 + \frac{2}{r}\partial_r \Phi_3 - (m^2 - 9\omega^2)\Phi_3 = -S_3(\Phi_1), \tag{58}$$

where

$$S_n(\phi_1) \equiv \frac{1}{\pi}\int_0^{2\pi} dt'\, V'_{nl}(\Phi_1 \cos(t'))\cos(nt') \tag{59}$$

$$\tag{60}$$

In eq. (58) we ignored the space-dependent mass term of the radiation mode Φ_3, proportional to $\sim V''(\Phi_1)$. Although this term is important to get quantitatively accurate predictions for decay rates, we ignore it here to illustrate the main effects increasing the longevity of oscillons.

We can identify the oscillon radiation mode as the inhomogeneous solution of eq. (58). The solution can be written down immediately using Green's functions,

$$\Phi_3(r) = \frac{\cos(k_3\, r)}{k_3\, r}\int_0^r dr'\, r' \sin(k_3\, r') S_3\left(\Phi_1(r')\right) + \frac{\sin(k_3\, r)}{k_3\, r}\int_r^\infty dr'\, r' \cos(k_3\, r') S_3\left(\Phi_1(r')\right) \tag{61}$$

with the definition $k_3 = \sqrt{(3\omega)^2 - m^2}$ The amplitude of $\Phi_3(r)$ at large distances from the oscillon is determined by the first term in eq. (61). As $r \to \infty$,

$$k_3\, r\, \Phi_3(r) \approx \cos(k_3\, r)\int_0^r dr'\, r' \sin(k_3\, r') S_3\left(\Phi_1(r')\right) \tag{62}$$

When the r.h.s. of eq. (62) becomes 0, the amplitude of radiation, and therefore the decay rate of the oscillon, becomes negligible. Of course, the energy loss never becomes 0 exactly, since the higher harmonics that we neglected will now become the dominant source of radiation. Nonetheless, whenever the r.h.s. of eq. (62) becomes 0 we expect an oscillon with significant lifetime. There are two distinct effects that lead to this; one is model dependent and one is completely generic.

Destructive interference: Without loss of generality, we can rewrite (62) as

$$\int_0^r dr' \left[\sin\left(k_3\,(r'-r)\right) + \sin\left(k_3\,(r'+r)\right)\right] J(r'), \tag{63}$$

with the definition $J(r) \equiv r S_3(\Phi_1(r))$. This way of writing the expression illuminates an important fact. The radiation is simply the sum of an outgoing wave $\propto \sin\left(k_3\,(r'-r)\right)$ and an ingoing wave reflected at the origin $\propto \sin\left(k_3\,(r'+r)\right)$, sourced by the same $J(r)$. For specific background geometries, and therefore for specific fundamental frequencies ω, these waves cancel exactly at the boundary of the oscillon $r \sim R_{osc}$. Since the source terms is 0 beyond this point, the total amplitude of the outgoing radiation suppressed. The value of ω where this cancellation happens is very sensitive to the functional form of $S_3(x)$ and to the shape of the fundamental mode $\Phi_1(r)$. It depends strongly on the model under consideration. Enhancement of the lifetime of the oscillon can in this case be understood as an interference experiment (see left panel in fig. 4).

Geometric Decoupling: In the limit of $m^2 - \omega^2 = \epsilon \ll 1$, the size of the fundamental mode of the oscillon $\Phi_1(r)$ grows unboundedly, scaling with $e^{-\sqrt{m^2-\omega^2}\, r}$. The source term $J(r) = r\, S_3(\Phi_1(r))$ follows suit. The amount of wavelengths of radiation k_3 that fit within the source therefore grows like $\sim m/(m^2-\omega^2)^{1/2} \gg 1$. The fast oscillating term $\sin(k_3\, r')$ in eq. (62) averages to 0, shutting off radiation. Note that geometric decoupling is generic and is expected for every higher harmonic of the oscillon as the frequency of oscillation approaches the mass scale of the field, regardless of the model under consideration. In the next section we will show that the limit of $\omega \to m$ corresponds to an approximate conservation of particles in the oscillon. It is therefore best

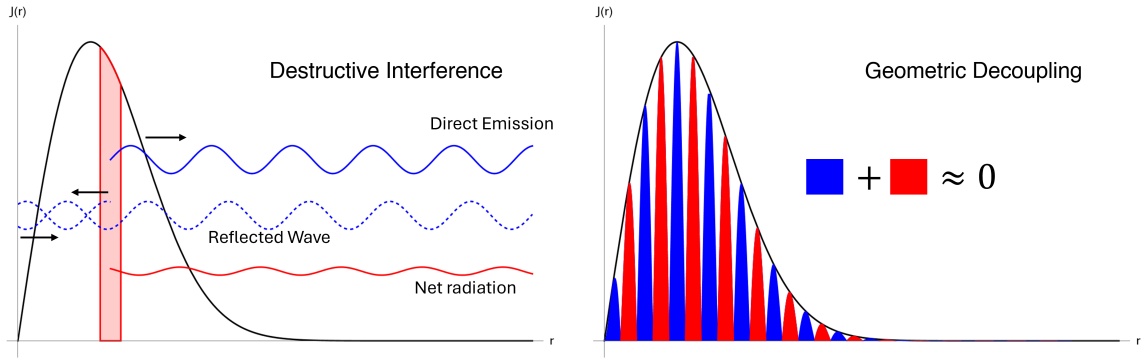

Figure 4: A sketch of the two main reasons for suppression of the decay rate of oscillons. *Destructive interference*: the fundamental mode of the oscillon acts as a continuous source (black background) for the radiation modes (overtones with $\omega > m$). The net radiation is the sum of a direct outgoing wave and a wave that is reflected at $r = 0$. For certain geometries of the source the net radiation is therefore shut off completely. *Geometric decoupling*: As the frequency of the fundamental mode $\omega \to m$, the wavelengths of the radiation modes become shorter and shorter with respect to the source. This means that the quick oscillations within the source effectively cancel. This is another way to understand why particle number is conserved in the nonrelativistic regime (see section 3.2).

described in the nonrelativistic regime.

In fig. 4 we sketch the two main mechanisms for oscillon longevity.

The death of the oscillon

We have established that an oscillon is described by a fundamental mode that sources radiation tails in the form of higher harmonics. The oscillon thus radiates energy at some rate $\dot{E}_\omega$, whose exact value depends on the background envelope $\Phi_1(r)$ and the details of the potential. Since the oscillons radiates continuously, it must change its internal structure to conserve energy. By construction, the fundamental mode $\Phi_1(r)$, solution of eq. (54), contains most of the energy E_ω of the oscillon. The background frequency ω is therefore continuously evolving, changing the shape of $\Phi_1(r)$. However, when $dE_\omega/d\omega = 0$ there is no way in which the oscillon can go. The localized solution therefore dismantles rapidly. This has been called the *energetic death* of the oscillon. In fig. 5 we show how the slow decay of an oscillon generally proceeds. The decay rate can shut off at specific values of $\omega < m$ due to the reasons outlined above, namely destructive interference and geometric decoupling. Whenever the radiation is small an oscillon with stable characteristics is observed. Note that destructive interference is not generic and is not expected to occur in every model. Geometric decoupling on the other hand is always expected, as it is related to the nonrelativistic limit of te scalar field theory.

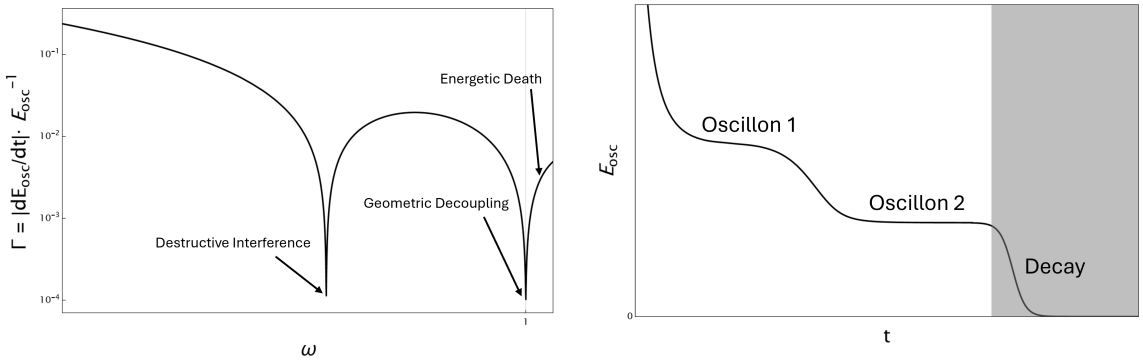

Figure 5: A sketch of the typical decay rates and energy evolution of an oscillon. Note that this plot is not based on any model and is just intended for schematic purposes. *Left:* The decay rate $\Gamma = \left|\dot{E}_{osc}/E_{osc}\right|$ of the oscillon against its frequency ω. The decay rate goes to zero at two particular values of ω. The first one is model dependent and is related to destructive interference. The second, as $\omega \to m$, is generic and has to do with geometric decoupling. Close to $\omega \sim m$ the decay rate rises again, the energetic death of the oscillon. *Right*: The associated evolution of the localized energy E_{osc}. Each dip in Γ is associated to a distinct oscillon with approximately stable characteristics.

3.3 The nonrelativistic regime

In section 3.2 we argued that one can usually ignore general relativistic effects when describing classical lumps. Then we showed in section 3.2.1 that classical lumps held together solely by selfinteractions are common; these are called oscillons. This description of lumps is adequate when the typical field value $\phi \sim \mathcal{O}(\Lambda)$ and the size of the lump $R \sim \mathcal{O}(m^{-1})$. In the weak-field limit $|\phi| \ll \Lambda$, the binding energy of oscillons due to selfinteractions can become of the same order as the Newtonian gravitational binding energy. This limit is interesting in itself, and we'll show that it leads to bound states of slow moving bosons, the nonrelativistic regime.

The expansion parameter in the nonrelativistic limit is the velocity of the particles with respect to the speed of light c [95, 96]. The dispersion relation of a (free) classical wave is given by

$$\omega = \sqrt{k^2 + m^2} \tag{64}$$

The velocity of the wave is the group velocity

$$v = \frac{\partial \omega}{\partial k} = \frac{1}{\sqrt{1 + m^2/k^2}} \tag{65}$$

Now, limiting ourselves to $v \equiv \epsilon \ll 1$, we conclude that $k/m \ll 1$. A nonrelativistic expansion is equivalent to a cutoff on the Fourier decomposition of the classical field.

The field can be written as

$$\phi(t,\vec{x}) = m^4 e^{-imt}\int_0^\epsilon \frac{d^4\epsilon'}{(2\pi)^4}\,\tilde{\phi}(\epsilon')e^{-i\frac{m\epsilon'^2}{2}t}e^{im\vec{\epsilon'}\cdot\vec{x}} + c.c. \tag{66}$$

where $\tilde{\phi}(\omega,k) = \tilde{\phi}(m\sqrt{1-\epsilon'^2},\epsilon' k) \equiv \tilde{\phi}(\epsilon')$ is the Fourier transform of the field. Without loss of generality we can write,

$$\phi(t,\vec{x}) = \frac{1}{\sqrt{2m}}e^{-imt}\,\psi(t,\vec{x}) + c.c. \tag{67}$$

with the identification,

$$\psi(t,\vec{x}) \equiv \sqrt{2}m^{9/2}\int_0^\epsilon \frac{d^4\epsilon'}{(2\pi)^4}\,\tilde{\phi}(\epsilon')e^{-i\frac{m\epsilon'^2}{2}t}e^{im\vec{\epsilon'}\cdot\vec{x}} \tag{68}$$

Looking at the Fourier expansion of the field, it becomes clear that the nonrelativistic limit corresponds to the limit were,

$$\left|\frac{\partial_t\psi}{m\psi}\right| \sim \mathcal{O}(\epsilon^2) \qquad \left|\frac{\partial_i\psi}{m\psi}\right| \sim \mathcal{O}(\epsilon) \tag{69}$$

To make the nonrelativistic expansion in terms of ϵ (or small velocities) consistent we additionally require that we are in a weak field limit.

$$\left|\frac{\psi}{\sqrt{m}\,\Lambda}\right| \sim \mathcal{O}(\epsilon) \tag{70}$$

To see that this is necessary, notice that nonlinearities in the equations of motion will source modes wit $k > m$ if we're not in the weak-field limit, causing a breakdown of the perturbative scheme.

In the nonrelativistic limit we are therefore working with scalar lumps that are dilute and oscillate near the natural frequency of the field m. In our discussion about oscillons we argued that we can completely neglect the gravitational sector when $\phi \sim \Lambda$ and $R \sim m^{-1}$. This doesn't apply to very dilute configurations. The Newtonian gravitational binding energy of the field can become of the same order as the self-energy originating from the selfinteractions of the field. We can approximate a dilute lump as a homogeneous field configurations with amplitude $\phi \sim \epsilon\Lambda$ and size $R \sim (\epsilon m)^{-1}$. The mass of such a configuration is approximately,

$$M_{dilute} \approx \epsilon^{-1}\frac{\Lambda^2}{m} \tag{71}$$

So even though we are dealing with a very dilute concentration of particles, the overall mass can be larger than that of the relativistic oscillons 50. To see what the dominant

binding force of the lump is we compare the gravitational binding energy to the self-energy coming from selfinteractions. For a nonlinear potential with even parity the dominant contribution to the self-energy comes from the quartic interactions. The two binding energies are,

$$E_G \approx -\frac{GM^2}{R} = -\epsilon^{-1}\frac{\Lambda^2}{M_{Planck}^2}\frac{\Lambda^2}{m} \tag{72}$$

$$E_I \approx -\left(\frac{\Lambda}{m}\right)^2 \phi^4 R^3 = -\epsilon\frac{\Lambda^2}{m} \tag{73}$$

where E_G is the Newtonian binding energy of the lump and E_I is the self-energy coming from self-interactions. If the size of the lump $R \gtrsim \frac{M_{Planck}}{\Lambda} m^{-1}$, the dominant binding force is gravity. In the nonrelativistic limit it's not always a good idea to ignore gravitational effects.

3.3.1 Including Newtonian Gravity

We want to include the effects of gravity to the dynamics of the nonrelativistic scalar field. In the Newtonian limit the metric becomes to lowest order in ϵ,

$$ds^2 = -\left(1 + 2U(\vec{x})\right) dt^2 + d\vec{x}^2 \tag{74}$$

We can plug this metric and the nonrelativistic field ansatz eq. (67) into the general action of eq. (40). Up to $\mathcal{O}(\epsilon^4)$ the nonrelativistic action is given by,

$$S = -\int dt\, d^3x \left(\frac{\nabla U \nabla U}{8\pi G} + \frac{\nabla\psi\nabla\psi^*}{2m} + mU\,|\psi|^2 - \frac{i}{2}\left(\dot{\psi}\psi^* - \dot{\psi}^*\psi\right) + V_{nl}(|\psi|) + h.h. + \mathcal{O}(\epsilon^5)\right) \tag{75}$$

The higher harmonics are terms like $\sim \psi^2 e^{-2imt}$ and can be ignored since we're interested in frequencies near m in the nonrelativistic regime[2]. The nonlinear self-interaction terms can be written as

$$V_{nl}(|\psi|) = \sum_{n=4}^{\infty} \frac{m^{2-n/2}}{\Lambda^{n-2}} \frac{\epsilon^{n-4}\lambda_n}{n!} |\psi|^n \tag{76}$$

Where we assume again that the potential is even. Note that we can safely ignore any term with $n > 4$, except if $\lambda_n \sim 1/\epsilon^{n-4}$. This might be considered unnatural from the EFT point of view, but is an interesting possibility nonetheless.

Something remarkable happens in the nonrelativistic limit. The lagrangian in (75) has a global symmetry under a $U(1)$ rotation of the field $\psi \to e^{i\theta}\psi$. The associated Noether charge is given by,

$$Q = \int d^3x\, |\psi|^2 \tag{77}$$

[2]These modes are effectively decoupled from the dynamics through a similar process as the geometric decoupling of oscillons with $\omega \to m$. In fact oscillons with $\omega \sim m$ are nonrelativistic.

Which is conserved exactly to lowest order in ϵ. The charge Q counts the total amount of particles in the field, showing explicitly that there are no number changing processes in the nonrelativistic limit. We can thus identify $n(t,\vec{x}) = |\psi(t,\vec{x})|^2$ with the particle density. The dynamics of the system are given by the so-called Schrödinger-Poisson (SP) equations of motion,

$$i\,\dot{\psi} = -\frac{\nabla^2\psi}{2m} + mU\psi + \frac{dV_{nl}}{d|\psi|}\frac{\psi}{|\psi|} \tag{78}$$

$$\nabla^2 U = 4\pi G\; m|\psi|^2 \tag{79}$$

The Poisson equation (79) justifies our identification of $|\psi(t,\vec{x})|^2 = n(t,\vec{x})$ since $\rho(t,\vec{x}) = m\,n(t,\vec{x})$ in the NR limit. We can now look for many-particle bound states, as localized solutions of the SP-equations.

3.3.2 Nonrelativistic non-topological solitons

We can search for solitons of eqs. (78) and (79) by taking the ansatz,

$$\psi = e^{im\gamma t}\Phi(r) \tag{80}$$

Note that γ in eq. (80), now represents the binding energy per particle in the condensate. The gravitational potential U is static for this ansatz. In what follows we assume the most natural attractive nonlinear potential[3], $V_{nl}(|\psi|) = -\frac{\lambda}{\Lambda^2}|\psi|^4$, with $\lambda \equiv \lambda_4/4! \sim \mathcal{O}(1)$, a positive dimensionless parameter. We obtain an ODE for the spatial envelope $\Phi(r)$,

$$\nabla^2\Phi(r) = 2m\left(m\gamma\Phi(r) + mU\Phi(r) - \frac{4\lambda}{\Lambda^2}\Phi(r)^3\right) \tag{81}$$

$$\nabla^2 U = 4\pi G\, m\Phi(r)^2 \tag{82}$$

To find solutions it is useful to make this set of equations dimensionless, by rescaling $x^\mu \to \tilde{x}^\mu/m$ and $\Phi(r) \to \sqrt{m}M_{Planck}\tilde{\Phi}(r)$. We obtain a set of equations which can be solved numerically,

$$\nabla^2\Phi(r) = 2\left(\gamma\Phi(r) + U\Phi(r) - 4\lambda\frac{M_{Planck}^2}{\Lambda^2}\Phi(r)^3\right) \tag{83}$$

$$\nabla^2 U = 4\pi\,\Phi(r)^2, \tag{84}$$

where we removed tildes for convenience. This way of writing the equations makes it apparent that in the limit of $\Phi(r) < (\Lambda/M_{Planck})^2$, the soliton properties will be dominated by the Newtonian potential, something we guessed at earlier. Similar to

[3]We could have repulsive selfinteractions as well, but given our previous discussion on oscillons, we will not consider that case here.

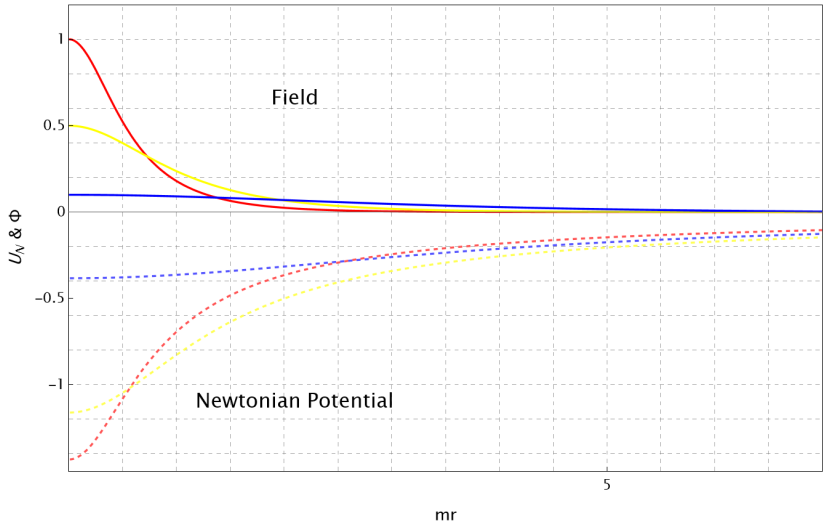

Figure 6: The field profile (full) and Newtonian potential (dashed) for three different values of the central density of the field. We plot one solution where selfinteractions dominate (red), one intermediate case (yellow) and one case where gravity dominates (blue). Here $(M_{Planck}/\Lambda)^2 = 10^1$.

the fundamental modes of oscillons, this set of equations has an infinite amount of decaying solutions labeled by the amount of nodes in $\Phi(r)$. We focus again on the lowest energy, nodeless configuration. In fig. 6 we show the field profile $\Phi(r)$ and the Newtonian potential $U(r)$ for three different values of the central density. Note that we plot here in dimensionless variables.

As the soliton becomes more dense, the selfinteractions dominate the binding energy per particle, γ more and more. It is interesting to see how this binding energy depends on the amount of particles in the condensate. As we'll argue, this is a statement about stability. We plot this dependence in fig. 7. We clearly see the two branches of the non-topological solitons, one where the solutions are bound by self-interactions and one where they are bound by gravity. The turnover point corresponds to dilute configurations with $\Phi(r=0) \lesssim (M_{Planck}/\Lambda)^2$. Note that the binding energy scales differently with N on the two branches. In particular, if the solution is dominated by selfinteractions, the nonrelativistic condensate can increase its binding energy by shedding particles. This results in the famous collapse instability of the nonlinear Schrödinger equation. Nonrelativistic condensates in three dimensions, bound together solely by selfinteractions are typically not expected for this reason [97]. The two asymptotic branches in fig. 7 can be understood from the scaling relations that the nonrelativistic equations obey in the limit of vanishing gravity and vanishing selfinteractions respectively. We summarize this in table 1. The solitons in these limits are related to each other the transformations given in table 1.

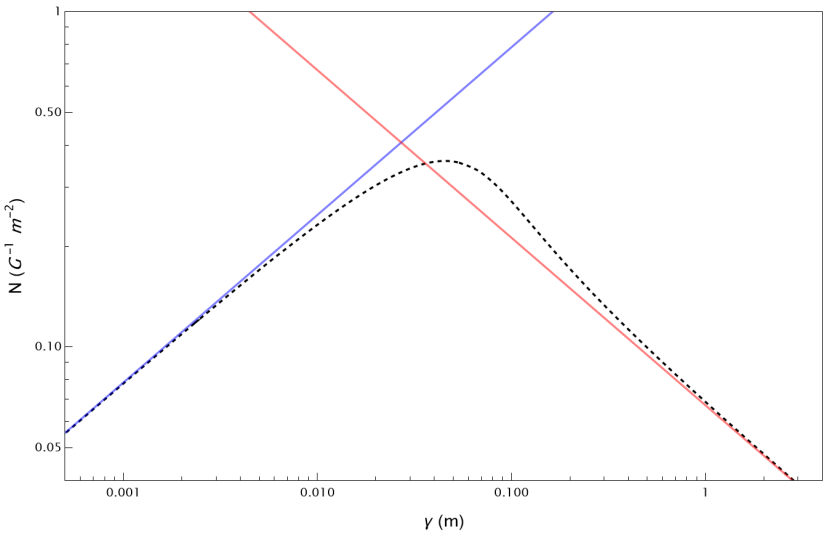

Figure 7: The dependence of the binding energy γ on the total amount of particles in the soliton N. The black dashed line corresponds to the true solution of the system of equations (83) and (84), while the blue and red line represent solutions solely bound by gravity and nonlinearities respectively. Here $(M_{Planck}/\Lambda)^2 = 10^2$. Note that it is not necessarily inconsistent to have $\gamma \sim 1$, since this is simply related to our choice of (M_{Planck}/Λ).

Vanishing selfinteractions	**Vanishing gravity**
$\psi \to \alpha^2\,\psi$	$\psi \to \alpha\,\psi$
$\gamma \to \alpha^2\gamma$	$\gamma \to \alpha^2\gamma$
$r \to \alpha\, r$	$r \to \alpha\, r$
$U \to \alpha^2\, U$	$U = 0$
$M \to \alpha\, M$	$M \to \alpha^{-1} M$
$E \to \alpha^3\, E$	$E \to \alpha\, E$

Table 1: The scaling relations in the limit of vanishing selfinteractions and gravity respectively. We can find new solitons by rescaling with any real value of α. Here M refers to the total conserved mass of the soliton while E is its energy.

In this chapter we've given a broad overview of the different type of bound states that exist in real scalar field theories. It is now time to talk about some of their phenomenological aspects.

4 The phenomenology of many-particle bound states

In the chapter 3 we discussed the different types of many-particle bound states that exist in generic models with selfinteractions. In particular, we highlighted that at different levels of compactness, various types of states exist. In order of decreasing density these are *oscillatons* (or *boson stars*), *oscillons* and *nonrelativistic solitons*. We showed that, although these carry different names, they originate from the same underlying principle: attractive interactions create a binding energy when bosons are close together.

An important aspect of these field configurations is that they are generally an attractor of the dynamics [84, 98–100]. That is to say that most lumps will tend to 'settle' into one of the solutions discussed in 3. This means that these states are not only interesting from the point of view of mathematical physics, but have also found many phenomenological applications in the past decades, particularly in the domain of cosmology. In this chapter we will give a nonextensive review of the phenomenological aspects of many-particle bound states. We will give particular emphasis to the formation of oscillons during a *preheating phase* in the early Universe and the role of non-topological solitons in *Ultra Light Dark Matter* models. We neglect further discussion about compact boson stars. Although these can have many interesting effects on observational cosmology [31, 33, 78, 101–103], they are less relevant to the results discussed in this thesis.

4.1 Oscillons from preheating

Many models of the early Universe include real scalars. They can dominate the total energy budget of the Universe (as is the case for *inflation* [104, 105]) or be mere spectators (as is the case for the axion during the *QCD phase transition*). Whichever the case, the field initially lies happily in its (adiabatic) vacuum state, which corresponds to a homogeneous field configuration with $\phi \sim \mathcal{O}(\Lambda)$. The field is kept in this state due to the Hubble friction coming from the background expansion of space. The friction term, proportional to $\sim H\dot{\phi}$ dominates the dynamics, fixing the scalar in place. This continues until Hubble friction becomes of the same order as potential driven motion, approximately when

$$H \equiv \frac{\dot{a}}{a} \approx \sqrt{\left|\frac{V'(\phi)}{\phi}\right|} \tag{85}$$

After this point, the scalar starts 'rolling' with its motion controlled by the potential. Note that in the free case, the r.h.s. of this equation is simply the mass of the field. However, with different potentials the field can start rolling at a lower energy scale.

If the scalar field dominates the energy budget of the Universe, it controls the value of the Hubble parameter in (85) as well as the r.h.s. of the equation. This gives rise

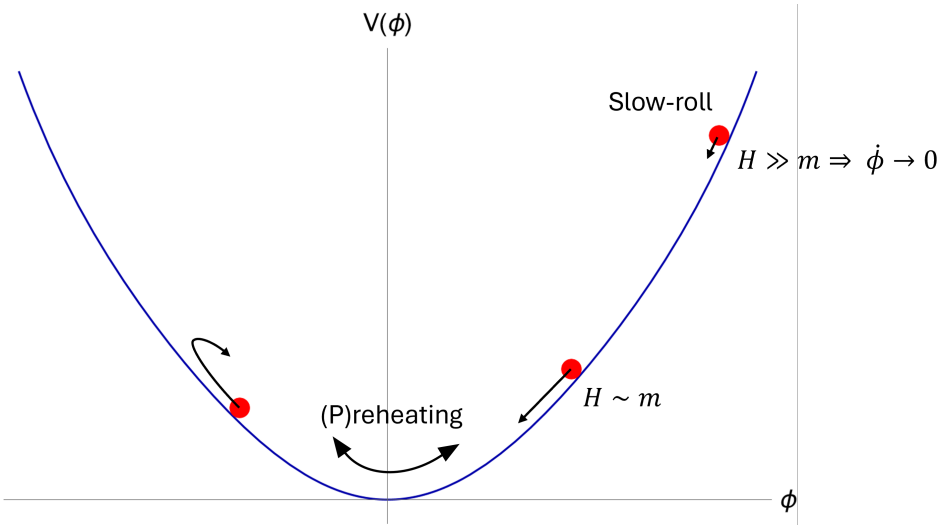

Figure 8: A homogeneous scalar field is frozen in place by Hubble expansion. However, as the Universe expands and H drops below the mass of the scalar m, the potential starts to dominate the dynamics. Eventually the scalar will start to roll around the minimum of its potential. In the context of inflation, this phase of evolution is called (p)reheating.

to an attractor solution, where ϕ and H are approximately constant until,

$$\epsilon \equiv \frac{M_{Planck}^2}{2}\left(\frac{V'(\phi)}{V(\phi)}\right)^2 \approx 1 \tag{86}$$

$$\eta \equiv M_{Planck}^2 \frac{V''(\phi)}{V(\phi)} \approx 1 \tag{87}$$

Here condition (87) is just a rewriting of (85). Since H is approximately constant during the attractor phase, the Universe is in *De Sitter*, and the scalefactor $a \propto e^{Ht}$ increases exponentially. This regime, called *inflation* is the leading paradigm for early Universe cosmology and sets the initial conditions of the thermal Big Bang. After the conditions (86) and (87) are met, the field starts to oscillate around its true minimum and we exit inflation. In the standard scenario, the scalar deposits its energy into a radiation field as it oscillates around the minimum of the potential, setting the stage for the thermal history of the Universe. This final breakup of the homogeneous scalar is called *reheating*, as it sets the the initial temperature of the Universe. A sketch of this is given in fig. 8.

For the reasons outlined above, the breakup of a homogeneous (real) scalar field as it oscillates around its potential minimum is an interesting study case. It is a generic setup that is expected to be relevant for any scalar degree of freedom as the Universe cools down and the expansion rate decreases. The initially homogeneous scalar can be thought of as a coherent state with a large number of particles $N \gg 1$. This warrants

the use of the classical equations of motion to study the dynamics,

$$\ddot{\phi} - \frac{1}{a^2}\nabla^2\phi + 3H\dot{\phi} + V'(\phi) = 0 \tag{88}$$

For a homogeneous initial condition $\phi(t, \vec{x}) = \phi(t)$, the solution of eq. (88) is simply a decaying anharmonic oscillation of the scalar. This is not a very interesting solution as it ignores semiclassical effects that are important in studying the breakup of the scalar [106]. First of all, the dynamics can change due to *particle decay* of ϕ into another field, let's call this field χ. If $2\,m_\chi < m_\phi$, we the decay process $\phi \to 2\,\chi$ is kinematically allowed. Since the particles in the coherent background decay democratically, this process doesn't actually spoil the validity of the classical approximation. It is best modeled by an adding extra friction term to the equations of motion,

$$\ddot{\phi} - \frac{1}{a^2}\nabla^2\phi + \Gamma_{decay}\dot{\phi} + 3H\dot{\phi} + V'(\phi) = 0 \tag{89}$$

When $\Gamma_{decay} \approx H$, ϕ will lose the remainder of its energy to the χ field. If ϕ plays the role of the *inflaton* in the early Universe, the energy density in the homogeneous field when $\Gamma_{decay} \approx H$, sets the reheating temperature $T_{reheating} \sim \rho^{1/4}$, after which standard cosmological history proceeds.

Besides the perturbative particle decay, another breakup channel of the homogeneous field exists. To see this note that in the semiclassical approximation, the field modes with $k \neq 0$ should not be interpreted as classical variables set identically to zero. Instead, we need to view them as quantum states that initially lie in their vacuum state. The equations of motion for the nonhomogeneous quantum modes of the field can be written as,

$$\ddot{\hat{\phi}}_{\vec{k}} + \omega_k^2\hat{\phi}_{\vec{k}} + V''_{nl}(\phi_0(t))\hat{\phi}_{\vec{k}} = 0 \tag{90}$$

Where we ignored the expansion of space since it will generally be subdominant in the situations we will be discussing. Note that eq. (90) looks exactly like a harmonic oscillator equation, albeit with a time-dependent oscillation frequency, $\omega_k(t)^2 \equiv \omega_k^2 + V''_{nl}(\phi_0(t))$. We have to account for this time-dependence when expanding in creation and annihilation operators,

$$\hat{\phi}_k = \frac{1}{\sqrt{2}}\left[v_k(t)\,\hat{a}^\dagger_{\vec{k}} + v_k^*(t)\hat{a}_{-\vec{k}}\right] \tag{91}$$

Where $\hat{a}^\dagger$ and $\hat{a}$ are creation and annihilation operators that are time-independent (we will return to these in a bit). The functions $v_k(t)$ are called mode functions and they absorb the time dependence of the oscillator frequency in eq. (90). Their equations of motion can be obtained in a straightforward manner,

$$\ddot{v_k}(t) + \omega_k^2 v_k(t) + V''_{nl}(\phi_0(t))v_k(t) = 0 \tag{92}$$

Equation (92) is a classical equation and is readily solved (numerically) to obtain expectation values of operators in the semiclassical limit. However, to be able to do this we need to define appropriate initial conditions: we need to define in what quantum state the field modes are. By assumption the state of the system is annihilated by the annihilation operator at $t = t_0$ in (91), so that $\hat{a}_{\vec{k}} |0\rangle = 0$ initially. This in itself is not enough to define the vacuum however, since different mode functions are related to each other by *Bogolyubov transformations*, so there is still an infinite set of states to take as the initial condition. To get the correct vacuum we want to find the mode functions that minimize the expectation value of the Hamiltonian at $t = t_0$. This minimization procedure leads to the following conditions on the mode functions,

$$v_k(t_0) = \frac{1}{\sqrt{\omega_k(t_0)}} \qquad \dot{v}_k(t_0) = i\sqrt{\omega_k(t_0)} \tag{93}$$

Note that if $\omega_k(t) = \omega_k$, we get back the standard canonical quantized Klein-Gordon field. With the initial conditions in (93) we can find observables of the quantized field configuration.

We could also have chosen to set the adiabatic vacuum at a slightly later time $t_1 > t_0$, with new creation and annihilation operators $\hat{b}_{\vec{k}}$, $\hat{b}^\dagger_{\vec{k}}$. The new vacuum is related to the old vacuum state via the Bogolyubov transformations,

$$\hat{b}_{\vec{k}} = \alpha_k \hat{a}_{\vec{k}} + \beta_k^* \hat{a}^\dagger_{-\vec{k}} \tag{94}$$

Where α_k and β_k are coefficients that depend on the respective mode functions of the vacua, with $\beta_k = 0$ if and only if $\omega_k(t) = \omega_k$. Note now what happens to the number of particles $\langle \hat{b}^\dagger_{\vec{k}} \hat{b}_{\vec{k}} \rangle$ when evaluated on our initial state of the vacuum.

$$\langle \hat{b}^\dagger_{\vec{k}} \hat{b}_{\vec{k}} \rangle = \langle 0_{t_0} | \hat{b}^\dagger_{\vec{k}} \hat{b}_{\vec{k}} | 0_{t_0} \rangle = \frac{1}{2} \langle 0_{t_0} | (\beta_k \vec{a}_{-\vec{k}}) \cdot (\beta_k^* \vec{a}_{-\vec{k}}) | 0_{t_0} \rangle = |\beta_k|^2 V \tag{95}$$

Where V is some volume factor. The time evolution of the frequency $\omega_k(t)$ has created particles 'out of nothing'. We thus unravel a new type of particle creation that can occur with a homogeneous scalar background. This type of decay of the scalar background is generally nonperturbative since we need to know the full solution of $v_k(t)$. Moreover, it can be explosive for certain background fields, leading to a large population of particles in the nonhomogeneous modes of the field in a short amount of time. This process of parametric resonance is referred to as *preheating* and we will show that this can lead to oscillon formation in the early Universe.

4.1.1 Oscillon formation

Now that we have a framework to treat nonhomogeneous modes in the semiclassical limit, we can see what happens with a particular specification of the background. In particular, we need to specify the evolution of the homogeneous mode $\phi(t)$ and the

scalar potential. Since we're interested in the formation of oscillons, we need to choose a $V(\phi)$ that supports them. We can take the simplest even polynomial that is shallower than quadratic [47, 107],

$$V(\phi) = \frac{1}{2}m^2\phi^2 - \frac{\lambda}{4}\phi^4 + \frac{g}{6m^2}\phi^6 \tag{96}$$

Where $\lambda, g > 0$ positive and dimensionless parameters. We additionally require that $\lambda^2 < 4g$ giving the field only one local minimum at $\phi = 0$. This might be considered unnatural from an EFT standpoint, but we ignore this fact for now. The solution for the background homogeneous field mode $\phi(t)$ is just some anharmonic periodic oscillation,

$$\phi(t) = \phi_0\, p(t) \qquad p(t+T) = p(t) \tag{97}$$

with T the period of oscillation. The mode equation (92) obtains the form,

$$\ddot{v_k}(t) + \omega_k^2 v_k(t) - \left(3\lambda\,\phi_0^2\, p(t)^2 - \frac{5g}{m^2}\phi_0^4\, p(t)^4\right) v_k(t) = 0 \tag{98}$$

We thus get an ODE for each wavenumber. The solution of eq. (98) can be found using Floquet theory [108]. The general solution of $v_k(t)$ can be written as,

$$v_k(t) = c\, P(t) e^{\mu_k t} \tag{99}$$

With c a constant and $P(t+T) = P(t)$ a function with the same periodicity as the background. The parameters μ_k are called Floquet exponents. Note that when μ_k has a real positive part, $v_k(t)$ grows exponentially. Whether this is the case is entirely dependent on the choice of ϕ_0, the amplitude of the background oscillation, and k the wavenumber of the mode under consideration. Note however that eq. (98) corresponds to the *instantaneous* mode equation, essentially neglecting the effect of the expansion of the background metric. In reality, the growth of the scale factor $a(t)$ causes a decay of the amplitude of the field $\phi_0 \to \phi_0\, a(t)^{-p}$ (with p positive and model dependent) and moreover stretches the wavelengths of modes so that $k \to k/a(t)$. The expansion of space causes the instantaneous mode equations to 'move through' the instability bands. This means that one generally expects significant amplification in at least a subset of the different $k-$modes, except when $\phi_0(t_0) \ll m/\sqrt{\lambda}$. The instability band of potential (96) is shown in fig. 9. We show the evolution of various physical modes as they get redshifted and the amplitude of oscillation of ϕ gets damped, assuming $\phi(t_0) = m/\sqrt{\lambda}$. It is typical that some of the modes move through the instability band.

So some of the nonhomogeneous field modes get amplified significantly. Note in particular that the field amplitude of a standing wave with wavenumber k grows as,

$$\langle\phi^2\rangle \propto \langle\left|\phi_{\vec{k}}\right|^2\rangle = |v_k(t)|^2 \propto e^{2\mu_k t} \tag{100}$$

The amplitude of unstable modes can therefore rapidly become of the same order as the background oscillation amplitude ϕ_0. This means that the linear semiclassical

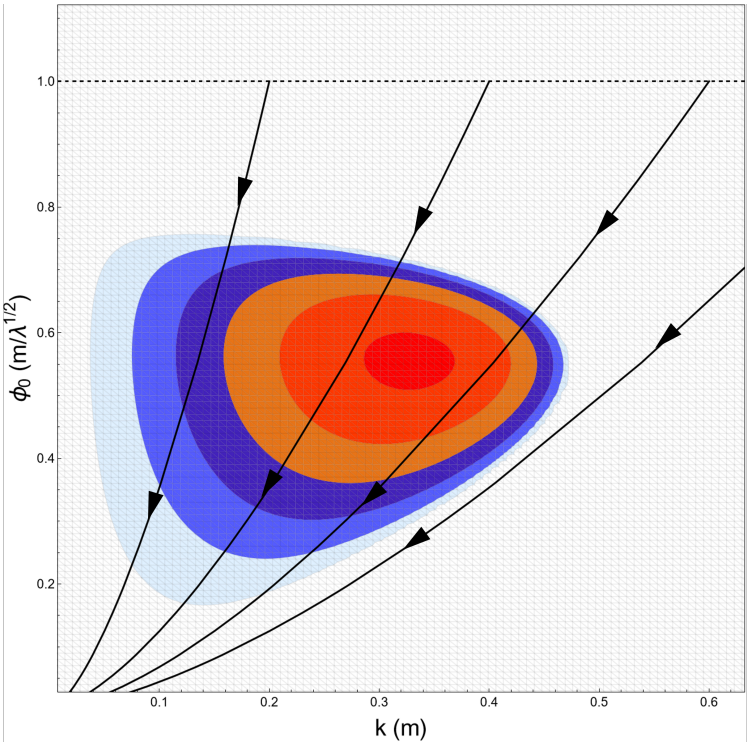

Figure 9: The main instability band of the potential in eq. (96), computed using Floquet theory. The contours signify regions with $\mu_k > 0.01m, 0.02m, 0.03m, 0.04m, 0.05m, 0.06m$ respectively. Although nothing gets amplified initially, the expansion of space redshifts wavelengths and dampens the amplitude of oscillation of the background. A subset of the modes therefore moves through the instability band as indicated by the black arrowed lines.

approximation is no longer an accurate description of the quantum field. To include nonlinear effects one therefore needs a prescription to deal with backreaction of the quantum operators $\hat{\phi}_{\vec{k}}$. The most popular paradigm to deal with this problem is to approximate the quantum operator as a classical field. The 'quantumness' is imprinted in the initial conditions of the field modes, whose values are pulled from a statistical ensemble that mimics the expectation values of the operators in the adiabatic vacuum,

$$\langle \left| \hat{\phi}_{\vec{k}} \right|^2 \rangle = \frac{1}{2\omega_k(t_0)} \qquad \langle \left| \hat{\dot{\phi}}_{\vec{k}} \right|^2 \rangle = \frac{\omega_k(t_0)}{2} \tag{101}$$

With these classical initial conditions, one can solve the system numerically on a lattice [109, 110]. Averaging the numerical results over many different instantiations of the fluctuations as defined in eqs. (101), should give accurate statistical results of the full quantum field theory. There are two ways to understand why this classical prescription gives the correct results. First, note that the mode functions are proportional to the expectation value of the number operator corresponding to the true vacuum of the

theory at $\phi = 0$. Using eq. (94), the number density of particles is given by,

$$\langle n_k \rangle \approx \frac{|\dot{v}_k|^2}{\omega_k} + \omega_k |v_k|^2 \tag{102}$$

So if the mode functions are amplified exponentially, the occupation number of the quantum state quickly blows up. Following our discussion in sec. 2, this is exactly the classical limit of the quantum field. It thus seems warranted to treat the nonhomogeneous field modes classically. Alternatively, we can view this stochastic approach as an instance of the *Truncated Wigner method* to deal with semiclassical backreaction. This approach can extend the quantum breaktime of a field theory and is especially suited for situations where the classical equations of motion contain instabilities, as is the case for preheating. From this perspective, the classicality of the nonhomogeneous modes is inherited from this initially classical background that corresponds to a coherent state of many particles. This point is discussed in more detail in paper [2].

Whichever the perspective taken, countless studies have shown that the amplification of nonhomogeneous modes leads to copious production of oscillons. Once the modes become nonlinear, the field profile is essentially a sum of standing waves $\propto \cos\left(\vec{k} \cdot \vec{x}\right)$. The large overdensities with typical wavelength $\sim a(t)/k$ naturally settle into oscillons that are general attractors of large scalar lumps. The number density of oscillons can be estimated with the simple formula,

$$n_{osc} \approx \left(\frac{k_{nl}}{a(t_{nl})}\right)^3 \tag{103}$$

Where k_{nl} is the comoving wavenumber of the mode that first becomes nonlinear and t_{nl} is the time at which this happens. Eq. (103) essentially counts the number of distinct peaks in a closed volume, and assumes each peak settles into an oscillon. In fig. 10 we show the results of a benchmark lattice simulation of the model with potential (96).

Many publications have shown that a significant portion of the energy of the homogeneous background can end up in the form of oscillons [44, 47, 50, 107, 111–113]. Depending on the context, this can have various phenomenological consequences. Note that a collection of well separated oscillons redshift like matter $\rho \propto a^{-3}$ since the mass of each oscillon is fixed by the internal field dynamics, and each individual oscillon thus behaves like a point particle. If the homogeneous background plays the role of the *inflaton* in the early universe, the formation of oscillons thus leads to an early matter dominated era. This influences the predictions for the reheating temperature, but also effectively shifts the observed modes of the CMB. The most recent results of Planck-2018 favor plateau potentials that support oscillons [57], so this is an intriguing possibility. In other preheating scenarios where the background field doesn't dominate the energy density of the Universe, oscillons can provide early seeds for dark matter

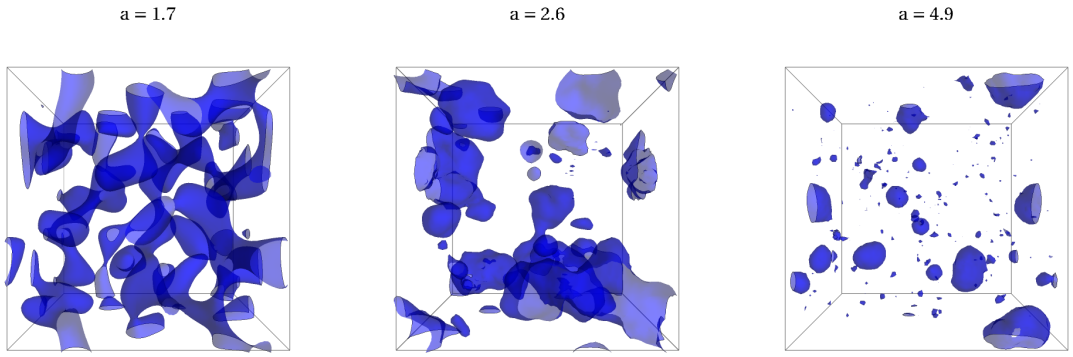

Figure 10: The results of a three dimensional lattice simulation for the model in (96) with $g = 4\lambda^2$. We show three different stages of fragmentation. The contours are drawn around regions of space where $\rho > 4\bar{\rho}$, (the average energy density). The simulation is initialized with $a = 1$. As space expands the homogeneous scalar fragments and settles into approximately spherical oscillons. These are the remnants at the end of the simulation.

Halos or play the role of dark matter themselves [114]. Finally, in certain models oscillons can collapse to form black holes, providing a new avenue for the formation of primordial black holes [115]. They can also be a source of stochastic gravitational.

4.1.2 Gravitational waves from oscillons

A large amplification of scalar modes during preheating is also accompanied by a stochastic gravitational wave background. This is because gradients in the scalar field source transverse-traceless (TT) modes of the metric,

$$\ddot{h}_{ij}^{TT} - \frac{1}{a^2}\nabla^2 h_{ij}^{TT} + 3H\,\dot{h}_{ij}^{TT} = \frac{2G}{a^2}\left[\partial_i\phi\,\partial_j\phi\right]^{TT} \tag{104}$$

It is clear that the source on the r.h.s. of eq. (104) becomes big as the gradients of the scalar get amplified due to parametric resonance. A stochastic gravitational wave background is generally expected in preheating, regardless of whether oscillons form or not. However, it has been noted in the literature that the formation of oscillons can have a specific imprint on the spectrum of gravitational waves.

If a large percentage of the energy of the scalar ends up in oscillons after the breakup of the homogeneous background, it means that most of the modes of the scalar have (locally) 'sphericalized', since oscillons are spherical objects. The TT-part of the energy-momentum tensor of a spherical scalar field configuration is exactly 0, and in [48] it was shown that the same can be said of spherical oscillons that are well separated. The generation of gravitational waves sourced by these sphericalized

modes of the oscillon is therefore suppressed relative to the rest of the spectrum. This translates into peaks and troughs in the stochastic GW signal. The troughs correspond exactly to the fundamental frequency and overtones of the oscillon $\sim m$, $3m$, $5m$... in an even potential. To be precise, note that the troughs are located at double the frequency of the oscillon harmonics, as the energy-momentum tensor is quadratic in the scalar field. This is shown in fig. 11 taken from [48]. Interestingly. the structure of the spectrum gives information about the shape of the scalar potential. Note that this characteristic structure associated to oscillon formation is not always visible, and depends on the details of the model, as was pointed out in [49]. Although the energy density of GWs produced in this manner typically falls within the sensitivity band of many experiments, their characteristic frequency from preheating after inflation is way too high for any current or planned experiments [49]. We can estimate the typical frequency of GW today, taking $f_i \sim m$ at formation and assuming preheating is immediately followed by reheating with temperature T_R. The gravitational waves get redshifted like radiation, so the frequency in the present Universe is, with T_0 the temperature of photons today,

$$f_0 = m\frac{T_0}{T_R} \approx 4.4 \cdot 10^{11}\ \text{Hz}\ \left(\frac{m}{10^{-6}\ M_{Planck}}\right)\left(\frac{T_R}{10^{13}\ \text{GeV}}\right)^{-1} \tag{105}$$

So for most models of inflation, the frequency spectrum from preheating lies beyond the gigahertz band, way beyond current experimental range, although there are some exceptions [116]. Of course, the estimate in (105) assumes the homogeneous background plays the role of the inflaton in the early Universe. If instead the scalar starts rolling later in cosmological history, so $m \ll T_R$, the stochastic background could be observable with current experiments. This possibility was explored in [45]. It was also pointed out that the rapid transition from an oscillon dominated phase with $w = 0$ to a radiation dominated phase with $w = 1/3$ in the early Universe can enhance the GW spectrum, particularly at low frequencies, since this transition can happen way after the oscillons have formed [50].

The phenomenology of oscillons is thus rich and varied but one typically needs a preheating type scenario, as outlined in this section, to form them. In section 3.2 we showed that in the limit of small velocities and weak fields, Newtonian gravity can dominate the dynamics. In certain dark matter models this can lead to the formation of large scale nonrelativistic solitons without the need of parametric resonance.

4.2 Ultra Light Dark Matter solitons

The standard paradigm of cosmology, ΛCDM, has two major components, a cosmological constant Λ contributing about 70% of the energy budget of the Universe, and a Cold Dark Matter (CDM) particle responsible for about 25% of the total energy. Although there are many independent probes supporting the presence of these components, their fundamental nature remains elusive. In the case of dark matter [117], it

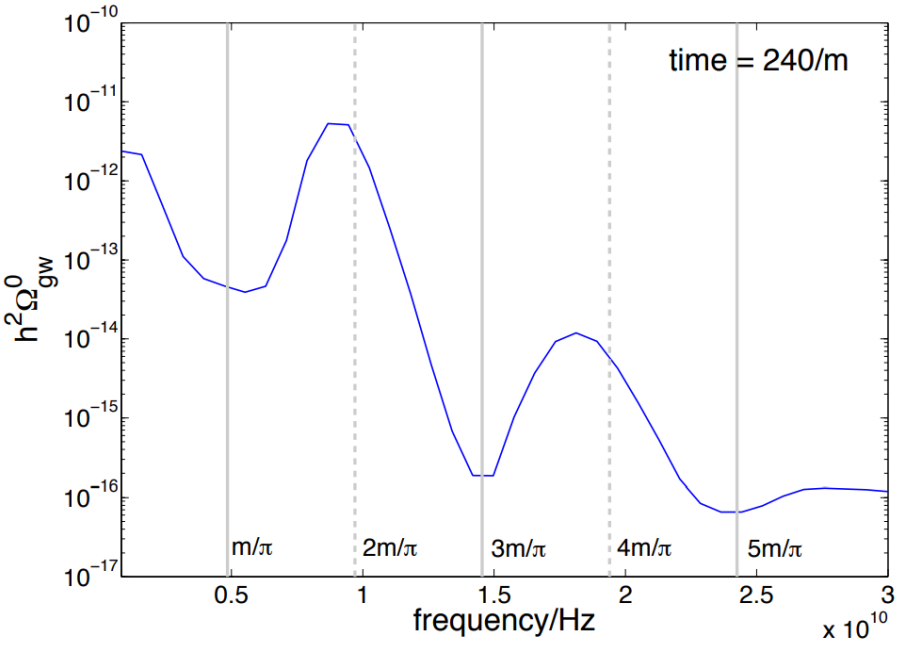

Figure 11: This plot is taken directly from [48]. It represents a gravitational wave spectrum associated to the formation of oscillons in a preheating scenario. Modes 'trapped' in oscillons are sphericalized and therefore stop emitting gravitational waves earlier. This is why we see troughs at double the fundamental frequency $\omega \sim m$ and its overtones $3\omega, 5\omega...$ (this was in an even potential with only odd overtones). The location of these in frequency space is given by $2\omega/(2\pi), 6\omega/(2\pi)...$, as the energy-momentum tensor in eq. (104) is quadratic in the scalar field. The gravitational spectrum thus contains information about the scalar potential.

is understood that it behaves as a pressureless fluid with equation of state parameter $w = 0$, but not much more is known about it[4]. One of the major goals of modern physics has been to find the fundamental constituent of this fluid, with no shortage of proposals. From new fundamental particles to macroscopic object like black holes, the possibilities span a mass rage of about 80 orders of magnitude. From rotation curves of galaxies one can conclude that the typical velocities of dark matter particles should be of order $v \sim 10^{-3}c$. Moreover, it is known that the average dark matter energy density in the Universe is about $\rho_{dm} \approx 1.35 \cdot 10^3$ eV/cm^3. With these two empirically established facts, we can estimate the amount of dark matter particles in a de Broglie volume.

$$N \approx \frac{\rho_{dm}}{m_{dm}} \lambda_{dB}^3 = \frac{\rho_{dm}}{m_{dm}} \left(\frac{2\pi\,\hbar}{m_{dm} v} \right)^3 \approx 10^4 \cdot \left(\frac{m_{dm}}{0.1\,\mathrm{eV}} \right)^{-4} \tag{106}$$

[4]It can be argued that the cosmological constant Λ is even more mysterious, but for the discussion on many-particle bound states we focus on dark matter.

This condition hints at an intriguing possibility for dark matter modeling. First note that the dark matter particle is necessarily bosonic if $m_{dm} \lesssim 0.1\,\mathrm{eV}$ because of the Pauli exclusion principle. Second, in that case it can be understood as a quantum coherent state at large occupation number. It is therefore described by a classical wave equation in the nonrelativistic regime, since $v \ll c$. Condition (106) sets the maximum mass scale for bosonic wave dark matter, described by the Schrödinger-Poisson set of equations (78) and (79). Wave dark matter has garnered considerable attention over the last decades as both the QCD Axion and axion-like particles in String theory fall in this category [24, 25].

There are various ways to create the required abundance of dark matter axions in the early Universe. The most straightforward way is through the *misalignment mechanism*. For now we assume that the initial misalignment angle of the axion field $\phi \sim \theta f_a$ is the same throughout the observable Universe. The axion field starts oscillating around its potential minimum, when the Hubble parameter $H \sim m_a$ the axion mass. The energy density in the axion field is $\sim \theta^2 m_a^2 f_a^2$ at that point. After this, the field starts oscillating and redshifts like matter. The energy density in axions at present time is thus given by

$$\rho_a(t_0) \sim m_a^2 f_a^2 \theta^2 \left(\frac{T_0}{T_{osc}}\right)^3 \approx \theta^2\, m_a^{1/2} f_a^2 M_{Planck}^{-3/2} T_0^3 \tag{107}$$

With T_0 the temperature of photons today. From this we can estimate Ω_a, the current axion density parameter

$$\Omega_a \sim 0.1\,\theta^2 \left(\frac{m_a}{10^{-6}\,\mathrm{eV}}\right)^{1/2} \left(\frac{f_a}{10^{13}\ \mathrm{GeV}}\right)^2 \tag{108}$$

Showing that we are able to produce the required amount of axions with $\theta \sim \mathcal{O}(1)$ through the misalignment mechanism. This estimate is based on an oversimplified picture of axion production, assuming no thermal dependence of the mass and not enforcing that the axion is the QCD axion. In reality there are many more mechanisms for producing a relic density of scalar particles, for example through the generation of a network of topological defects. For a good review of axion cosmology see for example [118].

4.2.1 CDM and the problems on small scales

Structure formation of particle dark matter can be studied by performing N-body simulations of a set of slow moving particles that interact gravitationally. These reproduce the observed large scale structure of our Universe with remarkable accuracy. However, at small scales $\sim$ kpc, simulations are in tension with the observed distribution of dark matter particles. Three main problems have been noted, and all have to do with the fact that dark matter overdensities are suppressed on small scales with respect to the predictions obtained from simulations. These problems have been dubbed *the missing*

satellite problem, the *too-big-to-fail problem* and the *cusp vs. core problem* [119, 120]. A brief description of each problem:

1. *Missing Satellite*: There are too few dwarf satellite galaxies in proximity to the Milky Way. Cold dark matter halos are generally expected to contain subhalos of ever smaller sizes, almost in a scale invariant way. These subhalos are not observed, although they could host faint galaxies.

2. *Too-big-to-fail*: There should be more subhalos within the local Universe massive enough to all but guarantee the collapse of baryonic matter within them. This leads to the presence of astrophysical objects that should make them observable. We don't see these massive halos and the ones we observe are less dense than expected.

3. *Cusp vs. core*: The density of dark matter should grow like $\sim 1/r^{\gamma}$, with $\gamma \sim 1$ towards the center of galaxies (the NFW-profile). Rotation curves of stars near the center of halos show that it instead flattens out. Empirical data thus favors a cored profile instead of the cuspy profile predicted by simulations.

It might be that these apparent tensions are due to limitations in the simulations and theoretical computations of structure formation in particle dark matter models. For example, these are typically not able to fully account for the presence baryonic matter which can alter the dynamics of structure formation. Note however that the cusp vs. core mismatch between observations and simulations persists in dwarf galaxies that contain little baryonic matter [121–123]. This solution is therefore not completely satisfactory.

Wave dark matter offers an elegant solution to the small scale problems of cold dark matter. The dark matter condensate is described by a superposition of waves with typical size given by the de Broglie wavelength,

$$\lambda_{dB} = \frac{2\pi\,\hbar}{m_{dm} v} \approx 0.38 \cdot \text{kpc} \left(\frac{m_{dm}}{10^{-22}\,\text{eV}}\right)^{-1} \left(\frac{v}{10^{-3}\,c}\right)^{-1} \tag{109}$$

So for extremely light wave dark matter, the De Broglie wavelength can become of galactic scale. Ultra Light Dark Matter (ULDM) has become one avenue for the resolution of some of the small scale problems of cold dark matter, since structure formation is naturally suppressed on scales smaller than De Broglie wavelength given by eq. (109). On scales $r \gg \lambda_{dB}$, the field behaves like the standard CDM paradigm and reproduces its successes.

4.2.2 Formation of gravitational solitons in ULDM

Since wave dark matter condensates are described by the Schrödinger-Poisson system of equations in (78) and (79), we might expect that they form long-lived non-topological solitons as described in section sec. (3.2). Their presence in dark matter

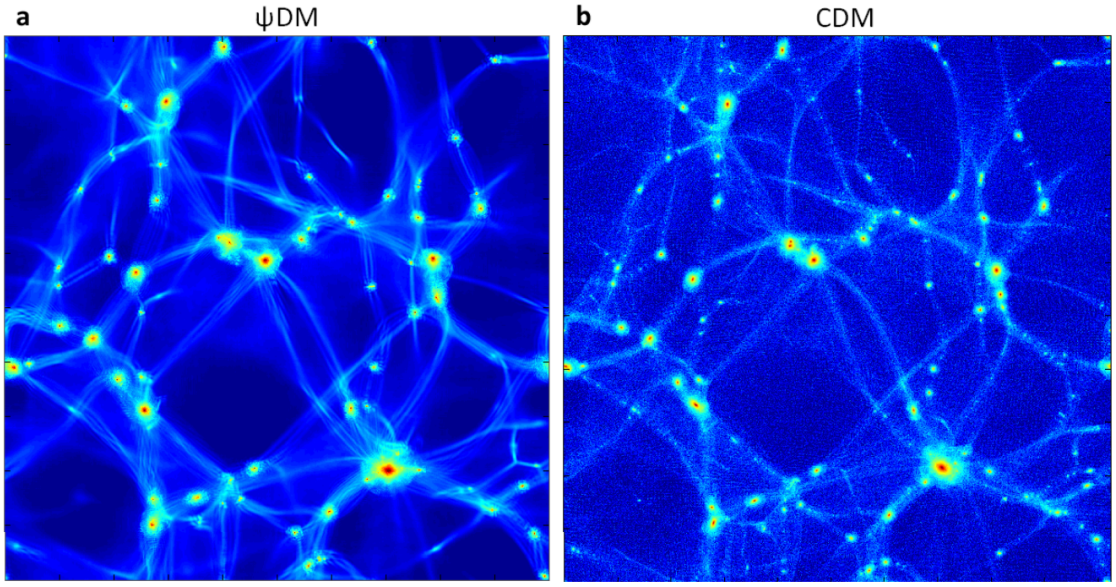

Figure 12: Plot taken from [29]. It highlights the difference in the large scale structure of wave an particle dark matter. These are two dimensional slices from cosmological simulations with similar initial conditions. Redder regions correspond to larger densities. In wave dark matter models the grainy particle structure of CDM is smoothened on scales smaller than the de Broglie wavelength. This mechanism suppresses structure on these scales, giving a natural solution to some of the problems of the standard paradigm. Interestingly, at the center of wave dark matter halos, a nonrelativistic soliton forms.

halos could have interesting phenomenological consequences and we would like to understand whether they are generally expected to be present within galaxies. The fact that the nonrelativistic soliton is a solution of the theory doesn't guarantee that it forms dynamically on observable timescales. We are thus interested in computing the *condensation time*, the time it takes for a halo of wave dark matter to condense into the groundstate soliton.

One can estimate this timescale by approximating a wave dark matter halo as a collection of *quasiparticles* of typical size given by λ_{dB}, the de Broglie wavelength, and effective mass $m_{eff} = \rho\lambda_{dB}^3$, with ρ the average density of dark matter in the halo. These quasiparticles are called *granules* and are the result of interference between the different waves in the halo. It can be shown that the dynamics of the granules are governed by standard kinematic equations used to study stellar diffusion in galaxies [124, 125]. In this framework, the condensation time is approximately equal to the *relaxation time*, the time it takes for the diffusion of the velocities of the granules to be of the same order as the virial velocity in the halo. We will compute this in more detail now following [24, 25, 126].

The dominant diffusion process in a dark matter halo is the two-point gravitational interaction between two quasiparticles. The change in velocity due to a gravitational scattering with impact parameter b is given by,

$$\delta v = \frac{2Gm_{eff}}{v\, b} \tag{110}$$

We assume a spherical homogeneous halo of mass M_h, of size R. The total number of quasiparticles N (or granules) is given by,

$$N \approx \frac{M_h}{m_{eff}} \tag{111}$$

A quasiparticle near the edge of the galaxy will experience approximately

$$\delta n = \frac{N}{\frac{4}{3}\pi R^3} 2\pi^2 R\, b\, db \approx \frac{9}{2}\frac{N}{R^2} b\, db \tag{112}$$

two-point scatterings with impact parameter between b and $b + db$ in one crossing time of the galaxy $\sim R/v$. Each scattering induces a change in velocity in an approximately random direction, with the magnitude given by eq. (110). This causes a drift in the mean square velocity of the quasiparticles, akin to a random walk in Brownian motion. The total drift due to all scatterings in one crossing time can be computed as an integral over the impact parameter,

$$\Delta v^2 = \int \delta v^2 \delta n = \int_{b_{min}}^{b_{max}} \frac{9}{2}\left(\frac{2G\, m_{eff}}{v\, b}\right)^2 \frac{N}{R^2} b\, db = 18\left(\frac{G\, m_{eff}}{v}\right)^2 \frac{N}{R^2} \ln C_o \tag{113}$$

where $C_o = b_{max}/b_{min}$. The condensation time is the time when the total change $\Delta v^2 \approx v^2$, effectively when the individual granules have significantly 'felt' each other. We can now estimate this time assuming $b_{max} = R$ and $b_{min} = \lambda_b = 1/(m\, v)$, and taking $v = v_{vir} = \sqrt{G\, M_h/R}$. First note that $C_o = N^{1/3}$; the logarithm of this number is at most an $\mathcal{O}(1)$ factor, so we ignore it. The amount of crossing times after which $\Delta v^2 = v^2$ is simply,

$$\#_{cond} \approx v^2 \cdot \left(18\left(\frac{G\, m_{eff}}{v}\right)^2 \frac{N}{R^2}\right)^{-1} \tag{114}$$

Rewriting this, we can find an expression in terms of the typical velocity v, the size of the galaxy R and the dark matter mass m. We get,

$$\#_{cond} \approx \frac{1}{32\pi^3} m^3 R^3 v^3 \tag{115}$$

Eq. (115) estimates how many halo crossing times are needed before condensation. The time is thus,

$$t_{cond} = \frac{R}{v}\,\#_{cond} \sim 10^{10}\,\mathrm{yr}\left(\frac{m}{10^{-22}\,\mathrm{eV}}\right)^3 \left(\frac{R}{5\,\mathrm{kpc}}\right)^4 \left(\frac{v}{300\,\mathrm{km/s}}\right)^2 \tag{116}$$

From this simple estimate we see that in typical galaxies, the soliton forms within a Hubble time $\sim 10^{10}$ yr for very light dark matter particles. The soliton naturally move to the center of the halo due to *dynamical friction*, leading to a cored density profile. This is how ULDM solves the *cusp vs. core* problem highlighted earlier. Note that the estimate of the condensation time of the soliton in (116) assumes a uniform homogeneous halo. If localized seeds of overdensities exist initially the condensation time can be shorter than the Hubble time for larger masses of the scalar (although only ULDM solves the small scale problems of CDM) [114, 127–129]. Selfinteractions between the scalar particles also alter this prediction [130, 131].

4.2.3 The core-halo relation

The formation of the soliton in cosmological simulations of wave dark matter has been observed in various works [29, 30]. The density profile of the core is well approximated by

$$\rho(r) = \frac{1.9\,(m/10^{-23}\,\mathrm{eV})^{-2}\,(r_c/\mathrm{kpc})^{-4}}{\left[1 + 9.1\cdot 10^{-2}\,(r/r_c)^2\right]^8}\; M_\odot\,\mathrm{pc}^{-3} \tag{117}$$

Where r_c is the size of the soliton. As expected it becomes of $\mathcal{O}(\mathrm{kpc})$ for light scalar masses, thus solving the *cusp vs. core* problem. For $r \gg r_c$ the density profile smoothly transitions into the celebrated NFW-profile as expected. We show a the spherical density of a typical ULDM halo in fig. 13.

To obtain constraints on ULDM models, it is an important problem to try and understand what the exact size of the soliton is, depending on the halo it is embedded in. This has led to the suggestion of various *core-halo relations*, trying to relate the soliton mass to the embedding halo mass. The first (and probably most cited) [30] relation proposes that,

$$M_s \propto M_h^{1/3} \tag{118}$$

Eq. (118) has been used in various studies to constrain models of ultra light dark matter [132–141]. It can be derived by equating the binding energy per particle in the halo to that of the soliton.

$$\left|\frac{E_h}{M_h}\right| = \left|\frac{E_s}{M_s}\right| \tag{119}$$

And using the scaling relations of the Schrödinger-Poisson equations. The core-halo relation is subject of academic debate [29, 30, 142–144] as it has been tested over a limited range of parameters; so the question remains how robust the constraints obtained using them are in actuality. In particular, it has been noted [145] that the soliton at the core of halos continues to accrete particles from its surroundings, deviating from the relation in (118) over time.

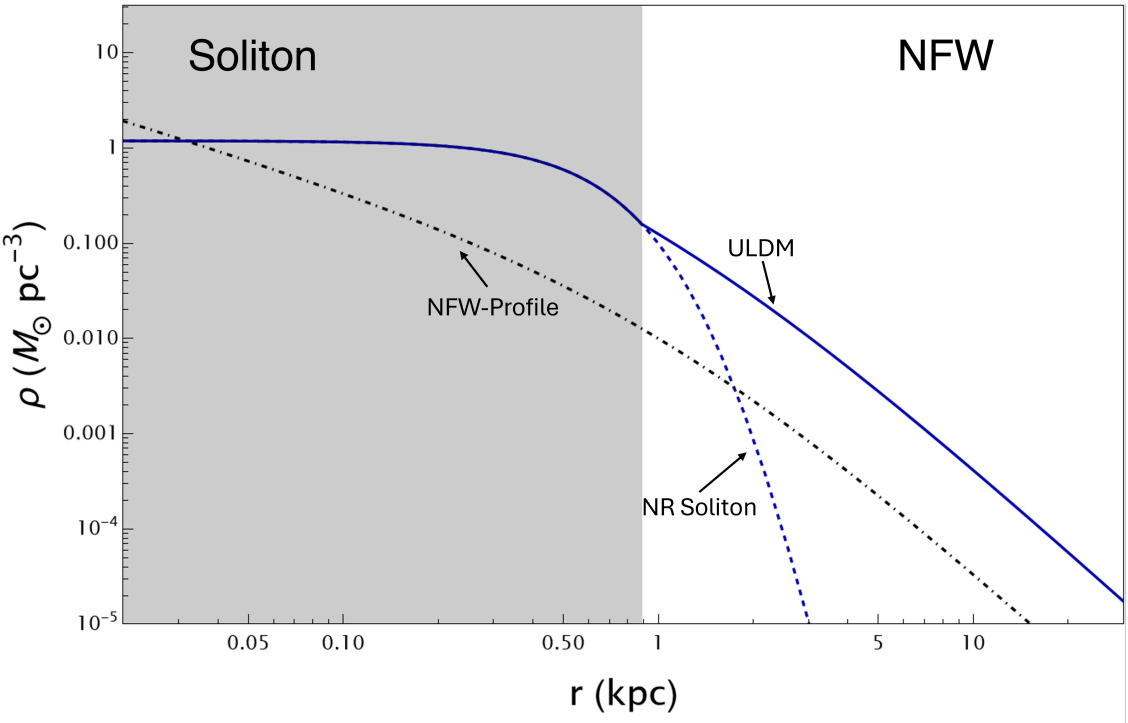

Figure 13: The structure of an ultra light dark matter halo. Here we show the density profile $\rho(r)$ (full blue line) averaged over longitudinal and azimuthal angles. The inner part of the halo $r <$ kpc is dominated by the soliton (blue dotted), while the outer part transitions to NFW (black dashed), reproducing CDM results.

In this section we have shown that nonrelativistic many-particle bound states exist in a popular family of dark matter models. Axions and axion-like particles fall within the category of wave dark matter which has therefore garnered considerable attention. If the scalar is ultralight $\sim 10^{-22}$ eV it can solve the small scale problems of the standard CDM paradigm. Moreover, solitons naturally form at the center of galaxies within a Hubble time for these light scalars. In the last chapter of the first part of this thesis we will review and discuss the main results in [1–5].

5 Results and discussion

In the previous chapters we have given a broad introduction to the topic of many-particle bound states in quantum field theory. In our work in [1–5] we have explored an discovered a variety of new aspects of these intriguing solutions of QFT. In this section we discuss the most important results of these investigations and place them in an adequate context. The discussion around the papers can be split into three different (but overlapping) topics, along which lines we'll structure this chapter. Papers [1] and [2] are concerned with the *phenomenology of multi-field non-topological solitons*. Papers [3] and [4] on the other hand aim at the *discovery and description of new oscillon states*. Finally in [5] we *test methods of including semiclassical backreaction*.

5.1 Phenomenology of multi-field non-topological solitons

Throughout this thesis we have centered the discussion of many-particle bound states around the simplest models of real scalars that support them. In particular, we've only looked at models with a single scalar degree of freedom. This is conform to the large majority of literature discussing these topics over the past decades. There are clear advantages of taking this approach. First, it is simpler to study these complicated nonlinear objects if we only need to worry about a single degree of freedom. Second, the phenomenology of a single scalar if often sufficient in describing experimental observations. Finally, one can use the single field dynamics to extract more general characteristics. Despite these advantages, there are theoretical indications that physics at the most fundamental scale should contain a multitude of scalar degrees of freedom. In that respect there is a clear need to go beyond the single field paradigm.

The Standard Model of particle physics describes almost all our observations of physics at the smallest experimental scale with a remarkable degree of accuracy. It only contains a single scalar, the Higgs field which could potentially support non-topological solitons. Indeed this possibility was explored in [146–148]. Despite this success, several fine-tuning tensions like the strong-CP and Hierarchy problems, and the wish to accommodate general relativity *at all scales* in the framework of quantum field theory have motivated the search for UV-extensions of the Standard Model. A broad class of such extensions falls under the umbrella of *supersymmetry*. Without going in too much detail, the basic idea of supersymmetry is to propose a fundamental symmetry between bosons and fermions. In this framework, each known particle has an associated superpartner with the same fundamental properties (above the superymmetric symmetry breaking scale) except for its spin quantum number. Interestingly, the superpartner of fermions are bosons, while the superpartners of bosons are fermions. To be consistent with experiment, supersymmetry has to be broken at some scale $\gg$ TeV, giving a large mass to the superpartners of the Standard Model. Nevertheless, if the superpartners exist they can be active at high energies, particularly in the early Universe. This means that there are many more, potentially well motivated, real scalars in the Universe. It

is therefore important to study many-particle bound states composed of multiple different scalar particles.

From this point of view, it's interesting to note that many of the inflationary potential favored by the Planck-2018 results [57,149] can be accommodated in supersymmetric theories. For this reason, various multi-field inflationary models have been considered in the literature. An important example of this are α-attractors [51–54,150–152], an inflationary model that can be realized in $\mathcal{N} = 1$ supergravity (a minimal supersymmetric extension of general relativity). These models are shown explicitly in figure eight of [57] as a class of models agreeing well with empirical constraints. If inflation is truly multi-field, one must consider the possibility of multi-field oscillon formation during preheating. Paper [1] explores this possibility.

Supersymmetry provides one direct motivation for the study of multi-field many-particle bound states. Another comes from the so-called *string axiverse*. It was shown in [56] that a generic prediction of string theory (which in itself is also a supersymmetric model) is the presence of a plenitude of axion-like particles, spanning a wide range of masses, between $10^{-33} - 10^{-10}$ eV. The exact amount of (pseudo)scalar particles depends on the way the extra dimensions of string theory are compactified, but what's clear is that one expects dozens to hundreds of scalars in the string axiverse. The phenomenological consequences, if observed, would provide support for the validity of string theory. In particular, one of the ultralight axions could play the role of wave-dark matter, as seen in section 4.2. From the string axiverse point of view, it is somewhat unnatural to only consider the presence of a single dark matter particle. Paper [2] is centered around this idea.

There is thus ample motivation to study many-particle bound states made out of multiple scalars. We made advances in the phenomenological study of these objects in [1] and [2]. We will now discuss the results in these works in more detail.

5.1.1 Paper 1. Symmetric multi-field oscillons

There are only a few examples of multi-field oscillons described in the literature [79,146–148], and they are usually hard to describe semi-analytically. In [1] we found oscillons in a multi-scalar theory with an arbitrary number of fields. One of the difficulties in describing multi-component oscillons is in the high dimensionality of the shooting problem, required for finding quasibreahter states, as outlined in section 3.2.1. To circumvent this issue we impose an explicit exchange symmetry on the potential. In particular, the potential we consider is the same if we interchange any two scalars $\phi_1 \leftrightarrow \phi_2$. The scalars are coupled via quartic coupling terms. The total Lagrangian of

the model with N real scalars can thus be written as,

$$\mathcal{L} = \sum_{i=1}^{N} \left(\frac{1}{2} \partial_\mu \phi_i \partial^\mu \phi_i - V(\phi_i) - \sum_{j<i} \frac{\Lambda}{2} \phi_i^2 \phi_j^2 \right) \tag{120}$$

And the potential $V(\phi)$ given by,

$$V(\phi) = \frac{1}{2} m^2 \phi^2 - \frac{\lambda}{4} \phi^4 + \frac{g}{6m^2} \phi^6 \tag{121}$$

One can argue that the type of symmetry we impose on our potential is somewhat ad hoc, however it turns out that some α-attractors do approximately realize such a potential. Nonetheless, it remains one of the major limitations of this work. In fact, these oscillons are very similar to Q-balls, and show the deep connections between these different types of configurations [83].

In this setup we are able to construct oscillons out of an arbitrary number of different constituents, by effectively mapping the model to a single field system. It is the first example of a semi-analytic description of multi-field oscillons in the literature. Focusing on the two and three field case (although there are no difficulties in analyzing more fields), we study their spatial structure, decay rate and stability. In particular, if $g \gg \lambda^2$, extremely long-lived, stable, multi-field oscillons exist.

To put this work in a cosmological context, we studied if and how multi-field oscillons form in the early Universe. Inspired by α-attractors, we study preheating where just one of the scalars, let's say ϕ_1 plays the role of the homogeneous oscillating background. The initial conditions thus explicitly break the symmetry of the potential. Nonetheless, multi-field oscillons still form, indicating that this result is generic. Multi-field oscillon formation proceeds in a unique way. First, the coherent background fragments and forms single-field oscillons as discussed in section 4.1. Eventually however, some of these oscillons amplify fluctuations in the spectator fields, leading to the formation of multi field oscillons. This formation mechanism is unique to models with multiple real scalars interacting with each other. In unpublished work, we found that this secondary preheating phase is accompanied by an extra burst of gravitational wave production.

5.1.2 Paper 2. Core and halo properties in multi-field wave dark matter

As discussed in section 4.2, wave dark matter with a fundamental mass around $\sim 10^{-22}$eV can solve the small scale problems of CDM. In particular, ultra light dark matter predicts the presence of a large gravitational soliton at the center of galaxies, hence the observed cored density profile in most halos. The question remains if there are actually theories whose nonrelativistic soliton solutions match the core we see in

experiments. In [153] it was argued that in fact, there are no single field theories that do so. The argument is the following: there is an approximate scaling between the observed central density of the core ρ_c and its size R_c. The observed scaling is $\rho_c \propto R_c^{-\beta}$, with $\beta \approx 1.3$. It is straightforward to show from the scaling relations in table 1 that the solitons in vanilla models of wave dark matter obey $\rho_c \propto R_c^{-4}$, very far off the observed relation. Even in more advanced modeling, $\beta \approx 1.3$ is hard to obtain. So single field ultra light dark matter seems to be in tension with the observed cores of galaxies, even though the prediction of a cored halo is one of its successes. Additionally, many other constraints in recent years have made single field ULDM less and less appealing [140, 154–158]. In [2] we therefore aim to investigate cores in multi-field ULDM models, with a particular focus on the scaling between ρ_c and R_c.

We focus on a minimal extension of single field ULDM by considering two massive scalars interacting only through gravity. By adding another degree of freedom the scaling relating different solitons is broken, allowing for a different relation between ρ_c and R_c. In this paper we develop a new method to find gravitational solitons in multi-field models, using an iterative procedure. Because the two scalars have different masses, the solitons of the theory have a unique nested structure, where the inner part is dominated by the more massive scalar, while the outer part is dominated by the lighter one. Fitting such a nested structure to rotation curves is yet to be done and is an interesting avenue for future research.

By performing spherically symmetric simulations of this model, we show that multi-field wave dark matter is able to reproduce all the desirable characteristics of single field ULDM. A randomly initialized bath of scalar particles condenses into a virialized halo with a groundstate soliton at its center, transitioning to an NFW outer tail. Using our numerical simulation, we were able to extract a multi-field version of the core-halo relation, similar to (118); however it remains an open question as to how robust this result is in cosmological and three dimensional settings.

Using our numerical results we show that multi-field solitons can be a solution to the tension highlighted in [153], but only if the ratio of the masses of the dark matter scalars obeys $m_1/m_2 \gtrsim 10^3$. Moreover, to fit the data accurately, the ratio of the number of particles of each species in a galaxy needs to scale with the total mass of the dark matter halo, $N_1/N_2 \propto M^\alpha$. We conclude in particular that more massive galaxies need a relative larger proportion of the lighter species in order to make the scaling parameter β consistent. This might seem somewhat unlikely but there are more recent results from three dimensional simulations that indicate that aspherical effects such as tidal stripping can cause depletion of the heavier species in environments where the light scalar is more prevalent [159, 160]. Moreover, for large ratios of the fundamental masses $m_1/m_2 \gtrsim 10^3$, the exact value of α required to reproduce $\beta \approx 1.3$ can be small. This is because the lighter species contributes much more mass to the soliton. From

this work we thus conclude that multi-field wave dark matter is an interesting avenue for future study. Of particular interest is to test our version of the core-halo relation in more realistic three dimensional simulations.

5.2 Discovery and description of new oscillon states

In section 3.2.1 we described the main properties of oscillons in a broad and model-independent way. Since oscillons are so ubiquitous in real scalar field theories, and are generally (mild) attractors of dynamic motion, it is worthwhile to go beyond the study of the the lowest energy oscillons of any given theory, what we called 'oscillon 1' and 'oscillon 2' in fig. 5. Oscillons can have a considerable lifetime during which their mass and other characteristics remain more or less constant. From this point of view, oscillons are true resonances of the theory that can be excited when the energy within a localized region exceeds the oscillon mass. Besides the preheating scenario outlined in section 4.1, this could also occur from the collapse of a network of topological defects in the early Universe, where the energy density can be even larger [26–28, 127–129, 161–164]. It is thus desirable to map all the oscillon resonances of a given theory regardless of their energy. The next two works should be understood from this perspective. In [3] we unravel the resonance structure of three dimensional oscillons in the important Sine-Gordon model while in [4] we show that a continuum of long-lived oscillon states exist in massless plateau potentials.

5.2.1 Paper 3. Oscillon spectroscopy

The Sine-Gordon model has quite some historical significance in the field of theoretical and mathematical physics. It is a model example of periodic scalar potentials,

$$V_{SG}(\phi) = m^2 f^2 \left(1 - \cos(\phi/f)\right) \tag{122}$$

In one dimension it contains stable breather states, oscillon like objects that do not radiate away energy. Moreover, these states are quantizable, providing an explicit example of a nonstatic classical background for which the radiative quantum corrections can be computed exactly [36–38]. Unfortunately, this property is lost in higher dimensions; however the SG-model remains relevant to the study of fields with a discrete shift symmetry, like axions or pions. In [3] we mapped the resonant structure of three dimensional oscillons in this potential, highlighting for the first time the importance of excited states.

It was first pointed out in [165] that the chiral Lagrangian of QCD contains two classical pionic oscillon states if the pion multiplet is displaced in a particular isospin direction. In that case the classical theory reduces to the Sine-Gordon model, and the two oscillons that were found are the lowest energy states in the theory. Note that these two oscillons don't persist in the full quantum chiral Lagrangian, because there are unstable perpendicular isospin directions that get excited and deplete the oscillon

rapidly. We found this in unpublished results. In [3] we show that a large amount of new oscillons exist in Sine-Gordon in three dimensions. These are understood as excitations of the groundstate oscillon and are characterized by the amount of nodes in their spatial profile. By performing the shooting exercise sketched in fig. 3 we can find oscillons with an arbitrary number of nodes and consequently large energy. The two previously known oscillons are simply the lowest energy, nodeless states.

Remarkably, in spherical symmetry, these excited oscillons can have lifetimes comparable to the two nodeless oscillons of $\mathcal{O}(10^2)$ oscillation periods. Since they can be much more massive, their narrowness $\propto M_{osc}\tau$ as a resonance is more significant (here τ is the lifetime of the state and M_{osc} is its mass). We thus show that oscillon states exist in a tower of resonances marked by two classically conserved numbers, the fundamental frequency, and the amount of nodes in the spatial structure. The particular resonant structure we found is due to the destructive interference of the radiation source as explained in section 3.2.1. Although this type of resonant structure is expected to exist beyond Sine-Gordon oscillons, the exact realization of it will be model-dependent.

One of the limitations of excited oscillons is that nodeful states are unstable in three dimensions. By performing numerical simulations we find that these oscillons are shorter lived in three dimensions, reducing the lifetime to $\mathcal{O}(10^1)$ oscillations. They tend to break up violently and settle into more stable nodeless oscillons. We only checked this explicitly for Sine-Gordon oscillons, and it remains an open question whether this is still true in other models.

5.2.2 Paper 4. Soft oscillons

Since the discovery of oscillons in the 90's [42], it has been standard lore that oscillons only exist in models of massive real scalars. The logic is that attractive interactions lower the on-shell mass of the particles, thus creating a binding energy. If there is no natural mass scale, this can not happen. However, recent advances have shown that this is not necessarily true [166]. If we simply look at the classical field theory this is not so surprising, one just needs attractive interactions to counteract the dispersive tendencies of localized wavepackets, regardless of the vacuum structure.

Although [166] did indeed show that oscillons can exist in gapless theories, they only considered potentials that were a small deformation of massive theories. In [4], we show that long lived oscillons of arbitrary size $R \to \infty$ and vanishing frequency $\omega \to 0$ exist in gapless plateau potentials. A typical potential we consider has the form,

$$V(\phi) = M^2\Lambda^2 \frac{(\phi/\Lambda)^4}{(1+(\phi/\Lambda)^2)^2} \tag{123}$$

where Λ is the cutoff of the theory and M is some mass scale far below the cutoff. Clearly, the vacuum is massless: $V(\phi) \to \phi^4$ as $\phi \to 0$. Since the oscillons that exist in

these theories have necessarily large sizes, we dubbed these *soft oscillons*. They come in a continuum of states label by their size R_o and can exist in any plateau potential, although their longevity is model dependent. This is the first example in the literature of long lived oscillons of arbitrary size. Moreover, since we only need a plateau potential to construct them, the requirements for their existence is minimal.

Soft oscillons have a few remarkable properties that distinguishes them from standard oscillons. They can be understood as a solution of the free field equations, since they have a large amplitude and live mostly on the plateau part of the potential. The free field equations are connected to spatial infinity by a static solution of the nonlinear equations of motion, what we call the *half-Domain wall* solution. This static solution acts as a confining cavity for the free field modes living within the oscillons. The cavity confines up to $\sim MR_o$ overtones of the fundamental frequency of the oscillon $\omega \propto R_o^{-1}$. The spectrum of soft oscillons is thus more rich than standard oscillons for which we only need to consider a few overtones. The spatiotemporal structure of soft oscillons is striking. It consists of two bouncing wave solutions, radiating away energy in regular pulses.

Certain aspects of soft oscillons need to be explored in future research. First, the correction to their lifetime due to asphericity is not yet fully under control. This is mainly due to the large resolution needed to study large localized objects, which is hard to attain in higher dimensions. More intriguing is the prospect of using soft oscillons as model analogues of localized objects in more complicated QFT's of massless particles, in particular gravity. The idea that black holes in a massless spin-2 theory (GR) have striking similarities to localized objects in simpler theories has been explored in the literature over the past decade [167]. In future work we aim to use soft oscillons as explicit testing beds for some of these ideas, since they share many similarities with black holes.

5.3 Testing methods of semiclassical backreaction

In section 2 we introduced the concept of the *quantum breaktime* of classical field configurations. It is inevitable that corrections proportional to $\hbar$ eventually spoil the classicality of the quantum mechanical coherent state. After this time, the one-point function of the field operator is no longer an (approximate) solution of the Euler-Lagrange equations of motion. Several methods have been developed over the last decade to go beyond semiclassics, and obtain predictions after the classical breaktime of the system by including backreaction from quantum fluctuations. In fact, one of these methods was outlined in section 4.1 when discussing preheating. These approximations are useful to obtain accurate predictions for many long lived classical objects, like the many-particle bound states described in this thesis. See for example [168]. The methods themselves are somewhat ad hoc however, and are taken as given in many works. For this reason it is paramount to test these methods against a full quan-

tum field theoretical computation. Given the complexity of such a calculation, this is typically impossible. For this reason we test two popular approaches to semiclassical backreaction in [5], but in a quantum field theory in $1+0$ dimensions, or better known as quantum mechanics.

5.3.1 Paper 5. Semiclassical backreaction: a qualitative assessment

Inspired by some famous models of (p)reheating in the early Universe [106] we consider a system of two (or three) coupled quantum harmonic oscillators. The Hamiltonian is given by,

$$\hat{H} = \frac{\hat{p}_x^2}{2m} + \frac{\hat{p}_y^2}{2M} + \frac{1}{2}m\omega^2\hat{x}^2 + \frac{1}{2}M\Omega^2\hat{y}^2 + \frac{\lambda}{2}\hat{x}^2\hat{y}^2 \tag{124}$$

This model contains many of the properties needed to test the validity of semiclassical methods: there exist 'classical' coherent states in each of the oscillators whose coherency is broken by the a dimensionless parameter $\tilde{\lambda} \propto \hbar$. Moreover, since the system can be solved exactly using numerical methods, the full quantum predictions are accessible. It is an ideal testbed for studying the concept of quantum breaking and the effectiveness of various approximation schemes. With this in mind we perform experiments with the following setup:

1. The x-variable plays the role of the classical coherent background and is put in a coherent state with large occupation number N.

2. The y-variable is initially placed in its adiabatic vacuum, and thus plays the role of quantum fluctuations.

3. The system is evolved using numerical methods. The classicality of x is lost over time due to the interaction term in (124).

We test three different semiclassical schemes against the full quantum mechanical solution of the system. These are the classical solution with no backreaction $x = x_0\cos(\omega t)$, the *Mean-field* method where we plug expectation values of the quantum operator $\hat{y}^2$ back into the classical equations of motion of x and finally the *Truncated Wigner* method, where predictions are obtained by averaging over a large number of classical paths with stochastic initial conditions. We check how all of these methods compare to the true quantum mechanical results.

The results show that both mean-field and truncated Wigner extend the breaktime of the classical solution considerably. They also highlight the importance of the dynamics of the background in determining the validity of semiclassical approximations. We find that if the classical background is unstable to small fluctuations, the quantum breaktime scales with $\log(N)$ instead of N. Semiclassical approximations can thus be trusted for less time in these situations. We also show that the stochastic truncated

Wigner is more suited to deal with unstable backgrounds while the opposite is true of mean-field. This is ultimately due to entanglement between the two quantum oscillators. In unstable situations the oscillators become entangled more quickly requiring additional degrees of freedom to simulate accurately. This is analogous to the different ways in which we deal with reheating and parametric resonance in the early Universe.

The results in [5] give a deeper understanding of the semiclassical approximation. It gives a prescription for which methods to apply when and for what reason. One of the major limitations of this work is that it deals solely with quantum mechanical systems. Although the results extend to systems with three modes as well, the question remains how the dynamics change in field theory. This is an important direction for future research.

5.4 Concluding remarks

Many things remain mysterious about many-particle bound states in quantum field theory. We wish to close the first part of this thesis by highlighting a few interesting directions for future research. Unfortunately, a consistent and systematic description of oscillons in general multi-field theories is still lacking. We showed that these objects can form generically in the early Universe and it is therefore paramount to get a better grasp of their properties. If the early Universe is dominated by the dynamics of many scalar degrees of freedom, it might be filled with multi-component oscillons.

The study of multi-field wave dark matter is still somewhat in its infancy, with various investigations popping up in recent years [2,159,169–171]. These models show some promise in alleviating the mounting constraints on the standard ULDM paradigm, with some unique phenomenological features, like a nested soliton at the center of galaxies. To constrain ultra light wave dark matter models a proper understanding of the effect of baryonic or other forms of matter on structure formation is needed, no matter the amount of scalars we decide to include in our modeling. This presents an important direction for future research. Indeed, it has been shown that the presence of point particles can alter the structure of the core in ULDM halos [172–174], softening current constraints on single field models.

Although semiclassical descriptions of quantum fields are used everywhere in the literature, we still lack a strong understanding of their range of validity. We have made some advances in this thesis but a more robust test of field theories is desirable. Of particular interest is the nature of the quantum remnant, the object that remains after the quantum breaktime of the classical system. We lack a way to describe these truly quantum configurations that are produced out of classical objects. For example, there is currently some debate surrounding the quantum remnant of a black hole. After losing mass to Hawking evaporation until the quantum breaktime, an object can remain that is much longer lived and lacks classical description [75, 76, 167]. Soft oscillons

might provide some progress in this regard as they are an analogue of black holes in a much simpler scalar theory.

In *The Tao of Physics* [175], written by Fritjof Capra in 1975, the author draws a striking parallel between modern physics and eastern mysticism. The last century of scientific advancements have painted a picture of the Universe that is ever changing, dynamic and uncertain. The earth's atmosphere is continuously bombarded by cosmic showers, measurements of physical observables are fundamentally random and even space itself is expanding at an ever increasing rate. Particles in quantum field theory are created, scattered and destroyed in a mere instant, resembling the cosmic dance of the Hindu god *Shiva*. Like our own consciousness, they exist for a fleeting moment in the history of the Universe. The struggle against change and decay is a hopeless endeavor. Many-particle bound states put up a noble effort in this regard, but their candle too will eventually flicker. As we've seen, their dying light can illuminate the underlying mysteries of physics. It is only fitting to conclude how we started, with a lesson from Siddhartha Gautama. *The world is afflicted by death and decay. But the wise do not grieve, having realized the nature of it.*

In the next part of this work we present the articles on which this thesis is based. It is unclear how the next big advancement in high energy physics will come about. The many-particle bound states described in this thesis provide a unique connection between the macroscopic and the microscopic, the classical and the quantum, the early and the late Universe. Whether the next big step finds its origin in a deeper understanding of these objects, is left as a challenge to the reader.

References

[1] F. van Dissel and E. I. Sfakianakis, *Symmetric multifield oscillons*, *Physical Review D* **106** (2022) .

[2] F. van Dissel, M. P. Hertzberg and J. Shapiro, *Core and halo properties in multi-field wave dark matter*, *Journal of Cosmology and Astroparticle Physics* **2024** (2024) 077.

[3] F. van Dissel, O. Pujolàs and E. I. Sfakianakis, *Oscillon spectroscopy*, *Journal of High Energy Physics* **2023** (2023) .

[4] F. van Dissel and O. Pujolàs, *Soft oscillons*, 2505.00890.

[5] F. van Dissel and G. Zahariade, *Semiclassical backreaction: A qualitative assessment*, *Physical Review D* **111** (2025) .

[6] S. M. Cohen and C. D. C. Reeve, *Aristotle's Metaphysics*, in *The Stanford Encyclopedia of Philosophy* (E. N. Zalta and U. Nodelman, eds.). Metaphysics Research Lab, Stanford University, Spring 2025 ed., 2025.

[7] Ptolemy, G. J. Toomer and O. Gingerich, *Ptolemy's Almagest*. Princeton University Press, 1998.

[8] S. Berryman, *Ancient Atomism*, in *The Stanford Encyclopedia of Philosophy* (E. N. Zalta and U. Nodelman, eds.). Metaphysics Research Lab, Stanford University, Winter 2022 ed., 2022.

[9] I. Newton, *Philosophiæ Naturalis Principia Mathematica*. England, 1687.

[10] M. Deutsch, *Evidence for the formation of positronium in gases*, *Physical Review* **82** (1951) 455.

[11] M. Deutsch, *The discovery of positronium*, in *Positron Annihilation*, pp. 517–524. Springer, 1985. DOI.

[12] M. Deutsch, *Evidence for the formation of positronium in gases*, *Physical Review* **83** (1951) 207.

[13] M. Deutsch, *Three-quantum decay of positronium*, *Physical Review* **83** (1951) 866.

[14] S. Berko and H. N. Pendleton, *Positronium*, *Annual Review of Nuclear and Particle Science* **30** (1980) 543.

[15] A. Einstein, *Quantentheorie des einatomigen idealen Gases*, pp. 237–244. John Wiley & Sons, Ltd, 2005. https://onlinelibrary.wiley.com/doi/pdf/10.1002/3527608958.ch27. https://doi.org/10.1002/3527608958.ch27.

[16] Bose, *Plancks Gesetz und Lichtquantenhypothese*, *Zeitschrift fur Physik* **26** (1924) 178.

[17] M. H. Anderson, J. R. Ensher, M. R. Matthews, C. E. Wieman and E. A. Cornell, *Observation of bose-einstein condensation in a dilute atomic vapor*, *Science* **269** (1995) 198 [https://www.science.org/doi/pdf/10.1126/science.269.5221.198].

[18] R. Brito, V. Cardoso, C. A. Herdeiro and E. Radu, *Proca stars: Gravitating bose–einstein condensates of massive spin 1 particles*, *Physics Letters B* **752** (2016) 291–295.

[19] M. Minamitsuji, *Vector boson star solutions with a quartic order self-interaction*, *Physical Review D* **97** (2018) .

[20] M. Jain and M. A. Amin, *Polarized solitons in higher-spin wave dark matter*, *Physical Review D* **105** (2022) .

[21] G. H. Derrick, *Comments on nonlinear wave equations as models for elementary particles*, *Journal of Mathematical Physics* **5** (1964) 1252.

[22] D. J. Kaup, *Klein-gordon geon*, *Phys. Rev.* **172** (1968) 1331.

[23] R. RUFFINI and S. BONAZZOLA, *Systems of self-gravitating particles in general relativity and the concept of an equation of state*, *Phys. Rev.* **187** (1969) 1767.

[24] L. Hui, J. P. Ostriker, S. Tremaine and E. Witten, *Ultralight scalars as cosmological dark matter*, *Physical Review D* **95** (2017) .

[25] L. Hui, *Wave dark matter*, *Annual Review of Astronomy and Astrophysics* **59** (2021) 247–289.

[26] M. Gorghetto, E. Hardy and G. Villadoro, *Axions from strings: the attractive solution*, *Journal of High Energy Physics* **2018** (2018) .

[27] M. Gorghetto, E. Hardy and G. Villadoro, *More axion stars from strings*, 2405.19389.

[28] M. Gorghetto, E. Hardy and G. Villadoro, *More axions from strings*, *SciPost Physics* **10** (2021) .

[29] H.-Y. Schive, T. Chiueh and T. Broadhurst, *Cosmic structure as the quantum interference of a coherent dark wave*, *Nature Physics* **10** (2014) 496–499.

[30] H.-Y. Schive, M.-H. Liao, T.-P. Woo, S.-K. Wong, T. Chiueh, T. Broadhurst et al., *Understanding the core-halo relation of quantum wave dark matter from 3d simulations*, *Physical Review Letters* **113** (2014) .

[31] C. Palenzuela, P. Pani, M. Bezares, V. Cardoso, L. Lehner and S. Liebling, *Gravitational wave signatures of highly compact boson star binaries*, *Physical Review D* **96** (2017) .

[32] M. Bezares, C. Palenzuela and C. Bona, *Final fate of compact boson star mergers*, *Phys. Rev. D* **95** (2017) 124005.

[33] M. Escudero, C. K. Pooni, M. Fairbairn, D. Blas, X. Du and D. J. Marsh, *Axion star explosions: A new source for axion indirect detection*, *Physical Review D* **109** (2024) .

[34] M. J. Ablowitz, D. J. Kaup, A. C. Newell and H. Segur, *Method for solving the sine-gordon equation*, *Phys. Rev. Lett.* **30** (1973) 1262.

[35] M. J. Ablowitz, D. J. Kaup, A. C. Newell and H. Segur, *Nonlinear-evolution equations of physical significance*, *Phys. Rev. Lett.* **31** (1973) 125.

[36] R. F. Dashen, B. Hasslacher and A. Neveu, *Nonperturbative methods and extended-hadron models in field theory. i. semiclassical functional methods*, *Phys. Rev. D* **10** (1974) 4114.

[37] R. F. Dashen, B. Hasslacher and A. Neveu, *Nonperturbative methods and extended-hadron models in field theory. ii. two-dimensional models and extended hadrons*, *Phys. Rev. D* **10** (1974) 4130.

[38] R. F. Dashen, B. Hasslacher and A. Neveu, *Particle spectrum in model field theories from semiclassical functional integral techniques*, *Phys. Rev. D* **11** (1975) 3424.

[39] S. Coleman, *Q-balls: S. coleman, nucl. phys. b262 (1985) 263*, *Nuclear Physics B* **269** (1986) 744.

[40] I. L. Bogolyubsky, *Oscillating Particle-Like Solutions of Nonlinear Klein-Gordon Equation*, *JETP Lett.* **24** (1976) 535.

[41] I. L. Bogolyubsky and V. G. Makhankov, *Lifetime of Pulsating Solitons in Some Classical Models*, *Pisma Zh. Eksp. Teor. Fiz.* **24** (1976) 15.

[42] M. Gleiser, *Pseudostable bubbles*, *Phys. Rev. D* **49** (1994) 2978 [hep-ph/9308279].

[43] E. J. Copeland, M. Gleiser and H. R. Muller, *Oscillons: Resonant configurations during bubble collapse*, *Phys. Rev. D* **52** (1995) 1920 [hep-ph/9503217].

[44] M. A. Amin, R. Easther, H. Finkel, R. Flauger and M. P. Hertzberg, *Oscillons after inflation*, *Physical Review Letters* **108** (2012) .

[45] N. Kitajima, J. Soda and Y. Urakawa, *Gravitational wave forest from string axiverse*, *Journal of Cosmology and Astroparticle Physics* **2018** (2018) 008–008.

[46] M. A. Amin, R. Easther and H. Finkel, *Inflaton Fragmentation and Oscillon Formation in Three Dimensions*, *JCAP* **12** (2010) 001 [1009.2505].

[47] M. A. Amin, *Inflaton fragmentation: Emergence of pseudo-stable inflaton lumps (oscillons) after inflation*, 1006.3075.

[48] S.-Y. Zhou, E. J. Copeland, R. Easther, H. Finkel, Z.-G. Mou and P. M. Saffin, *Gravitational waves from oscillon preheating*, *Journal of High Energy Physics* **2013** (2013) .

[49] T. Hiramatsu, E. I. Sfakianakis and M. Yamaguchi, *Gravitational wave spectra from oscillon formation after inflation*, *Journal of High Energy Physics* **2021** (2021) .

[50] K. D. Lozanov and V. Takhistov, *Enhanced gravitational waves from inflaton oscillons*, *Physical Review Letters* **130** (2023) .

[51] O. Iarygina, E. I. Sfakianakis, D.-G. Wang and A. Achúcarro, *Multi-field inflation and preheating in asymmetric α-attractors*, 2005.00528.

[52] O. Iarygina, E. I. Sfakianakis, D.-G. Wang and A. Achúcarro, *Multi-field inflation and preheating in asymmetric α-attractors*, 2005.00528.

[53] P. Christodoulidis, D. Roest and E. I. Sfakianakis, *Scaling attractors in multi-field inflation*, *JCAP* **12** (2019) 059 [1903.06116].

[54] P. Christodoulidis, D. Roest and E. I. Sfakianakis, *Attractors, Bifurcations and Curvature in Multi-field Inflation*, *JCAP* **08** (2020) 006 [1903.03513].

[55] B. Allanach and H. E. Haber, *Supersymmetry, part i (theory)*, 2024.

[56] A. Arvanitaki, S. Dimopoulos, S. Dubovsky, N. Kaloper and J. March-Russell, *String axiverse*, *Physical Review D* **81** (2010) .

[57] Y. Akrami, F. Arroja, M. Ashdown, J. Aumont, C. Baccigalupi, M. Ballardini et al., *Planck2018 results: X. constraints on inflation*, *Astronomy & Astrophysics* **641** (2020) A10.

[58] N. P. Proukakis, *Beyond gross-pitaevskii mean-field theory*, .

[59] L. Erdos, B. Schlein and H.-T. Yau, *Derivation of the gross-pitaevskii equation for the dynamics of bose-einstein condensate*, math-ph/0606017.

[60] E. H. Lieb and R. Seiringer, *Proof of bose-einstein condensation for dilute trapped gases*, *Physical Review Letters* **88** (2002) .

[61] S. Coleman and E. Weinberg, *Radiative corrections as the origin of spontaneous symmetry breaking*, *Phys. Rev. D* **7** (1973) 1888.

[62] M. E. Peskin and D. V. Schroeder, *An Introduction to quantum field theory*. Addison-Wesley, Reading, USA, 1995, 10.1201/9780429503559.

[63] T. Banks, *Modern Quantum Field Theory: A Concise Introduction*. Cambridge University Press, 2008.

[64] G. Dvali, C. Gómez and S. Zell, *Quantum break-time of de sitter*, *Journal of Cosmology and Astroparticle Physics* **2017** (2017) 028–028.

[65] L. Berezhiani and M. Zantedeschi, *Evolution of coherent states as quantum counterpart of classical dynamics*, *Physical Review D* **104** (2021) .

[66] T. Vachaspati and G. Zahariade, *Classical-Quantum Correspondence for Fields*, *JCAP* **09** (2019) 015 [1807.10282].

[67] T. Vachaspati and G. Zahariade, *Classical-quantum correspondence and backreaction*, *Phys. Rev. D* **98** (2018) 065002 [1806.05196].

[68] T. Vachaspati and G. Zahariade, *Classical-Quantum Correspondence and Hawking Radiation*, *JCAP* **04** (2019) 013 [1803.08919].

[69] M. Bojowald and D. Ding, *Canonical description of cosmological backreaction*, *JCAP* **03** (2021) 083 [2011.03018].

[70] M. Bojowald, *Canonical description of quantum dynamics**, *J. Phys. A* **55** (2022) 504006 [2301.05138].

[71] A. Ilderton and D. Seipt, *Backreaction on background fields: A coherent state approach*, *Physical Review D* **97** (2018) .

[72] J. Braden, M. C. Johnson, H. V. Peiris, A. Pontzen and S. Weinfurtner, *New Semiclassical Picture of Vacuum Decay*, *Phys. Rev. Lett.* **123** (2019) 031601 [1806.06069].

[73] G. Dvali and L. Eisemann, *Perturbative understanding of nonperturbative processes and quantumization versus classicalization*, *Phys. Rev. D* **106** (2022) 125019 [2211.02618].

[74] P. Copinger, J. P. Edwards, A. Ilderton and K. Rajeev, *Pair creation, backreaction, and resummation in strong fields*, *Phys. Rev. D* **111** (2025) 036009 [2411.06203].

[75] G. Dvali, J. S. Valbuena-Bermúdez and M. Zantedeschi, *Memory burden effect in black holes and solitons: Implications for PBH*, *Phys. Rev. D* **110** (2024) 056029 [2405.13117].

[76] G. Dvali, M. Zantedeschi and S. Zell, *Transitioning to Memory Burden: Detectable Small Primordial Black Holes as Dark Matter*, 2503.21740.

[77] A. Alexandre, G. Dvali and E. Koutsangelas, *New mass window for primordial black holes as dark matter from the memory burden effect*, *Phys. Rev. D* **110** (2024) 036004 [2402.14069].

[78] L. Visinelli, *Boson stars and oscillatons: A review*, *International Journal of Modern Physics D* **30** (2021) .

[79] M. Gleiser, N. Graham and N. Stamatopoulos, *Generation of coherent structures after cosmic inflation*, *Physical Review D* **83** (2011) .

[80] M. Gleiser, *d-dimensional oscillating scalar field lumps and the dimensionality of space*, *Phys. Lett. B* **600** (2004) 126 [hep-th/0408221].

[81] M. Gleiser, *Oscillons in scalar field theories: Applications in higher dimensions and inflation*, *Int. J. Mod. Phys. D* **16** (2007) 219 [hep-th/0602187].

[82] M. A. Amin and D. Shirokoff, *Flat-top oscillons in an expanding universe*, *Physical Review D* **81** (2010) .

[83] A. Alonso-Izquierdo, D. C. Martínez, T. Romańczukiewicz, K. Sławińska and A. Wereszczyński, *Excited oscillons and charge-swapping*, 2504.17382.

[84] J. Ollé, O. Pujolàs and F. Rompineve, *Recipes for oscillon longevity*, *Journal of Cosmology and Astroparticle Physics* **2021** (2021) 015.

[85] F. Blaschke, T. Romańczukiewicz, K. Sławińska and A. Wereszczyński, *Oscillons from Q-balls*, *Phys. Rev. D* **111** (2025) 036034 [2502.09136].

[86] G. Fodor, P. Forgacs, P. Grandclement and I. Racz, *Oscillons and Quasi-breathers in the phi**4 Klein-Gordon model*, *Phys. Rev. D* **74** (2006) 124003 [hep-th/0609023].

[87] G. Fodor, P. Forgacs, Z. Horvath and A. Lukacs, *Small amplitude quasi-breathers and oscillons*, *Phys. Rev. D* **78** (2008) 025003 [0802.3525].

[88] E. P. Honda and M. W. Choptuik, *Fine structure of oscillons in the spherically symmetric phi**4 Klein-Gordon model*, *Phys. Rev. D* **65** (2002) 084037 [hep-ph/0110065].

[89] H.-Y. Zhang, M. A. Amin, E. J. Copeland, P. M. Saffin and K. D. Lozanov, *Classical decay rates of oscillons*, *Journal of Cosmology and Astroparticle Physics* **2020** (2020) 055–055.

[90] G. Fodor, P. Forgacs, Z. Horvath and M. Mezei, *Computation of the radiation amplitude of oscillons*, *Phys. Rev. D* **79** (2009) 065002 [0812.1919].

[91] G. Fodor, P. Forgacs, Z. Horvath and M. Mezei, *Radiation of scalar oscillons in 2 and 3 dimensions*, *Phys. Lett. B* **674** (2009) 319 [0903.0953].

[92] G. Fodor, *A review on radiation of oscillons and oscillatons*, 1911.03340.

[93] D. Cyncynates and T. Giurgica-Tiron, *Structure of the oscillon: The dynamics of attractive self-interaction*, *Physical Review D* **103** (2021) .

[94] K. Mukaida, M. Takimoto and M. Yamada, *On longevity of i-ball/oscillon*, *Journal of High Energy Physics* **2017** (2017) .

[95] M. H. Namjoo, A. H. Guth and D. I. Kaiser, *Relativistic corrections to nonrelativistic effective field theories*, *Physical Review D* **98** (2018) .

[96] E. D. Schiappacasse and M. P. Hertzberg, *Analysis of dark matter axion clumps with spherical symmetry*, *Journal of Cosmology and Astroparticle Physics* **2018** (2018) 037–037.

[97] N. G. Vakhitov and A. A. Kolokolov, *Stationary solutions of the wave equation in a medium with nonlinearity saturation*, *Radiophys. Quant. Electron.* **16** (1973) 783.

[98] F. S. Guzman and L. A. Urena-Lopez, *Newtonian collapse of scalar field dark matter*, *Phys. Rev. D* **68** (2003) 024023 [astro-ph/0303440].

[99] F. S. Guzman and L. A. Urena-Lopez, *Evolution of the Schrodinger-Newton system for a selfgravitating scalar field*, *Phys. Rev. D* **69** (2004) 124033 [gr-qc/0404014].

[100] F. S. Guzman and L. A. Urena-Lopez, *Gravitational cooling of self-gravitating Bose-Condensates*, *Astrophys. J.* **645** (2006) 814 [astro-ph/0603613].

[101] X. Du, D. J. Marsh, M. Escudero, A. Benson, D. Blas, C. K. Pooni et al., *Soliton merger rates and enhanced axion dark matter decay*, *Physical Review D* **109** (2024) .

[102] H. Yoshino and H. Kodama, *Bosenova collapse of axion cloud around a rotating black hole*, *Progress of Theoretical Physics* **128** (2012) 153–190.

[103] J. Arakawa, J. Eby, M. S. Safronova, V. Takhistov and M. H. Zaheer, *Detection of bosenovae with quantum sensors on Earth and in space*, *Phys. Rev. D* **110** (2024) 075007 [2306.16468].

[104] D. Baumann, *Tasi lectures on inflation*, 0907.5424.

[105] D. Baumann, *Cosmological inflation: Theory and observations*, *Advanced Science Letters* **2** (2009) 105–120.

[106] L. Kofman, A. Linde and A. A. Starobinsky, *Towards the theory of reheating after inflation*, *Physical Review D* **56** (1997) 3258–3295.

[107] M. A. Amin, R. Easther and H. Finkel, *Inflaton fragmentation and oscillon formation in three dimensions*, *Journal of Cosmology and Astroparticle Physics* **2010** (2010) 001–001.

[108] M. A. Amin, M. P. Hertzberg, D. I. Kaiser and J. Karouby, *Nonperturbative dynamics of reheating after inflation: A review*, *International Journal of Modern Physics D* **24** (2014) 1530003.

[109] D. G. Figueroa, A. Florio, F. Torrenti and W. Valkenburg, *The art of simulating the early Universe – Part I*, *JCAP* **04** (2021) 035 [2006.15122].

[110] D. G. Figueroa, A. Florio, F. Torrenti and W. Valkenburg, *CosmoLattice: A modern code for lattice simulations of scalar and gauge field dynamics in an expanding universe*, *Comput. Phys. Commun.* **283** (2023) 108586 [2102.01031].

[111] K. D. Lozanov and M. A. Amin, *Self-resonance after inflation: Oscillons, transients, and radiation domination*, *Physical Review D* **97** (2018) .

[112] S. Antusch and S. Orani, *Impact of other scalar fields on oscillons after hilltop inflation*, *JCAP* **03** (2016) 026 [1511.02336].

[113] S. Antusch, F. Cefala and S. Orani, *Gravitational waves from oscillons after inflation*, *Phys. Rev. Lett.* **118** (2017) 011303 [1607.01314].

[114] J. Ollé, O. Pujolàs and F. Rompineve, *Oscillons and dark matter*, *Journal of Cosmology and Astroparticle Physics* **2020** (2020) 006–006.

[115] Z. Nazari, M. Cicoli, K. Clough and F. Muia, *Oscillon collapse to black holes*, *Journal of Cosmology and Astroparticle Physics* **2021** (2021) 027.

[116] Y. Cui and E. I. Sfakianakis, *Detectable gravitational wave signals from inflationary preheating*, *Physics Letters B* **840** (2023) 137825.

[117] A. Arbey and F. Mahmoudi, *Dark matter and the early universe: A review*, *Progress in Particle and Nuclear Physics* **119** (2021) 103865.

[118] C. O'Hare, *Cosmology of axion dark matter*, in *Proceedings of 1st General Meeting and 1st Training School of the COST Action COSMIC WSIPers — PoS(COSMICWISPers)*, COSMICWISPers, p. 040, Sissa Medialab, Apr., 2024, DOI.

[119] D. H. Weinberg, J. S. Bullock, F. Governato, R. Kuzio de Naray and A. H. G. Peter, *Cold dark matter: Controversies on small scales*, *Proceedings of the National Academy of Sciences* **112** (2015) 12249–12255.

[120] J. S. Bullock and M. Boylan-Kolchin, *Small-scale challenges to the λcdm paradigm*, *Annual Review of Astronomy and Astrophysics* **55** (2017) 343–387.

[121] W. J. G. de Blok, F. Walter, E. Brinks, C. Trachternach, S.-H. Oh and R. C. Kennicutt, *High-resolution rotation curves and galaxy mass models from things*, *The Astronomical Journal* **136** (2008) 2648–2719.

[122] R. K. de Naray, S. S. McGaugh and W. J. G. de Blok, *Mass models for low surface brightness galaxies with high-resolution optical velocity fields*, *The Astrophysical Journal* **676** (2008) 920–943.

[123] S. S. McGaugh, V. C. Rubin and W. J. G. de Blok, *High-resolution rotation curves of low surface brightness galaxies. i. data*, *The Astronomical Journal* **122** (2001) 2381–2395.

[124] B. Bar-Or, J.-B. Fouvry and S. Tremaine, *Relaxation in a fuzzy dark matter halo*, *The Astrophysical Journal* **871** (2019) 28.

[125] B. Bar-Or, J.-B. Fouvry and S. Tremaine, *Relaxation in a fuzzy dark matter halo. ii. self-consistent kinetic equations*, *The Astrophysical Journal* **915** (2021) 27.

[126] J. Binney and S. Tremaine, *Galactic Dynamics*. Princeton University Press, Princeton, 1987.

[127] J. N. Benabou, Q. Bonnefoy, M. Buschmann, S. Kumar and B. R. Safdi, *The cosmological dynamics of string theory axion strings*, 2312.08425.

[128] J. N. Benabou, M. Buschmann, J. W. Foster and B. R. Safdi, *Axion mass prediction from adaptive mesh refinement cosmological lattice simulations*, 2412.08699.

[129] J. N. Benabou, M. Buschmann, S. Kumar, Y. Park and B. R. Safdi, *Signatures of primordial energy injection from axion strings*, 2308.01334.

[130] K. Kirkpatrick, A. E. Mirasola and C. Prescod-Weinstein, *Relaxation times for bose-einstein condensation in axion miniclusters*, *Physical Review D* **102** (2020) .

[131] K. Kirkpatrick, A. E. Mirasola and C. Prescod-Weinstein, *Analysis of bose-einstein condensation times for self-interacting scalar dark matter*, *Physical Review D* **106** (2022) .

[132] N. Bar, D. Blas, K. Blum and S. Sibiryakov, *Galactic rotation curves versus ultralight dark matter: Implications of the soliton-host halo relation*, *Physical Review D* **98** (2018) .

[133] N. Bar, K. Blum and C. Sun, *Galactic rotation curves versus ultralight dark matter: A systematic comparison with sparc data*, *Physical Review D* **105** (2022) .

[134] L. E. Padilla, T. Rindler-Daller, P. R. Shapiro, T. Matos and J. A. Vázquez, *Core-halo mass relation in scalar field dark matter models and its consequences for the formation of supermassive black holes*, *Physical Review D* **103** (2021) .

[135] D. J. E. Marsh and J. C. Niemeyer, *Strong Constraints on Fuzzy Dark Matter from Ultrafaint Dwarf Galaxy Eridanus II*, *Phys. Rev. Lett.* **123** (2019) 051103 [1810.08543].

[136] B. T. Chiang, H.-Y. Schive and T. Chiueh, *Soliton oscillations and revised constraints from eridanus ii of fuzzy dark matter*, *Physical Review D* **103** (2021) .

[137] N. Bar, K. Blum, T. Lacroix and P. Panci, *Looking for ultralight dark matter near supermassive black holes*, *Journal of Cosmology and Astroparticle Physics* **2019** (2019) 045–045.

[138] Y. B. Ginat and B. Kocsis, *Constraining Axion Dark Matter with Galactic-Centre Resonant Dynamics*, 2502.08709.

[139] M. Aghaie, G. Armando, A. Dondarini and P. Panci, *Bounds on ultralight dark matter from nanograv*, *Physical Review D* **109** (2024) .

[140] N. Dalal and A. Kravtsov, *Excluding fuzzy dark matter with sizes and stellar kinematics of ultrafaint dwarf galaxies*, *Phys. Rev. D* **106** (2022) 063517 [2203.05750].

[141] P.-Y. Liao, G.-M. Su, H.-Y. Schive, A. Kunkel, H. Huang and T. Chiueh, *Deciphering the Soliton-Halo Relation in Fuzzy Dark Matter*, 2412.09908.

[142] P. Mocz, M. Vogelsberger, V. H. Robles, J. Zavala, M. Boylan-Kolchin, A. Fialkov et al., *Galaxy formation with becdm – i. turbulence and relaxation of idealized haloes*, *Monthly Notices of the Royal Astronomical Society* **471** (2017) 4559–4570.

[143] X. Du, C. Behrens, J. C. Niemeyer and B. Schwabe, *Core-halo mass relation of ultralight axion dark matter from merger history*, *Physical Review D* **95** (2017) .

[144] B. Schwabe, J. C. Niemeyer and J. F. Engels, *Simulations of solitonic core mergers in ultralight axion dark matter cosmologies*, *Physical Review D* **94** (2016) .

[145] A. S. Dmitriev, D. G. Levkov, A. G. Panin and I. I. Tkachev, *Self-Similar Growth of Bose Stars*, *Phys. Rev. Lett.* **132** (2024) 091001 [2305.01005].

[146] E. Farhi, N. Graham, V. Khemani, R. Markov and R. Rosales, *An oscillon in the su(2) gauged higgs model*, *Physical Review D* **72** (2005) .

[147] N. Graham, *An Electroweak oscillon*, *Phys. Rev. Lett.* **98** (2007) 101801 [hep-th/0610267].

[148] E. I. Sfakianakis, *Analysis of oscillons in the su(2) gauged higgs model*, 2012.

[149] N. Aghanim, Y. Akrami, M. Ashdown, J. Aumont, C. Baccigalupi, M. Ballardini et al., *Planck2018 results: Vi. cosmological parameters*, *Astronomy & Astrophysics* **641** (2020) A6.

[150] A. Linde, *Single-field α-attractors*, *Journal of Cosmology and Astroparticle Physics* **2015** (2015) 003–003.

[151] R. Kallosh and A. Linde, *Universality Class in Conformal Inflation*, *JCAP* **07** (2013) 002 [1306.5220].

[152] R. Kallosh, A. Linde and D. Roest, *Superconformal Inflationary α-Attractors*, *JHEP* **11** (2013) 198 [1311.0472].

[153] H. Deng, M. P. Hertzberg, M. H. Namjoo and A. Masoumi, *Can light dark matter solve the core-cusp problem?*, *Physical Review D* **98** (2018) .

[154] V. Iršič, M. Viel, M. G. Haehnelt, J. S. Bolton and G. D. Becker, *First constraints on fuzzy dark matter from lyman-α forest data and hydrodynamical simulations*, *Phys. Rev. Lett.* **119** (2017) 031302.

[155] M. P. Hertzberg and A. Loeb, *Quantum tunneling of ultralight dark matter out of satellite galaxies*, *Journal of Cosmology and Astroparticle Physics* **2023** (2023) 059.

[156] H. Y. J. Chan, E. G. M. Ferreira, S. May, K. Hayashi and M. Chiba, *The diversity of core–halo structure in the fuzzy dark matter model*, *Monthly Notices of the Royal Astronomical Society* **511** (2022) 943 [https://academic.oup.com/mnras/article-pdf/511/1/943/42375251/stac063.pdf].

[157] E. Armengaud, N. Palanque-Delabrouille, C. Yèche, D. J. E. Marsh and J. Baur, *Constraining the mass of light bosonic dark matter using sdss lyman-α forest*, *Monthly Notices of the Royal Astronomical Society* **471** (2017) 4606 [https://academic.oup.com/mnras/article-pdf/471/4/4606/19635244/stx1870.pdf].

[158] D. M. Powell, S. Vegetti, J. P. McKean, S. D. M. White, E. G. M. Ferreira, S. May et al., *A lensed radio jet at milli-arcsecond resolution – ii. constraints on fuzzy dark matter from an extended gravitational arc*, *Monthly Notices of the Royal Astronomical Society: Letters* **524** (2023) L84 [https://academic.oup.com/mnrasl/article-pdf/524/1/L84/54609011/slad074.pdf].

[159] H. N. Luu, P. Mocz, M. Vogelsberger, S. May, J. Borrow, S.-H. H. Tye et al., *Nested solitons in two-field fuzzy dark matter*, *Monthly Notices of the Royal Astronomical Society* **527** (2023) 4162–4172.

[160] H. Huang, H.-Y. Schive and T. Chiueh, *Cosmological simulations of two-component wave dark matter*, *Monthly Notices of the Royal Astronomical Society* **522** (2023) 515–534.

[161] R. Z. Ferreira, A. Notari, O. Pujolàs and F. Rompineve, *Collapsing domain wall networks: Impact on pulsar timing arrays and primordial black holes*, 2401.14331.

[162] A. Notari, F. Rompineve and F. Torrenti, *The spectrum of gravitational waves from annihilating domain walls*, 2504.03636.

[163] S. Das and F. Ferrer, *Gravitational waves from the Axiverse*, 2502.12153.

[164] F. Ferrer, E. Masso, G. Panico, O. Pujolas and F. Rompineve, *Primordial Black Holes from the QCD axion*, *Phys. Rev. Lett.* **122** (2019) 101301 [1807.01707].

[165] J. N. Hormuzdiar and S. D. H. Hsu, *Pion breather states in qcd*, *Physical Review C* **59** (1999) 889–893.

[166] P. Dorey, T. Romanczukiewicz, Y. Shnir and A. Wereszczynski, *Oscillons in gapless theories*, *Phys. Rev. D* **109** (2024) 085017 [2312.05308].

[167] G. Dvali, O. Kaikov and J. S. Valbuena Bermúdez, *How special are black holes? correspondence with objects saturating unitarity bounds in generic theories*, *Physical Review D* **105** (2022) .

[168] M. P. Hertzberg, *Quantum radiation of oscillons*, *Physical Review D* **82** (2010) .

[169] H. N. Luu, S. H. H. Tye and T. Broadhurst, *Multiple Ultralight Axionic Wave Dark Matter and Astronomical Structures*, *Phys. Dark Univ.* **30** (2020) 100636 [1811.03771].

[170] H. N. Luu et al., *Diverse dark matter haloes in Two-field Fuzzy Dark Matter*, 2408.00827.

[171] M. Gosenca, A. Eberhardt, Y. Wang, B. Eggemeier, E. Kendall, J. L. Zagorac et al., *Multifield ultralight dark matter*, *Phys. Rev. D* **107** (2023) 083014 [2301.07114].

[172] N. Bar, K. Blum, J. Eby and R. Sato, *Ultralight dark matter in disk galaxies*, *Physical Review D* **99** (2019) .

[173] J. Veltmaat, B. Schwabe and J. C. Niemeyer, *Baryon-driven growth of solitonic cores in fuzzy dark matter halos*, *Phys. Rev. D* **101** (2020) 083518 [1911.09614].

[174] E. Y. Davies and P. Mocz, *Fuzzy Dark Matter Soliton Cores around Supermassive Black Holes*, *Mon. Not. Roy. Astron. Soc.* **492** (2020) 5721 [1908.04790].

[175] F. Capra, *The Tao of Physics: An Exploration of the Parallels Between Modern Physics and Eastern Mysticism*. Shambhala, Boston, 1975.

Part II
Papers

6 Symmetric multi-field oscillons

Symmetric multi-field oscillons

Fabio van Dissel[1,2] and Evangelos I. Sfakianakis[1,2,3*]

[1] *Institut de Física d'Altes Energies (IFAE),*
The Barcelona Institute of Science and Technology (BIST),
Campus UAB, 08193 Bellaterra, Barcelona

[2] *Institute Lorentz of Theoretical Physics,*
Leiden University, 2333 CA Leiden, The Netherlands

[3] *Nikhef, Science Park 105,*
1098 XG Amsterdam, The Netherlands

Oscillons are long-lived, spatially localized field configurations, which are supported by attractive non-linearities in the scalar potential. We study oscillons comprised of multiple interacting fields, each having an identical potential with quadratic, quartic and sextic terms. We consider quartic interaction terms of either attractive or repulsive nature. In the two-field case, we construct semi-analytical oscillon profiles for different values of the potential parameters and coupling strength using the two-timing small-amplitude formalism. We use analytical and numerical techniques to explore the basin of attraction of stable oscillon solutions and show that, depending on the initial perturbation size, unstable oscillons can either completely disperse or relax to the closest stable configuration. We generalize our analysis to multi-field oscillons and show that the governing equations for their shape and stability can be mapped to the ones arising in the two-field case. Finally, we study the emergence of multicomponent oscillons in one and three spatial dimensions, both numerically and through Floquet theory.

* Email addresses: fvdissel@ifae.es; esfakianakis@ifae.es

CONTENTS

I. Introduction 82

II. Model 83

III. Two timing analysis 84

A. Oscillon profiles 88

IV. Stability Analysis 90

A. Extension of the V-K criterion 92

B. Oscillon Dynamics and Decay 92

V. Oscillon lifetime 97

VI. Generalization to many fields 99

A. Two-timing analysis 100

B. Stability analysis 101

VII. Oscillon Emergence and dynamics 102

A. Dynamical emergence in 1+1D 102

B. Single to multi-field oscillons in 1+1D 105

C. Single to multi-field oscillons in 3+1D 109

D. Analysis of results in terms of Floquet theory 110

VIII. Summary and Discussion 113

Acknowledgments 115

A. The V-K criterion 115

1. Two fields 116

a. Two-field system oscillating in phase 116

b. Two-field system oscillating out of phase 118

2. N fields 118

B. Aprroximate Floquet exponents 120

References 122

I. INTRODUCTION

Oscillons are part of a large family of soliton-like structures. The stability of these solutions can be traced back to non-linear terms in the theory, since a linear theory will in general force rapid dispersion of any localized wave-packet. In general, solitons can be classified according two characteristics. They are either completely static (ignoring propagation) or oscillate during their lifetime. Furthermore, their stability is either due to some conserved charge or to interactions between nonlinearities and dispersive effects.

Among such non-linear dynamics, oscillons [1–10], localized long-lived objects, have attracted significant attention in the early Universe cosmology community. Oscillons can arise in scalar field models where the potential is quadratic near the minimum and becomes shallower than quadratic ("flattens out") at larger field values. Currently, inflationary models that are preferred by observations are models that contain plateau-type potentials [11–14], which satisfy the necessary condition needed to support oscillons. Furthermore, numerical simulations have shown that the post-inflationary fragmentation of the inflaton in such models leads to copious production of oscillons [15].

Recently oscillons have seen renewed interest. Numerical simulations have revealed that oscillon formation after inflation is accompanied by the generation of significant amounts of gravitational waves [16–24]. Since gravitational waves can be one of the very few tools able to probe the end of inflation, the dynamics of oscillon formation, evolution and stability are becoming an essential part of early Universe cosmology.

Our current understanding of fundamental physics suggests that multiple scalar fields are likely to be present at high energies. In spite of this, most of the work on oscillons has focused on single-field models, ignoring decay channels of oscillons to other fields and –more interesting– the dynamics that can lead to oscillons comprised of multiple fields. Numerical simulations have uncovered two-field oscillons arising after hybrid inflation [25] and in an $SU(2)$ gauged Higgsed model [26], for which a semi-analytical construction of the observed oscillons was given in Ref. [10], along with a detailed study of their parameter dependent stability. The analysis of oscillons in an Abelian Higgs model can be found in Refs. [27, 28]. While a type of composite Q-balls have been found in Ref. [29] and further studied in Ref. [30], their comparison to composite oscillons is beyond the scope of the present work. Finally, oscillons were found in an $SU(2) \times U(1)$ model [31, 32], inspired by the electroweak sector of the Standard Model. In the case of the SU(2) Higgsed oscillon, a particular mass ratio between the Higgs and W fields was required for the oscillon to be stable. In particular,

oscillons where the Higgs mass was almost twice the W mass were found to be stable over very long time-scales. This observation (which was examined in detail in Ref. [10]) can be taken to imply that rather special conditions need to exist for multi-field oscillons to arise.

The current work aims to provide a detailed look into the conditions for the existence and stability of multi-component oscillons, albeit in a simplified model. We organize our presentation as follows. In Section II we describe the two-field model that we consider. In Section III we use the small-amplitude two-timing analysis to construct solutions for composite oscillons, comprised of the two fields oscillating in a phase-locked configuration. Section IV contains the stability analysis of oscillons against long-wavelength perturbations, which is an extension of the Vakhitov-Kolokolov criterion in the case of two interacting fields with identical potential structure, going beyond the specific potential that we chose. In section V we find qualitative and quantitative estimates for the lifetime of stable oscillons that were found in previous sections, following the methods developed in Refs. [33–35]. In section VI we generalize our analysis to a model containing an arbitrary number of interchangeable interacting fields. Finally, Section VII explores the emergence of multi-field oscillons from a variety of initial conditions. We provide our conclusions and outlook on future work in Section VIII.

II. MODEL

We consider a model of two identical real scalar fields, each with a quadratic-quartic-sextic potential and a two-to-two interaction term, which can be either attractive or repulsive. This form of the potential was first analyzed for single-field oscillons in Ref. [6], where a large sextic term was introduced to stabilize three-dimensional oscillons in a symmetric quadratic-quartic potential. We ignore the expansion of the Universe[1] and restrict ourselves to an action consisting of the two scalar fields on a Minkowski background with metric signature $(-,+,+,+)$:

$$S = -\int d^3x dt \left[\sum_{I=1,2} \left(\frac{1}{2}\partial_\mu \phi^I \partial^\mu \phi^I + \frac{1}{2} m^2 \left(\phi^I\right)^2 - \frac{\lambda}{4}\left(\phi^I\right)^4 + \frac{g}{6}\left(\phi^I\right)^6 \right) - \frac{\Lambda}{2}(\phi^1)^2(\phi^2)^2 \right] . \quad (1)$$

Before proceeding, it is worth noting both the restrictions that the action of Eq. (1) poses, as well as some theoretical motivation for considering it. We draw our example from the well-motivated area of α-attractors, specifically the T-model potential. Since metrics on hyperbolic spaces can be formulated in many different forms, following Möbius transformations [36], we follow the metric

[1] We will present numerical results for an expanding Universe in one spatial dimension in Section VII.

definition used in Refs. [37–39]

$$ds^2 = d\chi^2 + e^{2b(\chi)} d\phi^2 \,, \tag{2}$$

where $b(\chi) = \log\left(\cosh(\beta\chi)\right)$. The two-field potential for the T-model in this field basis is

$$V(\phi,\chi) = \alpha\mu^2 \left(\frac{\cosh(\beta\phi)\cosh(\beta\chi) - 1}{\cosh(\beta\phi)\cosh(\beta\chi) + 1}\right) \left(\cosh(\beta\chi)\right)^{2/\beta^2} \,, \tag{3}$$

where $\beta = \sqrt{2/3\alpha}$.

For small value of α, the potential around the origin is expanded as

$$\begin{aligned} V(\phi,\chi) \simeq\ & \frac{\mu^2}{6}\chi^2 - \frac{\mu^2}{54\alpha}\chi^4 + \frac{17\mu^2}{9720\alpha^2}\chi^6 + \frac{\mu^2}{6}\phi^2 - \frac{\mu^2}{54\alpha}\phi^4 + \frac{17\mu^2}{9720\alpha^2}\phi^6 \\ & + \frac{\mu^2}{6}\phi^2\chi^2 - \frac{\mu^2}{16\alpha^2}\phi^2\chi^2(\phi^2+\chi^2) + ... \end{aligned} \tag{4}$$

where we included terms up to sextic order in the fields and neglected higher order contributions in α in each term. For that we assume that the parameter α, which is inversely related to the field-space curvature, is small. We see that this expansion has the characteristics that we consider in the action of Eq. (1): two scalar fields with identical potential parameters, a negative quartic term and a very large sextic term (for $\alpha \ll 1$), as well as a quartic coupling. Ref. [37] reported the formation of oscillons during two-field preheating after inflation on a T-model potential, but did not provide a detailed analysis of their properties. Of course, the true T-model expansion differs from the idealized action of Eq. (1), in that it contains sextic interaction terms and it provides less freedom for choosing the various potential coupling strengths (see Fig. 1). Furthermore, the analysis of the T-model must also take into account the non-canonical kinetic structure, leading to the derivative couplings

$$\mathcal{L}_{\rm kin} \supset \frac{\chi^2}{3\alpha}(\partial\phi)^2 + \frac{2\chi^4}{27\alpha^2}(\partial\phi)^2 + ... \tag{5}$$

Oscillons in systems with non-canonical kinetic terms have been considered in the litetarure for single-field systems [8]. In the present work, we instead focus on the symmetric sextic potential of Eq. (1) and consider canonical kinetic terms for the two fields. An extension of the current analysis to realistic α-attractor models, taking into account the intricacies of derivative couplings, can reveal interesting phenomenology for this family of well-motivated and observationally relevant models and is left for future work.

III. TWO TIMING ANALYSIS

In this section we construct approximate profiles of two-field oscillons and compare them to the single-field oscillons found in Ref. [6]. Eq. (1) contains several physical parameters, such as the

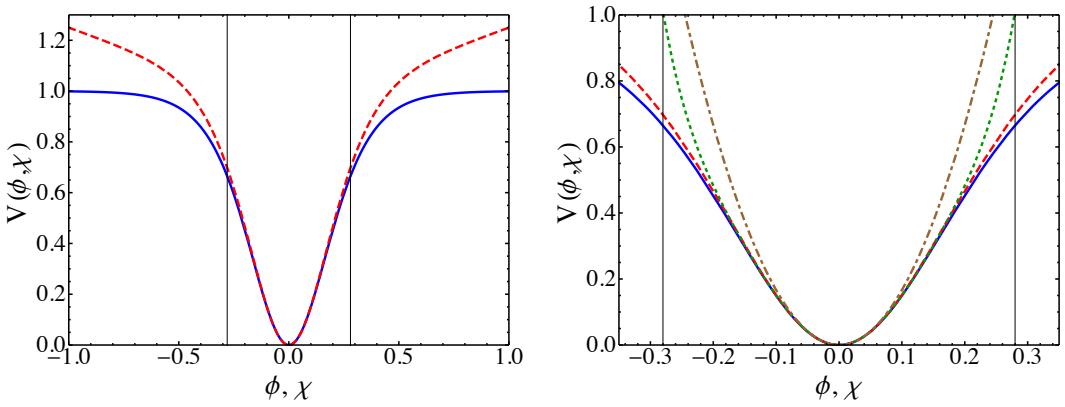

Figure 1. The T-model potential for $\chi = 0$ (blue solid) and $\phi = 0$ (red dashed), along with the sextic Taylor expansion (green dotted). The brown dot-dashed curve shows the quadratic term, which is steeper than the total potential, allowing in principle for oscillon formation in both ϕ and χ fields. The vertical lines show the field value of ϕ at the end of inflation.

mass of the two fields m, the coupling Λ and self couplings g and λ. It is convenient to work with dimensionless space-time variables and fields. This is done by the rescalings $x^\mu \to \tilde{x^\mu} = x^\mu m$, $\phi^I \to \tilde{\phi}^I = m^{-1}\lambda^{1/2}\phi^I$, $g \to \tilde{g} = (m/\lambda)^2 g$ and $\Lambda \to \tilde{\Lambda} = (1/\lambda)\Lambda$. The Lagrangian is then re-written as

$$\mathcal{L} = \frac{-\lambda}{m^4}\left(\sum_{I=1,2}\left(\frac{1}{2}\partial_\mu\tilde{\phi}^I\partial^\mu\tilde{\phi}^I + \frac{1}{2}\left(\tilde{\phi}^I\right)^2 - \frac{1}{4}\left(\tilde{\phi}^I\right)^4 + \frac{\tilde{g}}{6}\left(\tilde{\phi}^I\right)^6\right) - \frac{\tilde{\Lambda}}{2}(\tilde{\phi}^1)^2(\tilde{\phi}^2)^2\right) \tag{6}$$

For simplicity, in what follows we define $\{\tilde{\phi}^1, \tilde{\phi}^2\} \equiv \{\tilde{\phi}, \tilde{\chi}\}$ and drop all tildes. The Lagrangian of Eq. (6) leads to a system of two coupled equations of motion for ϕ and χ. In this work we focus our attention on spherically symmetric solutions $\phi(\vec{x}, t) \to \phi(r, t)$, leading to the equations of motion

$$\begin{aligned}
\partial_t^2\phi - \left(\partial_r^2 + \frac{2}{r}\partial_r\right)\phi + \phi &= \phi^3 - g\phi^5 + \Lambda\phi\chi^2\,, \\
\partial_t^2\chi - \left(\partial_r^2 + \frac{2}{r}\partial_r\right)\chi + \chi &= \chi^3 - g\chi^5 + \Lambda\chi\phi^2\,.
\end{aligned} \tag{7}$$

In d spatial dimension the above equations are altered by the substitution[2] $\frac{2}{r}\partial_r \to \frac{d-1}{r}\partial_r$. The attentive reader will immediately notice that these equations are symmetrical under exchange of the fields, meaning that sending $\chi \leftrightarrow \pm\phi$ in either of the equations gives back the other. This

[2] Additionally, in d dimensions the rescalings of the fields will also be different.

greatly simplifies the analytical search for oscillons which is more difficult (if at all possible) in general multi-component systems.

It is well established in the literature that oscillons live on long time- and large spatial scales [40–42]. This suggests a perturbative approach to extract oscillon solutions from the equations of motion, known as the small-amplitude two-timing analysis. The idea is that oscillons exhibit behaviour on two time scales, one capturing the natural frequency of the free field theory and one capturing the correction to this frequency characteristic for the non-linear potential. Furthermore, we attempt to capture oscillons which are slowly varying in space, hence are "broad". This behaviour is found by introducing new time and space variables

$$\tau = \alpha\epsilon^2 t\,,\ \rho = \epsilon r \tag{8}$$

where α is a free parameter and $\epsilon \ll 1$. While we expect all spatial variation to occur on the scale of ρ, the time variation occurs on two scales: t and τ. The (double) time derivatives in Eqs. (7) must now be interpreted as full time derivatives, leading to the equations

$$\begin{aligned}
\partial_t^2\phi + 2\alpha\epsilon^2\partial_t\partial_\tau\phi - \epsilon^2\left(\partial_\rho^2 + \frac{2}{\rho}\partial_\rho\right)\phi + \phi &= \phi^3 - g\phi^5 + \Lambda\phi\chi^2 + O\left(\epsilon^4\right)\,,\\
\partial_t^2\chi + 2\alpha\epsilon^2\partial_t\partial_\tau\chi - \epsilon^2\left(\partial_\rho^2 + \frac{2}{\rho}\partial_\rho\right)\chi + \chi &= \chi^3 - g\chi^5 + \Lambda\chi\phi^2 + O\left(\epsilon^4\right)\,.
\end{aligned} \tag{9}$$

Lastly, we assume that the amplitude of the oscillon profile also scales with the expansion parameter ϵ, allowing us to compute the effects of the non-linearities order-by-order. We therefore consider solutions of the form

$$\begin{aligned}
\phi(x,t) &= \sum_{n=1}\epsilon^n\phi_n(\rho,t,\tau)\,,\\
\chi(x,t) &= \sum_{n=1}\epsilon^n\chi_n(\rho,t,\tau)\,.
\end{aligned} \tag{10}$$

Inserting Eqs. (10) into Eqs. (9), the lowest order equations in ϵ are

$$\begin{aligned}
\partial_t^2\phi_1 + \phi_1 &= 0\,,\\
\partial_t^2\chi_1 + \chi_1 &= 0\,,
\end{aligned} \tag{11}$$

which are identical to the harmonic oscillator equation and capture the main oscillatory behaviour of the oscillon. The equations in the next non-trivial order in ϵ are

$$\begin{aligned}
\partial_t^2\phi_3 + \phi_3 &= \left(\partial_\rho^2 + \frac{2}{\rho}\partial_\rho\right)\phi_1 - 2\alpha\partial_t\partial_\tau\phi_1 + \phi_1^3 - \phi_1^5 + \Lambda\phi_1\chi_1^2\,,\\
\partial_t^2\chi_3 + \chi_3 &= \left(\partial_\rho^2 + \frac{2}{\rho}\partial_\rho\right)\chi_1 - 2\alpha\partial_t\partial_\tau\chi_1 + \chi_1^3 - \chi_1^5 + \Lambda\chi_1\phi_1^2\,.
\end{aligned} \tag{12}$$

Notice that we used the fact that g is large and have therefore written $g = 1/\epsilon^2$. The solutions to the harmonic oscillator Eqs. (11) are trivial. Therefore we can write $\phi_1 = \mathrm{Re}\{A(\rho,\tau)e^{-it}\}$ and $\chi_1 = \mathrm{Re}\{B(\rho,\tau)e^{-it}\}$; where $A(\rho,\tau)$ and $B(\rho,\tau)$ are complex functions[3]. Inserting this solution into Eqs. (12) and eliminating secular terms gives us the envelope equations of the system of oscillons

$$\begin{aligned} 2i\alpha\partial_\tau A + \left(\partial_\rho^2 + \frac{2}{\rho}\partial_\rho\right)A + \frac{3}{4}|A|^2A + \frac{\Lambda}{2}|B|^2A + \frac{\Lambda}{4}A^*B^2 - \frac{5}{8}|A|^4A = 0\,, \\ 2i\alpha\partial_\tau B + \left(\partial_\rho^2 + \frac{2}{\rho}\partial_\rho\right)B + \frac{3}{4}|B|^2B + \frac{\Lambda}{2}|A|^2B + \frac{\Lambda}{4}B^*A^2 - \frac{5}{8}|B|^4B = 0\,. \end{aligned} \tag{13}$$

These equations are of the Nonlinear Schrödinger type [43]. They control the behaviour of the oscillon on long time- and large spatial scales. To find solutions of these equations that are localized in space we insert the "oscillon ansatz". Since by assumption the oscillon is just some localized structure oscillating in time we should look for solutions of the form, $A(\rho,\tau) = a(\rho)e^{ic_1\tau}$ and $B(\rho,\tau) = b(\rho)e^{ic_2\tau}$; where a and b are real functions determining the spatial character of the oscillon. Due to the symmetry of the potential we can also set $c_1 = c_2 = c$. Inserting this into Eqs. 13, we obtain the profile equations of the oscillons.

$$\begin{aligned} -\alpha\, a + \left(\partial_\rho^2 + \frac{2}{\rho}\partial_\rho\right)a + \frac{3}{4}a^3 + \frac{3\Lambda}{4}b^2a - \frac{5}{8}a^5 = 0\,, \\ -\alpha\, b + \left(\partial_\rho^2 + \frac{2}{\rho}\partial_\rho\right)b + \frac{3}{4}b^3 + \frac{3\Lambda}{4}a^2b - \frac{5}{8}b^5 = 0\,, \end{aligned} \tag{14}$$

where we set $c = 1/2$. A few remarks about the parameter c are now in order. c is in essence a free parameter, as long as it is not too large. This is because it can always be absorbed into a redefinition of ϵ. We do require it to be positive, since the oscillon should behave as $a, b \to 0$ for $\rho \to \infty$, since they are localized solutions. We can therefore set $c = 1/2$ without loss of generality.

An interesting property arising due to the symmetry of the system now becomes apparent. Namely, any localized solution $a(\rho)$ of the equation

$$-\alpha\, a + \left(\partial_\rho^2 + \frac{2}{\rho}\partial_\rho\right)a + \frac{3}{4}(1+\Lambda)a^3 - \frac{5}{8}a^5 = 0 \tag{15}$$

directly solves the system of Eqs. (14) if we set $a = b$. We arrive at the same equation if we instead choose $a = -b$, meaning that the two fields oscillate out of phase. It is worth noting that in the one other case in the literature, where two-field oscillons were constructed using the two-timing analysis, Ref. [10], the masses of the two fields were chosen to have a $2:1$ ratio, meaning that for half the period of the light field, they were in phase, and for the other half they were out of phase.

[3] Note that this procedure is equivalent to going to the non-relativistic limit, where a real scalar field can be written as the real part of a complex wavefunction $\Psi(x,t)\exp^{-imt}$.

The difficulty of finding oscillon solutions in the coupled system of Eqs. (14) is therefore greatly reduced and can be related to the solutions for single-field oscillons in a quartic-sextic potential, which were studied in Ref. [6].

A. Oscillon profiles

In order to solve Eq. (15), we must first define the boundary conditions. At large distance from the origin, far away from the oscillon core, the non-linear terms become subdominant, hence Eq. (15) can be approximated as $\partial_\rho^2 a + (2/\rho)\partial_\rho a \approx \alpha a$, leading to $a(\rho) \propto e^{-\sqrt{\alpha}\rho}/\rho$. Finally, we require regularity at the origin. Eq. (15) can be re-written as

$$\frac{dE_\rho}{d\rho} = -\frac{2}{\rho}\left(\frac{\partial a}{\partial \rho}\right)^2 , \tag{16}$$

where

$$E_\rho = \frac{1}{2}\left(\frac{\partial a}{\partial \rho}\right)^2 - \frac{1}{2}\alpha\, a^2 + \frac{3}{16}(1+\Lambda)a^4 - \frac{5}{48}a^6 \tag{17}$$

would be the conserved energy for a one-dimensional system with the same potential. The right hand side of Eq. (16) is non-positive, hence the energy of any solution E_ρ will decrease as $\rho \to \infty$. Since the energy of a localized solution must be zero in the far-distance regime (this can be seen by inspecting Eq. (17)) we conclude that $E_\rho \geq 0$ at $\rho \to 0$. It is best to think about this in terms of the trajectories of solutions in phase space $(a, \partial_\rho a)$. Since we're interested in functions that are smooth at the origin, all trajectories start on the $\partial_\rho a = 0$ axis. Any trajectory will continuously intersect curves with $E_\rho = \text{const}$, and the constant value of these curves must decrease as $\rho \to \infty$. The $E_\rho = 0$ curve then defines the boundary between localized and non-localized solutions. Namely, a localized solution must intersect this curve in the origin. The requirement that the oscillon is smooth at the origin, meaning $\partial_\rho a|_{\rho=0} = 0$, and the fact that $E_\rho \geq 0$ there, leads to $\alpha < \alpha_c \equiv (27/160)(1+\Lambda)^2$, generalizing the constraint found in Ref. [6] for single-field oscillons[4], or equivalently $\Lambda = 0$. For $\alpha \to \alpha_c$ the oscillon becomes infinitely wide with an amplitude $a^2(\rho = 0) \to (9/10)(1+\Lambda)$.

It turns out that only a countable set $a_n(\rho)$ of localized trajectories can be drawn in phase space [44]. Here n is the amount of nodes of the solution. We conclude that there is exactly one zero-node solution of the profile equation, and thus one zero-mode oscillon for every choice of ϵ and α. We do not pursue solutions with $n \geq 1$, since they will have a higher energy than their

[4] We must note that our definition of the parameter α is related to the square of the parameter α used in Ref. [6].

zero-node counterpart, and thus are expected to be unstable. We used both the shooting and relaxation methods in order to find the corresponding oscillon profiles and check our results. Fig. 2 shows some characteristic profiles for $\Lambda = \pm 0.5$. For the one-dimensional case, Eq. 15 can be solved analytically to give

$$\phi(r) = \sqrt{\frac{9}{10}(1+\Lambda)}\sqrt{\frac{1-u^2}{1+u\cosh(2\sqrt{\alpha}r)}}\,, \tag{18}$$

where $u^2 = 1 - \alpha/\alpha_c$. For $\Lambda = 0$ we recover the results of Ref. [6].

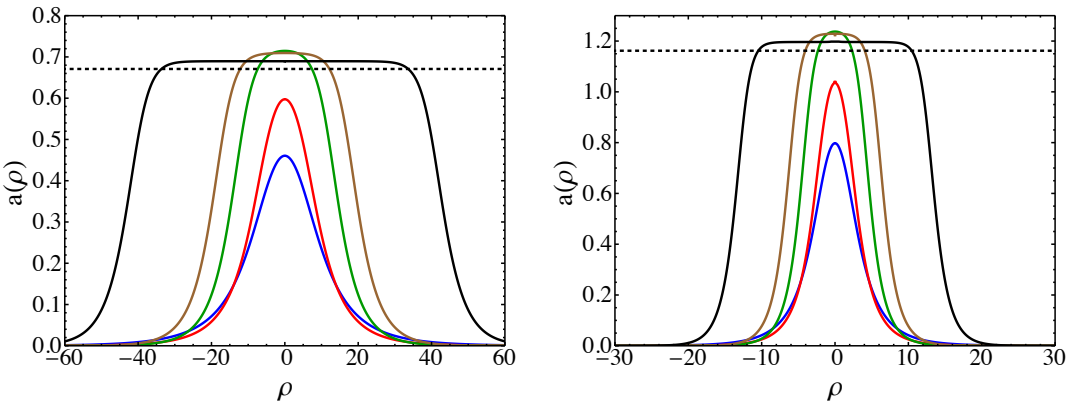

Figure 2. *Left*: Oscillon profiles as a function of the rescaled radius ρ for repulsive fields with $\Lambda = -0.5$ and $\alpha = 0.005, 0.01, 0.025, 0.03, 0.037$ (blue, red, green, brown and black, respectively). *Right*: Oscillon profiles for attractive fields with $\Lambda = 0.5$ and $\alpha = 0.045, 0.09, 0.22, 0.27, 0.33$ (blue, red, green, brown and black, respectively). We see the emergence of a flat-top shape in both cases. Furthermore, we compute that $\alpha_c = 0.042$ for $\Lambda = -0.5$ and $\alpha_c = 0.38$ for $\Lambda = 0.5$, leading to, $a(\rho = 0) \simeq 0.67$ and $a(\rho = 0) \simeq 1.16$ respectively, meaning that oscillons can acquire larger amplitudes in a system with attractive interactions.

Fig. 3 shows the width and height of the oscillons as a function for various interaction strengths between the two fields, attractive or repulsive, rescaled by the small-amplitude parameter ϵ. We see that in the non-interacting case of $\Lambda \to 0$, we recover the single-field results of Ref. [6]. Furthermore, fields which interact repulsively lead to a smaller range of oscillon amplitudes, ending in no oscillons for $\Lambda \to -1$, as is also evident by the form of $\alpha_c \sim (1+\Lambda)^2$. On the contrary, attractive interactions allow for oscillons with a larger amplitude.

Fig. 4 shows several characteristic values for the height and width of oscillons as a function of the coupling strength Λ. We see that the spread of oscillon heights, calculated as the difference

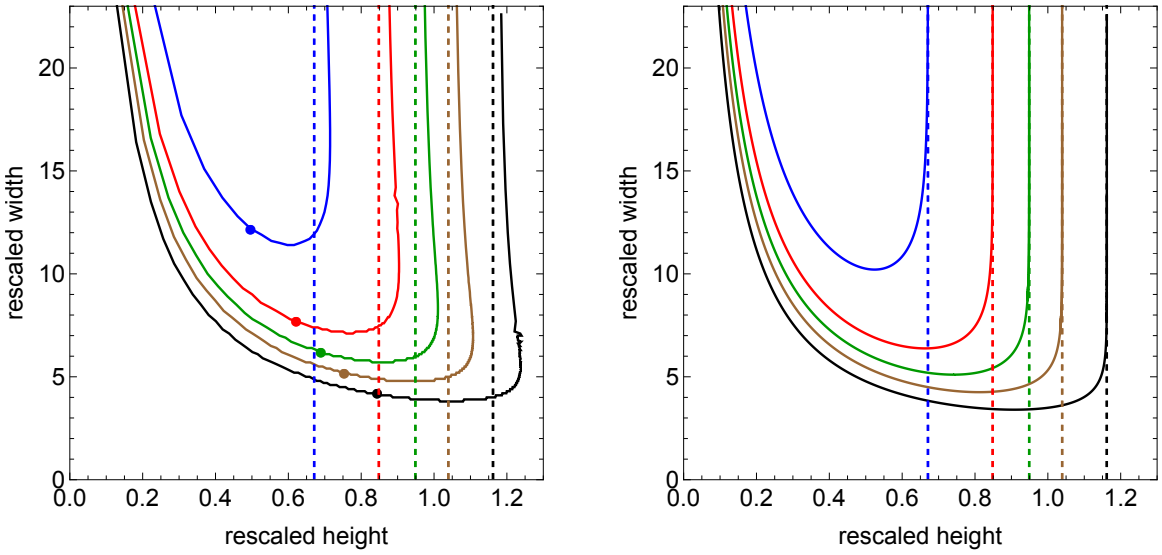

Figure 3. The height-width relation for the oscillon for $\Lambda = -0.5, -0.2, 0, 0.2, 0.5$ (blue, red, green, brown and black respectively) in 3 and 1 spatial dimensions (left and right respectively). We see that fields which interact repulsively lead to a smaller range of oscillon amplitudes, leading to no oscillons for $\Lambda \to -1$. On the contrary, attractive interactions allow for taller, as well as wider oscillons. The colored dots show the point where the oscillons change their stability properties in 3D, as explained in Section IV.

between the minimum height for stable oscillons and the maximum height, grows with Λ, being almost double for $\Lambda = 0.5$ compared to $\Lambda = -0.5$. The spread of the width is infinite, since arbitrarily wide oscillons can exist in theory. For larger values of the interaction strength Λ, narrower oscillons exist. In particular, the minimum width for oscillons with $\Lambda = -0.5$ is almost triple the corresponding value for $\Lambda = 0.5$.

IV. STABILITY ANALYSIS

It has been shown repeatedly in the literature that no true breather solutions like the oscillon can exist in nonlinear systems (with the notable exception of breathers in the one-dimensional Sine-Gordon model). In general there will always be (classical) outgoing radiation in the tails of the oscillon. Classically, this radiation is exponentially suppressed, which is why oscillons can be extremely long-lived [45]. Quantum mechanical radiation might play a more important role in real physical systems [46], but is beyond the scope of our present work. Radiation will in general perturb the oscillon system and it is therefore necessary to assess the stability of oscillons with respect to small perturbations. In the model we are investigating, let us consider small fluctuations

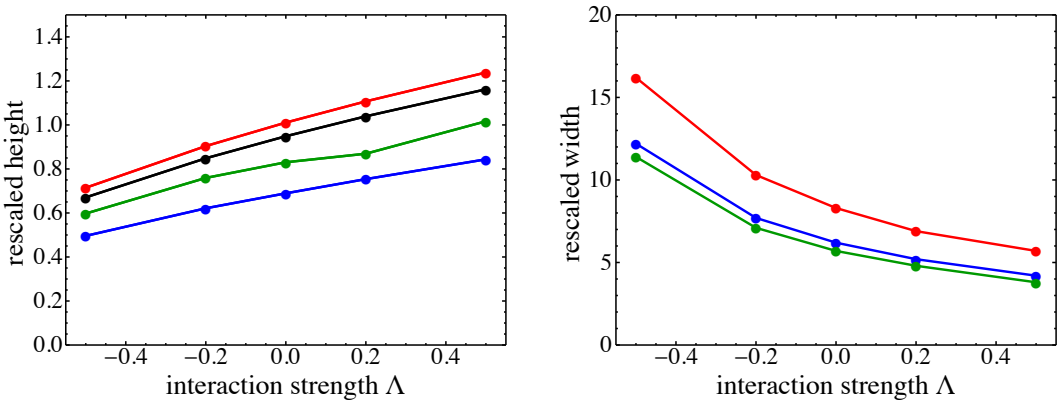

Figure 4. The height and width of 3-dimensional oscillons for the point of marginal stability (blue), the point corresponding to the minimum oscillon width (green) and the point corresponding to the maximum oscillon height (red). The black curve corresponds to the rescaled asymptotic oscillon height $\sqrt{\frac{9}{10}(1+\Lambda)}$.

$\delta(x,t), \Delta(x,t) \ll O(\epsilon)$ added to the oscillon solutions as

$$\begin{aligned} \phi(x,t) &= \phi_{osc}(x,t) + \delta(x,t)\,, \\ \chi(x,t) &= \chi_{osc}(x,t) + \Delta(x,t)\,. \end{aligned} \tag{19}$$

Plugging these into Eqs. (7), the equations of motion for the two fields, and keeping only terms linear in δ and Δ leads to[5]

$$\begin{aligned} \partial_t^2\delta + \delta - (\partial_r^2 + \frac{2}{r}\partial_r)\delta - 3\phi_{osc}^2\delta + 5g\phi_{osc}^4\delta - \Lambda\chi_{osc}^2\delta - 2\Lambda\phi_{osc}\chi_{osc}\Delta &= 0\,, \\ \partial_t^2\Delta + \Delta - (\partial_r^2 + \frac{2}{r}\partial_r)\Delta - 3\chi_{osc}^2\Delta + 5g\chi_{osc}^4\Delta - \Lambda\phi_{osc}^2\Delta - 2\Lambda\chi_{osc}\phi_{osc}\delta &= 0\,. \end{aligned} \tag{20}$$

Since the exact shape of the initial perturbation is in essence unpredictable, a full linear stability analysis would require solving Eq. (20) for arbitrary initial conditions. This requires solving the full Floquet matrix for the coupled nonlinear system. It turns out that, for this system, there is a useful simplification if we only consider perturbations that are about the same size as the oscillon itself. This is in essence an extension of the Vakhitov-Kolokolov criterion that has been used to assess stability of single-component oscillons [6].

[5] The terms that were ignored here (the terms only involving ϕ_{osc} and χ_{osc}) can by nature of the two-timing analysis not source instabilities. However, in Section V we will show that these terms are a source of outgoing radiation.

A. Extension of the V-K criterion

In Section III we have already shown that this system supports oscillons of the form

$$\begin{aligned}\phi_{osc}(x,t) &= \epsilon\ \mathrm{Re}\left\{a(\epsilon x)e^{it(1-\frac{\epsilon^2}{2})}\right\} = \epsilon\, a(\epsilon x)\cos\omega t\,,\\ \chi_{osc}(x,t) &= \epsilon\ \mathrm{Re}\left\{b(\epsilon x)e^{it(1-\frac{\epsilon^2}{2})}\right\} = \epsilon\, b(\epsilon x)\cos\omega t\,,\end{aligned} \tag{21}$$

where the frequency[6] is $\omega = 1 - \alpha\epsilon^2/2$. The symmetry of the system dictates that we have $a(\rho) = \pm b(\rho)$, as we have discussed in Section III. This allows us to turn Eqs. (21) into a single-variable system in order to derive and extend the V-K criterion, similarly to what was done in Ref. [6] for single-field oscillons. Within the validity of the VK criterion, oscillons are stable with respect to long-wavelength perturbations if and only if $dN/d\alpha > 0$, where

$$N = \int a^2(\rho)d^3\rho\,. \tag{22}$$

We present the details of the derivation in Appendix A. Fig. 5 shows the regions of stability, based on Eq. (22).

B. Oscillon Dynamics and Decay

Having constructed two-field oscillon solutions and extended the V-K criterion to examine their stability, we move to numerically demonstrate our results and understand the relevant time-scales of interest. As a benchmark case of unstable oscillons, we use profiles corresponding to $\alpha = 0.04\alpha_c$ and $\epsilon = 0.08$, for both attractive ($\Lambda = 0.5$) and repulsive ($\Lambda = -0.2$) interactions. which we perturb using the most unstable mode-functions computed in Section IV. However, while the perturbation shape is given, the perturbation amplitude is a free parameter. We define the perturbation amplitude as the relative size of the oscillon and perturbation mode-function at the origin

$$\delta_{\text{magn.}} = \frac{\delta(r=0,t=0)}{\phi_{\text{osc}}(r=0,t=0)}\,, \tag{23}$$

and consider various values for $\delta_{\text{magn.}}$. We investigate both the effect of placing the perturbation on both fields (with equal magnitude), and the effect of placing the perturbation on only one of the two fields and initializing the other field in the "perfect" oscillon configuration.

[6] In several oscillon studies, the frequency is taken to be of the form $\omega = \sqrt{1 - c\cdot h^2}$, where h is the oscillon height and c is some $\mathcal{O}(1)$ constant. This matches our expression to lowest order in perturbation theory when $h \propto \epsilon \ll 1$, which is true in the context of the small amplitude analysis used to construct oscillon solutions.

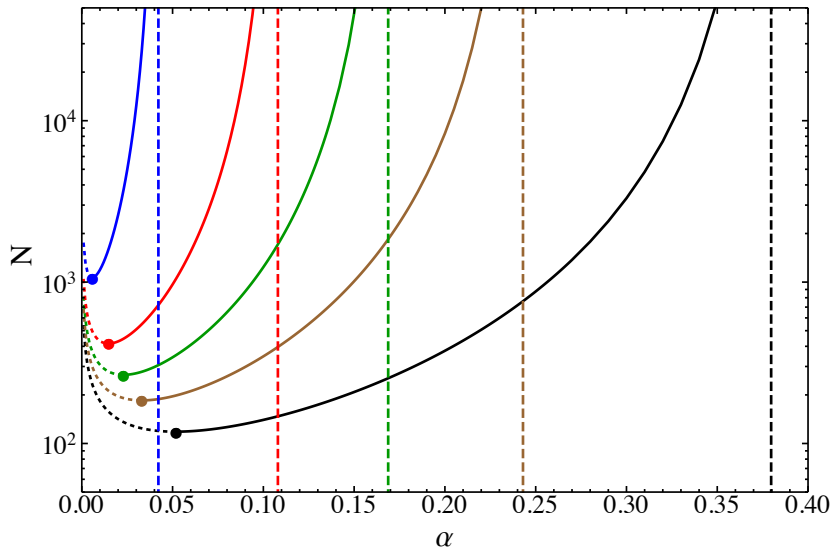

Figure 5. Schematic representation of the Vakhitov-Kolokolov stability criterion for two-field oscillons. We plot the quantity N, defined in Eq. (22), as a function of the phase-shift parameter α for $\Lambda = -0.5, -0.2, 0, 0.2, 0.5$ (blue, red, green, brown and black respectively). The vertical dashed lines correspond to the value of α_c for each case, while the solid (dotted) branches correspond to stable (unstable) oscillons.

Fig. 6 shows the time-evolution of the oscillon's energy density at the origin and width as a function of slow time $\tau = \epsilon^2 t$. First of all, it is evident that the slow time controls the relevant time-scales for the oscillon dynamics. The time of decay of the oscillon seems to occur at a similar order of magnitude in slow time. This can be traced back to the evolution Eqs. (13) for the complex functions $A(\rho, \tau)$ and $B(\rho, \tau)$, which are of the non-linear Schrödinger type, and control the dynamics of the oscillon envelope, on top of the fast oscillations, which occur on a timescale of $\mathcal{O}(m^{-1})$. We see that the magnitude of the initial perturbation plays a crucial role for the ultimate fate of the oscillon: small fluctuations $\delta_{\text{magn.}} \ll 1\%$ lead to a new semi-stable point for the width and height of the localized configuration. On the other hand, for larger $\delta_{\text{magn.}}$ the initial localized wave-packet simply disperses. We must note here, that initializing the two fields out of phase $a = -b$ and using the corresponding perturbation derived using Eqs. (A12) gives indistinguishable curves, and thus we do not plot them for clarity. This however confirms our analysis, that the phase of the two fields in the initial oscillon configuration, 0 or π, does not affect the subsequent

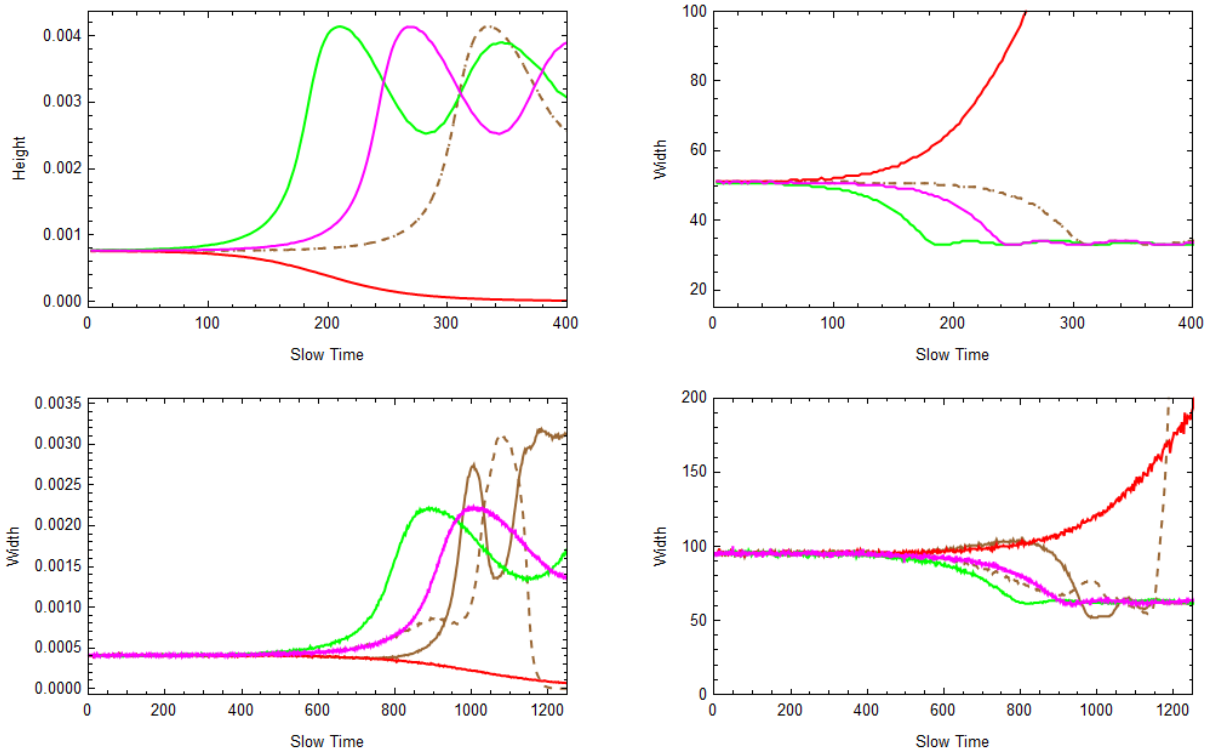

Figure 6. *Upper Panels:* The evolution of the oscillon peak energy density (left) and width (right) as a function of time $t(m^{-1})$ for $\Lambda = 0.5$, $\alpha = 0.04\alpha_c$ and $\epsilon = 0.08$. We perturb the oscillon by the most unstable mode with amplitude $\delta_{\text{magn.}} = -0.5\%, 0.05\%, 0.5\%$ (green, magenta and red respectively). The brown curve corresponds to perturbing only one of the two fields with $\delta_{\text{magn.}} = 0.2\%$ and initializing the other field as the "perfect" oscillon profile. The data for both fields is plotted for this curve (dashed and dotted line) but the difference is not perceivable since the fields quickly attract and undergo simultaneous collapse. *Lower Panels:* The same simulation for $\Lambda = -0.2$ with again $\alpha = 0.04\alpha_c$. Here the curves correspond to $\delta_{\text{magn.}} = -0.1\%, 0.01\%, 0.1\%$ (green, magenta and red respectively). We again plotted brown curves in a scenario where we only perturbed one of the fields with $\delta_{\text{magn.}} = 0.1\%$. The fate of the two oscillons differs as one of the field eventually disperses (dotted) while the other settles into a stable single-field oscillon (full). It is clear however that all of these multi-field oscillons contain unstable modes.

dynamics. We will show numerically in Section VII that the phase relation between the components of the oscillon arises dynamically when they form, leading to phase-locked fields, oscillating either in or out of phase.

Furthermore, one can ask whether having the exact form of the most unstable modes computed in the previous section is a necessary condition for oscillon decay. In single-field oscillons, one can see that any perturbation can be decomposed in a basis of eigen-functions of the operator $H_1 H_2$ [see Eqs. (A9) and (A10)], meaning a generic perturbation will include a component along the unstable

mode. In two-field systems, it is interesting to see how an initial perturbation is transferred from one field to the other. To check the validity of our analysis, we perturbed only the ϕ field, leaving the χ field profile identical to the perfect oscillon solution. Perturbing one of the fields with $\delta_{\text{magn.}}$ while leaving the other field intact leads in some cases to a similar evolution as perturbing both fields with $\delta_{\text{magn.}}/2$. For the specific cases that we plotted, this occurs for $\Lambda = 0.5$ when perturbing one of the fields with $\delta_{\text{magn.}} = 0.2\%$, leading to almost indistinguishable evolution from perturbing both fields with $\delta_{\text{magn.}} = 0.1\%$. We do not plot both these simulations in Fig. 6, because the results are visually identical (instead only one of these cases is plotted). This indicates that due to the interaction of the two fields and the symmetry of the system, a small initial perturbation is quickly distributed evenly among the two fields. In other cases we observed the complete dispersion of one field and the relaxation of the other towards a stable single-field oscillon solution (see lower panels of Fig. 6). In particular this occurred for $\Lambda = -0.2$, when we perturbed only one of the two fields by $\delta_{\text{magn.}} = 0.1\%$. From our numerical investigation it remains clear that the symmetric multi-field oscillons failing the VK-criterion contain unstable modes and will in general decay. However, when perturbed outside the $\phi = \pm\chi$ Ansatz, the dynamics can either restore or destroy the equality between the two fields. We will see that for $\Lambda > 0$ the two-field configuration is a strong attractor of the system. We note that it is not necessary to perturb the oscillon with the exact form of the perturbation given by the stability analysis of this Section, since unstable oscillons will eventually decay if perturbed, albeit on slightly different time-scales and with different final state, depending on the details of the perturbation. Finally, we also perturbed the oscillon with negative $\delta_{\text{magn.}}$ (meaning that the unstable mode is "flipped"). We observed that this leads to a collapse instability more often than the positive $\delta_{\text{magn.}}$ case. This highlights the sensitivity of the fate of the unstable oscillons on the initial conditions. Finally, we perturbed oscillons that are characterized as stable by the two-field version of the V-K criterion in various ways, seeing no decay over the total run of the simulation, lasting several hundred units of "slow time" $\tau = \epsilon^2 t$.

It is now important to understand this behaviour. Fig. 7 shows the trajectories of several perturbed oscillons on the height-width curve for oscillons[7] for $\Lambda = 0.5$ and $\Lambda = -0.2$. We see that unstable oscillons will surely move away from their initial configuration if perturbed. However their ultimate fate is not unique. It is known that localized solutions of the three-dimensional non-linear Schrödinger equation are unstable and undergo a collapse instability, meaning that their width becomes smaller and their amplitude becomes larger. For oscillons that are "mildly perturbed",

[7] In this plot, the height and width curve is derived from the energy density, not the profile of the oscillons. It is thus related to the one shown in Fig. 3, but is not identical to it.

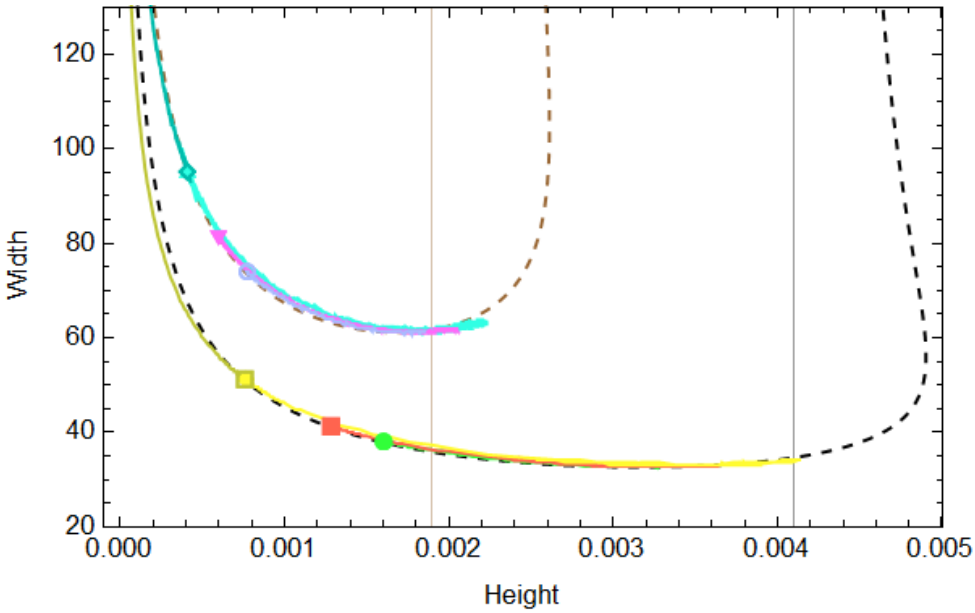

Figure 7. The height and width of oscillons undergoing decay for $\Lambda = 0.5$ and $\Lambda = -0.2$. These simulations were performed with $\epsilon = 0.08$. We plot the curves of oscillons undergoing collapse ($\delta_{magn} \ll 1\%$) where different colors correspond to different values of α with $\alpha = 0.04$ (cyan), $\alpha = 0.06$ (magenta), $\alpha = 0.08$ (purple) for $\Lambda = -0.2$ and $\alpha = 0.04$ (yellow), $\alpha = 0.07$ (red), $\alpha = 0.09$ (green) for $\Lambda = 0.5$. For $\alpha = 0.04$ we also plot curves corresponding to dispersion (dark yellow and dark cyan). Here α is given in terms of α_c. We also plot the "perfect" oscillon curves for $\Lambda = -0.2$ (brown) and $\Lambda = 0.5$ (black) and indicate the point of stability under VK with a gridline. It is clear that the oscillon configurations decay until they either disperse completely or find a new point of stability.

$\delta_{\text{magn.}} \ll 1\%$, this is exactly what we see at first: the unstable oscillons follow the height-width relation, on which their amplitude increases and their width decreases. This is the regime, where one can safely neglect the sextic term in the initial Lagrangian, equivalently the $|A|^4 A$ term in Eq. (13). Once the oscillon amplitude grows enough, so that the $|A|^4 A$ term becomes important, the oscillon is stabilized, which occurs near the minimum of the height-width curve. Beyond this point, the oscillon solution satisfies the V-K criterion. Because our simulation box does not allow for the energy to escape (it does not possess absorbing boundary conditions), the oscillon will never truly reach the "ideal" shape, and will instead stay in the vicinity of the first stable point on the height-width curve.

Oscillons that are perturbed by a large amount, which puts them too far away from the height-width curve, do not undergo this slow collapse instability, which would take them to a stable configuration. Using different perturbation types on the initial oscillon configuration amounts to

examining the basis of attraction for two-field oscillons, finding the approximate size of the initial perturbation below which the oscillon is allowed to "rearrange" itself into a stable configuration and above which the oscillon is completely destabilized. An important question remains, as to the oscillon configurations that arise naturally after inflation: it is not known if a universe that is governed by the Lagrangian of Eq. (1) during preheating will be dominated by single or multi-field oscillons. We are currently working on the corresponding three dimensional lattice simulations required to address this point and will present the results in a subsequent publication.

V. OSCILLON LIFETIME

It is a well known fact that oscillons are not exactly stable, but eventually lose their energy through an exponentially suppressed radiative tail [47, 48]. To make an assessment of the (cosmological) importance of the stable oscillons that were found in the previous sections we wish to find an estimate of their lifetimes. To do this we follow the analyses performed in Refs. [33–35]. The core reason why oscillon solutions are in general not stable (classically), even though they are long-lived, is that plugging in an oscillating solution $\sim \Phi_0 \cos(\omega t)$ into an equation of motion with nonlinear terms will in general lead to terms that are proportional to higher harmonics $\propto \cos(j\omega t)$ with $j > 1$. In general, these terms can be made to cancel out using some perturbative procedure (e.g. the two-timing analysis); but since in practice these perturbative techniques must end at some finite order and do not converge, there will always be residual terms of higher harmonics in the equations of motion. These terms will act as a source for radiative modes of the oscillon solution.[8] In order to estimate the decay rate of the oscillons constructed in Section III we follow the methods of Refs. [33–35]. To study the relevant radiative modes we perturb our oscillon solutions $\phi = \phi_{osc} + \delta$, $\chi = \chi_{osc} + \xi$, plug these into the equations of motion and linearize to obtain

$$\begin{aligned} \left[\partial_t^2 \phi_{osc} - \nabla^2 \phi_{osc} + V_{,\phi}(\phi_{osc}, \chi_{osc})\right] + \left[\partial_t^2 \delta - \nabla^2 \delta + V_{,\phi\phi}(\phi_{osc}, \chi_{osc})\delta + V_{,\phi\chi}(\phi_{osc}, \chi_{osc})\xi\right] = 0 \\ \left[\partial_t^2 \chi_{osc} - \nabla^2 \chi_{osc} + V_{,\chi}(\chi_{osc}, \phi_{osc})\right] + \left[\partial_t^2 \xi - \nabla^2 \xi + V_{,\chi\chi}(\chi_{osc}, \phi_{osc})\xi + V_{,\chi\phi}(\chi_{osc}, \phi_{osc})\delta\right] = 0 \end{aligned} \tag{24}$$

In the above equations we use the notation $V_{,\phi}(\phi_{osc}, \chi_{osc}) \equiv \partial_\phi V(\phi, \chi)|_{\phi\to\phi_{\rm osc}, \chi\to\chi_{osc}}$ for derivatives of the potential with respect to the fields. We now plug in our oscillon solutions $\phi_{\rm osc} = \Phi_0 \cos(\omega t)$ and $\chi_{\rm osc} \sim X_0 \cos(\omega t)$, where $\omega = 1 - \alpha\epsilon^2/2$. By virtue of the two-timing analysis, all

[8] A class of arbitrarily long-lived oscillons was recently discussed in Ref. [45].

terms proportional to $\cos(\omega t)$ in the first square bracket of Eqs. (24) cancel and we obtain

$$\begin{aligned}
&\partial_t^2\delta - \nabla^2\delta + \delta - \left(3\phi_{osc}^2 - 5g\phi_{osc}^4 + \Lambda\chi_{osc}^2\right)\delta - 2\Lambda\phi_{osc}\chi_{osc}\xi = \\
&\qquad\qquad \left(\frac{1}{4}\Phi_0^3 + \frac{1}{4}\Lambda\Phi_0 X_0^2 - \frac{5}{16}g\Phi_0^5\right)\cos(3\omega t) - \frac{1}{16}g\Phi_0^5\cos(5\omega t) \\
&\partial_t^2\xi - \nabla^2\xi + \xi - \left(3\chi_{osc}^2 - 5g\chi_{osc}^4 + \Lambda\phi_{osc}^2\right)\xi - 2\Lambda\phi_{osc}\chi_{osc}\delta = \\
&\qquad\qquad \left(\frac{1}{4}X_0^3 + \frac{1}{4}\Lambda X_0\Phi_0^2 - \frac{5}{16}gX_0^5\right)\cos(3\omega t) - \frac{1}{16}gX_0^5\cos(5\omega t)
\end{aligned} \tag{25}$$

Focusing on the solutions where the two fields within the oscillon oscillate in phase $\Phi_0 = X_0$ (the case where $\Phi_0 = -X_0$ is analogous); we add Eqs. (25) and introduce the new radiative mode $\Psi = \delta + \xi$ (in the case where the oscillons oscillate out of phase we would introduce $\Psi = \delta - \xi$) to obtain the single equation

$$\partial_t^2\Psi - \nabla^2\Psi + \Psi - \left(3(1+\Lambda)\phi_{osc}^2 - 5g\phi_{osc}^4\right)\Psi = \left(\frac{1}{2}\Phi_0^3 + \frac{1}{2}\Lambda\Phi_0^3 - \frac{5}{8}g\Phi_0^5\right)\cos(3\omega t) - \frac{1}{8}g\Phi_0^5\cos(5\omega t) \tag{26}$$

We are thus interested in wave-like solutions $\Psi_{rad}(r,t)$ of Eq. (26). Using the symmetry of our system we can then deduce that half the amplitude of this wave comes from the oscillon in the ϕ-field and the other half from the oscillon in the χ-field. Notice however that this calculation is equivalent to calculating the radiative mode of an oscillon in a single field with a slightly altered quartic term in the potential

$$V(\phi) = \frac{1}{2}\phi^2 - \frac{1}{4}(1+\Lambda)\phi^4 + \frac{g}{6}\phi^6\,. \tag{27}$$

As suggested in Ref. [33], when calculating the outgoing radiation of an oscillon in this type of potential, ignoring the spacetime-dependent effective mass term in the equation of motion for the perturbative mode will not alter the final result significantly. Thus we ignore the time-dependent coupling of Ψ on the left-hand-side of Eq. (26) and obtain the simpler equation

$$\partial_t^2\Psi - \nabla^2\Psi + \Psi = \left(\frac{1}{2}\Phi_0^3 + \frac{1}{2}\Lambda\Phi_0^3 - \frac{5}{8}g\Phi_0^5\right)\cos(3\omega t) - \frac{1}{8}g\Phi_0^5\cos(5\omega t)\,. \tag{28}$$

As was shown in Ref. [33], this equation can be solved by expanding $\Psi(r,t) = \sum_{j=1}^{\infty}\Psi_j(r)\cos(j\omega t)$. Obviously only $\Psi_3(r)$ and $\Psi_5(r)$ will not vanish in this specific case. The rate of energy loss of the oscillon is $dE/dt = 4\pi r^2 T_{0r}$, where T_{0r} is the Poynting vector in our spherically symmetric set-up. By averaging over time in the far distance regime

$$\langle T_{0r}\rangle = \langle\dot{\xi}\partial_r\xi\rangle + \langle\dot{\delta}\partial_r\delta\rangle = \frac{1}{2}\langle\dot{\Psi}\partial_r\Psi\rangle\,. \tag{29}$$

Following Ref. [33] we obtain the following analytic expression for the outgoing radiation at large radii

$$\Psi_{rad}(r,t) \approx \frac{1}{4\pi r}\left(S_3(k_3)\cos(k_3 r - 3\omega t) + S_5(k_5)\cos(k_5 r - 5\omega t)\right) , \tag{30}$$

where $k_j = \sqrt{(j\omega)^2 - 1}$ and $S_3(k)$ and $S_5(k)$ are the Fourier transforms of the terms on the right hand side of Eq. (28) proportional to the third and fifth harmonic respectively. Thus

$$S_3(k) = \int d^3r \left(\frac{1}{2}\Phi_0^3 + \frac{1}{2}\Lambda\Phi_0^3 - \frac{5}{8}g\Phi_0^5\right) e^{-ik\cdot r} = \int_0^\infty dr 4\pi r \frac{\sin(kr)}{k}\left(\frac{1+\Lambda}{2}\Phi_0^3 - \frac{5}{8}g\Phi_0^5\right) \tag{31}$$

and

$$S_5(k) = -\int d^3r \frac{1}{8}g\Phi_0^5 e^{-ik\cdot r} = -\int_0^\infty dr 4\pi r \frac{\sin(kr)}{k}\frac{1}{8}g\Phi_0^5 . \tag{32}$$

We find, similarly to Ref. [9], that $S_3 \gg S_5$. The analytic expression for the radiative modes of the oscillon given by Eq. (30) leads to the following expression for the decay rate of the oscillon

$$\Gamma_{osc} = \frac{1}{16\pi E_{osc}} \sum_{j=3,5} S_j(k_j)^2 \omega_j k_j . \tag{33}$$

By using the oscillon amplitude $\Phi_0 \equiv \epsilon a(\epsilon r)$, which corresponds to the solution of Eq. (15), we computed the value of Γ_{osc} using the method described above. We confirmed that the multi-peak structure of Γ found in Ref. [9] persists for different values of Λ, either positive or negative. In general, the oscillon lifetime increases as one decreases the small parameter ϵ. In our construction, this corresponds to increasing the strength of the sextic term. Fig. 8 shows the results derived by numerically integrating Eq. (33) for three-dimensional oscillons, using the value $\epsilon = 0.1$. For $\Lambda = 0$ we recover the results of Ref. [5]. We see that the decay rate increases for $\Lambda > 0$ compared to the single field case ($\Lambda = 0$) and correspondingly it decreases for $\Lambda < 0$. The maximum value of Γ increases from $\Lambda = 0$ to $\Lambda = 0.2$ and $\Lambda = 0.2$ to $\Lambda = 0.5$ by around one order of magnitude.

VI. GENERALIZATION TO MANY FIELDS

In this Section we generalize our model to a system of N interacting fields. Following the two-field analysis, we choose the following action where the fields exhibit an "exchange" symmetry:

$$S = -\int d^3x dt \left[\sum_{I=1}^{N}\left(\frac{1}{2}\partial_\mu\phi_I\partial^\mu\phi_I + \frac{1}{2}m^2(\phi_I)^2 - \frac{\lambda}{4}(\phi_I)^4 + \frac{g}{6}(\phi_I)^6\right) - \sum_{I\neq J}\frac{\Lambda}{2}(\phi_I)^2(\phi_J)^2\right] . \tag{34}$$

We briefly repeat the derivations presented above for two-field oscillons, showing that that the profile equations are solved by zero-modes of Eq. (15) with an altered cubic term. Furthermore, we show how to extend the V-K criterion to apply to the N-field system.

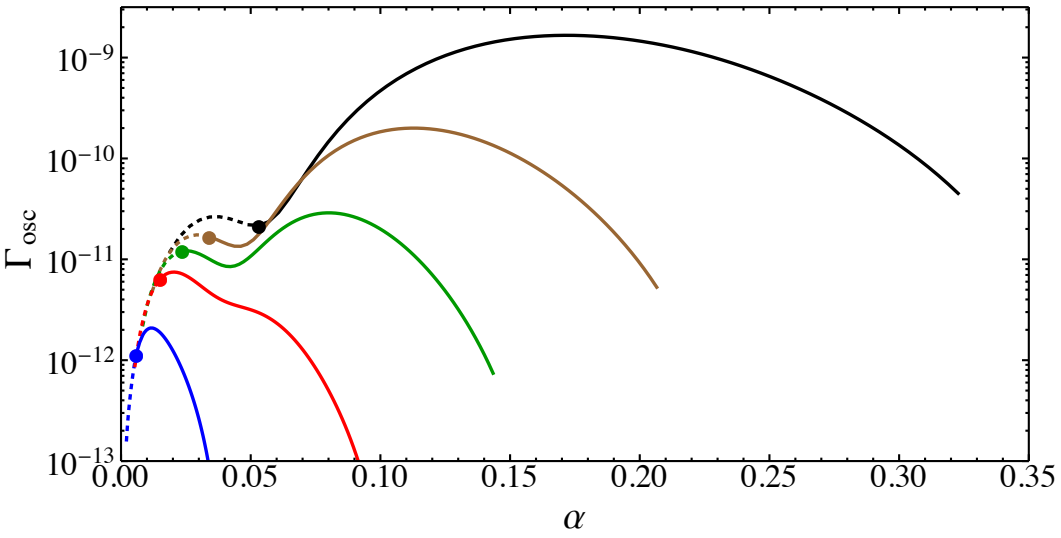

Figure 8. The decay rate of oscillons computed computed using Eq. (33) for $\epsilon = 0.1$, as a function of the frequency parameter α for $\Lambda = -0.5, -0.2, 0, 0.2, 0.5$ (blue, red, green, brown and black respectively). The solid (dotted) branches correspond to stable (unstable) oscillons according to the VK criterion.

A. Two-timing analysis

After rescaling the fields and spatial-temporal dimensions in the same way as was done in section II, the action of Eq. (34) results in N equations of motion for the N fields. The equation for the i-th field (assuming spherical symmetry) is

$$\partial_t^2\phi_i - (\partial_r^2 + \frac{2}{r}\partial_r)\phi_i + \phi_i = \phi_i^3 - g\phi_i^5 + \sum_{j\neq i}\Lambda\phi_i\phi_j^2 \tag{35}$$

Introducing the by now familiar two-timing analysis variables $\rho = \epsilon r$ and $\tau = \alpha\epsilon^2 t$, the equations become

$$\partial_t^2\phi_i + 2\alpha\epsilon^2\partial_t\partial_\tau\phi_i - \epsilon^2(\partial_\rho^2 + \frac{2}{\rho}\partial_\rho)\phi_i + \phi_i = \phi_i^3 - g\phi_i^5 + \sum_{j\neq i}\Lambda\phi_i\phi_j^2 + \mathcal{O}(\epsilon^4) \tag{36}$$

Finally looking for solutions $\phi_i = \epsilon\phi_{1,i} + \epsilon^2\phi_{2,i} + ...$ we can write down the $O(\epsilon)$ and $O(\epsilon^3)$ equations

$$\mathcal{O}(\epsilon): \ \partial_t^2\phi_{0,i} + \phi_{0,i} = 0 \tag{37}$$

$$\mathcal{O}(\epsilon^3): \ \partial_t^2\phi_{2,i} + \phi_{2,i} = (\partial_\rho^2 + \frac{2}{\rho}\partial_\rho)\phi_{0,i} - 2\alpha\partial_t\partial_\tau\phi_{0,i} + \phi_{0,i}^3 - \phi_{0,i}^5 + \sum_{j\neq i}\Lambda\phi_{0,i}\phi_{0,j}^2\,, \tag{38}$$

where we've again used $g = 1/\epsilon^2$. The rest of the derivation is entirely analogous to the one in Section III so we won't repeat it here. The procedure results in N profile equations

$$(\partial_\rho^2 + \frac{2}{\rho}\partial_\rho)a_i - \alpha a_i + \frac{3}{4}a_i^3 - \frac{5}{8}a_i^5 + \frac{3}{4}\Lambda \sum_{j\neq i} a_i a_j^2 = 0 \tag{39}$$

We thus need to find a set of N functions $a_i(\rho)$ that solve this system of equations. As before, the symmetry in the model greatly simplifies this question. We need to find localized solutions of the equation

$$(\partial_\rho^2 + \frac{2}{\rho}\partial_\rho)a - \alpha a + \frac{3}{4}(1 + \Lambda(N-1))a^3 - \frac{5}{8}a^5 = 0 \tag{40}$$

Then, setting any $n < N$ number of $a_i(\rho) = a(\rho)$ and the remaining $a_j(\rho) = -a(\rho)$ solves the system in Eq. (39). Notice that Eq. (40) has the same form as Eq. (15) with an altered cubic term. It will therefore have localized solutions, which are related to the ones for the two-field model by substituting the coupling strength Λ in the two-field case with the "effective" coupling strength $\Lambda(N-1)$ in the multi-field case. This is a proof of existence for such a solution, not uniqueness.

B. Stability analysis

For brevity, we move the full derivation of the stability of these N-field oscillons to long wavelength perturbations to Appendix A. Note however that performing the two-timing analysis and using the ansatz $\phi_{0,i} = \mathrm{Re}\left\{A_i(x,t)e^{-it}\right\}$ is equivalent to working in the nonrelativistic limit. In this limit, the Lagrangian has a conserved charge proportional to

$$\mathcal{Q} = i\int d^d x \sum_i \left(A_i^*(\dot{A}_i) - A_i(\dot{A}_i^*)\right) , \tag{41}$$

which reduces to the following after inserting the symmetric oscillon solution

$$\mathcal{Q} = N_{fields}\cdot \alpha\epsilon^2 \int d^d x \cdot a(x)^2 . \tag{42}$$

Since the oscillon has a conserved charge, we can apply the VK-criterion directly. To summarize, the oscillon is stable when $\dfrac{\partial \mathcal{Q}}{\partial \alpha\epsilon^2} > 0$. This is just an alternate and equivalent form of the VK-criterion that was given earlier in Eq. (22). The criterion for stability therefore still holds after a generalization of our model to N fields.

To conclude, we constructed oscillons in a model with N fields. Since we work in the nonrelativistic limit it is simple to show that the VK criterion still applies. Although we have not

performed a detailed analysis of the lifetime of these oscillons, the result is expected to be analogous to the two-field case. Namely, the computation of the radiation tail of these oscillons can be mapped to an equivalent calculation for single-field oscillons with an altered cubic term in the potential, as done in Section V for the two-field case.

VII. OSCILLON EMERGENCE AND DYNAMICS

Despite the mathematical construction and stability analysis of two-field oscillons, the question of their emergence in realistic scenarios and hence their cosmological consequences remains. In this section we provide a combination of simulations in one and three spatial dimensions, in both an expanding and a static background. The full three-dimensional simulations of oscillon formation after inflation and their GW signatures will be presented in a subsequent publication.

A. Dynamical emergence in 1+1D

To investigate the formation of oscillons in this model we performed a series of one-dimensional simulations of preheating-like scenarios on an expanding background. One of the fields, ϕ, was initialized as a homogeneous condensate, akin to the inflaton at the end of inflation. The other fields of the model $\chi, \theta, ...$ were then initiated in their vacuum, akin to spectator fields at the end of inflation. The simulations were strongly inspired by those performed in Ref. [49]. We see a clear sequence of events, leading from an oscillating ϕ condensate to a collection of composite oscillons.

- Parametric self-resonance leads to a fragmentation of the inflaton condensate and the formation of single-field oscillons.
- Parametric resonance of the spectator field(s) by the single-field oscillons leads to exponential growth of the spectator, akin to preheating and Floquet theory.
- Once the spectator field acquires a large enough value, non-linear interactions between the two (or more) fields lead to phase-locked long-lived configurations: composite oscillons.

Fig. 9 shows the energy density on the one-dimensional lattice at early and late times. The oscillons appear to become narrower, because we plot our data on a comoving grid. Furthermore, we clearly see the above stages of oscillon formation and evolution. In the left panel, the ϕ condensate has fragmented into localized configurations (oscillons), while the χ field remains small; we initialized the χ field with $\langle \chi_k^2 \rangle = \mathcal{O}(1/2k)$. The right panel clearly shows spikes of the χ field,

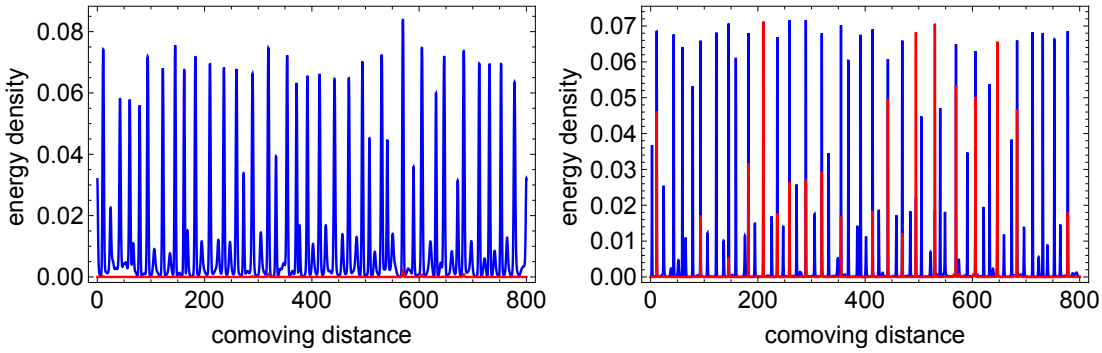

Figure 9. The energy density in the box for a two-field simulation, involving the fields ϕ and χ (blue and red respectively) for $t = 1750$ (m^{-1}) (left) and $t = 4500$ (m^{-1}) (right). The ϕ field starts with fluctuations on top of a classical homogeneous configuration (emulating the inflaton), while the the χ field is comprised solely of fluctuations initially.

positioned at the same locations as ϕ field oscillons. Interestingly, not all ϕ oscillons lead to an efficient amplification of the χ field. Furthermore, we see that the energy density spikes of the two fields are not equal in size. In fact, two-field composite oscillons in one spatial dimension exhibit a persistent energy exchange between the two fields, which we will describe more later.

Fig. 10 shows the characteristics of the oscillons in the one-dimensional simulation. In the top left panel we see the distribution of ϕ overdensities on the height-width plane. The formation of two populations is evident. A large number of overdensities closely follows the single-oscillon height-width curve. Furthermore, the early-time population of overdensities is largely or solely on this curve. For later times, we see a splitting between the single and two-field oscillon curves. The fact that the oscillons who deviate from the single-field curve do not follow exactly the two-field one is explained by the presence of a "breathing" mode between the two fields (see Section VII B). The final number of two-field oscillons is almost half that of their single-field counterparts. The lower panels of Fig 10 show the distribution of oscillons in equal bins of core energy density (amplitude). The left panel shows early times, with the orange curve corresponding to the initial stages of the emergence of $\phi - \chi$ oscillons. For later times (right panel) we see that the distribution is largely constant. Due to the finite bin size and the oscillon breathing mode, some oscillons will inevitably enter and exit adjacent bins, leading to small changes. However, the overall shape is indeed stable, allowing us to reach significant conclusions. Large amplitude oscillons are comprised of almost equal populations of one- and two-component configurations. Small amplitude oscillons on the other hand are almost entirely single-field. This can be easily understood as follows: Parametric resonance for χ is strongly sensitive to the amplitude of the pumping field ϕ. It is thus much more efficient for the

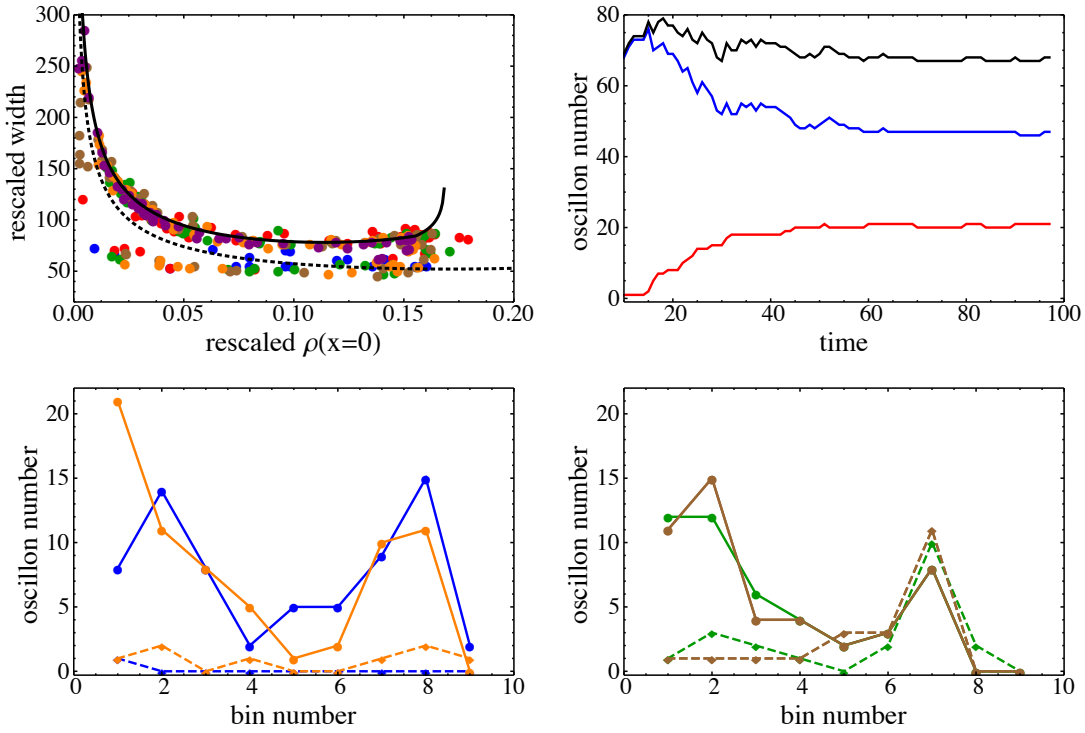

Figure 10. *Upper left:* The height width relation for overdensities in the ϕ field for $t = 1500, 2500, 3300, 4000, 5200, 6700$ (m^{-1}) (purple, brown, blue, red, green). The solid (dashed) line corresponds to the $\Lambda = 0$ ($\Lambda = 0.5$) analytical profiles. *Upper right:* The number of single- and double-component oscillons (blue and red respectively). The total number is in black. *Lower panels:* The number of one- and two-component oscillons (solid and dashed lines respectively) in equal bins of height for $t = 1500, 25000, 5200, 6700$ (m^{-1}) (blue, orange, green and brown respectively).

χ field to be excited in regions of large ϕ field, leading to a more efficient production of large field two-component oscillons. We will return to this point in Sections VII B, VII C and VII D. Finally, we checked the relative phase of the two fields in the two-field oscillons and found no preference for either in-phase or out-of-phase configurations.

Fig. 11 shows the formation of multi-component oscillons in a simulation involving three scalar fields. The system exhibits a similar evolution as in the two field case, with the ϕ fragmentation followed by single-field oscillon formation, which then leads to excitation of the spectator fields and the eventual emergence of composite oscillons. As in the two field case, not all single field oscillons lead to multi-field configurations. Interestingly the number of two- and three-component oscillons

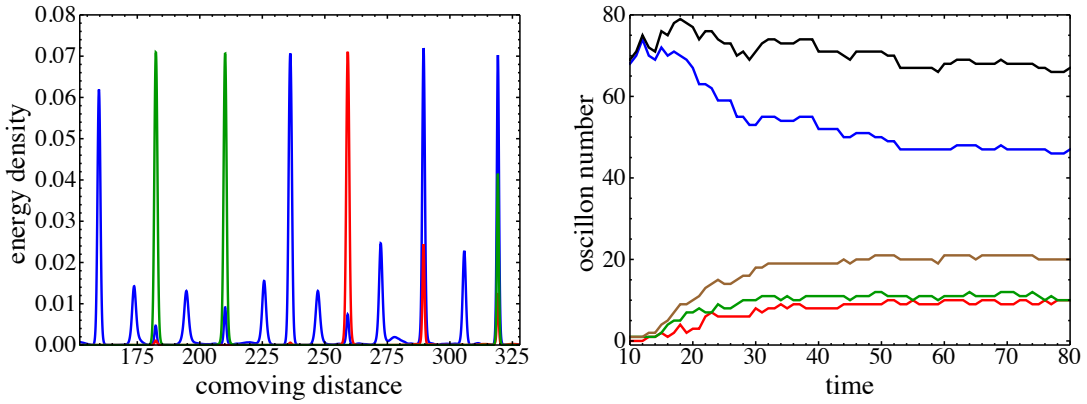

Figure 11. *Left:* The energy density in a zoomed-in part of the box for a three-field simulation, involving the fields ϕ, χ and θ (blue and red and green respectively) for $t = 3300$ (m^{-1}). The ϕ field starts with fluctuations on top of a classical solution (emulating the inflaton), while the the χ and θ fields are comprised solely of fluctuations initially. *Right:* The number of one-, two-component and three-component oscillons (blue, red and green respectively). The sum of two- and three-component oscillon is shown in brown and the total number of oscillons in black.

is nearly the same and the total number of multi-component oscillons is nearly equal to the number of two-component oscillons that emerged in the two-field simulation.

B. Single to multi-field oscillons in 1+1D

The results of Section VII A showcased the two-stage formation of composite oscillons on an expanding background for the one-dimensional case. In order to better understand the transition from single to multi-field oscillons, we focus on simulating single-field oscillons on a static background, which allows us to fully control the initial conditions and compare the numerical results to theoretical predictions. The decay into a multi-field configuration can be understood in the context of Floquet theory. Although obtaining analytical results can be challenging in a non-homogeneous background such as an oscillon, we show in Section VII D that significant intuition is gained by working in the homogeneous limit.

We initialize the ϕ field as an oscillon that is stable in the single field theory (with $\Lambda = 0$) and draw the fluctuations of the χ field from a Gaussian distribution with $\langle \chi_k^2 \rangle = 1/2k$, as in our lattice simulations. Alternatively, initializing the secondary field as a small perturbation of the same shape

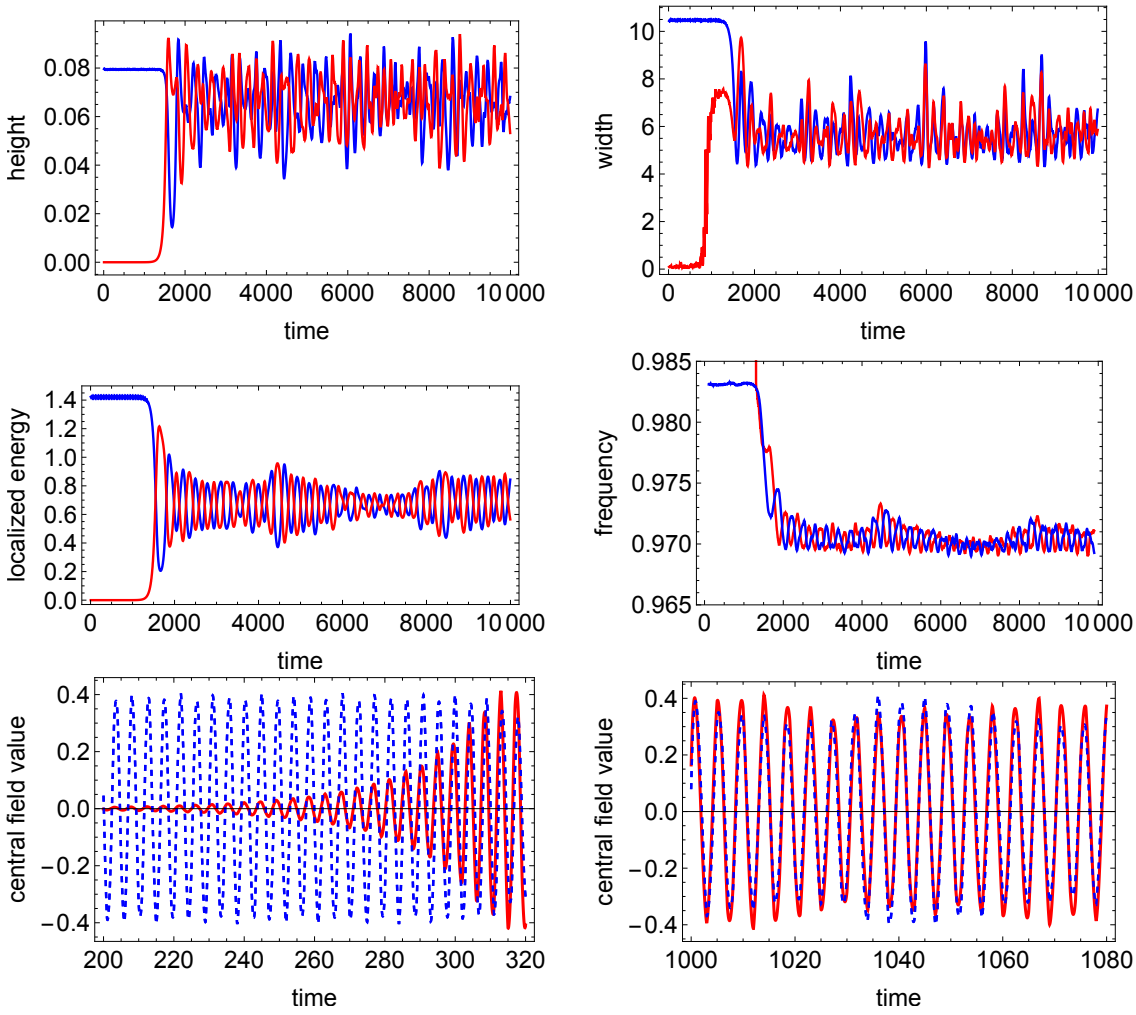

Figure 12. The evolution of various quantities in our simulations for the ϕ field (blue) and χ field (red). *Top left:* the evolution of the height of the energy density at the origin. *Top right:* the evolution of the width of the two fields defined as the distance where the energy density has decreased by a factor of $1/e$. *Middle left:* the evolution of the localized energy in the two fields. *Middle right:* The oscillation frequency of the two fields. *Bottom panels:* The amplitude of the fields at the origin at early (left) and late times (right). It is clear that the single-field oscillon evolves into a two-field configuration, where the fields are phase locked (oscillating in phase) and share common characteristics.

as the oscillon does not change the outcome of the simulation (although it somewhat accelerates the decay into a multi-field configuration). We will demonstrate this last point later on in this section.

Fig. 12 shows the evolution of the system for $\Lambda = 0.5$ and $g = 1/\epsilon^2 = 5$: from a single field oscillon with $\alpha = 0.99\alpha_c$ to a phase-locked two-field configuration. The upper panels show the evolution of the width and height (in energy density space) of the two fields. We clearly see the growth of a localized χ configuration, which backreacts on the ϕ-oscillon, leading to a composite

oscillon. We see that after $t \simeq 1500(m^{-1})$ the amplitude and width of the two fields oscillate around an average value, which is common for both. Inspecting the data we can postulate the existence of "breather" modes: stable perturbations atop the perfect oscillon solution that oscillate between the two fields (similarly to how we construct unstable modes in App. A). It seems that fewer of such breather modes exist in higher dimensions (see Section VII C).

The oscillation frequency behaves similarly. Initially, since the χ field is comprised of random fluctuations, one cannot speak of a single "coherent" frequency. As instabilities build up over time however, the two fields "lock" up into a single shared frequency as can be seen in the bottom panels. The localized energy in each field also exhibits strong oscillations of up to 40% around the average value. While the two components of the oscillon exchange energy with each other, the total configuration is still stable. This is strongly reminiscent of the behavior exhibited by oscillons in the $SU(2)$ gauged Higgs model [10], where stable two-field oscillons discovered in the reduced spherical Ansatz exhibit similar exchange of energy with a period much larger than the natural period of oscillation of the fields themselves.

Before concluding this section, we would like to explore the dependence of the evolution on the initial conditions for χ, by altering them in two ways: by drawing a different sample from the same aforementioned Gaussian distribution on the one hand and by initializing χ as a small "bump" with similar width to the ϕ oscillon, but very small amplitude.

We see in Fig. 13 that drawing a different sample from the same Gaussian distribution leads to a similar evolution with a phase-locked final state, albeit with the fields oscillating out of phase (in contrast to the situation of Fig. 12). This verifies our assumption in the analytical construction of the oscillon, where we distinguished between in and out of phase oscillons, while at the same time showing that these two phase configurations are the attractors of the system, depending only on the initial conditions.

On the other hand, by closely looking at the initial (linear) evolution of the χ field we see two stages: a small bump arising from the noise and the bump growing exponentially. This can be seen clearly in Fig. 14; where we note similar behaviour for the 1D and 3D systems. By initializing the χ field as a bump, we circumvent the first stage, without losing any information about the dynamical evolution of the two-field system. In what follows, this is exactly what we did in order to increase numerical efficiency.

Finally, we performed a numerical simulation for three fields. In Fig. 15 we show the evolution of a system initialized as a single field oscillon in the primary field ϕ, interacting with two fields initialized as small perturbations. We again see that at late times the three fields oscillate around

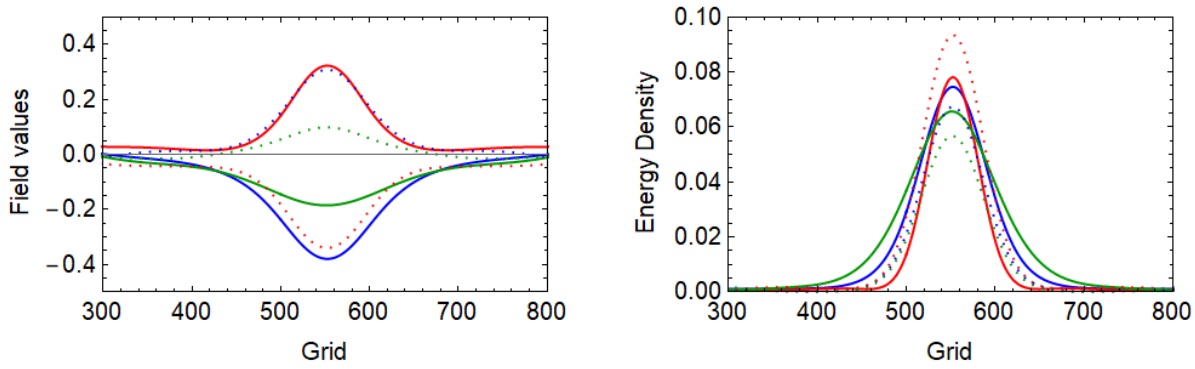

Figure 13. Time slices of the fields ϕ (full) and χ (dotted) at different times $t = 1900, 6000, 8000(m^{-1})$ (blue, red and green respectively). The parameters are the same as those in Fig. 12, but with a different Gaussian initialization for the field χ. Contrary to Fig. 12 the fields condense into an out-of-phase configuration.

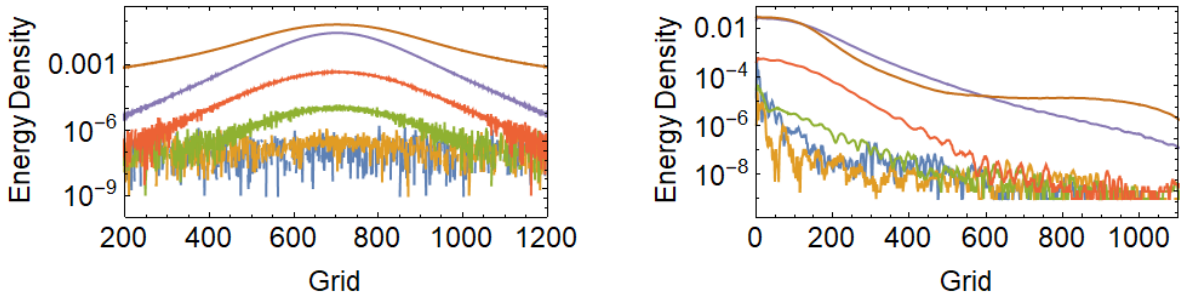

Figure 14. The evolution of the energy density (time moves from bottom to top) of the secondary field starting from Gaussian initial conditions. It is clear that, although the initial configuration is very noisy, the field aligns into a smooth configuration as the relevant modes get amplified due to Floquet instabilites. *Left:* 1-dimension with $\alpha_{init} = 0.99\alpha_c$, $\epsilon = 0.45$. *Right:* 3-dimensions with $\alpha_{init} = 0.5\alpha_c$ and $\epsilon = 0.2$. In both cases $\Lambda = 0.5$

a common value for the width and height, forming a phase-locked three-field oscillon with internal breathing modes between the fields. In the particular example plotted we observed a phase-locked state after $t \sim 5000(m^{-1})$ where initially one of the fields is oscillating out of phase with the other two fields. However we should report that due to the presence of the breathing modes a spontaneous change in behaviour is also possible, where a different type of phase-locking is suddenly reached.

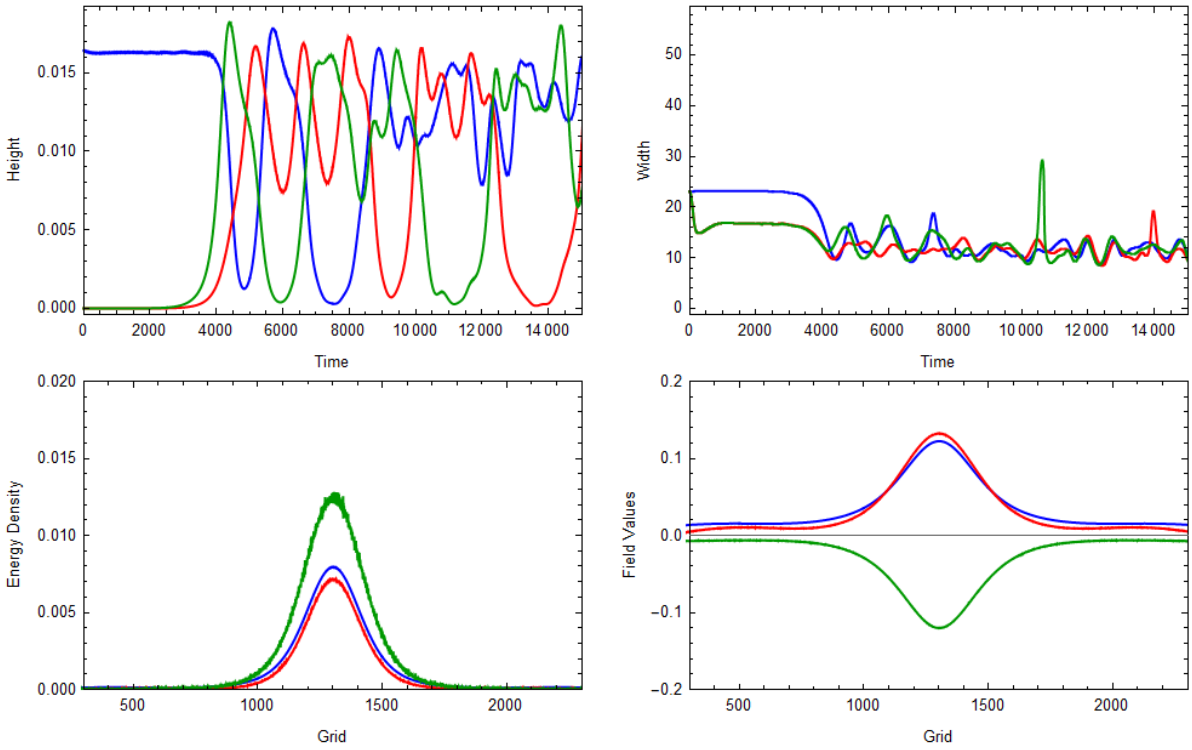

Figure 15. The decay of a single field oscillon to a three field composite oscillon. Although the presence of breathing modes doesn't allow the system to settle into a perfect symmetric state, all fields seem to oscillate around a common configuration. *Top:* The evolution of the height and width of the primary (blue) ϕ oscillon and the two secondary oscillons (green and red) that are formed after being initialized as a small perturbation. *Bottom:* the field configurations (both in field space and energy density) at $t = 10000(m^{-1})$ of the primary field (blue) and the two secondary fields (green and red). Here we used $\alpha = 0.99\alpha_c$ as initialization of the primary field and $\epsilon = 0.2$.

C. Single to multi-field oscillons in 3+1D

We now move to the the analogous three-dimensional case, anticipating full lattice simulation of preheating in three dimensions. Deferring the full lattice simulation for a future publication, we instead start with a single field spherically symmetric oscillon and study the transition to the multi-field configuration, similarly to Section VII B.

Specifically we initialize the ϕ field in the single oscillon configuration with $\epsilon = 0.1, 0.2$ and several values of α and the χ fields as a small localized overdensity (bump), as described in Section VII B. In Fig. 16 we show the evolution of the width and height of the single field oscillon towards the two-field solution at the end of the simulation. Clearly, similarly to the 1-dimensional case, the oscillon moves towards a composite structure. As can be seen from the error bars, we

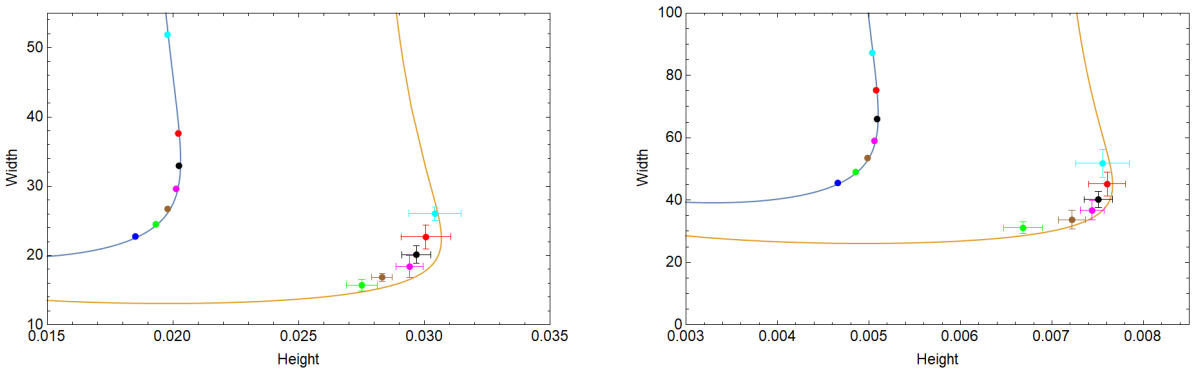

Figure 16. The evolution of the "perfect" single field oscillon, initially localized on the $\Lambda = 0$ curve (red) towards a two-field configuration falling approximately on the $\Lambda = 0.5$ curve (brown), agreeing with our theoretical predictions. For the final state, we average over the two fields and over various time slices to account for the effect of the breathing modes (hence, the error bars). The dots correspond to various initial conditions with $\alpha = 0.4, 0.45, 0.5, 0.55, 0.6, 0.65, 0.7(\alpha_c)$ (bottom to top). *Left:* $\epsilon = 0.2$. *Right:*$\epsilon = 0.1$. Note that in both cases only the single-field oscillon with $\alpha = 0.4\alpha_c$ (blue dot) does not evolve towards a composite solution.

see that the resulting configuration is much closer to the analytically constructed form of a two-field oscillon than its one-dimensional counterpart. In other words, the internal breathing mode exists, but is suppressed. We believe that the larger size of the internal breathing mode for one spatial dimension is connected to the increased stability for one-dimensional oscillons, compared to their three-dimensional counterparts. Otherwise, the results are qualitatively equivalent to the 1-dimensional case as represented in Fig. 12. It is noteworthy that we need to initialize the oscillon with a value of α much closer to α_c in order to see decay to a two-field solution in 1D: $\alpha_i \sim 0.95\alpha_c$ in 1D and $\alpha_i \sim 0.45\alpha_c$ in 3D; where the subscript i indicates the initial value of α of the background oscillon. This fact can be understood heuristically from the point of view of Floquet theory.

D. Analysis of results in terms of Floquet theory

In this subsection we explore the emergence of the multi-field oscillons as observed in the previous sections using semi-analytic techniques. We do this explicitly for two fields, but the intuition naturally extends to more fields. To first order in perturbations, the equation of motion of the secondary field χ is

$$\ddot{\chi} - \nabla^2\chi + \chi - \Lambda\phi^2\chi = 0\,, \tag{43}$$

Since χ is a small perturbation at early times, this equation governs its dynamics. Also, to first order in ϵ we write $\phi = \epsilon\Phi_0(x)\cos(\omega t)$. Switching to Fourier space and applying the convolution theorem we obtain

$$\ddot{\chi_k} + k^2\chi_k + \chi_k - \epsilon^2\Lambda\cos(\omega t)^2 \int \frac{d^dk}{(2\pi)^d}\Psi(k-k')\chi_{k'} = 0\,, \tag{44}$$

where $\Psi(k)$ is the Fourier transform of $[\Phi_0(x)]^2$. This equation can in principle be solved using Floquet theory, where the solutions are of the form $\chi_k(t) = e^{\mu_k t}P(t)$, where $P(t)$ is a periodic function. However the inhomogeneity of the background oscillon couples all different k-modes through the convolution term which makes the challenge of finding the Floquet exponents impossible. To understand the basic dynamics, we investigate the constant amplitude limit $\Phi_0(x) = \Phi_0(0)$, and incorporate the effect of the spatial extent of the oscillon heuristically. In this limit the wavenumbers decouple and it is a simple exercise to find the Floquet exponents μ_k. In appendix B we show how to find an approximate solution for the functions $\chi_k(t)$. They are of the form $\chi_k(t) \propto Re\{\cos(\omega t)e^{i\mu_k\tau}\}$ where $\tau = \epsilon^2 t$ is slow time and

$$\mu_k^2 = \frac{1}{4}\left(\alpha + \frac{k^2}{\epsilon^2} - \frac{3}{4}\Lambda\Phi_0^2\right)\left(\alpha + \frac{k^2}{\epsilon^2} - \frac{1}{4}\Lambda\Phi_0^2\right), \tag{45}$$

where Φ_0 is the rescaled height of the background oscillon at the origin and $\omega = 1 - \alpha\epsilon^2/2$ its frequency. If Eq. (45) has imaginary solutions the corresponding mode will grow exponentially. Eq. (45) makes it explicit that a two-field configuration will not emerge for repulsive interactions (negative Λ), so in what follows we focus on attractive interactions. Note that if we find an unstable mode for some ϵ_1 ($g = 1/\epsilon^2$ is the parameter multiplying the sextic term in our Lagrangian) at a wavenumber k_1, a different choice of ϵ_2 will have an unstable mode with the same Floquet exponent at $k_2 = \dfrac{\epsilon_2}{\epsilon_1}k_1$. Since the oscillon width scales like $R_{osc} \propto 1/\epsilon$, the range of validity of the homogeneous approximation also changes with ϵ. This explains why the decay of a single field oscillon into a two-field configuration does not seem to depend on the exact value of the small parameter[9] ϵ (see e.g. Fig. 16); though it might depend α and Φ_0 (these quantities are linked via the oscillon profile equation; Eq. (14)). This line of argument is also valid in the full inhomogeneous Floquet analysis, although it is impossible to find exact analytical expressions for the Floquet exponents in this case. The reasoning is confirmed in Fig. 17 where we plot the amplification of the energy in the χ field at early times for some of the simulations we performed in three dimensions.

[9] This may seem somewhat surprising since the height of the background oscillon scales with ϵ. Note however that the actual timescales of decay scale with ϵ^2. So although the oscillon will eventually decay to a two-field configuration, the process will take more time for smaller ϵ.

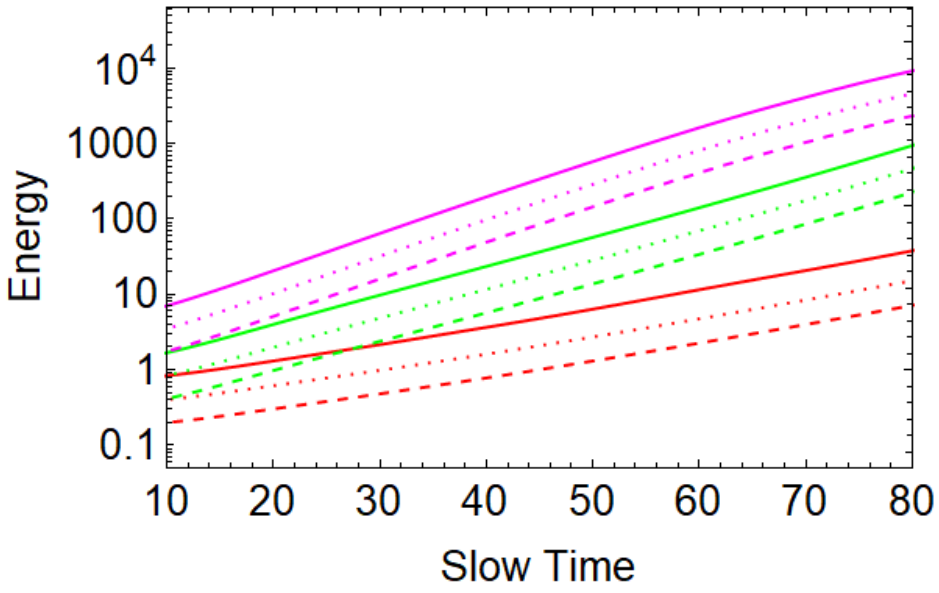

Figure 17. The amplification in the localized energy of the secondary field χ at early times in 3D on a log scale, with time rescaled as $\tau = \epsilon^2 t$ and $\alpha = 0.5\alpha_c$ (red), $\alpha = 0.6\alpha_c$ (green), $\alpha = 0.75\alpha_c$ (magenta). For each value of α we simulated three different values of ϵ: 0.05 (solid) 0.1 (dotted) and 0.2 (dashed). As expected, the amplification with respect to τ is independent of ϵ since the different linetypes are parallel to each other. There is a dependence on α which is allowed by Eq. (B7). Here we used $\Lambda = 0.5$

As expected, the amplification of the field with respect to slow time τ is independent of ϵ. We can use Eq. (B7) to find a crude estimate of the amplification of the localized energy which goes like $E_\chi \propto |\chi_{k,0}|^2 e^{2\mu_k \tau}$, where in general we found $\mu_k \sim \mathcal{O}(0.1)$ in units of m, agreeing with what we observe in Fig. 17.

Eq. (45) is valid in both 1D and 3D. In Fig. 18 we show the main instability band for different values of α and wavenumber k, with $\Lambda = 0.5$, for both three dimensions (left) and one dimension (right). The numerics of the previous sections have shown that in one dimension a single field oscillon settles into a two-field solution only when $\alpha \geq 0.95\alpha_c$; while in three dimensions this happens for $\alpha \geq 0.45\alpha_c$. This is merely a reflection of the invalidity of the approximation we have taken here. Since the oscillon has a width of order $R_{osc} \sim 1/\epsilon$, this approximation breaks down for some $k \ll \epsilon$. Correspondingly, when for a given α the oscillon solution is very wide, the approximation is valid for a larger range of $k-$modes. This helps us understand the difference between the 1D and 3D simulations. In Fig. 19 we plot the dependence of the width and height of the oscillon solution on α. Clearly, the three-dimensional solution has a larger width than the one dimensional solution for $\alpha \sim 0.45\alpha_c$ (also see Fig. 3). In Fig. 18 this information is conveyed by

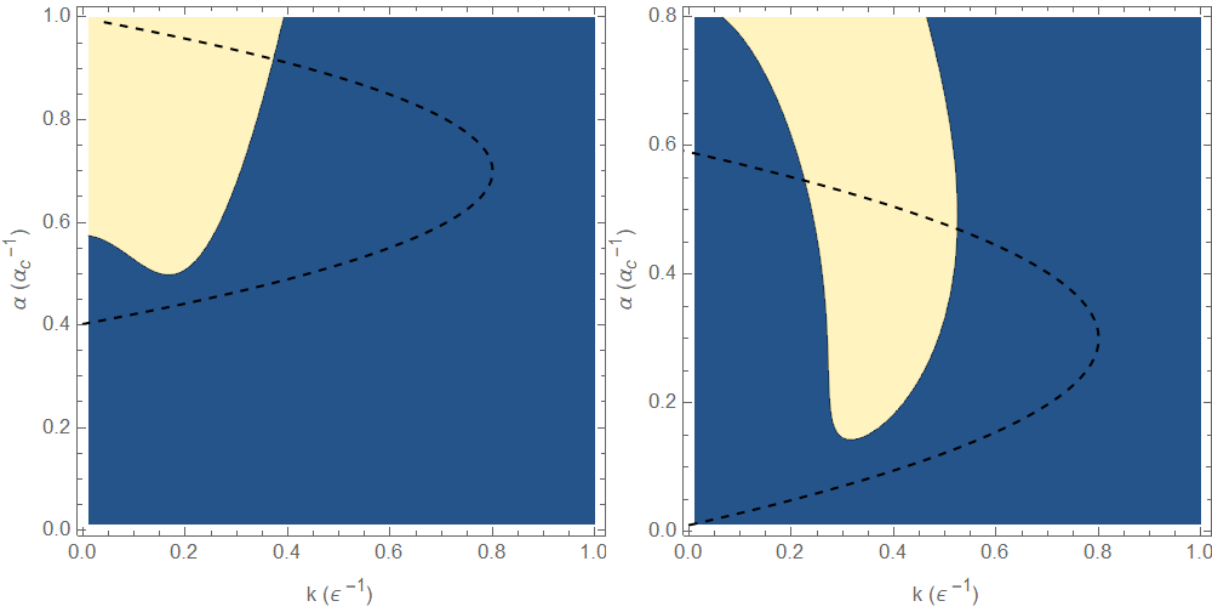

Figure 18. The instability bands for different wavenumbers k and different background oscillons parametrized by α in the homogeneous background approximation. Here we fixed $\Lambda = 0.5$. The bands look somewhat similar in 3D (left) and 1D (right), however due to the difference in shapes of the background oscillon, this approximation is valid over a larger region of parameter space in 3D. This is shown schematically by the black dashed line: the approximation is valid for the parameter space to the right of the line, where the oscillons are wider.

the black line going through the instability band: the approximation is only valid for wavenumbers that are to the right of this line. Note that the line drawn here is merely schematic.

VIII. SUMMARY AND DISCUSSION

Despite the oscillons' ubiquity in non-linear scalar field theories and their assumed presence in the early Universe, very few multi-field oscillons have been found and studied. In the present work we explored a symmetric system comprised of two interacting scalar fields and showed how genuine two-field oscillon solutions can be constructed.

We found two-field oscillon solutions in potentials with either an attractive or a repulsive interaction term. They are qualitatively similar to "flat-top" oscillons found in Ref. [6], with quantitative differences that depend on the sign and strength of the interaction term. The oscillons that emerge in the presence of an attractive non-linearity can be both taller (reaching higher central field values) and also narrower (having smaller width) than their single-field counterparts. In the case of repul-

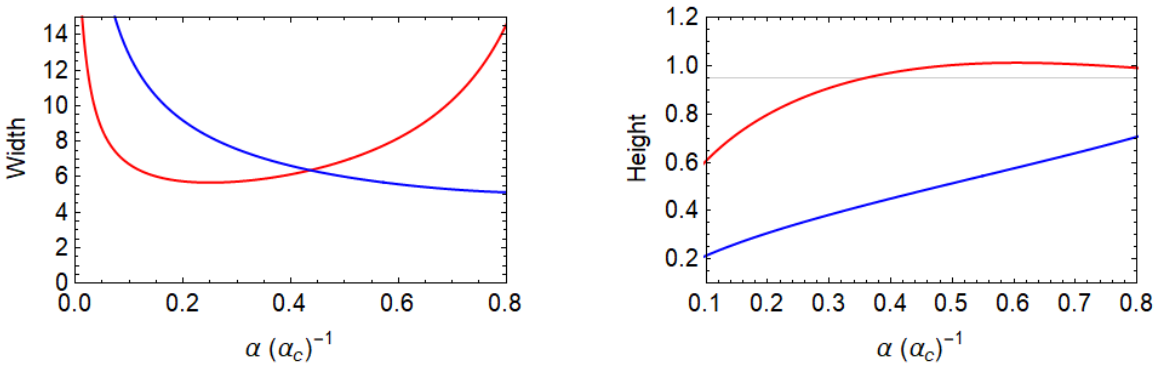

Figure 19. The dependence of the features of the background oscillon on α for 3D (red) and 1D (blue). We see that in three dimensions the asymptotic solution where width $\sim \infty$ and height $\sim \sqrt{9/10}$, is approximately valid for smaller α. This explains our observations in the previous sections since Eq. (B7) applies more accurately in this regime.

sively interacting fields, the range of possible oscillon amplitudes shrinks, until the repulsive term is strong enough to completely forbid the existence of oscillons, at least within the small amplitude two-timing framework.

The stability of non-linearity-supported localized structures can be assessed through the Vakhitov-Kolokolov (V-K) stability criterion. We formally extended the VK criterion, in order to be used in two-field systems. We checked the VK criterion against numerical simulations (assuming spherical symmetry throughout the evolution), finding excellent agreement between semi-analytical and fully numerical results. Our current proof holds for symmetric potentials and the generalization to arbitrary multi-field oscillons is left for future work. Furthermore, we explored the basin of attraction of stable oscillons, by perturbing unstable initial configurations. We found that, depending on the size of the initial perturbation, the unstable oscillons can either completely disperse, or relax to a stable oscillon configuration with a smaller width and larger height.

Since oscillons are long-lived configurations albeit with a finite lifetime (even classically), we adapted the methods used in the literature to compute the emitted scalar radiation and thus estimate the oscillon lifetime. The results we found are qualitatively and quantitatively similar to the single-field case, showing that the longevity of multi-field oscillons can be –at least– comparable to their single-field counterparts. We showed that the results for the two-field system can be naturally extended to models with an arbitrary number of fields, where each field has the same quadratic - quartic - sextic potential and all fields are pairwise coupled. We were able to construct multi-field oscillons, under certain conditions for the couplings, and prove their stability, by drawing

formal analogies to the single-field case. This opens the way for arbitrarily dense oscillons, comprised of multiple fields.

Finally, we studied the emergence of these multi-field oscillons. We performed simulations on an expanding lattice in one spacial dimensions, in a preheating-like scenario. We showed that the fragmentation of the inflaton proceeds in three distinct stages: the inflaton fragments into single field oscillons; the single-field oscillons amplify fluctuations in the spectator field(s); composite oscillons emerged. Prompted by these observations we analysed the decay of single field oscillons into multi-field oscillons, both in one and three spatial dimensions, in Minkowski space. The decay can be understood semi-quantitatively using floquet theory. Since the emergence of multi-field oscillons in three spatial dimensions follows the one-dimensional behaviour in Minkowski space, we expect that multi-field oscillons will also form in full three-dimensional simulations on an expanding lattice, which is left for a future publication.

Overall, our current work provides analytical tools for studying multi-component oscillons and opens up several avenues for future work, such as relaxing the symmetry structure of the potential and the assumption of spherical symmetry.

ACKNOWLEDGMENTS

We thank Ana Achúcarro for useful discussions and Mustafa Amin for suggestions regarding the lifetime of oscillons. We acknowledge support from IFAE, which is partially funded by the CERCA program of the Generalitat de Catalunya. EIS acknowledges support from the Dutch Organisation for Scientific Research (NWO). EIS also acknowledges support of a fellowship from "la Caixa" Foundation (ID 100010434) and from the European Union's Horizon 2020 research and innovation programme under the Marie Skłodowska-Curie grant agreement No 847648. The fellowship code is LCF/BQ/PI20/11760021. The research leading to these results has received funding from the ESF under the program Ayudas predoctorales of the Ministerio de Ciencia e Innovacin PRE2020-094420.

Appendix A: The V-K criterion

We present the derivation of the V-K stability criterion, applied first to the case of two-field oscillons and afterwards generalized to N fields.

1. Two fields

For clarity, we will separately analyze the two cases of oscillons where the two fields oscillate either in phase ($a = b$) or out of phase ($a = -b$).

a. Two-field system oscillating in phase

For oscillons comprised of the two fields oscillating in phase, $a = b$, the system of Eqs. (20) becomes

$$\begin{aligned}\partial_t^2\delta + \delta - (\partial_r^2 + \frac{2}{r}\partial_r)\delta - \epsilon^2 a^2(3+\Lambda)\cos^2(\omega t)\delta + \epsilon^4 5ga^4\cos^4(\omega t)\delta - \epsilon^2 2\Lambda a^2\cos(\omega t)\Delta =0\,,\\ \partial_t^2\Delta + \Delta - (\partial_r^2 + \frac{2}{r}\partial_r)\Delta - \epsilon^2 a^2(3+\Lambda)\cos^2(\omega t)\Delta + \epsilon^4 5ga^4\cos^4(\omega t)\Delta - \epsilon^2 2\Lambda a^2\cos(\omega t)\delta =0\,.\end{aligned} \tag{A1}$$

While Eqs. (A1) is rather complicated, the symmetries of the initial Lagrangian allow us to simplify the stability analysis, by introducing the new variable $\xi(x,t) = \delta(x,t) + \Delta(x,t)$, which reduces Eqs. (A1) to

$$\partial_t^2\xi + \xi - (\partial_r^2 + \frac{2}{r}\partial_r)\xi - \epsilon^2 3a^2(1+\Lambda)cos^2(\omega t)\xi + \epsilon^4 5ga^4 cos^4(\omega t)\xi = 0 \tag{A2}$$

This equation only depends on $\xi(x,t)$, greatly simplifying our calculations. Since we are interested in perturbations that are about the same size as the oscillon itself we perform the same change of variable as before $r \to \rho = \epsilon r$. Furthermore, we expect perturbations to oscillate near the oscillon frequency. To capture the growth or decay of the perturbation we should also introduce a new "slow" time variable $\tau = \epsilon^2 t$. We also introduce a time-scale related to the corrected oscillation frequency of the oscillon $T = \omega t$. As before we expect behaviour on both time scales, so $\xi(x,t) \to \xi(\rho, T, \tau)$, and partial time-derivatives become full derivatives. Looking for solutions that can be written as a power series in $\epsilon \ll 1$

$$\xi(\rho, T, \tau) = \sum_{n=0} \epsilon^n \xi_n(\rho, T, \tau) \tag{A3}$$

allows for a perturbative analysis of Eq. A2. The zeroth and first order equations are respectively

$$\partial_T^2\xi_0 + \xi_0 = 0 \tag{A4}$$

and

$$\partial_T^2\xi_1 + \xi_1 = -\left(\partial_T\partial_\tau - \alpha\partial_T^2 - \left(\partial_\rho^2 + \frac{2}{\rho}\partial_\rho\right) - 3a^2(1+\Lambda)(\cos T)^2 + 5a^4(\cos T)^4\right)\xi_0\,. \tag{A5}$$

The general solution of Eq. (A4) has the form

$$\xi_0(\rho, T, \tau) = u(\rho, \tau)\cos T + v(\rho, \tau)\sin(T)\,, \tag{A6}$$

where the functions $u(\rho, \tau)$ and $v(\rho, \tau)$ capture the potential growth of the perturbation on timescales of order τ. The V-K criterion provides a simple way to distinguish cases where perturbation grow exponentially based on the form of the oscillon itself. Namely, inserting Eq. (A6) into Eq. (A5) and eliminating secular terms on the right-hand side leads to equations for u and v

$$\partial_\tau u = H_1 v\,, \tag{A7}$$

$$\partial_\tau v = -H_2 u\,, \tag{A8}$$

where H_1 and H_2 are Hermitian, linear operators defined as

$$H_1 = \alpha - (\partial_\rho^2 + \frac{2}{\rho}\partial_\rho) - \frac{3}{4}(1+\Lambda)a^2 + \frac{5}{8}a^4 = 0\,, \tag{A9}$$

$$H_2 = \alpha - (\partial_\rho^2 + \frac{2}{\rho}\partial_\rho) - \frac{9}{4}(1+\Lambda)a^2 + \frac{25}{8}a^4 = 0\,. \tag{A10}$$

Separating variables as $u(\rho, \tau) \to u(\rho)e^{\Omega\tau}$ and $v(\rho, \tau) \to v(\rho)e^{\Omega\tau}$ the problem reduces to the linear equation

$$\Omega^2 u = -H_1 H_2 u\,. \tag{A11}$$

The question of whether the oscillon is stable to general long-wavelength perturbations is thus reduced to an eigenvalue problem. If the operator $-H_1H_2$ has at least one positive eigenvalue $\Omega^2 > 0$, perturbations can grow and the oscillon will in general be unstable. If not, perturbations simply oscillate, leading to an oscillon that is stable, within the limits of the perturbative expansion used to construct it. The problem can be solved using a similar procedure as Vakhitov and Kolokolov [50]. We do not present the entire proof here, as its intricacies will add little to the main goal of analyzing two-field oscillons. The criterion for stability states that $max(\Omega^2) < 0$ if and only if $dN/d\alpha > 0$, where N is defined in Eq. (22).

Before proceeding, we must make a final remark about the validity of this derivation. The criterion we presented above only states whether perturbation of the form $\xi(x,t) = \delta(x,t) + \Delta(x,t)$ will grow. In principle, the growth of the perturbation might only be present in δ or Δ. However, since the system is completely symmetric under exchange of the fields, we can only conclude that, if $\xi(x,t)$ grows, both $\delta(x,t)$ and $\Delta(x,t)$ will grow exponentially. The criterion should therefore be valid for the full two-field system and can be used as an indicator for the stability of two-field oscillons, at least ones that are comprised of interchangeable fields.

b. Two-field system oscillating out of phase

For oscillons comprised of the two fields oscillating out of phase, $a = -b$, the system of Eqs. (20) becomes

$$\partial_t^2\delta + \delta - (\partial_r^2 + \frac{2}{r}\partial_r)\delta - \epsilon^2 a^2(3+\Lambda)cos^2(\omega t)\delta + \epsilon^4 5ga^4 cos^4(\omega t)\delta + \epsilon^2 2\Lambda a^2 cos^2(\omega t)\,\Delta = 0\,,$$
$$\partial_t^2\Delta + \Delta - (\partial_r^2 + \frac{2}{r}\partial_r)\Delta - \epsilon^2 a^2(3+\Lambda)cos^2(\omega t)\Delta + \epsilon^4 5ga^4 cos^4(\omega t)\Delta + \epsilon^2 2\Lambda a^2 cos^2(\omega t)\,\delta = 0\,. \tag{A12}$$

Now, instead of looking for unstable modes in the combination $\xi = \delta + \Delta$, we introduce the corresponding variable $\psi \equiv \delta - \Delta$. By now subtracting the equations in (A12) The corresponding equation for ψ becomes

$$\partial_t^2\psi + \psi - (\partial_r^2 + \frac{2}{r}\partial_r)\psi - \epsilon^2 3a^2(1+\Lambda)cos^2(\omega t)\psi + \epsilon^4 5ga^4 cos^4(\omega t)\psi = 0\,. \tag{A13}$$

We see that the equation of motion for ψ in the case of $a = -b$ is identical to the one for ξ for $a = b$. The rest of the derivation follows exactly the same steps as before so we won't repeat them here. Hence the stability of the oscillon will be independent of the phase (0 or π) between the two fields, resulting in exactly the same V-K criterion as before. Namely, there are unstable perturbations of the oscillon if and only if $dN/d\alpha > 0$, where N is defined in Eq. (22).
In this section we have derived a nontrivial extension of the V-K criterion for assessing the stability of oscillons in this coupled system to long wave-length perturbations (perturbations about the same size as the oscillon). It is, to our knowledge, the first time that the criterion has been derived for multi-component oscillons.

Fig. 20 shows the most unstable modes computed by solving the eigenvalue problem of Eq. (A11) using the variational method for $\Lambda = -0.5$ and $\Lambda = 0.5$, corresponding to repulsive and attractive interactions respectively. We choose some values of α for each case, which give $\Omega^2 > 0$ in Eq. (A11) and thus lead to (radially) unstable oscillon solutions. We see that the spatial size of the unstable fluctuations is indeed similar to the width of the corresponding oscillons (see e.g. Fig. 2).

2. N fields

By solving the profile equations of Eq. (39) we have implicitly found oscillon solutions of the form $\phi_{i,osc} = \epsilon a_i \cos(\omega t)$, where $\omega = 1 - \alpha\epsilon^2/2$. To assess the stability of these solutions we add a small perturbation δ_i to the oscillon solution; $\phi_i = \phi_{i,osc} + \delta_i$. Plugging this ansatz into Eq. (35),

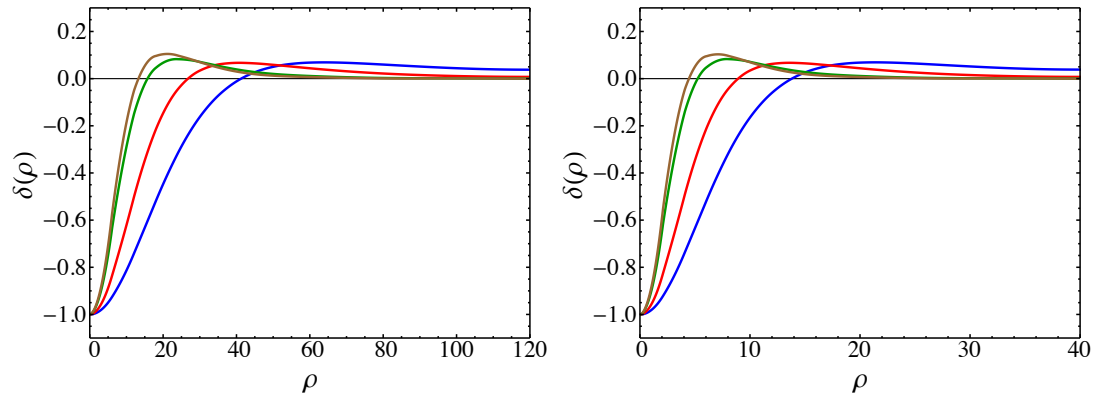

Figure 20. *Left*: The profiles of the most unstable modes of the corresponding oscillons with $\Lambda = -0.5$ and $\alpha = 0.00028, 0.00071, 0.0025, 0.0046$, (blue, red, green and brown respectively). These are calculated numerically using the variational principle. *Right*: The profiles of the most unstable modes of the corresponding oscillons with $\Lambda = 0.5$ and $\alpha = 0.0025, 0.0064, 0.0225, 0.04$ (blue, red, green and brown respectively). The profiles were rescaled such that $\delta(\rho = 0) = 1$. We see that the size of the unstable modes are similar to the size of the oscillon profile, shown in Fig. 2.

linearizing and ignoring source terms

$$\partial_t^2\delta_i - (\partial_r^2 + \frac{2}{r}\partial_r)\delta_i + \delta_i = \left(3\phi_{i,osc}^2 - g\phi_{i,osc}^4 + \Lambda\sum_{j\neq i}\left(\phi_{j,osc}^2 + 2\phi_{i,osc}\phi_{j,osc}\frac{\delta_j}{\delta_i}\right)\right)\delta_i \tag{A14}$$

Now, assuming that $a(\rho)$ is a solution of Eq. (40), we can set $n < N$ of the $a_i = a$ and $(N-n)$ of the $a_i = -a$. This configuration obviously solves the system of profile equations in Eqs. (39). If $a_i = a$ the equation for δ_i becomes (omitting all factors of ϵ for clarity)

$$\begin{aligned}\partial_t^2\delta_i - (\partial_r^2 + \frac{2}{r}\partial_r)\delta_i + \delta_i = \left(3a^2\cos^2(\omega t) - ga^4\cos^4(\omega t) + \Lambda(N-1)a^2\cos^2(\omega t)\right)\delta_i \\ + 2\Lambda a^2\cos^2(\omega t)\sum_{j\neq i}\delta_j - 2\Lambda a^2\cos^2(\omega t)\sum\Delta_j\,,\end{aligned} \tag{A15}$$

while for $a_i = -a$ the same equation becomes

$$\begin{aligned}\partial_t^2\Delta_i - (\partial_r^2 + \frac{2}{r}\partial_r)\Delta_i + \Delta_i = \left(3a^2\cos^2(\omega t) - ga^4\cos^4(\omega t) + \Lambda(N-1)a^2\cos^2(\omega t)\right)\Delta_i \\ + 2\Lambda a^2\cos^2(\omega t)\sum_{j\neq i}\Delta_j - 2\Lambda a^2\cos^2(\omega t)\sum\delta_j\,,\end{aligned} \tag{A16}$$

where we've renamed the perturbations $\delta_i \to \Delta_i$ if $a_i = -a$ for clarity. Adding the n equations of the form (A15) and the $N-n$ equations of the form (A16) together respectively we obtain the

equations

$$\partial_t^2\Omega - (\partial_r^2 + \frac{2}{r}\partial_r)\Omega + \Omega = \left(3a^2\cos^2(\omega t) - ga^4\cos^4(\omega t) + \Lambda(N-1)a^2\cos^2(\omega t)\right)\Omega \\ + 2\Lambda(n-1)a^2\cos^2(\omega t)\Omega - 2\Lambda n a^2\cos^2(\omega t)K \tag{A17}$$

and

$$\partial_t^2 K - (\partial_r^2 + \frac{2}{r}\partial_r)K + K = \left(3a^2\cos^2(\omega t) - ga^4\cos^4(\omega t) + \Lambda(N-1)a^2\cos^2(\omega t)\right)K \\ + 2\Lambda((N-n-1)a^2\cos^2(\omega t)K - 2\Lambda(N-n)a^2\cos^2(\omega t)\Omega\,, \tag{A18}$$

where we've introduced variables $\Omega = \sum \delta_i$ and $K = \sum \Delta_i$. Finally, we substract Eq. (A18) from Eq. (A17) and define the variable $\Xi = \Omega - K$ to obtain

$$\partial_t^2\Xi - (\partial_r^2 + \frac{2}{r}\partial_r)\Xi + \Xi = \left(3(1+\Lambda(N-1))a^2\cos^2(\omega t) - ga^4\cos^4(\omega t)\right)\Xi \tag{A19}$$

From here the derivation of the instability bands of Ξ is analogous to the derivation performed in section IV A. The difference being that $\Lambda \to \Lambda(N-1)$ with respect to Eq. (A2). However, this is exactly the change that occurs in the effective profile equation (40). The V-K criterion therefore still applies and the multi-field oscillon is stable if and only if $dN/d\alpha > 0$, where

$$N = \int a^2(\rho)d^3\rho\,, \tag{A20}$$

which is identical to Eq. (22).

Appendix B: Aprroximate Floquet exponents

We provide an approximate analytic method for computing the Floquet exponents of the equation

$$\ddot{\chi_k} + (k^2+1)\chi_k - \Lambda\epsilon^2\Phi_0^2\cos^2(\omega t)\chi_k = 0\,. \tag{B1}$$

Which is just the limit of Eq. (44) in which the oscillon is approximated as a homogeneous background. We can find perturbative solutions by introducing two time scales: the period $T = \omega t = 1 - \alpha\epsilon^2/2t$ and the slow time $\tau = \epsilon^2 t$. We also assume that the solution has characteristic behaviour on both timescales, similar to the two-timing analysis, meaning $\chi_k(t) = \chi_k(T,\tau)$. Finally, we are interested in modes for which $k = \kappa\epsilon$ where $\kappa = \mathcal{O}(1)$. Eq. (B1) becomes

$$\left(1-\alpha\epsilon^2\right)\ddot{\chi}_k + 2\epsilon^2\dot{\chi'}_k + \left(\epsilon^2\kappa^2+1\right)\chi_k - \Lambda\epsilon^2\Phi_0^2\cos^2(\omega t)\chi_k = 0 \tag{B2}$$

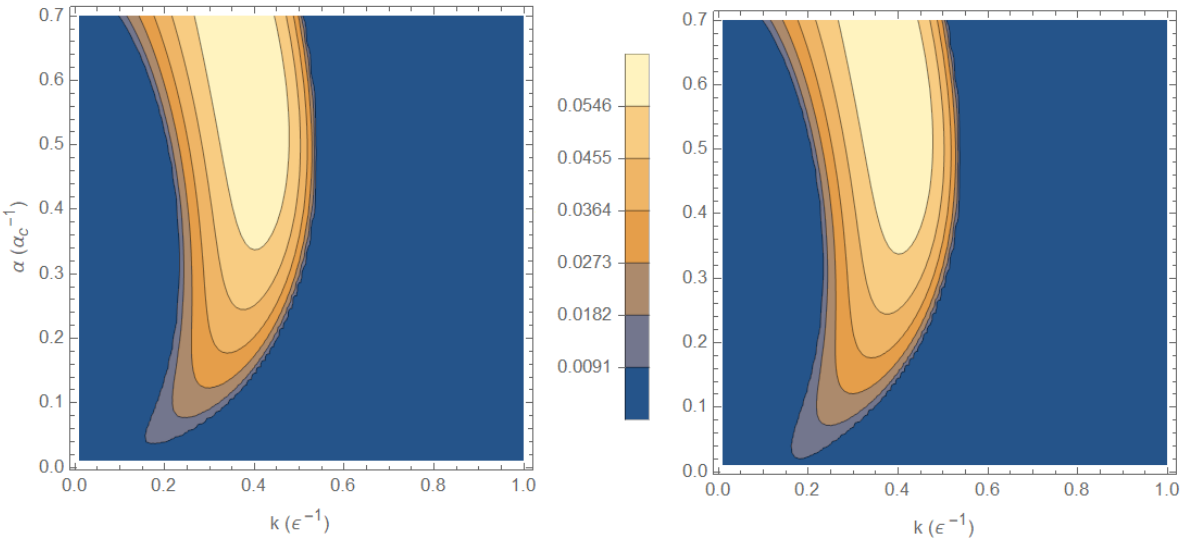

Figure 21. Comparison of the Floquet instability bands within the homogeneous approximation, computed with a full numerical analysis (left) for $\epsilon = 0.1$ and computed using Eq. (B7) (right). The instability bands agree extremely well, speaking to the validity of our analysis. Here we use $\Lambda = 0.5$.

where a dot denotes derivation with respect to T and a prime denotes derivation with respect to τ. We look for a perturbative solution $\chi_k = \chi_k^{(0)} + \epsilon\chi_k^{(1)} + \epsilon^2\chi_k^{(2)} + ...$

The $\mathcal{O}(\epsilon^0)$ gives the solution of $\chi_k^{(0)}$

$$\chi_k^{(0)} = A(\tau)\cos(T) + B(\tau)\sin(T) \tag{B3}$$

The $\mathcal{O}(\epsilon^1)$ equation does not provide any additional information. The $\mathcal{O}\left(\epsilon^2\right)$ equation is

$$\ddot{\chi}_k^{(2)} + \chi_k^{(2)} = \alpha\ddot{\chi}_k^{(0)} - 2\dot{\chi}_k'^{(2)} - \kappa^2\chi_k^{(0)} + \Lambda\Phi_0^2\cos^2(T) \tag{B4}$$

By plugging in Eq. (B3) into the right hand side of Eq. (B4) and requiring that the 0th-order perturbation doesn't induce resonances in the 2nd-order perturbation we obtain the following constraints on $A(\tau)$ and $B(\tau)$

$$\begin{aligned} 2B' &= -\left(\alpha + k^2 - \frac{3}{4}\Lambda\Phi_0^2\right)A \\ 2A' &= \left(\alpha + k^2 - \frac{1}{4}\Lambda\Phi_0^2\right)B \end{aligned} \tag{B5}$$

This system of equations can be trivially solved by applying ∂_τ on one of the two equations and using the other to elliminate the first derivative term, leading to

$$A'' + \left(\alpha + k^2 - \frac{3}{4}\Lambda\Phi_0^2\right)\left(\alpha + k^2 - \frac{1}{4}\Lambda\Phi_0^2\right)A = 0 \tag{B6}$$

with B obeying the same equation. The solutions are $A(\tau), B(\tau) \sim \cos(\mu_k \tau), \sin(\mu_k \tau)$. When μ_k is imaginary, the trigonometric functions become hyperbolic trigonometric functions, which for late times grow as $e^{Im[\mu_k]\tau}$. We thus arrive at the result expected by Floquet theory, where the Floquet exponents are given by

$$\mu_k^2 = \frac{(\alpha + \kappa^2 - \frac{3}{4}\Lambda\Phi_0^2)(\alpha + \kappa^2 - \frac{\Lambda}{4}\Phi_0^2)}{4} \,. \tag{B7}$$

This is the expression given in the main body of text. In Fig. 21 we compare the instability bands computed in this approximation with the full numerical Floquet analysis of Eq. (B1) for the case of $\epsilon = 0.1$ in three dimensions. As one can see, the perturbative method highlighted in this section agrees extremely well with the full computation.

---

[1] I. L. Bogolyubsky and V. G. Makhankov, On the Pulsed Soliton Lifetime in Two Classical Relativistic Theory Models, JETP Lett. **24**, 12 (1976).

[2] I. L. Bogolyubsky and V. G. Makhankov, Dynamics of Heavy Spherically-Symmetric Pulsons, Pisma Zh. Eksp. Teor. Fiz. **25**, 120 (1977).

[3] M. Gleiser, Pseudostable bubbles, Phys. Rev. **D49**, 2978 (1994), arXiv:hep-ph/9308279 [hep-ph].

[4] E. J. Copeland, M. Gleiser, and H. R. Muller, Oscillons: Resonant configurations during bubble collapse, Phys. Rev. **D52**, 1920 (1995), arXiv:hep-ph/9503217 [hep-ph].

[5] S. Kasuya, M. Kawasaki, and F. Takahashi, I-balls, Phys. Lett. **B559**, 99 (2003), arXiv:hep-ph/0209358 [hep-ph].

[6] M. A. Amin and D. Shirokoff, Flat-top oscillons in an expanding universe, Phys. Rev. **D81**, 085045 (2010), arXiv:1002.3380 [astro-ph.CO].

[7] M. Kawasaki, F. Takahashi, and N. Takeda, Adiabatic Invariance of Oscillons/I-balls, Phys. Rev. **D92**, 105024 (2015), arXiv:1508.01028 [hep-th].

[8] M. A. Amin, K-oscillons: Oscillons with noncanonical kinetic terms, Phys. Rev. **D87**, 123505 (2013), arXiv:1303.1102 [astro-ph.CO].

[9] M. Ibe, M. Kawasaki, W. Nakano, and E. Sonomoto, Decay of I-ball/Oscillon in Classical Field Theory, JHEP **04**, 030, arXiv:1901.06130 [hep-ph].

[10] E. I. Sfakianakis, Analysis of Oscillons in the SU(2) Gauged Higgs Model, (2012), arXiv:1210.7568 [hep-ph].

[11] R. Kallosh and A. Linde, Universality Class in Conformal Inflation, JCAP **1307**, 002, arXiv:1306.5220 [hep-th].

[12] R. Kallosh, A. Linde, and D. Roest, Superconformal Inflationary α-Attractors, JHEP **11**, 198, arXiv:1311.0472 [hep-th].

[13] M. Galante, R. Kallosh, A. Linde, and D. Roest, Unity of Cosmological Inflation Attractors, Phys. Rev. Lett. **114**, 141302 (2015), arXiv:1412.3797 [hep-th].

[14] B. J. Broy, M. Galante, D. Roest, and A. Westphal, Pole inflation — Shift symmetry and universal corrections, JHEP **12**, 149, arXiv:1507.02277 [hep-th].

[15] M. A. Amin, R. Easther, H. Finkel, R. Flauger, and M. P. Hertzberg, Oscillons After Inflation, Phys. Rev. Lett. **108**, 241302 (2012), arXiv:1106.3335 [astro-ph.CO].

[16] S.-Y. Zhou, E. J. Copeland, R. Easther, H. Finkel, Z.-G. Mou, and P. M. Saffin, Gravitational Waves from Oscillon Preheating, JHEP **10**, 026, arXiv:1304.6094 [astro-ph.CO].

[17] S. Antusch, F. Cefala, and S. Orani, Gravitational waves from oscillons after inflation, Phys. Rev. Lett. **118**, 011303 (2017), [Erratum: Phys. Rev. Lett.120,no.21,219901(2018)], arXiv:1607.01314 [astro-ph.CO].

[18] J. Liu, Z.-K. Guo, R.-G. Cai, and G. Shiu, Gravitational Waves from Oscillons with Cuspy Potentials, Phys. Rev. Lett. **120**, 031301 (2018), arXiv:1707.09841 [astro-ph.CO].

[19] K. D. Lozanov and M. A. Amin, Self-resonance after inflation: oscillons, transients and radiation domination, Phys. Rev. **D97**, 023533 (2018), arXiv:1710.06851 [astro-ph.CO].

[20] M. A. Amin, J. Braden, E. J. Copeland, J. T. Giblin, C. Solorio, Z. J. Weiner, and S.-Y. Zhou, Gravitational waves from asymmetric oscillon dynamics?, Phys. Rev. **D98**, 024040 (2018), arXiv:1803.08047 [astro-ph.CO].

[21] N. Kitajima, J. Soda, and Y. Urakawa, Gravitational wave forest from string axiverse, JCAP **1810**, 008, arXiv:1807.07037 [astro-ph.CO].

[22] J. Liu, Z.-K. Guo, R.-G. Cai, and G. Shiu, Gravitational wave production after inflation with cuspy potentials, Phys. Rev. **D99**, 103506 (2019), arXiv:1812.09235 [astro-ph.CO].

[23] K. D. Lozanov and M. A. Amin, Gravitational perturbations from oscillons and transients after inflation, Phys. Rev. **D99**, 123504 (2019), arXiv:1902.06736 [astro-ph.CO].

[24] T. Hiramatsu, E. I. Sfakianakis, and M. Yamaguchi, Gravitational wave spectra from oscillon formation after inflation, (2020), arXiv:2011.12201 [hep-ph].

[25] M. Gleiser, N. Graham, and N. Stamatopoulos, Generation of Coherent Structures After Cosmic Inflation, Phys. Rev. D **83**, 096010 (2011), arXiv:1103.1911 [hep-th].

[26] E. Farhi, N. Graham, V. Khemani, R. Markov, and R. Rosales, An Oscillon in the SU(2) gauged Higgs model, Phys. Rev. D **72**, 101701 (2005), arXiv:hep-th/0505273.

[27] V. Achilleos, F. Diakonos, D. Frantzeskakis, G. Katsimiga, X. Maintas, E. Manousakis, C. Tsagkarakis, and A. Tsapalis, Oscillons and oscillating kinks in the Abelian-Higgs model, Phys. Rev. D **88**, 045015 (2013), arXiv:1306.3868 [hep-th].

[28] F. Diakonos, G. Katsimiga, X. Maintas, and C. Tsagkarakis, Symmetric solitonic excitations of the (1 + 1)-dimensional Abelian-Higgs classical vacuum, Phys. Rev. E **91**, 023202 (2015), arXiv:1404.1607 [hep-th].

[29] E. J. Copeland, P. M. Saffin, and S.-Y. Zhou, Charge-Swapping Q-balls, Phys. Rev. Lett. **113**, 231603

(2014), arXiv:1409.3232 [hep-th].

[30] Q.-X. Xie, P. M. Saffin, and S.-Y. Zhou, Charge-swapping q-balls and their lifetimes (2021), arXiv:2101.06988 [hep-th].

[31] N. Graham, An Electroweak oscillon, Phys. Rev. Lett. **98**, 101801 (2007), [Erratum: Phys.Rev.Lett. 98, 189904 (2007)], arXiv:hep-th/0610267.

[32] N. Graham, Numerical Simulation of an Electroweak Oscillon, Phys. Rev. D **76**, 085017 (2007), arXiv:0706.4125 [hep-th].

[33] H.-Y. Zhang, M. A. Amin, E. J. Copeland, P. M. Saffin, and K. D. Lozanov, Classical decay rates of oscillons, Journal of Cosmology and Astroparticle Physics **2020** (07), 055–055.

[34] M. Ibe, M. Kawasaki, W. Nakano, and E. Sonomoto, Decay of i-ball/oscillon in classical field theory, Journal of High Energy Physics **2019**, 10.1007/jhep04(2019)030 (2019).

[35] K. Mukaida, M. Takimoto, and M. Yamada, On longevity of i-ball/oscillon, Journal of High Energy Physics **2017**, 10.1007/jhep03(2017)122 (2017).

[36] J. J. M. Carrasco, R. Kallosh, A. Linde, and D. Roest, Hyperbolic geometry of cosmological attractors, Phys. Rev. **D92**, 041301 (2015), arXiv:1504.05557 [hep-th].

[37] T. Krajewski, K. Turzyński, and M. Wieczorek, On preheating in α-attractor models of inflation, Eur. Phys. J. C **79**, 654 (2019), arXiv:1801.01786 [astro-ph.CO].

[38] O. Iarygina, E. I. Sfakianakis, D.-G. Wang, and A. Achucarro, Universality and scaling in multi-field α-attractor preheating, JCAP **1906**, 027, arXiv:1810.02804 [astro-ph.CO].

[39] O. Iarygina, E. I. Sfakianakis, D.-G. Wang, and A. Achucarro, Multi-field inflation and preheating in asymmetric α-attractors, (2020), arXiv:2005.00528 [astro-ph.CO].

[40] G. Fodor, P. Forgacs, Z. Horvath, and M. Mezei, Radiation of scalar oscillons in 2 and 3 dimensions, Phys. Lett. B **674**, 319 (2009), arXiv:0903.0953 [hep-th].

[41] M. Gleiser and D. Sicilia, A General Theory of Oscillon Dynamics, Phys. Rev. D **80**, 125037 (2009), arXiv:0910.5922 [hep-th].

[42] P. Salmi and M. Hindmarsh, Radiation and Relaxation of Oscillons, Phys. Rev. D **85**, 085033 (2012), arXiv:1201.1934 [hep-th].

[43] V. E. Zakharov and S. V. Manakov, On complete integrability of the nonlinear Schrödinger equation, Teor. Mat. Fiz. **19**, 551 (1974).

[44] Z. K. Yankauskas, Radial field distributions in a self-focusing light beam, Radiophysics and Quantum Electronics **9**, 261 (1966).

[45] J. Olle, O. Pujolas, and F. Rompineve, Recipes for Oscillon Longevity, (2020), arXiv:2012.13409 [hep-ph].

[46] M. P. Hertzberg, Quantum Radiation of Oscillons, Phys. Rev. D **82**, 045022 (2010), arXiv:1003.3459 [hep-th].

[47] G. Fodor, P. Forgács, Z. Horváth, and M. Mezei, Radiation of scalar oscillons in 2 and 3 dimensions, Physics Letters B **674**, 319–324 (2009).

[48] G. Fodor, P. Forgács, Z. Horváth, and M. Mezei, Computation of the radiation amplitude of oscillons, Physical Review D **79**, 10.1103/physrevd.79.065002 (2009).

[49] M. A. Amin, Inflaton fragmentation: Emergence of pseudo-stable inflaton lumps (oscillons) after inflation (2010).

[50] N. Vakhitov and A. Kolokolov, Stationary solutions of the wave equation in a medium with nonlinearity saturation, Radiophys Quantum Electron **18**, 783 (1973).

7 Core and halo properties in multi-field wave dark matter

Core and Halo Properties in Multi-Field Wave Dark Matter

Fabio van Dissel[1], Mark P. Hertzberg[2,3,4], Jared Shapiro[2*]

[1] *Institut de Física d'Altes Energies (IFAE)*

Campus UAB, 08193 Bellaterra (Barcelona) Spain

[2] *Institute of Cosmology, Department of Physics and Astronomy*

Tufts University, Medford, MA 02155, USA

[3] *Institute of Theory and Computation, Center for Astrophysics*

Harvard University, Cambridge, MA 02138, USA

[4] *Center for Theoretical Physics, Department of Physics*

Massachusetts Institute of Technology, Cambridge, MA 02139, USA

In this work, we compute multi-field core and halo properties in wave Dark Matter models. We focus on the case where Dark Matter consists of two light (real) scalars, interacting gravitationally. As in the single-field Ultra Light Dark Matter (ULDM) case, the scalar field behaves as a coherent BEC with a definite ground state (at fixed total mass), often referred to in the literature as a gravitational soliton. We establish an efficient algorithm to find the ground and excited states of such two-field systems. We then use simulations to investigate the gravitational collapse and virialization, starting from different initial conditions, into solitons and surrounding halo. As in the single-field case, a virialized halo forms with a gravitational soliton (ground state) at the center. We find some evidence for an empirical relation between the soliton mass and energy and those of the host halo. We use this to then find a numerical relation between the properties of the two. Finally, we use this to address the issue of alleviating some of the tensions that single-field ULDM has with observational data, in particular, the issue of how a galaxy's core and radius are related. We find that if galaxies of different masses have similar percentages of the two species, then the core-radius scaling tension is not addressed. However, more general possibilities occur if the relative abundance of species in each halo correlates with the total mass of the galaxy. If this is the case, the model predicts several other phenomenological signatures.

* Email addresses: fvdissel@ifae.es; mark.hertzberg@tufts.edu; jared.shapiro@tufts.edu

CONTENTS

I. Introduction 129

II. The Schrödinger-Poisson system 130

A. The Non-Relativistic Limit of Scalar Fields 131

B. Static Solutions 133

C. Iterative Procedure 133

D. Sample Solutions 135

III. Dynamical Evolution, Virialization & Halo Formation 137

A. Numerical Experiments 137

B. Empirical Findings 140

1. The formation of the halo 140

2. The relationship between the halo and the soliton 143

IV. Cosmological Implications 146

V. Conclusions and Outlook 151

VI. Acknowledgements 154

A. Ground State Gravitational Solitons 155

B. Understanding the scaling parameter β 155

C. Relation between Soliton Properties and Halo Mass 159

References 161

I. INTRODUCTION

The nature of dark matter remains an important open question. One of the leading candidates for dark matter is a very light boson. For this candidate to make up all the dark matter in the universe, they must have a large number density in the galactic halos. In this case, the particle's occupancy number can be very large, meaning that the theory can be approximated by classical field theory. These classical fields enjoy wave-like properties, such as interference, etc.

One motivation comes from the idea of ultra-light axions, whose presence can be accommodated in fundamental physics [1]. In this case, it is plausible that the particles have a mass on the order of $m \sim 10^{-21}\,\mathrm{eV}$, or so. Then, the particle's de Broglie wavelength in a galaxy can be huge. Since typical virial velocities in galaxies are $v \sim 10^{-5} - 10^{-3}\,\mathrm{c}$, the corresponding de Broglie wavelength $\lambda_{dB} \sim h/(mv)$ can be on the order of kpc, or so. Such large de Broglie wavelengths smooth out the centers of galaxies, producing a core rather than a cusp, and can reduce small scale structure generally [2]. For many years this has been suggested as a feature, as some of the simplest simulations of dark matter show a moderately spiky feature near the center, rather than that seen in observations. Whether this so-called "core-cusp problem" is real or not remains a matter of debate. Nevertheless it has historically provided one motivation to consider the phenomenological consequences of ultra-light bosonic dark matter. Furthermore, the idea of ultra-light bosons as dark matter is interesting in its own right as it provides new wave-phenomenology, such as interference patterns, not present in standard (heavy) dark matter models.

Despite these interesting motivations, in the last few years, observational constraints on single component Ultra Light Dark Matter (ULDM) have become more and more severe [3–8]. There is therefore increasing interest in opening up more parameter space in the ULDM picture by adding more light scalars to the model [9–15]. For example, this can suppress the heating of stars near cores, suppressing the effect mentioned in Ref. [3]. Moreover, multiple light scalars is often argued as more natural from the point of view of fundamental physics (e.g., [1]).

In this work, we will pay particular attention to another apparent tension that exists between single component ULDM and observational data; there are hints from data on galaxies (e.g., see Ref. [16]) that the size of the galactic core R_c and the corresponding density ρ_c obey an approximate scaling relation $\rho_c \propto 1/R_c^\beta$, with $\beta \sim 1$ (in fact the value $\beta \approx 1.3$ is a best fit value to a set of galaxies. However, in Ref. [17] it was shown that this scaling relation is not compatible with any single-field bosonic model. In the simple Newtonian gravity dominated regime, the single-field bosonic model predicts a relation $\rho \propto 1/R_c^\beta$ with $\beta = 4$. Furthermore, Ref. [17] showed that if a

self-interacting potential V is included, there is no choice that leads to the observed scaling with stable solutions.

In Ref. [18], it was suggested that a two-field bosonic model may help the situation. Here it is explained that the space of solutions is increased, leading to a larger array of possibilities than the precise $\rho_c \propto 1/R_c^4$ prediction of the single field model in the Newtonian gravity dominated regime.

In this work, we wish to improve upon this work on multi-field models in several ways: (i) we will calculate the space of solitonic solutions more carefully, (ii) we introduce a prescription that allows one to automate the solitonic solution for multi-field models, (iii) we run simulations (albeit within a spherically symmetric restriction) to obtain scaling relations, (iv) we learn the trends of the space of solitons that naturally arise from different kinds of initial conditions, (v) we lay out the requirements in how the relative fraction of fields must occupy different galaxies in order to better explain the data, or else, to falsify the proposal.

Our paper is organized as follows: In Section II we start with the relativistic theory of two-scalar fields, and take the nonrelativistic limit, and describe the basic solitonic (static) solutions. In Section III we formulate a numerical dynamical treatment, from different choices of initial conditions, to determine which types of solitons emerge. We obtain some empirical scaling relations from these results, albeit the validity of this scaling needs to be subjected to larger scrutiny in future work. In Section IV we present possible cosmological implications of these results, through establishing a multi-field relation between the soliton's properties and the halo mass. In Section V we conclude and discuss our findings. Finally, in the Appendices, we provide more details on the phenomenology of the model.

II. THE SCHRÖDINGER-POISSON SYSTEM

We consider two scalar fields minimally coupled to gravity with action (signature -+++, units $\hbar = c = 1$):

$$S = \int d^4x\sqrt{-g}\left[\frac{\mathcal{R}}{16\pi G} + \mathcal{L}_{\mathcal{M}}\right] \tag{1}$$

Where the matter contribution to the action is provided by two massive (real) scalars

$$\mathcal{L}_{\mathcal{M}} = -\frac{1}{2}\partial_\mu\phi_1\partial^\mu\phi_1 - \frac{1}{2}\partial_\mu\phi_2\partial^\mu\phi_2 - \frac{1}{2}m_1^2\phi_1^2 - \frac{1}{2}m_2^2\phi_2^2 \tag{2}$$

Where m_1 and m_2 are the masses of ϕ_1 and ϕ_2 respectively. We can also add higher order nonlinear terms in a potential, but this is the leading-order terms for any two-scalar system. Terms proportional to higher powers of ϕ are in general also present, in particular if the scalar under consideration

is an axion-like particle, self-interactions should be present from a cosine-like potential. However, in the current work we will assume to be in a regime where we can safely neglect those terms and focus on the dynamics of the system given in Eqs. (1) and (2). Since we are concerned with Dark Matter, we can assume the typical velocities of the scalar particles to be of order $v \sim 10^{-5} - 10^{-3}c$, which is the typical velocities of particles in a galactic halo (from dwarfs to large galaxies). Therefore, we can safely move to the non-relativistic regime, in which we treat gravity in the Newtonian limit.

A. The Non-Relativistic Limit of Scalar Fields

The non-relativistic limit of the action in Eq. (1) has been extensively discussed in the literature. We present a brief derivation here. The basic procedure is to decompose each real scalar in a sum of complex degrees of freedom, after factorizing out its primary oscillations in an e^{-imt} factor, as follows

$$\phi_1 = \frac{1}{\sqrt{2m_1}}\left(\psi(\vec{x},t)e^{-im_1 t} + c.c.\right) \tag{3}$$

$$\phi_2 = \frac{1}{\sqrt{2m_2}}\left(\chi(\vec{x},t)e^{-im_2 t} + c.c.\right) \tag{4}$$

The non-relativistic limit then corresponds to assuming that the complex degrees of freedom ψ and χ are slowly varying in space and time. Relatedly, we preserve the degrees of freedom by building an action that involves only <u>one</u> derivative acting on ψ, χ, rather than the two derivatives acting on ϕ_1, ϕ_2. We are in the limit where $|\nabla\psi| \ll m_1|\psi|$ and $|\dot{\psi}| \ll m_1|\psi|$. Similarly $|\nabla\chi| \ll m_2|\chi|$ and $|\dot{\chi}| \ll m_2|\chi|$. Lastly, we assume to be in a weak field limit where $\frac{|\psi|}{\sqrt{m_1}M_{Pl}} \sim \frac{|\chi|}{\sqrt{m_1}M_{Pl}} \ll 1$ ($M_{Pl} = 1/\sqrt{G}$). In this limit, gravity becomes Newtonian, with the only relevant term in the metric being $g_{tt} = -1 - 2U$, where U is the gravitational potential. The Lagrangian density then becomes (to lowest dynamical order)

$$\begin{aligned}\mathcal{L}_{nr} \;=\; & -\frac{\nabla U \nabla U}{8\pi G} - \frac{1}{2m_1}\nabla\psi\nabla\psi^* - \frac{1}{2m_2}\nabla\chi\nabla\chi^* - U\left(m_1|\psi|^2 + m_2|\chi|^2\right) \\ & + \frac{i}{2}\left(\dot{\psi}\psi^* - \dot{\psi^*}\psi\right) + \frac{i}{2}\left(\dot{\chi}\chi^* - \dot{\chi^*}\chi\right)\end{aligned} \tag{5}$$

Interestingly, in this non-relativistic limit, there is an accidental pair of $U(1)$ global symmetries in Eq. (5) (the action is invariant under a change of the field's phase). So the system contains two conserved quantities $N_1 = \int d^3x\, n_1(\vec{x},t)$ and $N_2 = \int d^3x\, n_2(\vec{x},t)$, with corresponding number densities $n_1(\vec{x},t) = |\psi|^2$ and $n_2(\vec{x},t) = |\chi|^2$. These are just the number densities of the particles of the two respective species (the mass density is then given by $\rho_i(\vec{x}) = m_i n_i(\vec{x})$), which is conserved in the non-relativistic regime as particle number changing processes are relativistic and suppressed.

The expressions for the masses and energies in each field are

$$M_\psi = \int d^3x\, m_1|\psi|^2 \quad \text{and} \quad M_\chi = \int d^3x\, m_2|\chi|^2 \tag{6}$$

$$K_\psi = \int d^3x\, \frac{1}{2m_1}\nabla\psi\nabla\psi^* \quad \text{and} \quad K_\chi = \int d^3x\, \frac{1}{2m_2}\nabla\chi\nabla\chi^* \tag{7}$$

$$W_\psi = \int d^3x\, \frac{m_1 U}{2}|\psi|^2 \quad \text{and} \quad W_\chi = \int d^3x\, \frac{m_2 U}{2}|\chi|^2 \tag{8}$$

With M_i, K_i and W_i the mass, kinetic and gravitational energy of each field respectively. The total energy of the system is given by (neglecting the rest mass energy which always dominates in the NR-regime)

$$E_{tot} = K_\psi + K_\chi + W_\psi + W_\chi \tag{9}$$

By varying the above action, the dynamics are described by the well-known Schrödinger-Poisson system of equations

$$i\dot{\psi} = -\frac{\nabla^2}{2m_1}\psi + m_1 U\psi \tag{10}$$

$$i\dot{\chi} = -\frac{\nabla^2}{2m_2}\chi + m_2 U\chi \tag{11}$$

where the gravitational potential U is the solution to the Poisson equation

$$\nabla^2 U = 4\pi G\left(m_1|\psi|^2 + m_2|\chi|^2\right) \tag{12}$$

This set of equations will form the basis of our study, which to first order, should describe the dynamics of scalar dark matter particles on galactic scales. Since we will exploit it later, we note that there is a scale transformation that leaves this set of equations invariant. In particular,

$$\psi(\vec{x},t) \to \lambda^2\,\psi(\lambda\vec{x},\lambda^2 t) \tag{13}$$

$$\chi(\vec{x},t) \to \lambda^2\,\chi(\lambda\vec{x},\lambda^2 t) \tag{14}$$

$$U(\vec{x}) \to \lambda^2\,U(\lambda\vec{x}) \tag{15}$$

Where in Eq. (15) we suppress the dependence of U on t as the gravitational potential is itself nondynamical, and purely sourced by the presence of the scalar fields.

Eqs. (10) (11) and (12) describe the behavior of a coherent Bose-Einstein condensate, with conserved particle numbers N_1 and N_2. To understand the dynamics of the system, it is therefore quintessential to find its static solutions at fixed particle number, akin to the eigenstates of the Hamiltonian in quantum mechanics.

B. Static Solutions

The static solutions of the Schrödinger-Poisson system are those solutions whose gravitational potential remains constant over time. Therefore the time-dependence of the scalar has to be a pure space-independent phase. In particular, one can look for solutions of the form

$$\psi(\vec{x},t) = \left(\frac{\sqrt{m_1}M_{Pl}}{\sqrt{4\pi}}\right)\Psi(r)e^{-i\gamma m_1 t} \tag{16}$$

$$\chi(\vec{x},t) = \left(\frac{\sqrt{m_1}M_{Pl}}{\sqrt{4\pi}}\right)\Phi(r)e^{-i\kappa m_2 t} \tag{17}$$

Where γ and κ are chemical potentials for each of the species. We limit our search to spherical solutions, as those are the ones that generally will minimize the energy of the configuration. We can take the radial profiles, Ψ and Φ, to be real functions without loss of generality.

The problem is thus reduced to solving the eigenvalue problem characterized by the following set of equations, where we introduced dimensionless variables through $\tilde{x}_\mu = m_1 x_\mu$

$$\nabla^2\Psi = 2\left(U-\gamma\right)\Psi \tag{18}$$

$$\nabla^2\Phi = 2\left(\frac{m_2}{m_1}\right)^2\left(U-\kappa\right)\Phi \tag{19}$$

with the gravitational Poisson equation

$$\nabla^2 U = \left(\Psi^2 + \frac{m_2}{m_1}\Phi^2\right) \tag{20}$$

where in spherical symmetry the Laplacian is

$$\nabla^2 = \partial_r^2 + \frac{2}{r}\partial_r \tag{21}$$

We are looking for localized solutions of the above set of equations. We first fix the central amplitude of the fields to $\Psi(0) = \Psi_0$ and $\Phi(0) = \Phi_0$. Next, imposing the regularity conditions $\partial_r\Psi(0) = \partial_r\Phi(0) = \partial_r U(0) = 0$, the system can effectively be solved through a two-parameter shooting method. The ground state solutions are those in which the fields have no nodes, and monotonically approach zero at large r.

C. Iterative Procedure

In the single field case, there is only one chemical potential and the shooting method is rather straightforward (work on the single field case includes Refs. [19–22]). However, we found that it's

difficult to find the localized solution, while shooting the two parameters γ and κ simultaneously. We thus employ an iterative method which we found to converge efficiently. First, we split the gravitational potential into two parts, $U(r) = U_\Psi(r) + U_\Phi(r)$, where

$$\nabla^2 U_\Psi = \Psi^2 \tag{22}$$

$$\nabla^2 U_\Phi = \frac{m_2}{m_1}\Phi^2 \tag{23}$$

The iterative method can then be summarized as

1. Initially, set $U_\Phi = 0$ and find the localized solution of the system

$$\nabla^2 \Psi = 2\left(U_\Psi + U_\Phi - \gamma\right)\Psi \tag{24}$$

$$\nabla^2 U_\Psi = \Psi^2 \tag{25}$$

   (even though in this very first step $U_\Phi = 0$, we formally include it in the first equation here, as this will be important when we repeat the procedure, which will involve a nonzero U_Φ). This system can be solved straightforwardly using shooting methods familiar from the single field case as it involves only one parameter γ.

2. Updating the solution of U_Ψ obtained from step 1, find the localized solution of the system

$$\nabla^2 \Phi = 2\left(\frac{m_2}{m_1}\right)^2\left(U_\Psi + U_\Phi - \kappa\right)\Phi \tag{26}$$

$$\nabla^2 U_\Phi = \frac{m_2}{m_1}\Phi^2 \tag{27}$$

   Again, there is no difficulty in finding the localized solutions of this system as it involves only one parameter κ.

3. Iterate through steps 1 and 2, making sure to update the gravitational potentials at each step until convergence of the solutions is reached. We define convergence by the two eigenvalues γ and κ. In practice, we see that these two parameters don't change after a certain number of iterations after which we stop the procedure.

In practice, we find that this method converges after $\mathcal{O}(10)$ iterations. Note that this method can straightforwardly be extended to include non-gravitational interactions between the scalars, such as quartic interactions. However, for realistic models, such interactions are normally negligible, and in any case, is beyond the scope of the current work.

At fixed central density Ψ_0 and Φ_0, there are an enumerable infinite amount of solutions labeled by n_1 and n_2, indicating the number of nodes in Ψ and Φ respectively. To find any particular solution we have to solve for Ψ and Φ with the appropriate number of nodes through each iteration. In the remainder of this work, we will focus on the ground state (no nodes) configurations with $n_1 = n_2 = 0$, as it is expected that those are the gravitational solitons that form at the center of galaxies. We are thus able to find the static ground state solutions of the Schrödinger-Poisson system of equations at fixed central densities Ψ_0, Φ_0.

The scaling relations of Eqs. (13), (14) and (15) then allow us to find any solution that has the same ratio of central densities $f = \dfrac{\Phi_0}{\Psi_0}$, as this ratio is conserved through the transformation. Therefore, it is only necessary to find the ground state soliton once for each ratio of central densities, noting also that if the ratio is extreme, the ground state effectively becomes the single-field soliton. The properties of the different solutions are related to each other via

$$M_{\Psi,f,\lambda} = \lambda M_{\Psi,f,0} \quad \text{and} \quad M_{\Phi,f,\lambda} = \lambda M_{\Phi,f,0} \tag{28}$$

$$K_{\Psi,f,\lambda} = \lambda^3 K_{\Psi,f,0} \quad \text{and} \quad K_{\Phi,f,\lambda} = \lambda^3 K_{\Phi,f,0} \tag{29}$$

$$W_{\Psi,f,\lambda} = \lambda^3 W_{\Psi,f,0} \quad \text{and} \quad W_{\Phi,f,\lambda} = \lambda^3 W_{\Phi,f,0} \tag{30}$$

Where the subscript $f, 0$ corresponds to a reference value at each ratio f. In what follows we will take the reference solutions to be the solutions where $\Psi_0 = 1$ and $\Phi_0 = f$.

D. Sample Solutions

In Fig. 1 top panel and bottom panel, we show some ground state solitons with $m_2/m_1 = 1/2$ and $m_2/m_1 = 1/5$ respectively. We see that there is nontrivial behavior. In particular, the cyan curve crosses the magenta and orange curves for the second field $\Phi(r)$. We can understand this as follows: The cyan curve for Φ is so high (for small r) that it carries a large amount of mass. This means the fields are concentrated around this heavy center. However, as we lower the central value in Φ to the magenta or orange curve, the mass is reduced, the gravitational pull is reduced, and the fields are more spread out. In Fig. 2 we plot the mass density profiles for a solution with a comparable total mass in the two fields ($O(50\%)$ difference). These correspond to the magenta (top panel) and orange (bottom panel) in Fig. 1 respectively. The larger De Broglie wavelength of the light field is visible, resulting in an interesting density profile, that is initially dominated by the heavy field, and then gets dominated by the lighter field. Due to this wave effect, the lighter field can dominate the total mass of the system despite a small central density by concentrating

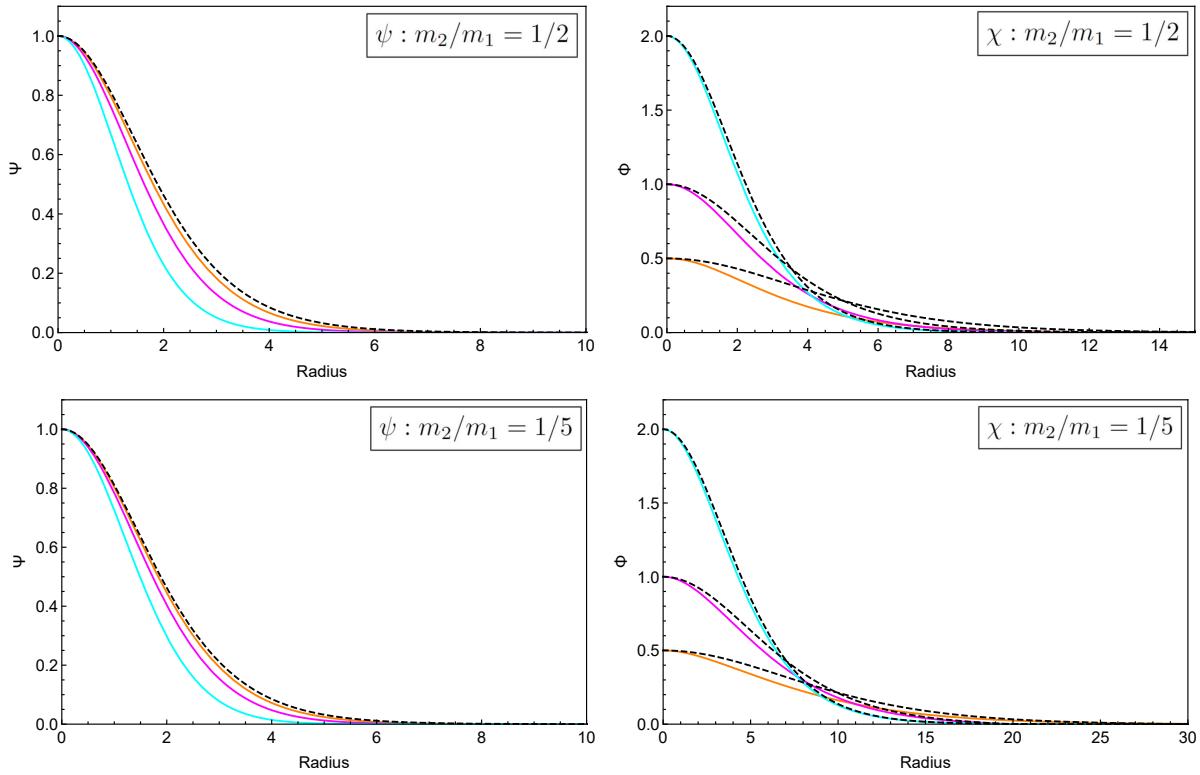

Figure 1. *Top panel:* Some ground state soliton solutions in the case where $m_2/m_1 = 1/2$. *Bottom panel:* Some ground state soliton solutions in the case where $m_2/m_1 = 1/5$. Here we plot three cases: one where the heavier field dominates the central density contribution (orange), an intermediate case (magenta), and a case where the light field dominates (cyan). The black dashed line corresponds to the single-field solution which matches best in the case where one of the two fields dominates the total mass of the solution. *Left:* The field profile of the heavy field $\Psi(r)$. *Right:* The field profile of the light field $\Phi(r)$

particles farther away from the origin. This introduces an interesting question: how does the ratio of the total mass of the solitons, hereby referred to as $F = M_\psi/M_\chi$, depend on the ratio of central field values f? We plot this information in Fig. 3 for various ratios of fundamental masses m_2/m_1. As expected, the smaller the ratio m_2/m_1, the sooner the lighter species tends to dominate the mass of the soliton. Interestingly, the dependence seems to follow an approximate power law.

Given that indeed these static solutions of the Schrödinger-Poisson system exist, we can investigate their dynamics. In particular, are the solutions that we found actually stable? Second, do they form dynamically under generic conditions? We address the first point in Appendix A, and the second will be the main concern of the next section.

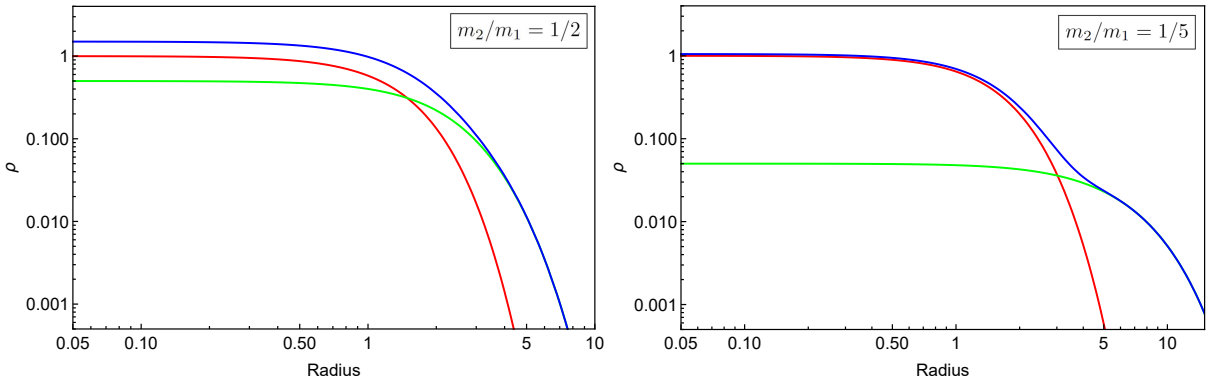

Figure 2. The mass density profile for a typical ground state soliton solution. We plot the mass density ρ for the heavy field (red), light field (green), and the total sum (blue). The nested nature of the soliton is clearly visible, where initially the heavy field dominates the total density near the center. However, due to the larger De Broglie wavelength of the lighter field, there exists a "turnover point" where the light field starts to dominate. *Left:* $m_2/m_1 = 1/2$ corresponding to the magenta profiles of Fig. 2. *Right:* $m_2/m_1 = 1/5$ corresponding to the orange profiles of Fig. 2.

III. DYNAMICAL EVOLUTION, VIRIALIZATION & HALO FORMATION

It is well known that single-field ULDM dynamically forms virialized Dark Matter halos with an approximately constant density core and an NFW-like tail. The core can be thought of as a highly populated ground state soliton, similar to those found in section II B. The ULDM halos that form in (cosmological) simulations have been argued to match observations of rotation curves better than standard CDM by suppressing small-scale structure. Some of the relevant issues are *Core vs. Cusp, Missing Satellite*, and *Too Big To Fail Problems*. It's important to check that multi-field ULDM still forms halos with these properties, as there would be no reason to consider them if they do not.

In this section, we study the dynamics of multi-field ULDM enforcing spherical symmetry, by performing simulations of the virialization of a cloud of two-field ULDM. We acknowledge the limitations of enforcing spherical symmetry. However, as we'll show, our results are highly suggestive and provide enough evidence to make cosmological extrapolations.

A. Numerical Experiments

We are interested in answering two questions concerning the multi-field Schrödinger Poisson system of equations. Firstly, is the system able to virialize from generic initial conditions, forming a cored solitonic center with an NFW tail? Then if this does indeed happen, can we identify a

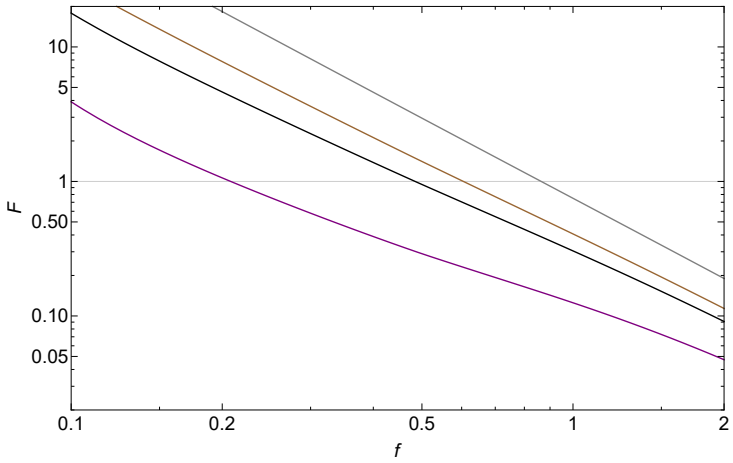

Figure 3. The dependence of the ratio of total mass in each species $F = M_\psi/M_\chi$ on the ratio of central field values $f = \Phi(0)/\Psi(0)$ for the groundstate solitons of the SP-system. We plot the curves for various mass ratios: $m_2/m_1 = 1/5$ (purple), $m_2/m_1 = 2/5$ (black), $m_2/m_1 = 1/2$ (brown) and $m_2/m_1 = 4/5$ (grey). As can be understood intuitively, the lighter field will tend to dominate the total mass sooner due to its large De Broglie wavelength. A gridline is added as a visual aid, when $F = 1$, or when both fields have the same total mass in the soliton solution.

relationship between the properties of the soliton core and the halo as a whole? In [23, 24] the relation between the core and halo masses in single-field ULDM was first discussed. It has since then been discussed in numerous works. We are interested in whether similar dependencies exist in the multi-field system.

To study these questions we perform numerical simulations of the Schrödinger Poisson system of Eqs. (10),(11) and (12) with an Runge-Kutta-4 integrator for time integration. At each time step, we solve the Poisson equation with and sixth-order accurate ODE solver. We use the following change of variables to obtain a dimensionless set of equations

$$\tilde{x}^\mu = m_1 x^\mu \quad ; \quad \tilde{\psi} = \left(\frac{\sqrt{4\pi}}{\sqrt{m_1} M_{pl}}\right)\psi \quad ; \quad \tilde{\chi} = \left(\frac{\sqrt{4\pi}}{\sqrt{m_1} M_{pl}}\right)\chi \tag{31}$$

Where tildes refer to dimensionless quantities. The SP-equations then become

$$i\dot{\tilde{\psi}} = -\frac{\nabla^2}{2}\tilde{\psi} + U\tilde{\psi} \tag{32}$$

$$i\dot{\tilde{\chi}} = -\frac{m_1\nabla^2}{2m_2}\tilde{\chi} + \frac{m_2}{m_1}U\tilde{\chi} \tag{33}$$

$$\nabla^2 U = \left(|\tilde{\psi}|^2 + \frac{m_2}{m_1}|\tilde{\chi}|^2\right) \tag{34}$$

It is also noteworthy that under this change of variables we get natural definitions of dimensionless masses and energy related to dimensionful quantities as $\tilde{M} = \left(m_1/M_{pl}^2\right) M$ and $\tilde{E} = \left(m_1/M_{pl}^2\right) E$. Eqs. (32), (33) and (34) only explicitly depends on m_1/m_2. As long as the non-relativistic description of the scalars is valid, the overall dynamics thus only depend on the ratio of fundamental masses. In what follows we drop the tilde and work with dimensionless quantities unless explicitly stated. We investigate the virialization starting from two distinct types of initial conditions.

1. Gaussian field profiles parameterized by

$$\psi(r,0) = \left(\frac{16M_\psi^2}{\pi R_\psi^6}\right)^{\frac{1}{4}} e^{-\frac{1}{2}\left(\frac{r}{R_\psi}\right)^2} \tag{35}$$

$$\chi(r,0) = \left(\frac{16m_1^2M_\chi^2}{\pi m_2^2 R_\chi^6}\right)^{\frac{1}{4}} e^{-\frac{1}{2}\left(\frac{r}{R_\chi}\right)^2} \tag{36}$$

   Where M_ψ, M_χ, R_ψ and R_χ are free parameters. Note that the phase of the complex fields is 0 everywhere initially. The fields are thus identically real at $t = 0$.

2. Random initialization of a gas of particles with specific velocity dispersion. Specifically, we initialize in Fourier space with,

$$\psi(|k|,0) = \psi_{k,re} + \psi_{k,im}i \tag{37}$$

$$\chi(|k|,0) = \chi_{k,re} + \chi_{k,im}i \tag{38}$$

   Where the different coefficients of ψ_k and χ_k are taken as Gaussian variables with variance given by $\sigma_\psi^2 = 2^{\frac{7}{2}}\pi^{\frac{5}{2}} M_\psi e^{-\frac{k^2}{2}}$ and $\sigma_\chi^2 = 2^{\frac{7}{2}}\pi^{\frac{5}{2}} \left(\frac{m_1}{m_2}\right)^4 M_\chi e^{-\frac{m_1^2k^2}{2m_2^2}}$. Once all the coefficients are determined we perform an inverse Fourier transform to obtain the initial conditions in real space. This initialization will more closely model the randomness to be expected of an overdensity of Dark Matter before collapsing. However, we noted that they generally take longer to collapse, and the Gaussian profile is still valuable in terms of computational efficiency.

For both type of initial conditions, we have another requirement on the parameters that we use to set the initial field profiles. Namely, we require the system to be bounded at the initial time; thus the total energy is smaller than 0. Finally, it is important to note that not necessarily all particles in our initial conditions will tend to collapse and produce a virialized halo. Some will tend to leave the gravitationally bounded domain towards infinity. As we only possess finite computational

power, we accommodate this by defining a physical box in which we measure properties of the halo, surrounded by an absorbing boundary layer, in which escaped particles can decay. To be explicit, we follow the procedure outlined in [25]. Having discussed our numerical setup, we now move on to our results. In sec. III B we discuss our findings from the numerical time evolution of the two-field SP-system. First, in sec. III B 1, we show that the two-field system, like its single field counterpart, generically forms a virialized halo with a groundstate solitonic core at its center. Then, in sec. III B 2 we highlight a possible relation between halo and core that allows us to find the unique soliton we expect to be present at the center of a specific galaxy, given its conserved quantities, E_h, M_ψ and M_χ.

B. Empirical Findings

The virial theorem states that $E_{kin} = \frac{1}{2}|E_{grav}|$ for a stable gravitationally bound system. In our setup, we are thus interested in configurations that obey

$$\frac{K}{|W|} = \frac{K_\psi + K_\chi}{|W_\psi + W_\chi|} = \frac{1}{2} \tag{39}$$

within our numerical domain. It is not obvious that the virial theorem applies to ULDM halos. An elegant proof of this is given in [26], which is easily generalizable to multi-field systems. In our simulations, we found that, regardless of initialization, the system virializes. We show the evolution of the virial coefficient $K/|W|$ in Fig. 4. In practice, we evolve from our initial conditions until sufficient time has passed for the system to virialize and become approximately static. We then take measurements of this "model" halo which has formed in our numerical domain.

1. The formation of the halo

Regardless of initial conditions, eventually, a regime is reached where condition (39) is obeyed. We show this for some typical initial conditions in Fig. 4. The remaining gravitationally bound structure can be seen as a model Dark Matter halo (or Boson star) supported by "Quantum" pressure. Virialization happens through a combination of gravitational collapse and the ejection of fast-moving matter to the absorbing boundary layer. In this work, we do not make statements about the precise timescales involved in these processes. However, we note that virialization proceeds more efficiently in the case where the initial conditions are "undercooled" ($k/|W| < 1/2$) as opposed to "overcooled" ($k/|W| > 1/2$). In the latter case, our setup tends to eject more matter into the absorbing layer, requiring more time. Understanding all the timescales involved in condensing into

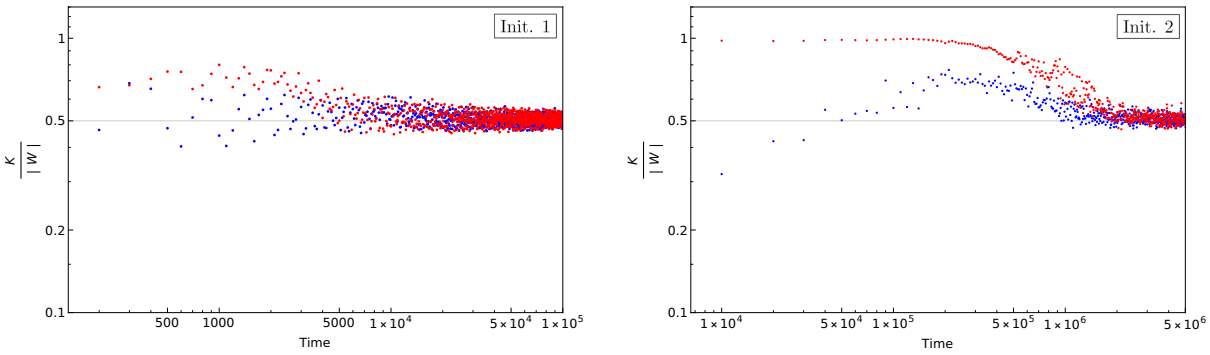

Figure 4. Typical evolution of the virial coefficient $K/|W|$ for undercooled (meaning $K/|W| < 0.5$ initially) (blue) and overcooled (meaning $K/|W| > 0.5$ initially) (red) initial conditions. Although the undercooled situation oscillates around 0.5 earlier, eventually both situations tend to virialization, in a sense carrying no memory of the initial conditions. *Left:* Initialization from a Gaussian packet following Eqs. (35) and (36). *Right:* Initialization from random initial conditions following Eqs. (37) and (38). A Gaussian initialization takes about one order of magnitude less time to form a virialized configuration and hence offers large computational benefits.

a two-field bound halo, is a very important endeavor, but beyond the scope of this work. We plan to address these questions in the future with more representative 3D simulations. In Figs. 5 and 6 we show the process of virialization for typical cases of each type of initialization highlighted in the previous section. For these simulations, we took two benchmark mass ratios of $m_2/m_1 = 1/2$ and $m_2/m_1 = 1/5$. The halo has the properties that we expect from ULDM: a centralized core with an NFW tail. Assuming that the typical velocities of the particles in the halo are the same, the lighter field has a larger De Broglie wavelength $\lambda = 1/mv$. This can be seen especially in the core where the lighter field has a broader density profile. The overall mass density can thus transition between being dominated by the more massive field to being dominated by the lighter field, potentially leading to interesting observational signatures. Lastly, note that even though virialization happens faster in the case where we initialize with a Gaussian field profile (which makes intuitive sense as the phases of the fields are already correlated over large distances initially), the virialized final products of the simulations have similar properties across different initializations, in a way "erasing" the memory of the initial conditions.

An important question remains: are the cores of these halos the gravitational solitons found in Sec. II B? To check this we take the final ratio of the density profiles of the two fields and use the algorithm of II B to solve for the corresponding ground state solitons. The results are shown in

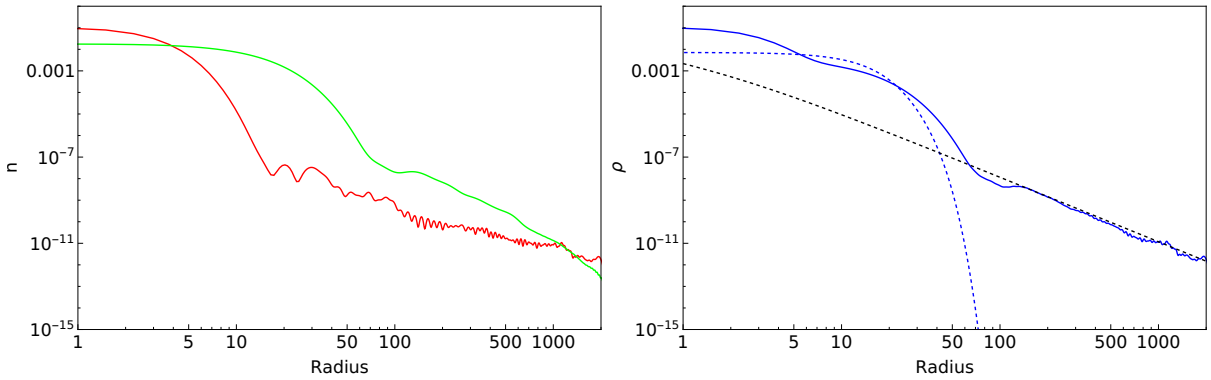

Figure 5. The (spherical) gravitational collapse of our two-field system, starting from a Gaussian packet following Eqs. (35) and (36) with $m_2/m_1 = 1/5$. *Left:* The time-averaged number density profiles of the heavy (red) and light (green) fields. We see that the fields form a cored halo with a decaying tail. The decaying tail is not exactly NFW although it clearly follows some power law. *Right:* The initial (dashed) and final time-averaged (full) mass density profiles. The tail of the full mass density profile follows NFW almost exactly (black dashed line). The nested ground state soliton is also clearly visible.

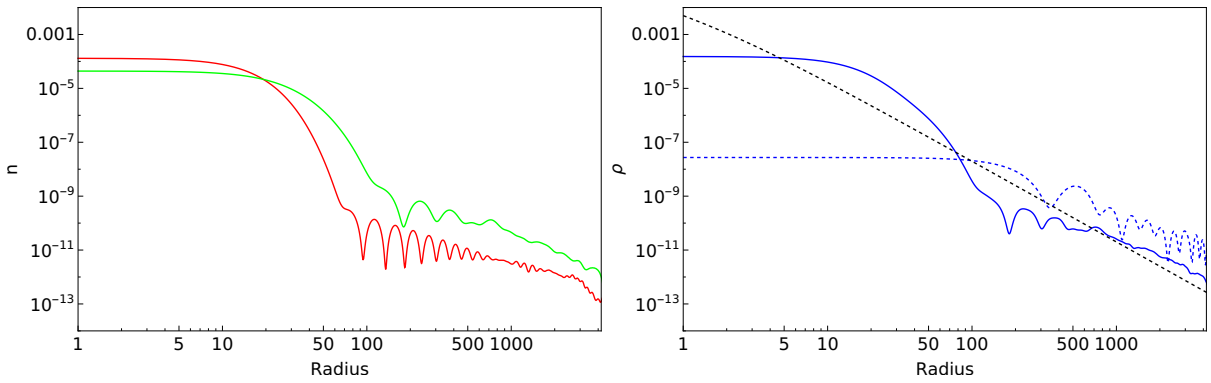

Figure 6. The same plots as in Fig. 5 with $m_2/m_1 = 1/2$ and starting from random initial conditions through Eqs. (37) and (38). The initial conditions do not seem to greatly impact the final result of the simulation: a virialized cored halo with an NFW tail. Here we can also clearly see the analogy to density granules in spherical symmetry: dips and peaks in the profile supported by pressure gradients.

Fig. 7 It seems clear that the core of the halo can indeed be interpreted as a static solution of the two-field Schrödinger-Poisson system. Although these solitons are in principle static when isolated, we observe oscillation around the true static solution of $O(10\%)$, due to interactions with the halo. This is not altogether unexpected and can be explained as a wave-interference effect as was done in [27] and [28]. We also want to note that Refs. [9, 10] reported on certain situations (depending on the relative abundance of particles and the ratio of fundamental masses m_2/m_1) where the

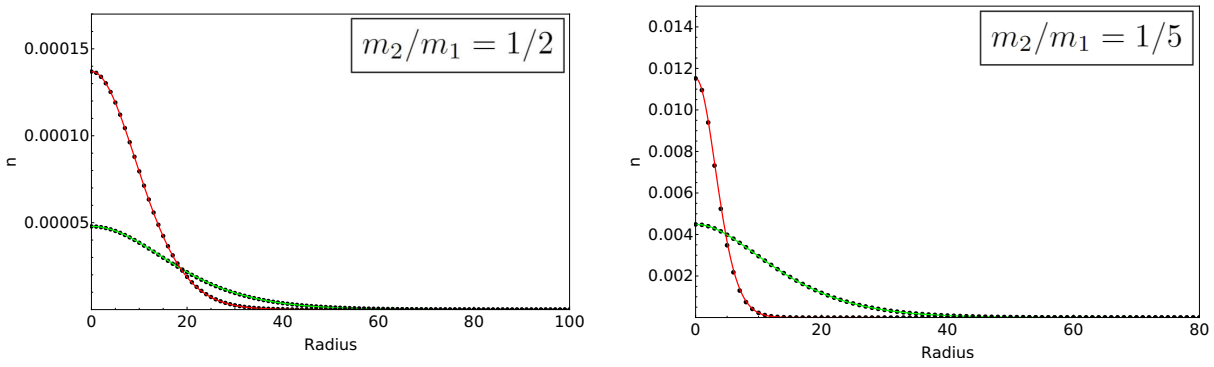

Figure 7. The number density profile of the heavy (red) and light (green) fields at the end of two of our simulations. In black dotted, we plot the corresponding two-field soliton that matches the central number density of the two fields. The core of our halo is exactly one of the gravitational solitons found earlier in this work. Although here we only show the product of two simulations, we found that a nested two-field soliton can always be found at the center of a properly virialized halo, including for different mass ratios m_2/m_1. *Left:* $m_2/m_1 = 1/2$ *Right:* $m_2/m_1 = 1/5$.

two-field soliton was not able to form due to tidal interactions between the different components during the formation of the halo. We wish to report that we did not observe this in our simulations. In particular, we always observed a two-field soliton at the center of the virialized halos that we generated. However, we acknowledge that this might in part be due to the limitations of imposing spherical symmetry on our system.

Although we now have seen that a two-field soliton forms at the center of virialized halos, we still have no way to know what particular soliton should be present in what halo (e.g. what is the ratio of central densities of the two fields). In other words, what is the thermodynamic equilibrium of the halo-soliton system. To constrain multi-field models of ULDM, this is an important question to answer. Namely, we are interested in relating the properties of the halo to the solitonic core.

2. The relationship between the halo and the soliton

In studies of structure formation of (single-field) ULDM models, an interesting relation was discovered between core mass M_c (mass contained in the region where the mass density remains 50% of the central density and the halo mass M_h. Previous work [23, 24] found the following scaling

$$M_c \propto a^{-1/2} M_h^{1/3} \tag{40}$$

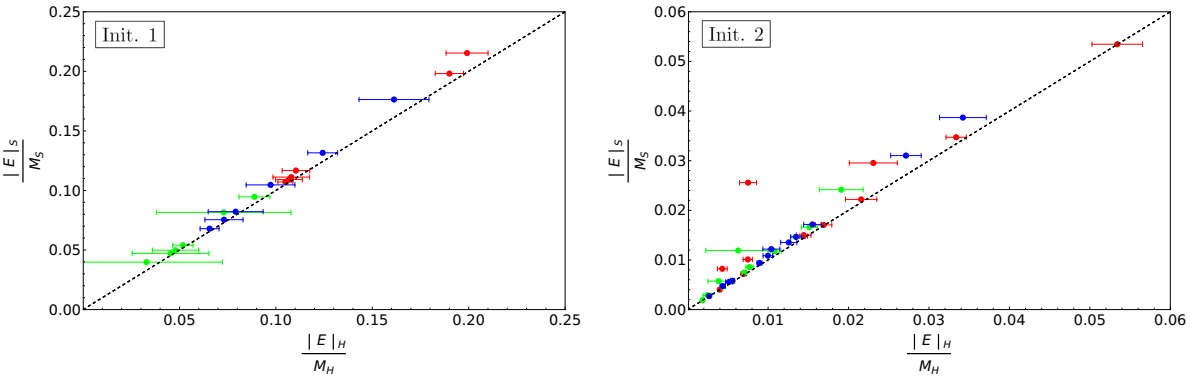

Figure 8. The energy per unit mass for the full halo obtained as the final product of our simulation (y-axis) versus the energy per unit mass for the soliton at the center (x-axis), for $m_2/m_1 = 1/2$. We plot the values for the heavy field (red), light field (green), and the full system (blue). In black dotted, we plot the line $y = x$. Although there remains large uncertainty, these results are highly suggestive. *Left:* starting from a Gaussian packet following Eqs. (35) and (36). *Right:* The same plot but for the halos obtained from random initialization following Eqs. (37) and (38).

where a is the scale factor of the Universe. This relation has been somewhat disputed in the literature [29–33], but most groups agree that some type of scaling is present, with (40) the most commonly cited one. Somehow, the wave nature of ULDM connects the properties of the central soliton to those of the enveloping halo. The question has to be asked whether a similar connection holds when considering multiple fields. In [30] it was suggested that the scaling (40) can be explained through an empirical "thermodynamic" relation that is obeyed in the halo, namely

$$\frac{|E_h|}{M_h} = \frac{|E_s|}{M_s} \tag{41}$$

The energy per unit of mass has the same value in the halo and the central soliton. Using (41) together with some considerations from collapse models of overdensities, one can arrive at (40) rather straightforwardly. However, this is in large part due to the simple scaling of the single-field solitons, and a simple scaling like (40) is not expected to exist in our two-field system.

However, we can ask if a relation like (41) still exists. In the multi-field case, there are more potential relations to be explored. In particular, we can consider the energy per unit mass in the system as a whole, but also at the level of each field individually. We checked this for the different virialized halos of our simulations by comparing the properties of the halo in the full numerical box with the ones of the soliton core. The properties of the core are taken by solving for the appropriate soliton solution, using the algorithm of Sec. II B. We plot the results in Figs. 8 and 9, separating the different types of initializations and mass ratios m_2/m_1 we have considered.

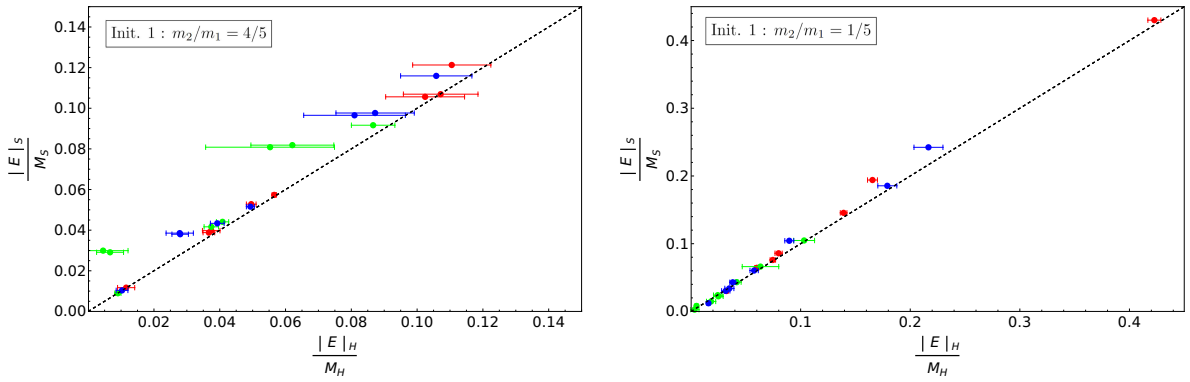

Figure 9. The same data as plotted in Fig. 8 starting from a Gaussian packet following Eqs. (35) and (36) for different mass ratios. We choose the Gaussian initialization because it tends to relax to a virialized halo faster, and thus speeds up computations. *Left:* $m_2/m_1 = 4/5$. *Right:* $m_2/m_1 = 1/5$. Qualitatively, the results agree with Fig. 8, namely that the energy per unit mass has the same value in the soliton, as it has in the halo.

Looking at Figs. 8 and 9, there seems to be fairly compelling evidence for the following three empirical relations:

$$\frac{|E_{h,tot}|}{M_{h,tot}} = \frac{|E_{s,tot}|}{M_{s,tot}}; \quad \frac{|E_{h,\psi}|}{M_{h,\psi}} = \frac{|E_{s,\psi}|}{M_{s,\psi}}; \quad \frac{|E_{h,\chi}|}{M_{h,\chi}} = \frac{|E_{s,\chi}|}{M_{s,\chi}} \tag{42}$$

Where the subscripts refer to the halo and soliton of the total system and the two fields individually. We want to place a caveat here, as we have to note that the radial simulations generally yielded halos whose masses were dominated by the central soliton. The relations in Eqs. (42) are then satisfied somewhat trivially. Checking whether these relations emerge in general is left for the future as it requires 3D simulations that go beyond the scope of this work.

Interestingly, if the relations in (42) hold generically, one is completely able to determine which solitonic core is present in which galaxy, based on the conserved quantities of the system, namely E_h, M_ψ and M_χ. There is exactly one soliton solution that can satisfy these properties and the system is neither over or under determined. Let's outline an algorithm that can solve for a particular soliton solution, starting from E_h, M_ψ and M_χ.

1. Using the algorithm of Sec. II B, we obtain a function of $|E_{s,fr,tot}|/M_{s,f,tot}$ for the soliton solutions with central densities $\Psi_0 = 1$ and $\Phi_0 = f$. Through the scaling relations of Eqs. (28), (29) and (30), we then know what the scaling parameter λ should be for each ratio of central densities in order to satisfy $|E_{h,tot}|/M_{h,tot} = |E_{s,f,tot}|/M_{s,f,tot}$.

2. Similarly, we can create functions $|E_{s,f,\psi}|/M_{s,f,\psi}$ and $|E_{s,f,\chi}|/M_{s,f,\chi}$. At each ratio of central

density, we have to satisfy

$$|E_\psi| = \lambda^2 M_\psi \frac{|E_{s,f,\psi}|}{M_{s,f,\psi}} \quad \text{and} \quad |E_\chi| = \lambda^2 M_\chi \frac{|E_{s,f,\chi}|}{M_{s,f,\chi}} \tag{43}$$

Where at each ratio we have determined λ in step 1.

3. Realising that $E_\psi + E_\chi = E_h$ and using Eq. (43) we can rewrite Eqs. (43) to obtain

$$|E_h| = \lambda^2 \left(M_\psi \frac{|E_{s,f,\psi}|}{M_{s,f,\psi}} + M_\chi \frac{|E_{s,f,\chi}|}{M_{s,f,\psi}} \right) \tag{44}$$

This equation will only be satisfied for one particular ratio of central densities (and through step 1 λ). We will then have found the appropriate soliton solution.

This type of computation allows us to know what multi-field soliton should exist in a given halo when we know its conserved quantities. We will use this in the next section to discuss the cosmological implications of two-field ULDM.

IV. COSMOLOGICAL IMPLICATIONS

The major success of the ULDM paradigm lies in its ability to suppress structure on small scales, matching observations [16] . The presence of a solitonic core at the center of collapsed halos is a strong prediction and its properties can in principle be used to obtain observational constraints. In fact, in previous work one of us argued that the properties of the single-field solitons disfavor most ULDM models [17]. Central to the argument is the relation between the core central density ρ_c and the core radius R_c (the radius at which the soliton density drops by 50%). The observational results, when fitting rotation curves with a cored density profile are given in Fig. 10. Fig. 10 suggests a scaling of $\rho_c \propto 1/R_c^\beta$, with the best fit provided by $\beta \approx 1.3$. Now the problem arises: if the cores are provided by gravitational solitons of the ULDM field, there are no single-field models that contain such a scaling. In particular, if the scalar has no self-interactions, the scaling is always $\rho_c \propto 1/R_c^4$. This can be easily seen through the transformation of Eq. (13). Interestingly, one finds more promise in the multi-field models under consideration here, as was first pointed out in [18]. As there are distinct soliton solutions at each ratio of the central density (not related through a simple scaling relation), the solitons interpolate between the two asymptotes where one of the fields dominates the mass, and we are again in the regime of $\rho_c \propto 1/R_c^4$. In this way a whole new region of parameter space becomes available. We show this schematically in Fig. 11.

We now want to see whether the two-field scenario can actually solve the issue, considering the previous sections of this work. In particular, do we expect the solitons that form, to actually have

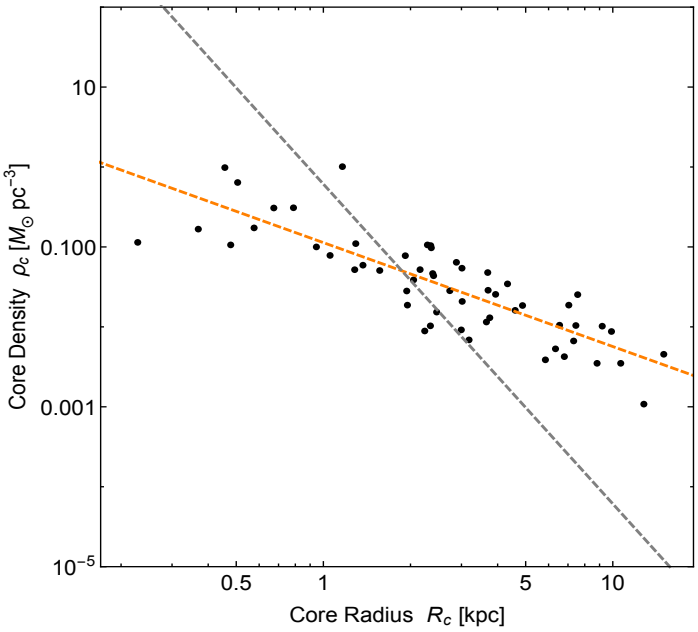

Figure 10. The best-fit parameters of the Core Density ρ_c and Core Radius R_c of 56 galaxies obtained from [34]. The data suggests a scaling of $\rho_c \propto 1/R_c^\beta$ with $\beta \approx 1.3$ (see dashed orange line). This puts a strain on all single-field ULDM models, since they predict a value of β significantly higher, namely $\beta = 4$ (see gray dashed line). This apparent contradiction was first highlighted in [17] (and this figure is reproduced from Ref. [17], plus the added gray line). As we'll see, multi-field models alter this precise theoretical prediction.

the correct scaling? We want to note that in a similar way as schematically outlined above, multi-component ULDM can "escape" other constraints that exist for single-field models. In particular in [30] a tension is highlighted, coming from rotation curve data. By opening up the parameter space of possible solitons that are present in the core, this apparent problem can also be alleviated.

To make comparisons with Cosmology we need to put back dimensions into our story. To do this we consider $m_1 = 5 \times 10^{-22}\,\text{eV}$. Different masses might be considered (and even match the data of Fig. 10 better), but won't change the overall conclusions. As first noted in [18], to accommodate all the galaxies in Fig. 10, we need at least $m_2/m_1 \approx 10^{-3}$. Since it is numerically intense to generate data about the core solitons for these values of the mass ratio, we limit ourselves to some benchmark cases. The overall, qualitative conclusions are valid for any value of the mass ratio[1].

Using the relations of Eq. (42) and the algorithm discussed at the end of Sec. III B 2 we can generate a mock galaxy data set containing the information about the soliton expected to be present at the center of the halo. To do this we need to input the conserved quantities: the total energy

[1] It is still an open question whether any two-field soliton can form realistically, which might put tension on the conclusions presented here; see [9, 10].

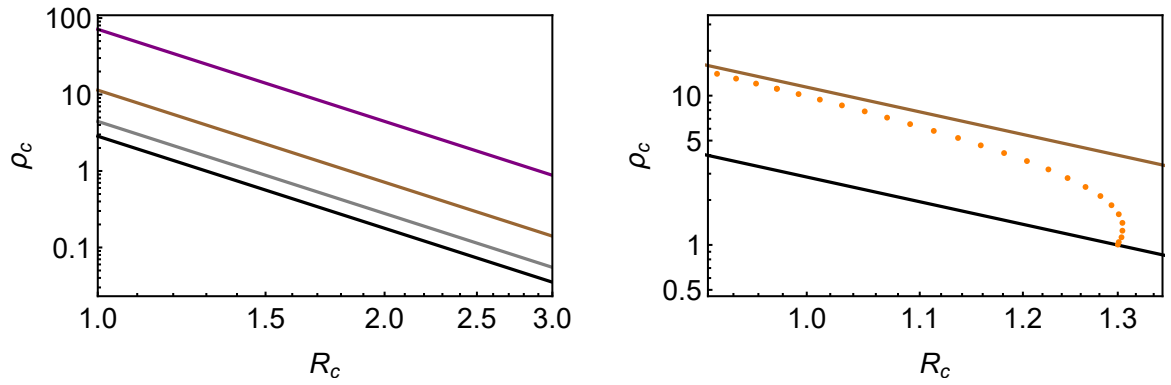

Figure 11. *Left:* The various scalings of ρ_c versus R_c for single-field gravitational solitons in terms of dimensionless variables. The single-field solitons all follow a scaling of $\rho_c \propto 1/R_c^4$. Here we plot the scalings corresponding to $m_2/m_1 = 1$ (black, the line corresponding to the heavy field), $m_2/m_1 = 4/5$ (gray), $m_2/m_1 = 1/2$ (brown) and $m_2/m_1 = 1/5$ (purple). *Right:* The full two-field gravitational soliton solutions with $m_2/m_1 = 0.5$ (orange scatter), where the ratio of central field values Φ_0/Ψ_0 is increased from 0 to ∞. The full solution interpolates between the two asymptotes thus opening up the entire region of parameter space enclosed by these lines.

$|E_h|$ and the masses of the two fields M_ψ and M_χ. We will assume that the energy of the halo is that of a non-moving overdensity of particles (so no kinetic energy), with a constant overdensity profile given by $\rho = 10^{-5}\rho_0$ where $\rho_0 = 1.8 \times 10^{-9}\,\mathrm{eV}^4$ matches the intergalactic (IGM) density of about 1 proton per cubic meter. The energy of such a cloud is then given by $E_h = -\frac{3}{5}\frac{GM^{5/3}\rho^{1/3}}{(3/4\pi)^{1/3}}$, with $M = M_\psi + M_\chi$ the total mass. To generate our set we then only need to make an assumption for the total mass in the galaxy M and the relative abundance of the two species of particles $F = M_\psi/M_\chi$. To generate a mock sample of galaxies, we choose $M = 10^k M_{MW}$, where k is taken from a uniform distribution with boundaries between $[-1, 1]$. We use $M_{MW} = 10^{12} M_\odot$, the Milky Way mass. Finally, we need to choose F. The most natural thing might be to assume that the relative abundance does not change with the galactic mass. However, it might also be interesting to investigate the possibility of F depending on M. In particular, we will look at $F \propto M$ and $F \propto 1/M$, as well as $F =$ Const. To investigate an extremely exotic scenario we also looked at $F \propto M^3$. The proportionality factor is an $O(1)$ number in all cases. We plot the expected solitons for the four scenarios in Fig. 12. In each case, we choose the value of F from a Gaussian distribution centered around its expected average value μ_F ($\mu_F = 1/4$, $\mu_F \propto M$, $\mu_F \propto 1/M$, $\mu_F \propto M^3$, respectively) with a variance of $\sigma_F = 0.25\mu_F$.

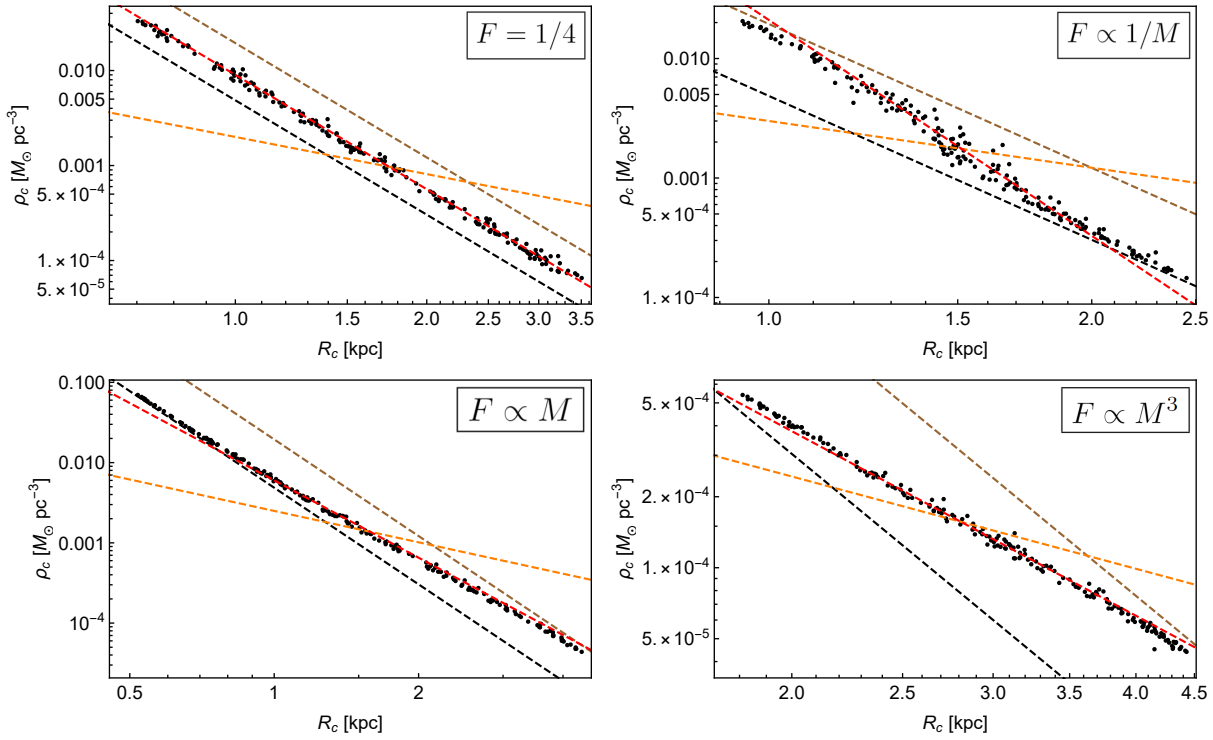

Figure 12. The properties of the solitons of our mock galaxy set as generated through the method highlighted in the text (black scatter). The properties of the single-field solitons of the heavy and light species are also shown (black and brown dotted). In each plot, we chose a different dependence for the ratio of total mass of each species F, with $F = 1/4$ (top left), $F \propto M$ (bottom left), $F \propto 1/M$ (top right) and $F \propto M^3$ (bottom right). The emperical scaling of $\rho_c \propto 1/R_c^{1.3}$ is shown as the orange dotted line. As expected, the species that dominates the mass of the galaxy also dominates the soliton properties. We can thus find solitons living in the region of parameter space between the two extremal asymptotes. The scaling of ρ_c versus R_c can then differ from the single-field story. The red dotted line gives the approximate new scaling that emerges and in particular, we have $\rho_c \propto 1/R_c^4$ (top left), $\rho_c \propto 1/R_c^{3.2}$ (bottom left), $\rho_c \propto 1/R_c^6$ (top right) and $\rho_c \propto 1/R_c^{2.6}$ (bottom right). For the case that F is positively correlated with the mass of the galaxy M, we see that the tension with Fig. 10 can be alleviated.

Inspecting Fig. 12 we see that non-trivial scalings only emerge when the ratio of masses in the galaxies is dependent on the total galaxy mass. This makes intuitive sense: if the ratio of masses is the same across every halo, one would expect that the ratio of core densities of the two fields is also the same. This is what happens in our mock data set. In this case, we are back in the scaling regime through the transformations of Eqs. (13), (14) and (15) and the soliton central density scales with $\rho_c \propto 1/R_c^4$. To reconcile the two-field model with Fig. 10 we need a non-trivial function for the mass ratio F. Allowing the halo to be dominated by different species in different limits of its total

mass, causes the soliton solution to interpolate between the two asymptotic single-field solutions. This is the source of the non-trivial scaling. Of course, we could have chosen different functions for the ratio F, which would change the exact scaling of the galaxies in the interpolating region. It is important to understand what type of scaling one actually needs to obtain $\beta = 1.3$.

It is possible to get an estimate for the scaling that emerges, given the dependence of $F \propto M^{\alpha}$ and the ratio of fundamental masses m_2/m_1. In appendix B we show how to get the following approximate formula for β

$$\beta \approx -\frac{\log(0.075^{4/3\alpha}) + \log(\left(\frac{m_2}{m_1}\right)^2)}{\log(0.075^{-1/3\alpha}) + \log(\left(\frac{m_2}{m_1}\right)^{-1})} \tag{45}$$

Which we note has quite a considerable amount of uncertainty due to the exponential sensitivity of the parameters (see appendix B). Eq. 45 has some interesting properties. Besides predicting the approximate scaling parameter β to be expected at any mass ratio m_2/m_1 and α, it also contains information about the ratio of the total mass of the heaviest and lightest galaxies. Furthermore, it also implies a correlation between the total mass of a galaxy and its core properties. These aspects are discussed in more detail in appendices B and C. Using Eq. (45) we can find the necessary α to reproduce $\beta = 1.3$ for any m_2/m_1. Using this we can create mock galaxy sets that obey the correct scaling of $\beta = 1.3$. We show this in Fig. 13. The necessary value of α is predicted by Eq. (45). Unfortunately, it is numerically difficult to check whether Eq. (45) holds for even smaller ratios of the masses m_2/m_1 but in what follows we can speculate taking into account these large uncertainties. A particularly interesting case has (as first pointed out in [18]) $m_2/m_1 = 10^{-3}$ since for $m_1 \sim 10^{-21}\,\mathrm{eV}$ and $m_2 \sim 10^{-24}\,\mathrm{eV}$ all the datapoints in Fig. 10 can be fitted by a groundstate soliton. Essentially, all the data falls in between the two extremal single-field lines. For this mass ratio, we find that $\alpha \approx -0.5$ reproduces the correct scaling. It would thus be necessary for more massive galaxies to contain a larger abundance of the lighter species of particles. It is clear, that some nontrivial scaling of $F \propto M^{\alpha}$ is needed. Interestingly, for $m_2/m_1 \sim 10^{-3}$, our model predicts that the ratio of masses of the heaviest and lightest galaxies be about $\sim O(10^2 - 10^3)$, matching good estimates of the data of the galaxies considered in Fig. 10 (also see appendix C). In the conclusions, we comment on whether scenarios, where the relative abundance of particle species varies across different galaxies, can be accommodated in viable cosmological models. A detailed study structure formation in multi-wave ULDM goes beyond the scope of this work, although we plan to address it in future studies. It is clear, however, that multi-field models do not trivially solve the scaling issue highlighted in [17]. On a more basic level the above exercise hints at other

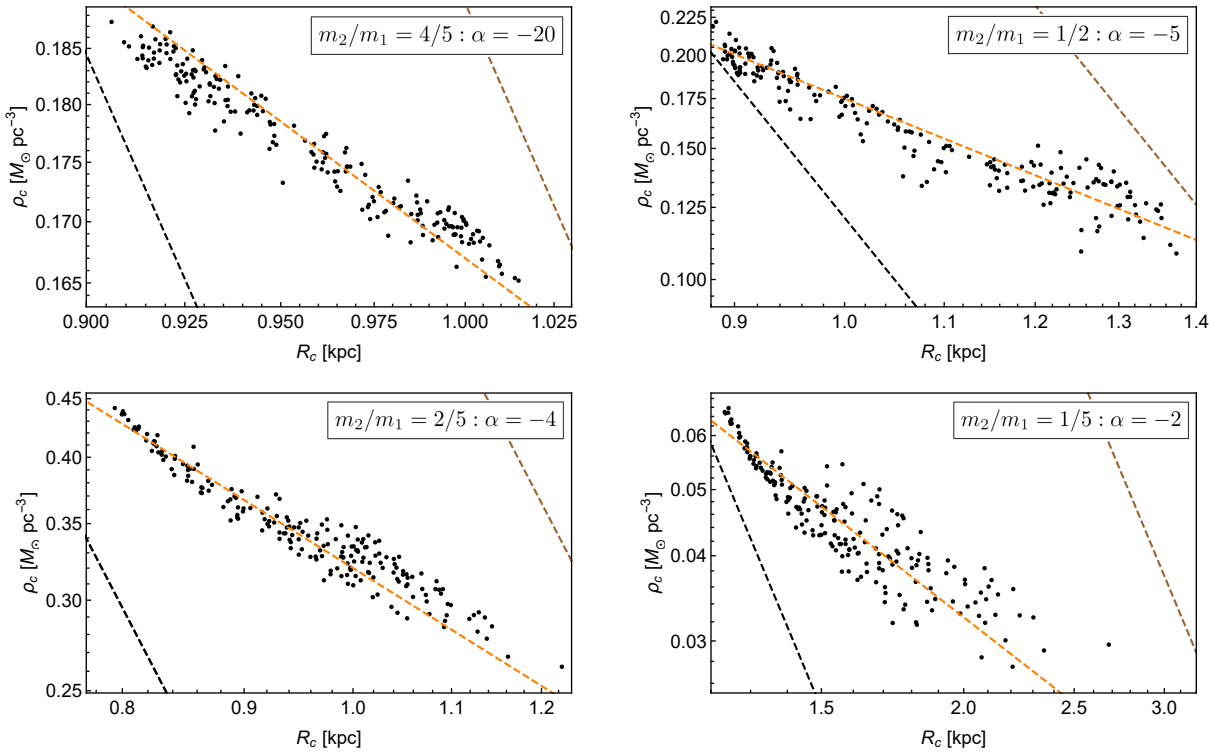

Figure 13. A similar plot as Fig. 12, but with α chosen using Eq. (45) such that the correct scaling of $\beta = 1.3$ is obtained (orange dotted line). We plot this for various m_2/m_1: 4/5 (top left), 1/2 (top right), 2/5 (bottom left), 1/5 (bottom right). The values of α as (approximately) given by Eq. (45) are -20, -5, -4 and -2 respectively.

correlations to be tested against empirical data. In particular, the value taken for the halo energy $E_h = -\frac{3}{5}\frac{GM^{5/3}\rho^{1/3}}{(3/4\pi)^{1/3}}$, common in the literature, combined with Eqs. (42) predicts the correlation between galaxy mass and central density of the core; and the correlation between galaxy mass and core radius. This is true for the multi-field models under consideration here but is equally valid when the core is comprised of just a single field. These correlations can thus be used to distinguish between the two. In appendix C we test this condition against the experimental data and highlight a tension that seems generic for ULDM models but can be alleviated by adding more fields to the picture. It is even plausible that one can consistently address both the scaling tension of Fig. 10 and this other tension. We will now summarize and conclude this work.

V. CONCLUSIONS AND OUTLOOK

In this work, we discussed many of the phenomenological features of the minimal extension of the standard Ultra Light Dark Matter paradigm with an additional light scalar. Since our results only

depend on the ratio of fundamental masses m_2/m_1 we mostly focused on a dimensionless analysis in which we wanted to paint the imprints of this model in broad strokes. We plan to perform a more comprehensive study of large scale structure formation in the future. The first order of business for any extension of ULDM is to see whether it is successful in suppressing structure on small scales since this is the motivation for the original model. Through a large number of simulations, albeit performed in spherical symmetry, we were able to confirm that this is indeed still the case for the two-field model under consideration. Starting from a variety of initial conditions, we found that virialized structures form eventually, with a centralized core matched to an NFW-like tail that extends to the edge of the halo. The core, a characteristic feature of ULDM can be identified with the groundstate soliton of the now multi-field SP-system. To confirm this we developed an iterative procedure to find eigenstates, referred to as gravitational solitons. Although we focused primarily on the lowest energy state, the method can easily be extended to find excited states, and even to other models which include (self-)interactions. Interestingly, these cores typically show a double feature in their density profile, where the heavier field dominates the soliton near the galactic center, but then gets dominated by the lighter species at some crossover point due to the larger De Broglie wavelength of the latter. To the best of our knowledge, this type of feature has not yet been explored (extensively) in the fitting of galactic rotation curves. Since this type of feature seems to be a generic prediction of multi-field wave Dark Matter, this type of exercise would be an interesting avenue for future research.

In previous work [17], it was demonstrated that single scalar field models do not fit the core-cusp data in galaxies; the problem is that although one can fit a single galaxy by the appropriate choice of particle mass m, the trend among galaxies is incorrect. In particular, the core density versus core radius relation is observed to be $\rho_c \propto 1/R_c^\beta$, with $\beta \approx 1.3$, however, the single field model predicts $\beta = 4$. Therefore it is important to consider the multi-field case, as done here. In this case, the ratio of the fundamental particle masses provides a parameter in the problem and so does the ratio of total mass in the galaxy. Relatedly, there is a much larger space of soliton solutions, compared to the single field case.

In [18] it was first hinted that the issue might be addressed in a multi-field model. However, to show this, one needs to understand which core solution is expected to be present in any particular halo. In other words, what is the thermodynamic equilibrium state of the halo-soliton system? This question is yet to be definitively answered in the single-field case and is probably even more complex in our model. In our simulations, we find good agreement with the emperical relations of Eqs. (42), which we use to develop an algorithm to predict the core solution of any halo based on its

conserved quantities. We acknowledge the uncertainties in these observed relations, in particular, due to the limits of spherically symmetric simulations. It would be interesting to see if one can understand the condensation of the halo-soliton system in the spirit of [31, 33], however many of our conclusions are independent of the exact form of the halo-soliton equilibrium as long as one believes there exists such a thing. If the relative abundance of the two species is the same for all galaxies, then the theoretical prediction of $\rho_c \propto 1/R_c^4$ remains. In this case, multi-field models do not provide an improved fit to the data. However, quite interestingly, if the relative abundances systematically change from lighter galaxies to heavier galaxies, then more general values of β can be achieved.

By parameterizing, the scaling of the relative fraction as $F \propto M^\alpha$, with α some power, we considered the more general prediction for β. There turns out to be significant dependence on the ratio of particle masses. An approximate formula for the value of β as a function of α and the particle mass ratio m_2/m_1 is given in Eq. (45). For more discussion see the Appendix. This formula suggests that the observed value of $\beta = 1.3$ is generally achieved if the value of α is negative. In other words, one consistently needs the more massive galaxies to be populated by a relatively larger abundance of the lighter species of particles. Some examples are given in Figure 13. The ratio of particle masses does need to be quite significant; at least a ratio of 1000 or more, to cover the observed spread of galaxies (this point was nicely made in Ref. [18]). For this rather large hierarchy of particle masses, our numerics currently do not have enough precision to determine α with high confidence. However, pinning down α for such a ratio of masses is a natural step for future work.

So for multi-field ULDM to have some improved fit to the data, one needs a non-trivial scaling of relative abundances among galaxies. Curiously, there is some evidence in the literature that during the formation process of a halo, the lighter species can cause tidal stripping of the heavier species [9, 10]. However, how this affects the final scaling relation of relative abundances deserves investigation. Even if the effect is small, we expect that this could already be sufficient for the most interesting mass ratios of $m_2/m_1 < 10^{-3}$, as Eq. (45) seems to suggest that for smaller mass ratios the necessary α approaches closer to 0. Exploring whether a small negative value of α can emerge dynamically is an important avenue for future research.

If indeed multi-field wave Dark Matter is the way to solve the scaling issue of Fig. 10, we can derive two other predictions that serve as consistency checks. In particular, we can get an estimate of the ratio of masses of the most massive and lightest galaxies in our dataset, which for $m_2/m_1 < 10^{-3}$ seems consistent with the dataset under consideration. Furthermore, we predict that the total mass of galaxies is positively correlated to the dilutedness of the core. In particular,

the more massive the galaxy, the larger the core is in spatial extent, and the smaller its central density. Interestingly, this is different from the prediction of single-field ULDM which through relation Eq. (40) predicts the opposite and these correlations can thus be used to distinguish the two. These aspects of the model are highlighted in appendices B and C.

Future work can involve 3-dimensional simulations, rather than the spherically symmetric simulations performed here. Furthermore, more refined simulations would be useful to definitively establish the core-halo relations that we have seen here. Another possible option is to go beyond two-fields to N-fields. While we think the two-field case is indicative of the trend for larger N, relative to the single species case, it is worth exploring in more detail. In fact, large N has a phenomenological motivation: ULDM single models lead to significant density fluctuations that can cause heating and redistribution of stars in a way that is incompatible with data [3]. However, for large N, these density fluctuations are reduced as $\sim 1/\sqrt{N}$ due to a random walk; hence the heating effects should become small. Then the core-halo and core-radius relations become critical in evaluating the ULDM proposal, as we have explored here.

To conclude, extensions of ULDM with more light degrees of freedom have many interesting phenomenological features originating from the properties of their cores. There is reason to believe that these models can resolve an issue with ULDM highlighted by one of us in [17] if there are dynamical ways in which the relative abundance of the two species can universally depend on the total halo mass. We showed that if this is the case the model makes two other phenomenological predictions, in particular about the ratio of the most massive and lightest galaxies, and the correlation between the dilutedness of the core and the halo mass. These serve both as a crosscheck and an interesting avenue for future investigation. For masses $m_2/m_1 < 10^{-3}$ all of these crosschecks agree with experimental data, although with some healthy amount of uncertainty. It is therefore clear that these models of Multi-Field ULDM warrant further research to remove some of these uncertainties.

VI. ACKNOWLEDGEMENTS

We thank Rodrigo Vicente and Demao Kong for various useful discussions. We are also thankful to Davi Rodrigues for providing the empirical data we present in Appendix C and which is first presented in Refs. [16, 34]. We aslo thank him for useful remarks on the draft of this paper. M. P. H. is supported in part by National Science Foundation grant PHY-2310572. F. D. acknowledges the support from the Departament de Recerca i Universitats from Generalitat de Catalunya to the

Grup de Recerca 00649 (Codi: 2021 SGR 00649) and funding from the ESF under the program Ayudas predoctorales of the Ministerio de Ciencia e Innovación PRE2020-094420.

Appendix A: Ground State Gravitational Solitons

It is important to check whether the method highlighted in section II B actually yields ground state solutions of the two-field SP system. In order to check this explicitly we ran simulations where the initial conditions were set to be exactly one of the zero-node solutions we found using the algorithm of Sec. II B. A proper ground state of the system should have a constant density profile for many periods of oscillations in complex fieldspace. We found that this is the case for all our zero-node solutions. To check these properties it is useful to define the following quantities

$$\frac{|\delta n_\psi(0,t)|}{n_\psi(0,0)} = \frac{|1-|\psi(0,t)|^2|}{|\psi(0,t)|^2} \quad \text{and} \quad \frac{|\delta n_\chi(0,t)|}{n_\chi(0,0)} = \frac{|1-|\chi(0,t)|^2|}{|\chi(0,t)|^2} \tag{A1}$$

$$\frac{|\delta N_{50,\psi}(t)|}{N_{50,\psi}(0)} = \frac{|1-N_{50,\psi}(t)|}{N_{50,\psi}(0)} \quad \text{and} \quad \frac{|\delta N_{50,\chi}(t)|}{N_{50,\chi}(0)} = \frac{|1-N_{50,\chi}(t)|}{N_{50,\chi}(0)} \tag{A2}$$

Where we define N_{50} as the total amount of particles in each species, within the radius that initially contains 50% of the total amount of particles of that species. In Figs. 14 and 15 we show this for two benchmark cases in which the two fields have comparable mass content and central density (in particular, the magenta ($m_2/m_1 = 1/2$) and cyan ($m_2/m_1 = 1/5$) profiles of Fig. 1).

As is expected of ground state solitons the quantities defined in Eqs. (A1) and (A2) are conserved for these solutions up to at most one part in one hundred (which is also somewhat dependent on the resolution of the simulation). This indicates that both the central densities and overall density profile of the two species stay constant. Finally, we observe that the real and imaginary parts of the two fields oscillate out of phase (with a phase-shift of $\pi/2$) as is to be expected of an eigenstate of the system. Interestingly the periods of oscillation need not be the same and can differ widely. These results for the benchmark cases, where both species have comparable total mass give us confidence in concluding that our algorithm is sufficient to find the ground state solitons of the two-field SP system.

Appendix B: Understanding the scaling parameter β

It is possible to get a good understanding of what scalings typically emerge, given the dependence of $F \propto M^\alpha$ and the ratio of fundamental masses m_2/m_1. As a starting point, one can approximate

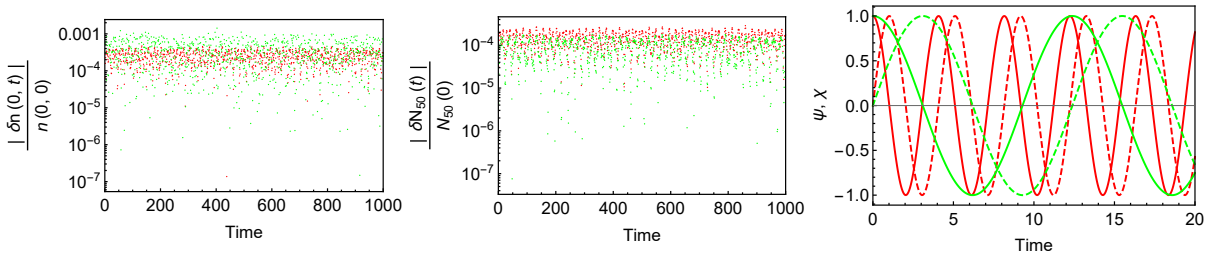

Figure 14. Some of the dynamical properties of the benchmark soliton for $m_2/m_1 = 1/2$ (the magenta profile in Fig. 1). *Left:* The relative variation of the central density as defined in (A1) for the heavy field ψ (red) and the light field χ (green). *Middle:* The relative variation of the density profile as defined through (A2) for the heavy field ψ (red) and the light field χ (green). *Right:* The real (full) and imaginary (dashed) parts of the heavy field ψ (red) and the light field χ (green) at the origin. As expected the real and imaginary parts oscillate out-of-phase with a phase shift of $\pi/2$.

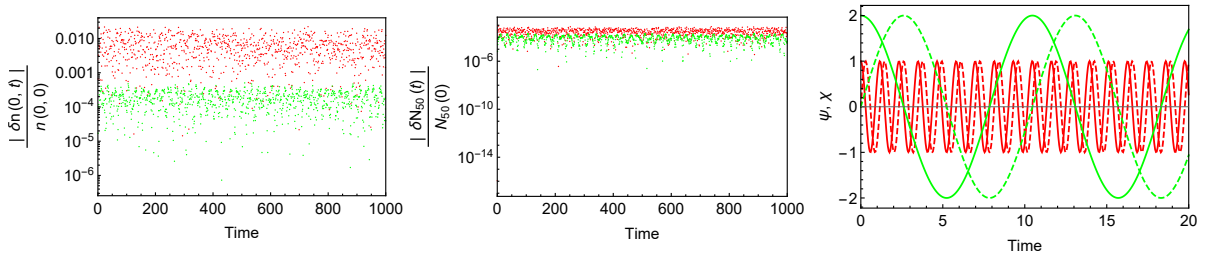

Figure 15. Some of the dynamical properties of the benchmark soliton for $m_2/m_1 = 1/5$ (the cyan profile in bottom panel of Fig. 1). *Left:* The relative variation of the central density as defined in (A1) for the heavy field ψ (red) and the light field χ (green). *Middle:* The relative variation of the density profile as defined through (A2) for the heavy field ψ (red) and the light field χ (green). *Right:* The real (full) and imaginary (dashed) parts of the heavy field ψ (red) and the light field χ (green) at the origin. As expected the real and imaginary parts oscillate out-of-phase with a phase shift of $\pi/2$.

the red dotted lines of Fig. 12 as straight lines interpolating between the two extremal single-field scalings. In the single-field limit, we can immediately find the exact core solution by solving for the effective λ in Eqs. (13) and (14), which through Eqs. (42) must have $\lambda^2 \propto |E_h|/M_h$. If the halo collapsed from a homogeneous over-density, $E_h \propto M_h^{5/3}$. Thus, finally we conclude, for $F \propto M^\alpha$, that $\lambda \propto F^{1/3\alpha}$. The scaling $\rho_c \propto R_c^\beta$ that emerges is then

$$\beta \approx \frac{\log(\rho_{c,\chi}) - \log(\rho_{c,\psi})}{\log(R_{c,\chi}) - \log(R_{c,\psi})} = \frac{\log(\left(\frac{m_2}{m_1}\right)^2 \left(\frac{\lambda_\chi}{\lambda_\psi}\right)^4)}{\log(\left(\frac{m_2}{m_1}\right)^{-1} \left(\frac{\lambda_\chi}{\lambda_\psi}\right)^{-1})} = \frac{\log(\left(\frac{m_2}{m_1}\right)^2 \left(\frac{F_\chi}{F_\psi}\right)^{4/3\alpha})}{\log(\left(\frac{m_2}{m_1}\right)^{-1} \left(\frac{F_\chi}{F_\psi}\right)^{-1/3\alpha})} \tag{B1}$$

Where the subscript ψ and χ should be understood as the values of F and λ for which the respective field completely dominates the core soliton and thus its core density and radius. More intuitively

one can understand the values of F_χ and F_ψ as follows: if $F > F_\psi$ we assume the stable equilibrium state is such, that the core (at least to the level that is observationally distinguishable) is completely dominated by the heavier ψ field. The opposite is true whenever $F < F_\chi$, when the lighter χ field determines the properties of the core. Interesting scalings thus emerge whenever $F_\chi < F < F_\psi$ as can be seen in Fig. 12 as the interpolating region in between the two asymptotes. Note that this line of reasoning holds regardless of what the actual equilibrium state of any given halo is, as long as one assumes that an equilibrium state exists and that one should have $F_\psi > F_\chi$. Although we are determining F_ψ and F_χ using the algorithm of Sec. III B 2, our results should be quite general, regardless of the validity of Eqs. (42). Inspecting Eq. (B1) we see that the exact scaling that emerges depends on m_2/m_1, α, and finally F_χ/F_ψ. Interestingly this reasoning allows us to make another prediction for the model, namely, the ratio of the most massive and lightest galaxies in the "scaling" regime is given by

$$\frac{M_{heavy}}{M_{light}} = \left(\frac{F_\chi}{F_\psi}\right)^{\frac{1}{\alpha}} \tag{B2}$$

We can then solve for $\dfrac{F_\chi}{F_\psi}$ in Eq. (B1) in terms of β and α en plug this back into Eq. (B2). Interestingly α drops out to obtain

$$\frac{M_{heavy}}{M_{light}} = \left(\frac{m_2}{m_1}\right)^{\frac{-3(\beta+2)}{4+\beta}} \tag{B3}$$

This is a crosscheck, independent of the specific halo-soliton equilibrium state, that we will come back to later since any Dark Matter model can not have this ratio be either too small or too large. Eq. B1 has two branches which asymptote to $\beta = -2$ in the limit $|\alpha| \to \infty$, independent of m_2/m_1. The two branches approach the asymptote from different directions, and it is thus possible to obtain any value of the scaling parameter β, given the right α. Although the solution for $\alpha = 0$ is not well defined, the limit of $\alpha \to 0$ gives $\beta = -4$ as expected. To solve the tension in Fig. 10 in any meaningful way it is thus necessary that the ratio of abundances of Dark Matter species scales with the total mass of the galaxy in a universal way. However, to get a general estimate for β, we need an approximation for F_χ/F_ψ, which could in general depend on m_2/m_1. Although it is very hard to predict a priori what the ratio of these quantities should be for any given m_2/m_1, we can get an idea for the trend of F_χ/F_ψ by investigating the results in Fig. 12 and analogous results for different mass ratios. In particular, we find the scaling parameter β explicitly using the method highlighted in Sec. IV at fixed $\alpha = 1$, for four different mass ratios $m_2/m_1 = 1/5, 2/5, 1/2, 4/5$. We then solve for F_χ/F_ψ in Eq. (B1). We find that the value of F_χ/F_ψ is slightly increasing as we lower the ratio of m_2/m_1. Admittedly there is quite some uncertainty in these conclusions and our results

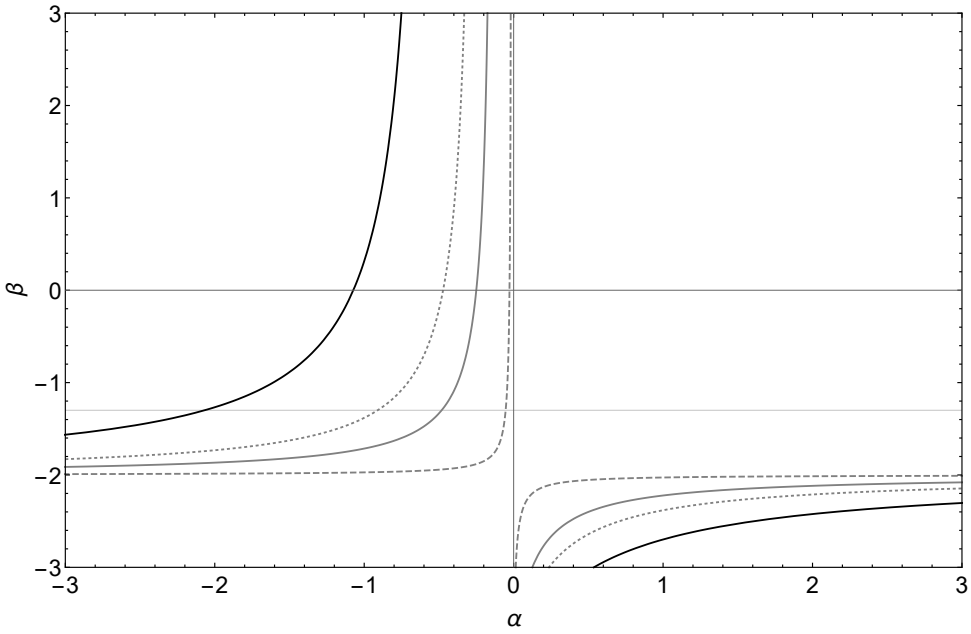

Figure 16. The expected value of β depending on α for two different mass ratios $m_2/m_1 = 1/5$ (black) and $m_2/m_1 = 1/1000$ (grey). The two branches of the solution approach $\beta = -2$ from different directions and intersect the correct value of $\beta = -1.3$ when $\alpha < 0$. Due to the uncertainty in the exact equilibrium state of the halo-soliton system for the small mass ratio $m_2/m_1 = 1/1000$, we also plot the curves for two other values of F_χ/F_ψ, increasing (dashed) and decreasing (dotted) it by a factor of 10. We see that the necessary value of α does not depend too strongly on the exact equilibrium state of the halo-soliton system.

are also consistent with $F_\chi/F_\psi \approx 0.075$ (constant) for smaller values of m_2/m_1, which is what one could expect looking at the dependency of the ratio of total mass in the solitons themselves on the central field values in Fig. 3, which seem to follow simple power laws. Also, $F_\chi/F_\psi < 1$ is required by consistency ($F_\chi > F_\psi$ would indicate that the heavier species dominates the soliton only when there is a smaller abundance of the heavier particle present, which, although intriguing, we exclude here). We thus assume $F_\chi/F_\psi = 0.075$ to obtain

$$\beta \approx \frac{\log(0.075^{4/3\alpha}) + \log(\left(\frac{m_2}{m_1}\right)^2)}{\log(0.075^{-1/3\alpha}) + \log(\left(\frac{m_2}{m_1}\right)^{-1})} \tag{B4}$$

In Fig. 16 we plot the dependence of β on α for two different ratios of m_2/m_1. The two branches of the solution are visible, intersecting the correct value of $\beta = 1.3$ for a single value of α. This value is represented as the gridline in Fig. 16. Using Eq. (B4) we can estimate the necessary α to reproduce $\beta = -1.3$ for any m_2/m_1. A particularly interesting case has (as first pointed out in [18]) $m_2/m_1 = 10^{-3}$ since for $m_1 \sim 10^{-21}\,\mathrm{eV}$ and $m_2 \sim 10^{-24}\,\mathrm{eV}$ all the datapoints in Fig. 10 can be

fitted by a groundstate soliton. Essentially, all the data falls in between the two extremal single-field lines. With our assumption that $F_\chi/F_\psi = 0.075 =$ Constant, independent of the exact value of m_2/m_1, we find that $\alpha \approx -0.5$ to reproduce the correct scaling. However, as there is quite some uncertainty in the exact value of F_χ/F_ψ, we also investigated what would be needed if we increase and decrease the assumed value of F_ψ/F_χ by a factor of 10. It turns out that the dependence of this exact value is not too strong and that α fluctuates between -1 and -0.1. The range is shown with the three gray lines in Fig. 16. Interestingly, for this ratio of m_2/m_1, the ratio of the heaviest and lightest galaxies, for $\beta = -1.3$, through Eq. (B3) is $M_{heavy}/M_{light} = 215 \sim O(10^2 - 10^3)$, conforming to the dataset under consideration (see also Appendix C). This result is independent of F_χ/F_ψ and serves as a good sanity check for the validity of the two-field model as the solution of the scaling problem. While the exact value of α needed is somewhat approximate due to the uncertainty in F_χ/F_ψ and the exact equilibrium the soliton-halo system reaches in this two-field model we obtain a clear trend of what would be needed in multi-component ULDM models to solve the tension highlighted in Fig. 10. In particular a small negative value of α.

Appendix C: Relation between Soliton Properties and Halo Mass

There is another hidden prediction in the generated datasets of Sec. IV. In particular, it relates the total mass of each galaxy to the central core properties. To zeroth-order it is simple to see how these quantities are correlated in the mock galaxy sets we generated. In particular, with the assumptions taken, the energy per unit mass of the halo is positively correlated to the halo mass: $E_h/M_h \propto M_h^{2/3}$. If we were dealing with a single-field system and the energy per unit mass in the halo were the same as in the soliton (as we're assuming here), we would immediately conclude that the mass of the soliton scales as $M_s \propto \lambda M_0 = M_h^{1/3} M_0$, as suggested in Eq. (40). At zeroth-order there then should be a positive correlation between the soliton mass and the halo mass. In the single-field limit, this translates into a positive correlation between core density and halo mass, and a negative correlation between core radius and halo mass. In the two field case these correlations (in the interpolating region in which both species are important in determining the properties of the core) depend entirely on which branch of Eq. (B1) the solution for β is found. On the $\alpha \to \infty$ branch the correlations are the same as in the single-field case. However, on the opposite branch of $\alpha \to -\infty$ the correlations are reversed. We show in Fig. 17 what the behavior is for the galaxies generated in Sec. IV, with $m_2/m_1 = 1/2$ and the correct scaling of $\beta = -1.3$ (in particular the top right graph of Fig. 13). Since here we have $\alpha < 0$ the correlation between galaxy mass and core

central density is negative, while the opposite is true for the core radius and galaxy mass. It is important to note that the opposite would indeed be the case if the solution was found for $\alpha > 0$, agreeing with the single field limit. We can compare this prediction with empirical data from [34] and [16]. Combining the two sources we obtain estimates of core properties and halo masses for 56 galaxies. The estimates are obtained by fitting rotation curves with different DM density profiles. In particular, the virial mass plotted here M_{vir} corresponds to the mass of the best-fit NFW profile integrated up to r_{200}, defined through

$$M_{NFW}(r_{200}) = 200\frac{4\pi}{3}r_{200}^3\rho_{\rm crit} \tag{C1}$$

Where $\rho_{\rm crit}$ is the critical cosmological density. We want to note that the exact definition of the virial mass impacts the implied virial mass. In general, it is not easy to find a consistent definition of the mass of a galaxy, that is exempt from systematics. In particular, using different fits for the density profiles of galaxies will lead to a different implied virial mass. For example, in other works the Burkert profile was used to fit rotation curves and derive the mass of each galaxy [35, 36], changing the results somewhat. The results are plotted in Figs. 18. Although the correlations are weak, the

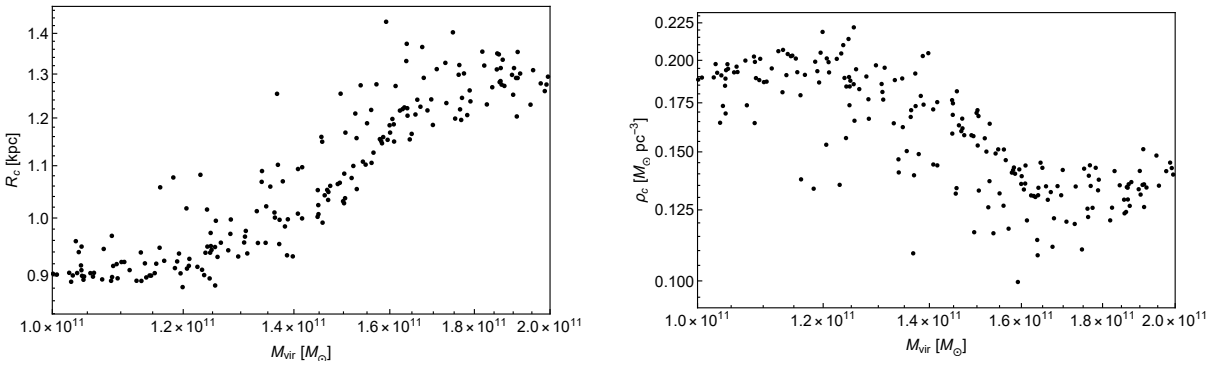

Figure 17. The core density and radius versus the total virial mass for the galaxies of in the top right corner of Fig. 13. Since here we have $\alpha < 0$ the correlation between galaxy mass and core central density is negative, while the opposite is true for the core radius and galaxy mass. This agrees with the weak correlations of Fig. 18 and we want to stress that we expect this to hold in general for two-field ULDM models if $\beta = -1.3$, since this is only possible on the $\alpha < 0$ branch of Eq. (45).

data seems to be in tension with single component ULDM models. One can alleviate this tension for $\alpha < 0$ (we defined α through $F = M_\psi/M_\chi \propto M^\alpha$, the dependence of the relative abundance of species on the total galaxy mass). In fact, one can reconcile both the tension highlighted here and that of Fig. 10, since for $\beta = -1.3$, $\alpha < 0$ necessarily. The data puts strain on the single-field models suggesting the scaling of Eq. (40), which are not able to produce these correlations (if

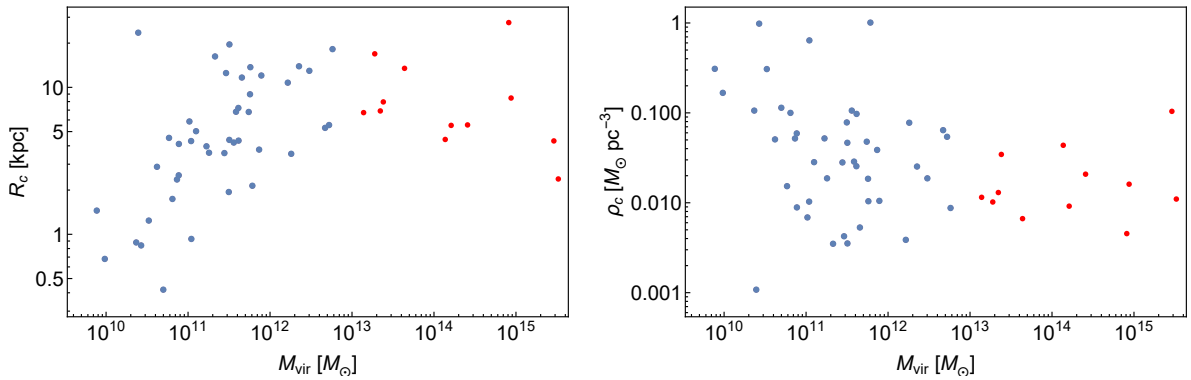

Figure 18. The core density and radius versus the total virial mass for the galaxies of Fig. 10. The data shows a hint of some possible correlation, especially if we exclude galaxies that we consider to have unphysical masses of $M_{vir} > 10^{13} M_\odot$ (which are plotted in red here). Even with this exclusion, however, the correlation is not very strong. Nonetheless, a positive correlation between the core radius and virial mass, and a negative correlation between the core density and virial mass can be seen. This contradicts the scaling of Eq. (40), but interestingly agrees with the mock galaxies of Fig. 13.

Eq. (40) holds). There is however large uncertainty in these conclusions, as the correlation in the experimental data is weak, and the definition of the virial mass is not exempt from systematics. A more comprehensive and complete analysis of the relation between the core properties and halo mass of various galaxies is an interesting avenue for future research.

---

[1] Asimina Arvanitaki, Savas Dimopoulos, Sergei Dubovsky, Nemanja Kaloper, and John March-Russell, "String axiverse," Physical Review D **81** (2010), 10.1103/physrevd.81.123530.

[2] Wayne Hu, Rennan Barkana, and Andrei Gruzinov, "Cold and fuzzy dark matter," Phys. Rev. Lett. **85**, 1158–1161 (2000), arXiv:astro-ph/0003365.

[3] Neal Dalal and Andrey Kravtsov, "Not so fuzzy: excluding fdm with sizes and stellar kinematics of ultra-faint dwarf galaxies," (2022), arXiv:2203.05750 [astro-ph.CO].

[4] Vid Irš ič, Matteo Viel, Martin G. Haehnelt, James S. Bolton, and George D. Becker, "First constraints on fuzzy dark matter from lyman-alpha forest data and hydrodynamical simulations," Physical Review Letters **119** (2017), 10.1103/physrevlett.119.031302.

[5] Eric Armengaud, Nathalie Palanque-Delabrouille, Christophe Yè che, David J. E. Marsh, and Julien Baur, "Constraining the mass of light bosonic dark matter using SDSS lyman-alpha forest," Monthly Notices of the Royal Astronomical Society **471**, 4606–4614 (2017).

[6] Hei Yin Jowett Chan, Elisa G M Ferreira, Simon May, Kohei Hayashi, and Masashi Chiba, "The diversity of core–halo structure in the fuzzy dark matter model," Monthly Notices of the Royal Astronomical

Society **511**, 943–952 (2022).

[7] Devon M Powell, Simona Vegetti, J P McKean, Simon D M White, Elisa G M Ferreira, Simon May, and Cristiana Spingola, "A lensed radio jet at milli-arcsecond resolution – II. constraints on fuzzy dark matter from an extended gravitational arc," Monthly Notices of the Royal Astronomical Society: Letters **524**, L84–L88 (2023).

[8] Mark P. Hertzberg and Abraham Loeb, "Quantum tunneling of ultralight dark matter out of satellite galaxies," JCAP **02**, 059 (2023), arXiv:2212.07386 [astro-ph.CO].

[9] Hsinhao Huang, Hsi-Yu Schive, and Tzihong Chiueh, "Cosmological simulations of two-component wave dark matter," Monthly Notices of the Royal Astronomical Society **522**, 515–534 (2023).

[10] Hoang Nhan Luu, Philip Mocz, Mark Vogelsberger, Simon May, Josh Borrow, S. H. Henry Tye, and Tom Broadhurst, "Nested solitons in two-field fuzzy dark matter," (2023), arXiv:2309.05694 [astro-ph.CO].

[11] Mateja Gosenca, Andrew Eberhardt, Yourong Wang, Benedikt Eggemeier, Emily Kendall, J. Luna Zagorac, and Richard Easther, "Multifield ultralight dark matter," Physical Review D **107** (2023), 10.1103/physrevd.107.083014.

[12] Noah Glennon, Nathan Musoke, and Chanda Prescod-Weinstein, "Simulations of multifield ultralight axionlike dark matter," Physical Review D **107** (2023), 10.1103/physrevd.107.063520.

[13] Mudit Jain, Mustafa A. Amin, Jonathan Thomas, and Wisha Wanichwecharungruang, "Kinetic relaxation and bose-star formation in multicomponent dark matter- i," (2023), arXiv:2304.01985 [astro-ph.CO].

[14] Joshua Eby, Madelyn Leembruggen, Lauren Street, Peter Suranyi, and L.C.R. Wijewardhana, "Galactic condensates composed of multiple axion species," Journal of Cosmology and Astroparticle Physics **2020**, 020–020 (2020).

[15] Mustafa A. Amin, Mudit Jain, Rohith Karur, and Philip Mocz, "Small-scale structure in vector dark matter," Journal of Cosmology and Astroparticle Physics **2022**, 014 (2022).

[16] Davi C. Rodrigues, Antonino del Popolo, Valerio Marra, and Paulo L. C. de Oliveira, "Evidence against cuspy dark matter haloes in large galaxies," Monthly Notices of the Royal Astronomical Society **470**, 2410–2426 (2017).

[17] Heling Deng, Mark P. Hertzberg, Mohammad Hossein Namjoo, and Ali Masoumi, "Can light dark matter solve the core-cusp problem?" Physical Review D **98** (2018), 10.1103/physrevd.98.023513.

[18] Huai-Ke Guo, Kuver Sinha, Chen Sun, Joshua Swaim, and Daniel Vagie, "Two-scalar bose-einstein condensates: from stars to galaxies," Journal of Cosmology and Astroparticle Physics **2021**, 028 (2021).

[19] Pierre-Henri Chavanis, "Mass-radius relation of Newtonian self-gravitating Bose-Einstein condensates with short-range interactions: I. Analytical results," Phys. Rev. D **84**, 043531 (2011), arXiv:1103.2050 [astro-ph.CO].

[20] P. H. Chavanis and L. Delfini, "Mass-radius relation of Newtonian self-gravitating Bose-Einstein condensates with short-range interactions: II. Numerical results," Phys. Rev. D **84**, 043532 (2011),

arXiv:1103.2054 [astro-ph.CO].

[21] Enrico D. Schiappacasse and Mark P. Hertzberg, "Analysis of Dark Matter Axion Clumps with Spherical Symmetry," JCAP **01**, 037 (2018), [Erratum: JCAP 03, E01 (2018)], arXiv:1710.04729 [hep-ph].

[22] Luca Visinelli, Sebastian Baum, Javier Redondo, Katherine Freese, and Frank Wilczek, "Dilute and dense axion stars," Phys. Lett. B **777**, 64–72 (2018), arXiv:1710.08910 [astro-ph.CO].

[23] Hsi-Yu Schive, Tzihong Chiueh, and Tom Broadhurst, "Cosmic structure as the quantum interference of a coherent dark wave," Nature Physics **10**, 496–499 (2014).

[24] Hsi-Yu Schive, Ming-Hsuan Liao, Tak-Pong Woo, Shing-Kwong Wong, Tzihong Chiueh, Tom Broadhurst, and W-Y. Pauchy Hwang, "Understanding the core-halo relation of quantum wave dark matter from 3d simulations," Physical Review Letters **113** (2014), 10.1103/physrevlett.113.261302.

[25] F. Siddhartha Guzmá n and L. Arturo Ureña-López, "Evolution of the schrödinger-newton system for a self-gravitating scalar field," Physical Review D **69** (2004), 10.1103/physrevd.69.124033.

[26] Lam Hui, Jeremiah P. Ostriker, Scott Tremaine, and Edward Witten, "Ultralight scalars as cosmological dark matter," Physical Review D **95** (2017), 10.1103/physrevd.95.043541.

[27] Xinyu Li, Lam Hui, and Tomer D. Yavetz, "Oscillations and random walk of the soliton core in a fuzzy dark matter halo," Physical Review D **103** (2021), 10.1103/physrevd.103.023508.

[28] Shan-Chang Lin, Hsi-Yu Schive, Shing-Kwong Wong, and Tzihong Chiueh, "Self-consistent construction of virialized wave dark matter halos," Physical Review D **97** (2018), 10.1103/physrevd.97.103523.

[29] Philip Mocz, Mark Vogelsberger, Victor H. Robles, Jesú s Zavala, Michael Boylan-Kolchin, Anastasia Fialkov, and Lars Hernquist, "Galaxy formation with BECDM – i. turbulence and relaxation of idealized haloes," Monthly Notices of the Royal Astronomical Society **471**, 4559–4570 (2017).

[30] Nitsan Bar, Diego Blas, Kfir Blum, and Sergey Sibiryakov, "Galactic rotation curves versus ultralight dark matter: Implications of the soliton-host halo relation," Physical Review D **98** (2018), 10.1103/physrevd.98.083027.

[31] D. G. Levkov, A. G. Panin, and I. I. Tkachev, "Gravitational bose-einstein condensation in the kinetic regime," Physical Review Letters **121** (2018), 10.1103/physrevlett.121.151301.

[32] A. S. Dmitriev, D. G. Levkov, A. G. Panin, and I. I. Tkachev, "Self-similar growth of bose stars," (2023), arXiv:2305.01005 [astro-ph.CO].

[33] A. S. Dmitriev, D. G. Levkov, A. G. Panin, and I. I. Tkachev, "Self-similar growth of bose stars," (2024), arXiv:2305.01005 [astro-ph.CO].

[34] Davi C. Rodrigues, Paulo L. de Oliveira, Jú lio C. Fabris, and Gianfranco Gentile, "Modified gravity models and the central cusp of dark matter haloes in galaxies," Monthly Notices of the Royal Astronomical Society **445**, 3823–3838 (2014).

[35] Pengfei Li, Federico Lelli, Stacy McGaugh, and James Schombert, "A comprehensive catalog of dark matter halo models for SPARC galaxies," The Astrophysical Journal Supplement Series **247**, 31 (2020).

[36] Davi C. Rodrigues, Alejandro Hernandez-Arboleda, and Aneta Wojnar, "Normalized additional velocity distribution: Testing the radial profile of dark matter halos and MOND," Physics of the Dark Universe

41, 101230 (2023).

8 Oscillon spectroscopy

Oscillon spectroscopy

Fabio van Dissel, Oriol Pujolàs and Evangelos I. Sfakianakis*

Institut de Física d'Altes Energies (IFAE)

The Barcelona Institute of Science and Technology (BIST)

Campus UAB, 08193 Bellaterra (Barcelona) Spain

The sine-Gordon model in 3+1 dimensions is known to admit two oscillons of different energy and frequency but comparable lifetime. We show that the oscillon spectrum includes more spherically symmetric "states". We identify new high-amplitude oscillons by allowing the field profile to have a number of nodes. For each number of nodes, we find 2 states with a comparable lifetime to the nodeless ones. Oscillons with nodes are, however, unstable to non-spherical perturbations and so their lifetime is significantly reduced. Interestingly, these states are seen to fragment into a collection of nodeless oscillons. The heavy nodeless oscillon is quite remarkable: despite its energy, it is stable against fragmentation. Moreover, it has considerably small oscillation frequency, meaning that it can be interpreted as a rather relativistic bound state.

* Email addresses: fvdissel@ifae.es; pujolas@ifae.es; esfakianakis@ifae.es

CONTENTS

I. Introduction 168

II. Quasi-breather approximation 172

A. Fundamental Oscillons 175

B. Excited Oscillons 177

III. Numerical Evolution in Spherical Symmetry 178

A. Experimental Setup 180

1. Initial Conditions and radiated power 180

2. Definition of Oscillon States and their Lifetime 183

B. Results 184

1. Fundamental Oscillon States 186

2. Excited Oscillon States 187

IV. Transitions 190

1. Adiabatic Transitions 190

2. Transitions in 3D 190

V. Conclusions 195

Acknowledgements 196

A. Multi-frequency oscillon solution 196

B. Basin of attraction 198

References 199

I. INTRODUCTION

Oscillons are fascinating objects: they are non-perturbative bound states of bosonic fields held together by self-interactions but unprotected against decay. The tension between these two factors results in oscillons being evaporating quasi-bound states with a finite (but often considerably large) lifetime. Mathematically, this translates into the existence of quasi-attractor, localized and radiative solutions of the field equations, which are long-lived. Usually, these do not admit closed form solutions. Indeed, oscillons arise quite generically in simple scalar theories, including the "sine-Gordon" (SG) model in $3+1$ dimensions, which is of relevance for axions and which will be the main focus of this work. The lifetime of oscillons is model dependent, but even in common theories like SG it reaches $\sim 10^3 m^{-1}$.

Since even in classical field theory oscillons must be constructed numerically (except in special cases, where analytic approximations are available), their "discovery" [1–5] was somewhat overlooked. More recently, they have gained substantial interest and several aspects have been further investigated, including their formation, longevity, their classical and quantum radiation as well as the model dependence of their behaviour, see e.g. [6–15] and [16] for a recent review. Oscillons have been shown to emerge naturally in scenarios ranging from preheating to bubble collisions (see e.g. [5, 17–28]), giving a gravitational wave signature [21, 23, 29, 30]. They also play a major role in dark matter [12, 31–36] and can be produced in topological defect networks [4, 37–43].

The aim of this work is to study one aspect that has received relatively little attention: models that lead to oscillons typically admit not one but several oscillons. In fact, there is a rather well defined discrete *spectrum of oscillons* of increasing energy. One might expect that these higher energy oscillons must have a short lifetime. Surprisingly enough, several of the "excited" oscillons have a lifetime comparable to the lowest-lying oscillon.

For concreteness, we shall present and study these new excited oscillons in the SG model. The potential is

$$V(\phi) = f^2 m^2 \left(1 - \cos\phi\right)$$

where ϕ is the dimensionless field rescaled by the decay constant f, m is the mass of ϕ quanta and we assume $m \ll f$. Ignoring 4π factors, f is the UV cutoff of the theory, so $m \ll f$ translates into weak coupling. Our statements should extend qualitatively to other potentials, though quantitatively important differences may arise.

Oscillons can be also understood in Quantum Field Theory as states with a high occupation

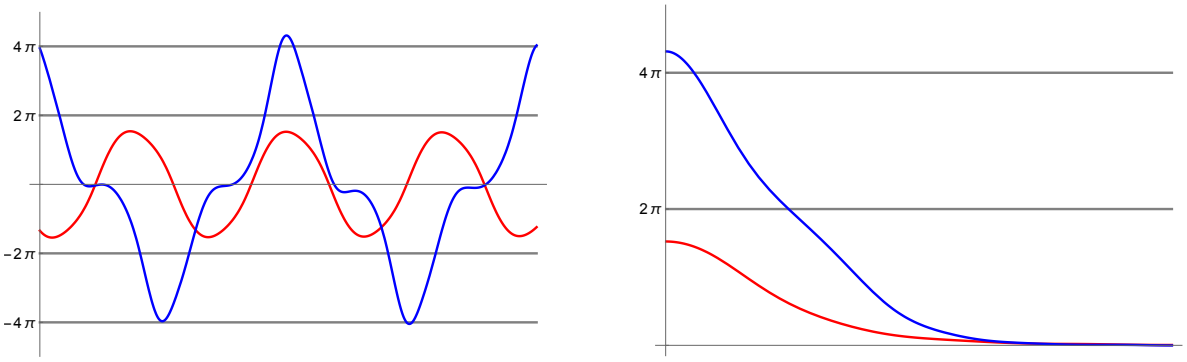

Figure 1. Left: Amplitude of the field at the origin as a function of time, $\phi(t,0)$, for the two 'fundamental' oscillons of the sine-Gordon model in $3+1$ dimensions. Right: Field amplitude as a function of the radius to the center.

number N of the same single-particle state, see [44–46] and [12]. For potentials with negative self-interaction, this state must be somehow preferred. However at weak coupling, $\lambda = m^2/f^2 \ll 1$, the energy gain is only effective for $N \sim 1/\lambda$ [44–46]. This results into a large collective coupling, whence oscillons become non-perturbative. In this large occupation number limit, the mean-field description should be applicable, meaning that these states can be captured by solving classical field equations of motion. States with $N \sim f^2/m^2$ translate into classical field configurations with sizeable excursions $\phi \sim \mathcal{O}(1)$. The total mass of these configurations scales as f^2/m, with oscillon-dependent prefactors[1]. Obtaining the oscillon spectrum thus becomes a non-perturbative problem – there is no small expansion parameter.

Most of the literature on oscillons in the SG theory in $3+1$ dimensions refers to the lowest energy attractor oscillon. In this configuration the field at the origin $\phi(t,0)$ oscillates within the first period of the potential, that is $|\phi| \lesssim 2\pi$, as shown in Fig. 1. Interestingly, the SG model is known to admit another oscillon [47, 48], where $\phi(t,0)$ oscillates in a larger range, reaching values of $\pm 4\pi$, also shown in Fig. 1. Let us emphasize a few (very) remarkable properties of the $\pm 4\pi$ attractor:

- The total rest mass is about 4 times larger than the usual one. Yet, it is very stable – as mentioned, its lifetime is comparable to the standard $\pm 2\pi$ oscillon.
- As it is obvious from Fig. 1, it contains a significant harmonic composition. The first harmonic (oscillating at 3ω) represents about 20% of the profile $\phi(t,0)$. This harmonic has high enough frequency to be a radiation mode, however it is somehow "trapped" in the oscillon core.

[1] Since they oscillate with frequency close to m and are localized in a radius of order m^{-1}, the highest gradients are typically at most $\sim fm$, well below the cutoff scale of the effective field theory, $\sim f^2$.

- This solution is quite attractive to initial conditions with high enough (and localized enough) energy.

- Depending on the initial conditions, the numerical evolution of the field equations starting near this attractor transitions adiabatically from the $\pm 4\pi$ attractor to the $\pm 2\pi$ one (thus collecting a total lifetime of more than $2000m^{-1}$).

- Most remarkably, the oscillation frequency is quite low, $\omega \simeq 0.58m$, to be compared with $\omega \simeq 0.92m$ of the "usual" oscillon. This is quite extraordinary as the standard interpretation is that the difference between the mass of the field and the frequency of the oscillon $(m - \omega)$ represent the binding energy per quantum in the solution. This is, then, a significantly relativistic bound state. Since, generally, the relativistic regime tends to make bound states significantly harder to understand, this system can provide useful insights.

These observations open up many questions: Are there more oscillons (of similar lifetimes)? Is there any solution that explores even higher amplitudes? Is the oscillon spectrum discrete? Are they stable? Are there transitions among different oscillon states, and how do they proceed?

In this work we address these questions. We construct a sequence of new excited spherically symmetric oscillons with the defining property that they contain a given number of nodes. By "node" we mean a point in the radial coordinate where the field amplitude vanishes at all times.[2] Oscillons with this kind of nodes are of course not expected to be attractors to generic initial conditions.[3]

However, the point of view of this work is to reveal the bound-state spectrum of the theory, or at least part of it. In some sense this is analogous to looking for the spectrum of resonances in QCD. Even if most of them are unstable and/or difficult to produce in practice, the spectrum of states with given properties (e.g. spherical symmetry) is certainly well posed.

The spectrum of oscillon solutions that we find is shown in Fig. 2, where we see that they span a large range in central amplitude and total energy (rest mass). We do not go beyond states with 3 nodes, but in principle the sequence continues, perhaps indefinitely. Each point corresponds to a different oscillon that keeps the number of nodes for a significant time, which we demand to be comparable to the lifetime of the lowest lying oscillon. Table I summarizes the basic properties of these states. The error bars indicate the range in amplitude ϕ_0 and frequency ω that is explored by each oscillon during its lifetime.

[2] Our notion of "node" and of "excited oscillon" thus differs from previous works, in particular from Ref. [49]. Oscillons with nodes were also discussed in Ref. [22], albeit in the small amplitude limit.

[3] Oscillons with nodes can be attractors to initial conditions with nodes, as shown in appendix B.

Quite interestingly, we find that i) the spectrum of oscillons is discrete; ii) the central field value ϕ_0 takes on specific values, which are close to multiples of 2π; iii) oscillons with large amplitude $\phi_0 \gtrsim 4\pi$ exist, at the expense of introducing nodes; iv) there are more examples of very relativistic oscillons (with ω significantly below m).

The spectrum shown in Fig. 2 is obtained using a combination of analytic and numerical methods. Introducing a single frequency ansatz, we reduce the equation of motion to an effective one-dimensional problem. This provides a guess which is used as the initial condition for simulating an oscillon with nodes but which does not correspond to the actual oscillon profile. The field then quickly relaxes to an excited oscillon with nodes and high harmonic content, meaning that these "guess" initial conditions fall inside the basin of attraction of these oscillons.

Two remarks are in order. First, it is clear that the sine-Gordon model has a larger class of spherically symmetric solutions, in the form of spherical domain walls (kinks) with an initial radius $R_0 \gg 1/m$. With perfect spherical symmetry, after a time of order R_0 they reach small sizes and bounce back emitting radiation and re-bounce a number of times [50]. In a way, then, these solutions are similar to oscillons. (In fact, some of them end up trapped in oscillons) Of course, there is a continuum of solutions of this form and their lifetime is large, but we discard them as we are interested in states with well defined properties (number of nodes, radius, etc) staying constant or at most changing adiabatically throughout the lifetime.

Second, the spectrum in Fig. 2 is selected by imposing both a long lifetime and spherical symmetry. Relaxing the symmetry can of course impact on the actual lifetime of these states – as it clearly also affects the spectrum. (With less symmetry, multi-oscillon solutions could exist.) In Section V we study how allowing for aspherical modes affects these states. As it turns out, the lifetimes of oscillons with nodes are affected, but the heavy nodeless one is not. Quite remarkably, we see the breakup of an "excited" oscillon to a (large) collection of nodeless ones.

The current work is organized as follows. In Section II we describe the model and provide analytical constructions for oscillons, using both as single-frequency ansatz as well as considering contribution from higher harmoncis. We provide oscillon solutions with up to 3 nodes and examine their properties. Section III contains an extensive set of numerical simulations, where the evolution of oscillons is computed in the spherical ansatz. In Section IV we discuss possible transitions between oscillon states and show three-dimensional simulations. We conclude and provide suggestions for future work in Section V.

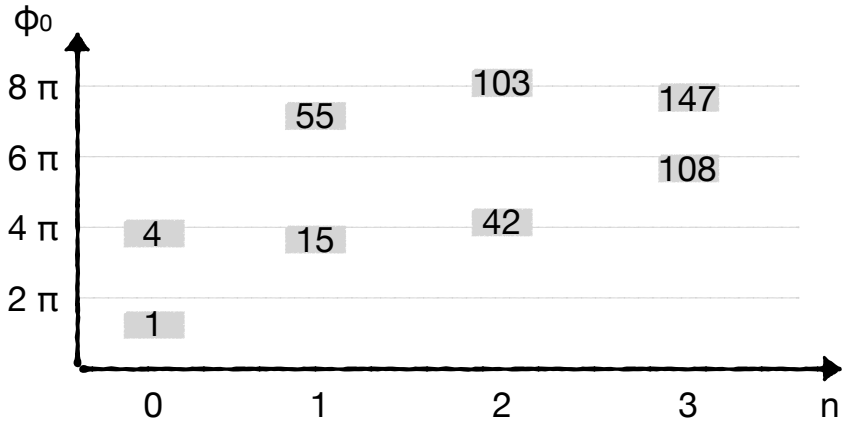

Figure 2. The spectrum of long-lived spherically symmetric oscillon configurations. The horizontal axis corresponds to the number of nodes and the vertical axis shows the maximum field excursion at the center of the oscillon. We stopped our exploration at oscillons with three nodes. The number in each box in the above plot shows the mass of each oscillon, with respect to the mass of the lowest-mass oscillon state, which is $\simeq 400 f^2/m$.

II. QUASI-BREATHER APPROXIMATION

The action we use is

$$\Phi = f^2 \int d^3x\, dt \, \left[\frac{1}{2}\partial_\mu\phi\partial^\mu\phi - m^2(1-\cos\phi)\right] , \tag{1}$$

where we have pulled out an overall factor given by the decay constant f so that the field ϕ is dimensionless. Finding the spherically symmetric oscillons in this theory reduces then to looking for the configurations $\phi(r,t)$ that solve the equation of motion

$$\frac{\partial^2\phi}{\partial t^2} - \frac{\partial^2\phi}{\partial r^2} - \frac{2}{r}\frac{\partial\phi}{\partial r} + m^2\,\sin\phi = 0 \ , \tag{2}$$

with outgoing radiation boundary conditions.

The construction of oscillons starts by treating them as "quasi-breather", a periodic localized configuration, and optimizing the radial profile and the frequency to identify slowly radiating configurations. One starts with a single-frequency ansatz

$$\phi(r,t) = \Phi(r)\sin(\omega t) \tag{3}$$

with $\omega < m$ for the oscillon solution to exist. By inserting this ansatz into the action and integrating

over time over a period $2\pi/\omega$, we arrive at the effective action

$$S_{\text{eff}} = f^2 \int d^3x \left\{ \frac{1}{4}\omega^2\Phi^2 + \frac{1}{4}[\nabla\Phi]^2 - [1 - J_0(\Phi)] \right\} \tag{4}$$

which in turn leads to the equation of motion for the amplitude $\Phi(r)$

$$\frac{d^2\Phi}{dr^2} + \frac{2}{r}\frac{d\Phi}{dr} + \omega^2\Phi - 2J_1(\Phi) = 0 \ , \tag{5}$$

where J_n are Bessel functions of the first kind. The solution $\Phi(r)$ needs to be regular (zero derivative) at the origin and vanish at spatial infinity. This equation of motion has an intuitive mechanical analogue; that of a point particle moving in a one-dimensional potential well with potential $U_{\text{eff}} = \frac{1}{4}\omega^2\Phi^2 - [1 - J_0(\Phi)]$. In this analogy r is the time coordinate and the term $-\frac{2}{r}\dot{\phi}$ describes friction. The boundary conditions for finding oscillon solutions are equivalent to a ball starting at some large value $\Phi(r = 0)$ and rolling towards the origin, reaching it in infinite "time" $r \to \infty$. Fig. 3 shows the effective potential for different values of the oscillon frequency ω.

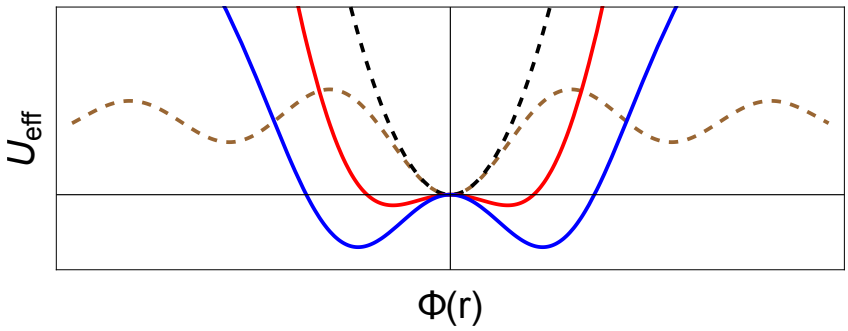

Figure 3. The effective potential for the single-frequency ansatz for $\omega = 0.5, 0.8$ (blue and red respectively). The dashed lines correspond to $\frac{1}{4}\Phi^2$ (black) and $1 - J_0(\Phi(r))$ (brown).

The simple numerical procedure for finding oscillon solutions includes choosing a frequency $\omega < 1$ and searching for the proper value of $\Phi(r) = 0$ that leads to $d_r\Phi(r \to \infty) = 0$, corresponding to a solution where the point particle is released at rest from some amplitude and asymptotically reaches the origin.

This of course neglects the case of the ball overshooting the point at the origin and probing negative values of Φ, later to return and reach the origin in infinite time from the left. Each time the ball overshoots the local maximum at the origin, the corresponding oscillon solution acquires a node. This construction leads to a two-parameter family of solutions, which is continuous in $\omega < 1$ and discrete in the number of nodes, ranging from 0 to infinity (in principle).

Since the above construction (and any oscillon) does not lead to exact solutions of the equation of motion of the full system, oscillons in general will also have a radiating tail at higher harmonics. By introducing only the third harmonic[4], the ansatz becomes

$$\phi(r,t) = \Phi(r)\sin(\omega t) + \Phi_3(r)\sin(3\omega t)\ . \tag{6}$$

Assuming $\Phi_3 \ll \Phi$, it is straightforward to see whether there are special points in solution space, where the third harmonic is non-radiating. All we need to do is solve the equation

$$\frac{d^2\Phi_3(r)}{dr^2} + \frac{2}{r}\frac{d\Phi_3(r)}{dr} + (3\omega)^2\Phi_3(r) - J_0(\Phi(r))\Phi_3(r) = 2J_3(\Phi(r)) \tag{7}$$

where the emergence of Bessel functions of different order is described in Appendix A. The inhomogeneous solution to the above equation can be found through the Greens's function method

$$\Phi_3(r) = \int_0^r \mathcal{G}(r,r')2J_3(\Phi(r'))dr' \tag{8}$$

The condition for a localized third harmonic solution is simply the vanishing of the above integral for $r \to \infty$. This is also derived in Ref. [51] using arguments based on destructive interference.

When the amplitude of the main harmonic $\Phi(r)$ grows larger, so do in general the corresponding higher harmonics. This means that after some point, the linear approximation of Eq. (7) fails to capture the dynamics of the system, since the third harmonic will be large enough to back-react onto the first harmonic. Ref. [51] proposed a quasi-breather construction that allows one to include the contribution of higher harmonics, taking their mutual interactions into account. In this formalism, the oscillon is described (taking only the first and third harmonics into account) as $\phi \simeq \Phi_1\sin(\omega t) + \Phi_3\sin(3\omega t) + c_3\cos(3\omega t)$, where the term c_3 is added in order to allow for outgoing radiation at $r \to \infty$, which wouldn't be possible with an expansion solely in terms of sines or cosines. The equations that one needs to solve are

$$\frac{d^2\Phi_1}{dr^2} + \frac{2}{r}\frac{d\Phi_1}{dr} + \omega^2\Phi_1 + f\left(\Phi_1,\Phi_3\right) = 0 \tag{9}$$

$$\frac{d^2\Phi_3}{dr^2} + \frac{2}{r}\frac{d\Phi_3}{dr} + 9\omega^2\Phi_3 + g\left(\Phi_1,\Phi_3\right) = 0 \tag{10}$$

$$\frac{d^2c_1}{dr^2} + \frac{2}{r}\frac{dc_3}{dr} + 9\omega^2c_1 + h\left(\Phi_1,\Phi_3\right)c_3 = 0 \tag{11}$$

where f, g, h are functions of Φ_1 and Φ_3 and we assumed that c_3 can still be treated in the linearized approximation. The derivation and exact form of these equations is given in Appendix A.

[4] We refer to the mode oscillating at the fundamental frequency ω as the first or fundamental harmonic. For notational clarity, we must stress the difference between the terminology "fundamental oscillon", having no nodes as shown in Fig. 2 and the fundamental frequency / harmonic, which we define here.

A. Fundamental Oscillons

We start by constructing and studying the "fundamental" oscillon solutions, which in this context means oscillons without nodes in their spatial profile. Fig. 4 shows the two long-lived oscillon states that emerge for $\omega/m \simeq 0.56, 0.92$ (left and right panels), along with a "random" solution at $\omega = 0.7$. It is clear that the solution shown in the middle panel has a much larger radiating tail, leading to a faster loss of energy. This drives the oscillon towards the long-lived solution at $\omega \simeq 0.92$.

Fig. 4 contains interesting information about the structure of the fundamental oscillons in the three dimensional sine-Gordon equation. We first notice the long-distance behavior: The first harmonic is exponentially decaying, while the third and fifth ones are oscillating, both in the sine and in the cosine. However, the two terms in each harmonic have a constant shift of $\pi/2$, leading to a traveling wave towards infinity. Thus this regime represents the radiation emanating from the oscillon.

We see that for the longer lived oscillons ($\omega/m = 0.56, 0.92$) the radiation tail is about one order of magnitude smaller than a "random" solution with $\omega/m = 0.7$. Furthermore, for the oscillon with $\omega/m = 0.56$, the radiation of the third harmonic is several orders of magnitude suppressed and the decay is controlled by the fifth harmonic. For the case of $\omega/m = 0.92$ the opposite occurs and the fifth harmonic is vastly subdominant.

From the sequence of panels in Fig. 4 we see how the third harmonic evolves as a function of the frequency and the oscillon height. The height of the first harmonic becomes larger for smaller frequencies and this leads to a more significant excitation of the third harmonic. For $\omega = 0.56$ the third harmonic is non-perturbatively large close to the oscillon core. In this range of frequencies, the third harmonic is largely confined, as is evident from the significant difference between the sine and cosine terms near the core as well as from the difference between the value of the third harmonic near and far from the core of the oscillon. Contrary to that, the fifth harmonic is always perturbative (much smaller than the first harmonic). Furthermore, the structure of the three first harmonics elucidates the difference between near and far regions of the oscillon. In the far region, the two terms in each harmonic constituting the radiating tail have a phase difference of $\pi/2$, whereas near the core they are in phase. For $\omega = 0.7$ we see that both higher harmonics change behavior near $r = 3$. Interestingly for the long-lived oscillon of $\omega/m = 0.56$ the third harmonic becomes radiating for $r \gtrsim 6$ and the fifth harmonic for $r \gtrsim 4$, meaning that the core and tail of the oscillon can be perceived slightly different for different harmonics.

Since oscillons are not exact solutions of the equation of motion and they contain small radiating

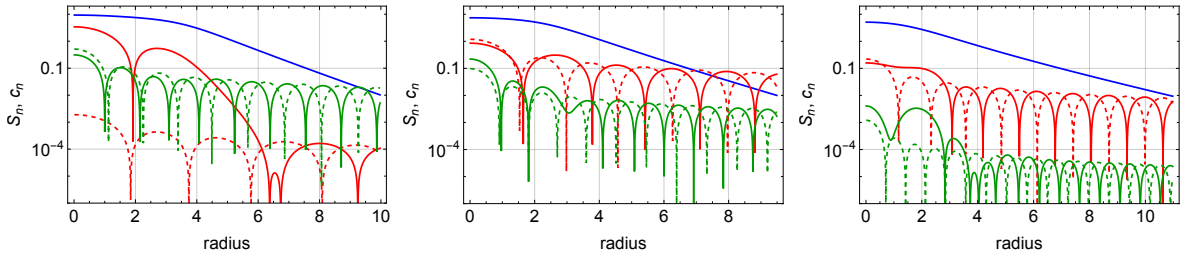

Figure 4. Oscillon solutions for $\omega = 0.56, 0.7, 0.92$ (left to right). The first, third harmonic and fifth harmonics are shown in blue, red and green respectively (solid for sines and dashed for cosines)

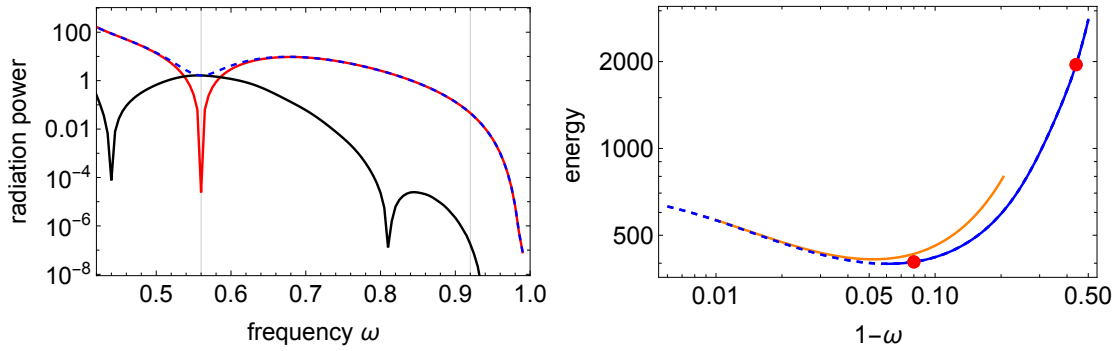

Figure 5. *Left:* The radiated power of the node-less oscillons in the third and fifth harmonic (red and black respectively), along with the total radiated power (blue-dashed). *Right:* The oscillon energy as a function of frequency (blue). The two red dots correspond to the two long-lived states. The solid (dashed) part corresponds to states which are stable (unstable) with respect to long-wavelength perturbations. The orange curve shows the particle number N (defined as E_{osc}/ω), around the point where the stability behavior changes.

tails (even suppressed ones), one can define the rate at which energy is expelled from the oscillon towards infinity. The energy loss is directly related to the change in oscillon energy per unit time $\Gamma_E(\omega) = -\dot{E}(\omega)$ and is shown in Fig. 5. We see that the third harmonic has a dip at $\omega \simeq 0.56$. By "zooming" in close to this dip, we can see the third harmonic vanish at large distances, within the numerical accuracy limits of our calculation. At this point, the energy loss is dominated by the fifth harmonic. Thus $\omega \simeq 0.56$ defines a local minimum in energy loss, where a long-lived oscillon state is expected to exist. The behavior of the energy loss at high frequencies, close to $\omega = 1$ is somewhat different. The energy loss there decreases monotonically, without providing a clear local minimum. As the oscillon loses energy, its frequency increases. However, this cannot continue arbitrarily, since the energy function has a minimum for $\omega \simeq 0.93$, meaning that after this point the oscillon cannot lose energy and evolve adiabatically, leading to its sudden decay. This has been coined "energetic

death" [51].

We can look for oscillon configurations in the space of instantaneous solutions, which are able to retain their global properties over a substantial amount of time. Simply put, we can look for solutions, whose frequency does not change over a long period of time. From the quantities derived in the semi-analytic oscillon solution, we can compute the evolution of the instantaneous frequency of the system by solving the following equation numerically

$$\int_{\omega_0}^{\omega} \frac{dE/d\omega'}{\Gamma_E(\omega')} d\omega' = -\int_{t_0}^{t} dt' \tag{12}$$

Fig. 6 shows two clear minima of $\dot{\omega}/\omega$, the relative evolution of the instantaneous frequency. One is at $\omega \simeq 0.56$, as expected, and the other can be found at $\omega \simeq 0.92$, leading to an concrete definition of long-lived oscillon states.

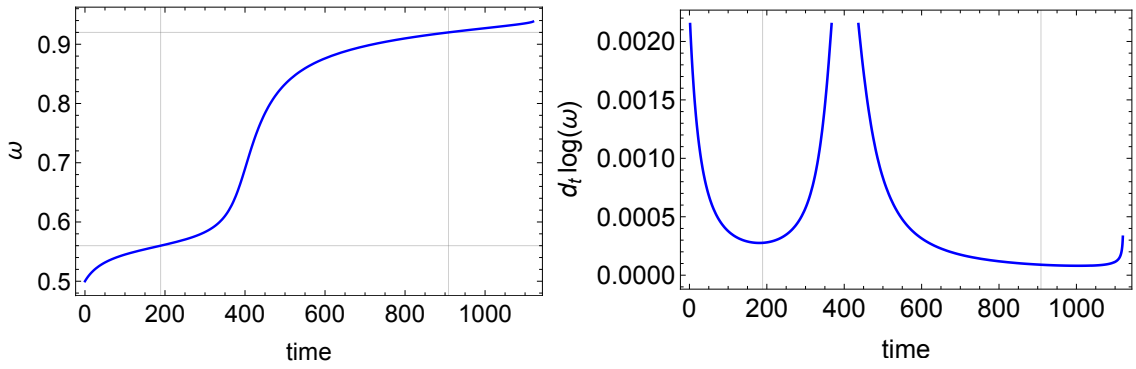

Figure 6. *Left:* The evolution of the instantaneous frequency $\omega(t)$ as a function of time. We can clearly see two plateaus, corresponding to well-defined oscillons. *Right:* The relative change in frequency $\dot{\omega}/\omega$, clearly pointing to the existence of two clear oscillon states, at $\omega \simeq 0.56$ and $\omega \simeq 0.92$.

B. Excited Oscillons

We now move to oscillon solutions with $1, 2$ and 3 nodes. By performing the same shooting process, in order to find oscillon solutions, but starting with a slightly larger amplitude at $r \simeq 0$, we discover a family of oscillon solutions where the shape of the first (fundamental) harmonic exhibits a node, a point in space where the amplitude vanishes. We should note that, within the validity of our construction method, the total amplitude does not vanish at all times, due to the fact that the higher harmonics do not vanish at the same point. However, they are vastly subdominant (one order of magnitude or more). We will thus use the characterization of nodes based on the first harmonic and keep in mind that in reality they are "approximate nodes".

Fig. 7 shows the structure of oscillons with 1, 2 and 3 nodes for two different frequencies each. One corresponds to a solution where the decay rate exhibits a local minimum, leading to long-lived state, whereas the other frequency does not possess such features. We see a similar behavior as the one shown in Fig. 4, with the outgoing radiation being suppressed for certain values of the frequency. Interestingly, the higher harmonics are in general suppressed at the nodes. In some cases, (some) higher harmonics show an outgoing radiation-like behavior, meaning that the sine and cosine terms are exactly out of phase. In order to capture this, we simply add the squares of the two contributions to the harmonic in question (black lines in Fig. 7). This should not have features for outgoing radiation, or whenever the sine and cosine terms oscillate out of phase.

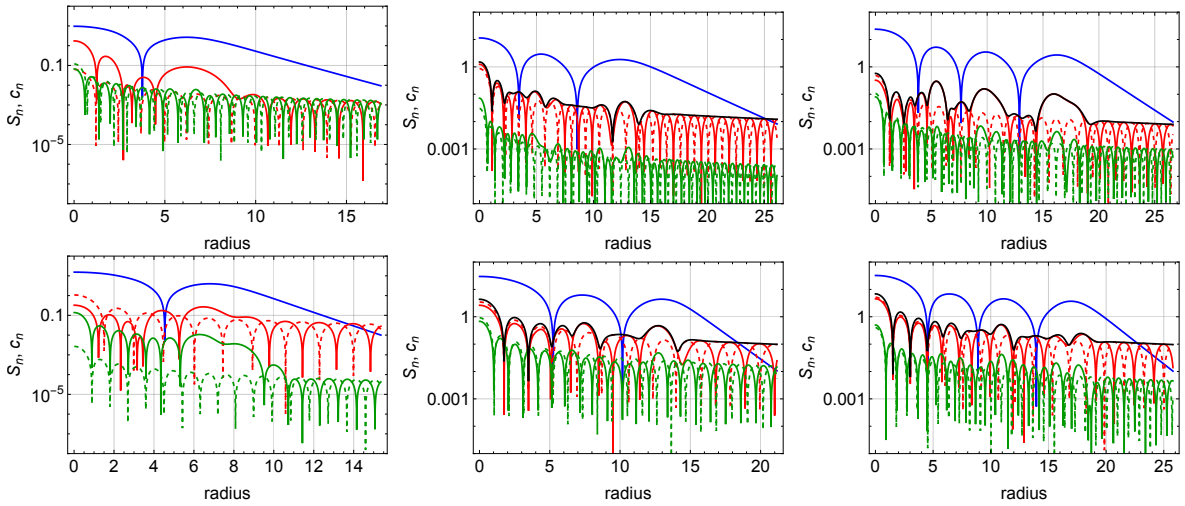

Figure 7. Oscillon solutions for $n = 1, 2, 3$ nodes (left to right). The upper panels correspond to long-lived solutions, $\omega = 0.86, 0.92, 0.82$ respectively. The lower panels correspond to "random" solutions $\omega = 0.7, 0.6, 0.7$ respectively. The first, third harmonic and fifth harmonics are shown in blue, red and green respectively (solid for sines and dashed for cosines). The black curve corresponds to the sum of squares of the corresponding sine and cosine terms of one higher harmonic.

III. NUMERICAL EVOLUTION IN SPHERICAL SYMMETRY

In this section we take an "experimental" point of view and use numerical methods to study the oscillon states of the sine-Gordon model. We employ a simple central difference algorithm to study the time evolution of these states imposing spherical symmetry and implementing absorbing boundary conditions (we will discuss the nontrivial question of non-spherical breakup of oscillon states in Section IV). We checked that our results are robust to a variety of integration schemes

and resolutions. The main points of this section can be summarized as follows:

- We take a different viewpoint here than the one provided in Section II. There, the quasi-breather picture gives a continuously connected spectrum of oscillon-like configurations. We'll show that, although some aspects of the dynamics of oscillon states can be captured in this way, generically other effects dominate the evolution of the system. We thus take a more restrictive approach to what we call a "state": *an oscillating field configuration that is able to retain most of its properties during its lifetime.* Although these properties can be understood in the quasi-breather framework, our current definition naturally leads to the emergence of a discrete spectrum of states.

- The single-frequency ansatz defines the initial conditions of our "experiment", labeled by frequency (continuous) and number of nodes in the spatial profile (discrete). We observe that not all of these initial conditions relax to our definition of a state[5]. Using the quasi-breather picture we can semi-analytically predict where these states exist, finding good agreement with experiment. However, this framework doesn't seem appropriate to predict the overall lifetime of the states, which is dominated by additional instabilities. This effect is especially prevalent for states that carry nodes. Lifetimes discussed in this section are thus directly extracted from numerical simulations.

- As instabilities play an important role for the dynamics of these oscillons, the overall lifetime of the states is tied to the exact initial conditions that we choose (starting with a large perturbation around the exact state leads to an earlier onset of decay). When assigning lifetimes, we include uncertainties to account for this.

- We find a discrete spectrum of long lived oscillon states. We characterize states as "long lived", when they have a lifetime comparable ($\gtrsim 50\%$) to the fundamental (lowest energy) state. By adding more and more nodes to the initial conditions a seemingly boundless spectrum emerges, with ever increasing central amplitude and total mass M (rest energy). We explicitly checked that states can be found with up to 3 nodes in the spatial profile, and there is no a priori reason to suspect that this process can't continue up to an arbitrary number of nodes. It is at this point not clear if this is a property of the sine-Gordon model with its infinite degenerate minima, and this question will be addressed in future work. Our results are summarized in Table I.

[5] We present a closer investigaton of the basin of attraction in Appendix B.

n	ω $(\cdot m)$	Φ_0 $(\div 2\pi)$	τ_{sp} $(\cdot 10^2 m^{-1})$	M $(\cdot 10^2 f^2/m)$	$M\tau_{sp}$ $(\cdot 10^6\, f^2/m^2)$
0	0.58(5)	1.92(9)	9.5(5)	17.0(8)	1.6(2)
0	0.92(1)	0.68(5)	7.0(5)	3.8(2)	0.27(3)
1	0.56(4)	3.6(4)	6.0(5)	210(40)	13(3)
1	0.86(2)	1.8(2)	6(1)	56(1)	3.4(6)
2	0.70(5)	4.1(8)	3.5(1.0)	392(7)	13(4)
2	0.92(1)	2.1(1)	5(1)	160(10)	8(2)
3	0.82(2)	3.8(2)	7(1)	557(8)	39(6)
3	0.91(2)	2.8(1)	5.5(5)	410(20)	23(3)

Table I. Properties of long lived, spherically symmetric oscillon solutions: node number (n), frequency (ω), field amplitude at the center (Φ_0), lifetime ($\tau_{\rm sp}$), mass M and narrowness ($M\tau_{\rm sp}$). We list only oscillon states which retain well defined properties (e.g., the number of nodes) for a lifetime comparable to the lowest mass oscillon. The variance is indicated in parenthesis notation, e.g. $\omega = 0.58(5) \Rightarrow 0.53 \leq \omega \leq 0.63$. The lifetime is written as τ_{sp} emphasizing the fact that these are lifetimes obtained in spherical symmetry. It seems that the lifetime is significantly shortened if aspherical perturbations are included.

A. Experimental Setup

1. *Initial Conditions and radiated power*

The results of our numerical experiment are entirely determined by the evolution of the system through the equation of motion, Eq. (2), as well as by the initial and boundary conditions. We impose spherical symmetry on the system $\phi(\vec{x}, t) \to \phi(r, t)$, and implement an absorbing boundary condition at $r \to \infty$ and a Neumann boundary condition at $r = 0$; $\partial_r \phi(0, t) = 0$. This uniquely defines the problem, once the initial conditions are specified. To probe the space of possible oscillon states we use the single-frequency ansatz to guide our choice of initial conditions. This was described in Section II and numerically calls for the solution of Eq. (5) with boundary conditions $\partial_r \Phi|_{r=0} = 0$ and $\Phi(r \to \infty) = 0$. In practice, the boundary condition at infinity is substituted for the boundary condition at a finite but large radius, where the equation of motion can be approximated as

$$\frac{d^2\Phi}{dr^2} + \frac{2}{r}\frac{d\Phi}{dr} + (\omega^2 - m^2)\Phi \simeq 0 \tag{13}$$

which leads to the trivial solution $\Phi \sim \frac{1}{r} e^{-\sqrt{m^2-\omega^2}\, r}$. At fixed frequency, this procedure defines a discrete spectrum of initial conditions for our setup, where the solutions are labeled by the amount of nodes in the spatial profile $\Phi(r)$. We then choose initial conditions to satisfy the single-frequency

ansatz, with $\phi(r,0) = \Phi(r)$ and $\partial_t \phi(r,t)|_{t=0} = 0$. In practice, true oscillons have a non-negligible contribution from higher harmonics.

The presence of higher harmonics in the full solution has three effects which can be studied numerically as well as analytically within the quasi-breather picture outlined in Sec. II

- There is a significant deviation of the spatial and temporal profile of the oscillon states with respect to the single-frequency ansatz. This effect is especially noticeable in large amplitude oscillons.
- The oscillon radiates and thus loses energy through unbounded higher harmonics.
- As the oscillon loses energy it is forced to adiabatically change its frequency and find solutions that live “close-by" in the attractor sense, but have smaller energy.

In Fig. 8 we compare the energy of the single-frequency ansatz with the energy obtained from the quasi-breather formalism, which contains contributions from higher harmonics. We see that the difference is small.

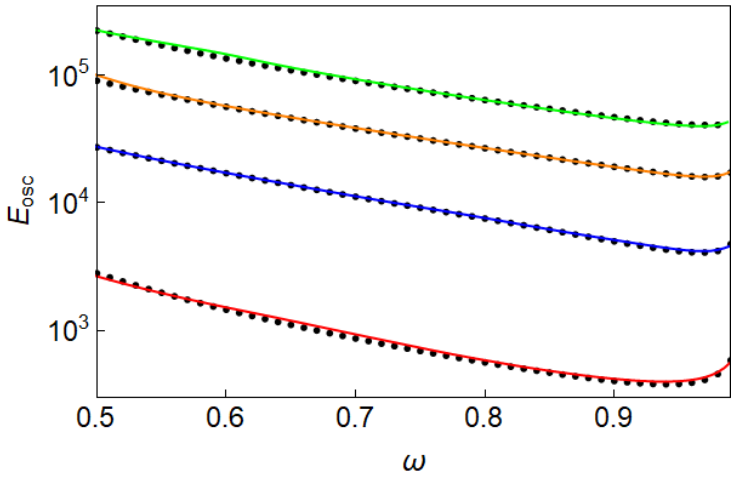

Figure 8. Comparison of the energy (or rest mass) obtained analytically with the full harmonic content in the quasi-breather formalism (color) and the single-frequency ansatz (black dotted) of the oscillon-like configurations of the sine-Gordon model, for different number of nodes in the spatial profile: 0 (red), 1 (blue), 2 (orange) and 3 (green). The difference is negligible.

In our numerical experiment we observe that an initial condition of the form of the single-frequency ansatz (3) generically latches onto an oscillon configuration with corresponding fundamental frequency set by Eq. (5), but with non-negligible contributions from higher harmonics.

Notice the nomenclature here; an oscillon configuration is not equivalent to our definition of a state: either the configuration decays quickly or it changes its features too much throughout its lifetime. These configurations do, however, define a continuously connected space of oscillon solutions, whose properties we can measure (soon after initializing)[6]. These solutions have the full harmonic content sourced by the single-frequency ansatz and can thus be compared to the analytically constructed quasi-breathers of Sec. II. Of particular interest is the energy that the oscillon solutions radiate, which we can obtain through the expression

$$|\dot{E}_{osc}| = 4\pi R^2 \langle T_{0r} \rangle |_{r=R} = 4\pi R^2 \left\langle \dot{\phi} \partial_r \phi \right\rangle |_{r=R} \,, \tag{14}$$

where brackets indicate time averages and the measurement should be taken at a radius R that is away from the oscillon bulk. We obtain numerical data by initializing with the single-frequency ansatz at different values of ω, letting the field relax to an oscillon solution for a fixed amount of time, and then measuring T_{0r} away from the oscillon bulk for three oscillation periods. $|\dot{E}_{osc}|$ for each ω is obtained by averaging the measured values of T_{0r}. This procedure defines another way to estimate the oscillon properties at fixed ω, independent from the quasi-breather formalism and rooted entirely in numerics. In Fig. 9 we compare the energy radiated by the quasi-breathers constructed in Section II and the oscillon solutions in our experiment. We see that the oscillon solutions agree qualitatively well with the quasi-breather formalism, although the latter often underpredicts the amount of energy that the oscillon solution radiates. This is on one hand due to the fact that the we are forced to include a finite number of harmonics in the quasi-breather calculation (a limitation that the numerical measurement doesn't have), and on the other hand because of the uncertainty in our prescription for numerically measuring the properties of the oscillon solutions at fixed ω.

As seen before in Section II, the radiated energy is highly suppressed for specific values of the frequency ω. Assuming that the configurations are able to adiabatically follow the "instantaneous" space of oscillon solutions, we can predict where proper oscillon states should exist: these are those configurations in the space of solutions that are able to retain their global properties over a substantial amount of time. For example, there are clear plateaus when investigating the evolution of the system through $\omega(t)$ using Eq. (12) (see Fig. 6), during which the configuration is able to retain its global properties. While the oscillon configuration lives on the plateau it has a well defined mass and binding energy. Note that these plateaus do not necessarily exist during the evolution of the system, as this reasoning is based on the assumption that the oscillon configurations are

[6] In practice we take measurements by initializing with the single-frequency ansatz, waiting a few periods for the system to relax and finally measuring observables over one or two oscillation periods.

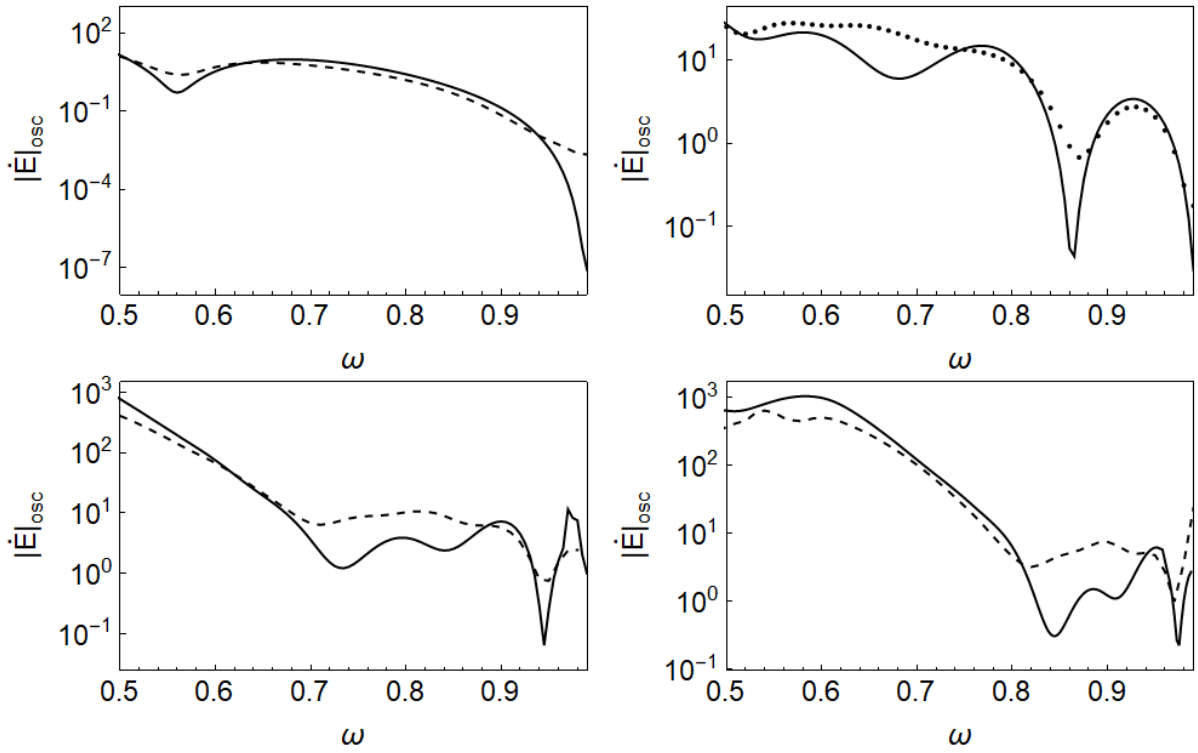

Figure 9. Radiated power obtained analytically using the quasi-breather formalism (solid) and numerically using the prescription described in the main text (dashed) for the oscillon configurations of the sine-Gordon model, for different number of nodes in the spatial profile: zero node (top left), one node (top right), two node (bottom left) and three node (bottom right) solutions. The two methods provide independent estimates at fixed ω. Although they agree qualitatively well, there are quantitative differences. The actual time evolution of an oscillon follows the overall estimate quite closely as it evolves adiabatically, increasing ω.

adiabatically connected. However, it gives a hint as to where we might find oscillon states: oscillon configurations that retain their global properties over a long period of time. In Section III A 2 we make these notions more concrete by providing a definition of an oscillon state.

2. Definition of Oscillon States and their Lifetime

We define an oscillon state as an oscillon configuration that during its lifetime satisfies the following criteria:

1. The fundamental frequency (or binding energy per particle) of the solution doesn't change by more than 10%.

2. The state has a well defined mass, meaning that it doesn't vary by more than 20%.

3. If the spatial profile contains a node, it must retain it.

4. The overall lifetime has to be at least 50% of the ground state (lowest energy oscillon state).

With these definitions we look for oscillon states "experimentally", meaning through a series of simulations. If the dynamical evolution of the system were fully adiabatic we could find all the states immediately by numerically solving Eq. (12), essentially combining the data in Figs. 8 and 9. This process gives clear predictions as to where the oscillon should be able to obey our definition of a state. While our simulations confirm that this happens for the nodeless oscillon configurations, it does not occur for oscillons that contain a node in their spatial profile. These solutions eventually shed their node and leave the adiabatic curve. We thus consider the adiabatic predictions as the most probable locations in parameter space where well-defined oscillon states exist and look for them through a series of simulations, initialized with different profiles derived from Eq. (5).

B. Results

Here we present the main results of this paper. Using the definition of a state given in Section III A 2 we are able to extract a discrete spectrum of oscillon states with different masses. By increasing the number of nodes in the spatial profile a seemingly boundless spectrum of states emerges. We explicitly checked that states can be found with up to 3 spatial nodes, and have no a priori reason to think that this process should stop (although stability issues might require the initial conditions to be highly fine-tuned).

As mentioned previously, there is a clear difference in the evolution of the solutions with- and without nodes. Starting from the single-frequency ansatz, the nodeless solution is able to adiabatically probe all the oscillon configurations[7], up until its "energetic death"[8]. Solutions with nodes typically excite instabilities that drive them away from this type of adiabatic evolution. We will comment on the nature of these instabilities later. The distinction in behavior is made clear in Fig. 10 where we plot (colored scatter) the radiation that the oscillon emits during its entire lifetime, until either no localized energy remains or the field loses its node. Different colors represent different simulations initialized with the single-frequency ansatz. It is clear that the nodeless oscillon is able to evolve adiabatically from $\omega \sim 0.5$ until $\omega \sim 1$ where it decays. An oscillon with nodes (in Fig. 10 we only show the case with one node, but similar conclusions hold for solutions

[7] This is strictly speaking only true when starting from the single-frequency ansatz. More general initial conditions can excite instabilities and leave the adiabatic curve.

[8] This term was first coined in [51] to indicate the moment where the oscillon has to decay as adiabatic evolution requires an increase in energy of the solution, which is not available due to energy conservation.

with more nodes) generally loses its node(s) before it can transition to $\omega \sim 1$. We need more than one initialization to map the entire space of oscillon solutions. Since there is no way of knowing in what region of parameter space oscillons with nodes evolve adiabatically, we are forced to look for states through a process of trial and error. However, the information gathered so far allows us to do so in a systematic way:

1. Using the predictions for the adiabatic evolution of the system we identify potential oscillon states.

2. Once identified, we check through numerical simulation whether the oscillon is able to survive long enough to qualify as a state (starting from the single-frequency ansatz).

3. We explicitly check if the evolution of the oscillon follows our adiabatic prediction.

If the oscillon survives these three steps of scrutiny we identify it as a proper state and take measurements of its properties by averaging over its lifetime. The process is less complicated for the nodeless oscillons as they evolve adiabatically. This predicts the existence of two states which were previously found in Ref. [48]. In Fig. 11 it becomes evident why we classify certain oscillons as

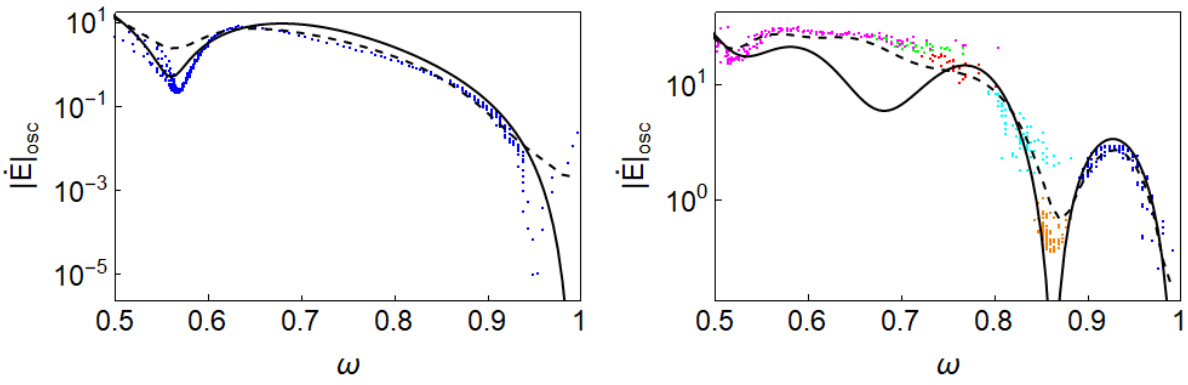

Figure 10. The radiation emitted by the oscillon versus its frequency ω extracted from the full numerical evolutions starting with different initial conditions, represented by different colors. The black curves are the analytic (solid) and numerical (dahsed) estimates shown in Fig. 9. *Left:* The nodeless case. A single initialization traces out the whole range of ω. *Right:* The case with one node. In this case, the node is lost past some ω and multiple initial conditions (different colours) are needed to cover the entire range.

states. The different clusterings in parameter space indicate that there are certain preferred oscillon configurations which we identify as states. Each clustering corresponds to a different initialization of the field with the single-frequency ansatz. We gave clusterings belonging to profiles with the

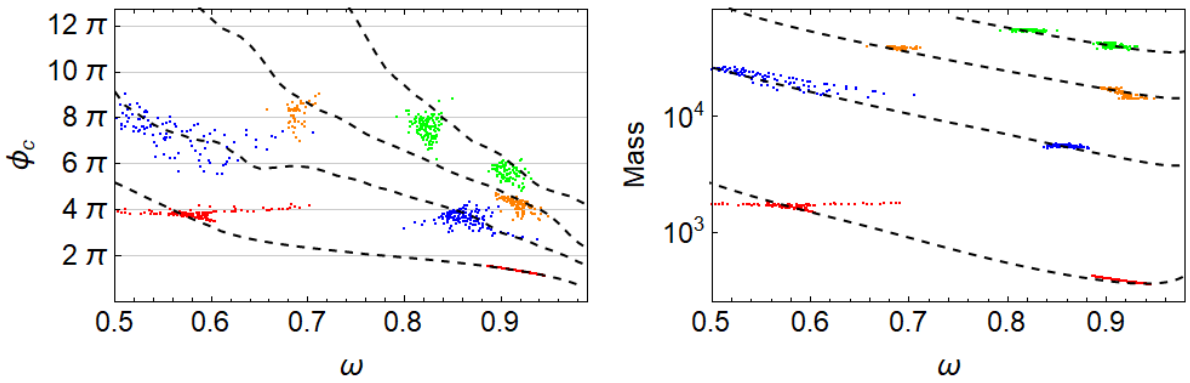

Figure 11. The clustering of oscillon-like configurations in parameter space. On the left panel we plot the maximal central field amplitude (measured over one period) while on the right panel we show the mass of the states, defined as the energy that remains localized within a radius that initially contains 90% of the total energy. It is clear that the field clusters around points which we define as states in this paper. Different clusterings correspond to different initializations while clusterings with the same color correspond to states with the same number of nodes: 0 (red), 1 (blue), 2 (orange) and 3 (green). The black dashed line in the correspond to the predictions of the oscillon configurations obtained from numerics at fixed ω.

same number of nodes the same color. The datapoints in Table I are computed by averaging over the different clusters. Note that this is true in particular for the fundamental frequency ω, which is computed by measuring the zero-crossings of the field at the origin. Since ω evolves somewhat during the evolution of the state, the values given in Table I do not necessarily correspond to those of the single-frequency initialization. In fact, to observe the state it is better to initialize with an ω that is somewhat below the value given in Table I. Finally, masses are defined as the energy that remains localized within a radius that initially contains 90% of the total energy. We will now discuss some characteristics of the different states in more detail.

1. Fundamental Oscillon States

There exist two nodeless oscillon states in the sine-Gordon model in three spatial dimensions. We explicitly confirmed their existence and characteristics. Their space- and time- profiles are shown in Fig. 1. The heavier state has a fundamental frequency of $\omega \sim 0.58$ and has about four times the mass of the lighter state with $\omega \sim 0.92$. The lighter state turns out to be the lightest state we find in our oscillon spectroscopy of the sine-Gordon model (also including oscillons with nodes). We therefore refer to it as the ground state. Interestingly, the lifetime of the lower frequency (heavier) state is actually larger than that of the ground state.

What seems typical for the nodeless oscillons is that once the field settles into an oscillon configuration, it can evolve adiabatically very efficiently, increasing its frequency ω. In this way, the scalar field can transition through the two nodeless states if initialized with the right initial conditions, effectively having a coherent lifetime that is the sum of that of the two individual states. In particular, this is what happens when initializing with the single-frequency ansatz (see Fig. 10) near $\omega \sim 0.58$, but does not necessarily happen when starting with more generic initial conditions. We will comment on these types of transitions in Section IV. Eventually, when the oscillon reaches a frequency of $\omega \simeq 0.93$, it decays. At this point the oscillon needs to increase its energy in order to continue to increase ω. As this is not possible, the state quickly decays. This type of decay was coined "energetic death" in [51] and seems to be generic for oscillons in potentials that can be written as a power series. As mentioned previously, the decay of the states with nodes is of a different nature.

The two nodeless states act as very strong attractors of the sine-Gordon model. We observed that, starting from a generic Gaussian field profile, the field quickly settles into one of the nodeless states (which of the two is somewhat dependent on initial conditions). In this case the adiabatic transition through the two states is somewhat less efficient, since the oscillon configurations are perturbed to a larger degree by the initial conditions. In other words, adiabatic evolution can stop even for nodeless states before "energetic death".

2. Excited Oscillon States

Here we present the oscillon states we found for oscillons that contain nodes in their spatial profile. Interestingly, we are able to identify two states for each number of nodes, replicating "accidentally" the pattern of the nodeless states. In Figs. 12, 13 and 14 we present their space- and time- profiles. Interestingly, as the field oscillates around 0 the nodes stay approximately in the same location. Furthermore, even though we start from a single-frequency ansatz, the states get large contributions from higher harmonics. In this sense these states are also attractors of the model, although we didn't observe them starting from a Gaussian profile, and instead needed to initialize with profiles that contained the correct number of nodes. The less attractive nature of these oscillons ultimately ties in with the fact that states with nodes contain instabilities that force them to decay before energetic death.

Initializing with the single-frequency ansatz we see that the oscillon temporarily is able to evolve following the prediction of Eq. (12). Naively, we would expect the oscillon to then transition through

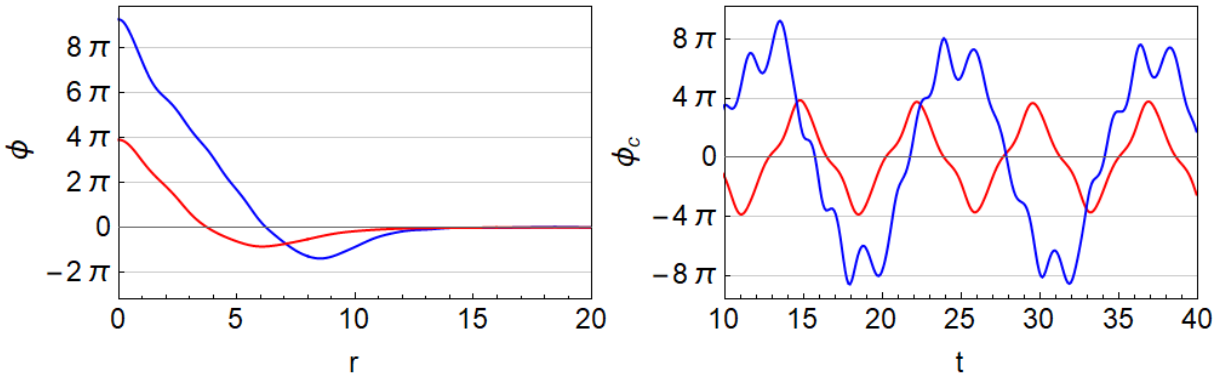

Figure 12. The spatial and temporal profiles for the oscillon states found with a single node in their spatial profiles. In the spatial profile (left) we show the field profiles of the oscillon at maximum amplitude, while in the temporal profile (right) we show the amplitude of the field at the origin as the state evolves.

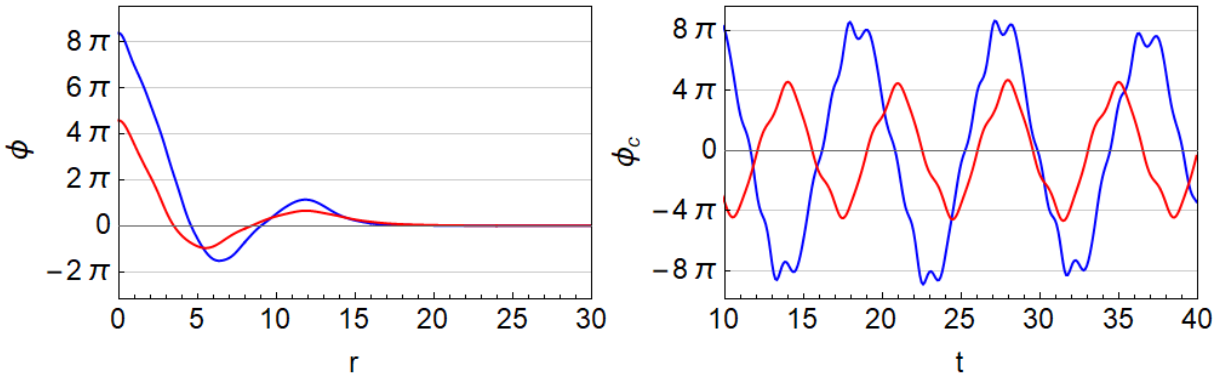

Figure 13. The spatial and temporal profiles for the oscillon states found with two nodes in their spatial profiles.

the two states and eventually decay due to energetic death, similar to the nodeless case. However, this type of transition was never observed, and a different type of instability, which forces the oscillon to lose its node(s) takes over. We suspect the origin to be the following: as the scalar waves from the bulk of the oscillon move through the nodes towards spatial infinity, the location of the node has to oscillate. This eventually forces the oscillon to shed its node as it strays too far from adiabatic evolution. We observe that the shedding of the node(s) is a violent event in which a lot of scalar radiation is emitted. Depending on initial conditions, the field sometimes decays into one of the nodeless states.

One might expect that, starting with initial conditions that are "closer" to the true oscillon solution (so a solution that contains content from higher harmonics instead of the single-frequency

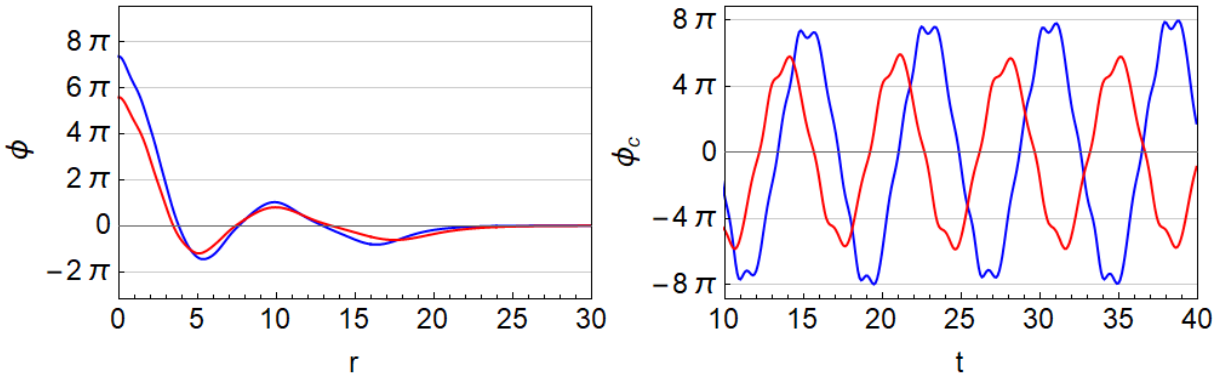

Figure 14. The spatial and temporal profiles for the oscillon states found with three nodes in their spatial profiles.

ansatz), one could have a delayed decay of the states as the initial perturbation of the system is smaller. To test this hypothesis we constructed oscillon configurations containing contributions from higher harmonics using the quasi-breather formalism, and used this as initial conditions instead of the single-frequency ansatz. Doing this, we observed slightly altered lifetimes, which we have taken into account by adding uncertainties to our inferred lifetimes.

Table I contains the most important characteristics of the long-lived oscillon states with up to three nodes. We see that, while the energy is monotonically increasing, as we increase the number of nodes, the same is not true for the lifetime. The lifetime is of the same order for most long-lived states that we found, ranging from $300m^{-1}$ to $900m^{-1}$. We see that the two-node oscillons are less long-lived than both single-node and three-node ones, indicating that it is at least plausible that long-lived states with more nodes can be found. On the other hand, the rest mass increases between the most stable 0-node and the 3-node oscillons, ranging from $M = 3.8 \times 10^2$ to $M = 5.6 \times 10^4$ in units of f^2/m.

The product $M\,\tau$ is also quite intriguing. It is natural to identify $1/\tau$ as the decay width and view these states as resonances, as usual in particle physics. The outcome is that they correspond to very narrow resonances. Then $M\,\tau$ measures the narrowness of the state (the larger the narrower). It is quite large, and similar for all long-lived oscillon states, $M\tau \simeq \big(\mathcal{O}(10^6) - \mathcal{O}(10^7)\big)(f/m)^2$. It even increases mildly with the number of nodes. (As we discuss in Sec. IV, away from the spherical ansatz, the lifetime is reduced by about 1 order of magnitude for oscillons with nodes). Finally, it is worth noting that the maximum central amplitude of the field profile seems to usually be equal to a multiple of 2π which correspond to the minima of the sine-Gordon potential.

IV. TRANSITIONS

Transitions between oscillon states can be classified in two ways. First, a state can transition when it excites instabilities, perturbing the oscillon solution and forcing it to decay to one or more decay products. Since these instabilities can be aspherical, the problem needs to be studied in three dimensions. The second type of transition has already been alluded to in the text: an adiabatic transition between oscillon states. We reemphasize this point before moving on to the three dimensional question.

1. Adiabatic Transitions

As noted before, the nodeless oscillon solutions typically evolve adiabatically until they decay due to energetic death. The nodeless oscillon state with $\omega \sim 0.58$ is therefore able to transition to the groundstate at $\omega \sim 0.92$ as energy radiates away from the oscillon bulk. The transition can be seen clearly in Fig. 15, where we plot the mass of the oscillon solution over time (defined as the energy within the radius that initially contains 90% of the total energy in the field) for a field configuration initialized with the single-frequency ansatz at $\omega = 0.55$. The field transitions through the two states where its mass is approximately constant (white regions), separated by a fast adiabatic transition (middle gray shaded region). Finally, it decays through energetic death (right gray shaded region). A transition as in Fig. 15 always happens when initializing with the single-frequency ansatz, but for completeness we report that, starting from more generic initial conditions (as e.g. a Gaussian), we observed a slightly different evolution with an earlier onset of decay. The transition through the second state was less complete in these cases due to the larger initial perturbation to the true oscillon solution.

2. Transitions in 3D

In the previous sections we computed the lifetime of excited sine-Gordon oscillons by restricting the evolution to spherically symmetry. However, localized configurations in three spatial dimensions can decay asphericallly, in some cases leading to the formation of groups of localized objects, see e.g. Ref. [52]. Even starting from spherical initial conditions it's still a possibility that quantum mechancical perturbations get parametrically amplified due to coupling with the spherical background. There is no good reason to expect that this amplification is necessarily smaller for aspherical modes than for spherical ones, and the lifetimes given in Table I could be altered signif-

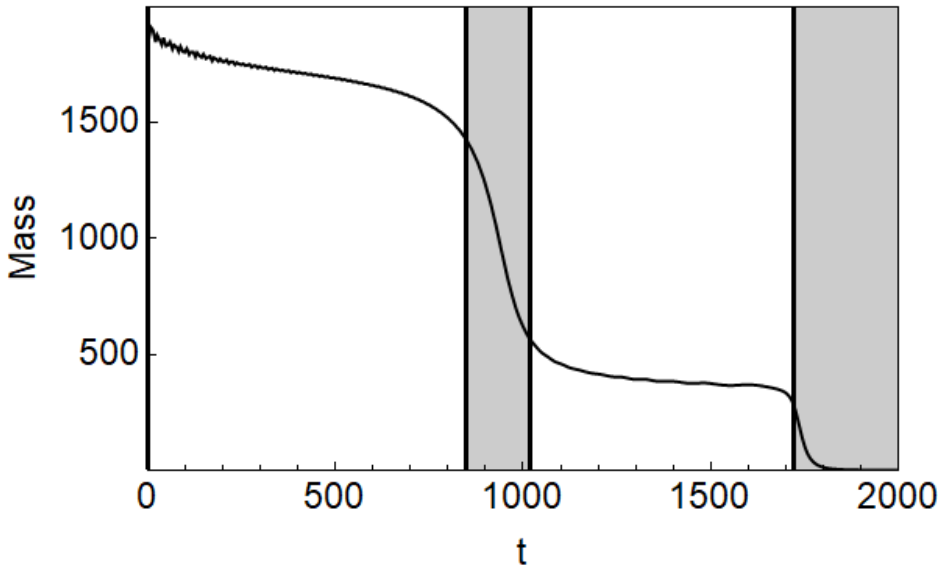

Figure 15. The adiabatic transition between the two nodeless oscillon states of the sine-Gordon model. Starting from the single-frequency ansatz, the field first settles into the low ω state (right white region) before transitioning (middle gray region) to the groundstate. Eventually, the groundstate decays quickly due to energetic death.

icantly in 3+1 dimensions. To investigate this we performed three-dimensional lattice simulations of the states we found in spherical symmetry. We again took as initial conditions the spherical single-frequency ansatz of the various states found in spherical symmetry, which were then perturbed with small fluctuations. For the nodeless states, we see no significant difference in lifetime. However, it seems that oscillon states with nodes are susceptible to aspherical transitions to one or more of the nodeless states. These transitions persist, even when no fluctuations are added to the initial conditions. This indicates that numerical perturbations alone can be amplified and trigger the transitions. In Figs. 16 and 17 we show some snapshots of these simulations. One can note that the perturbation is numerical as the breakup follows the symmetry of the underlying cubic lattice. Beyond the limitations of inherent numerical noise, there is reason to believe that the decay itself is a physical effect.

We can obtain some heuristic understanding of the fragmentation process shown in Figs. 16 and 17 as follows. Considering the limit where the amplitude at the center is large $\Phi_0 \gg 1$, the equation of motion of a small perturbation living atop of the oscillon state in Fourier space is

$$\delta\ddot{\phi}_k + \left(k^2 + \cos(\phi_{osc}(t,r))\right)\delta\phi_k = 0 \tag{15}$$

with $\phi_{osc}(t,r)$ being the background oscillon. For $\Phi_0 \gg 1$, the time dependent effective mass has

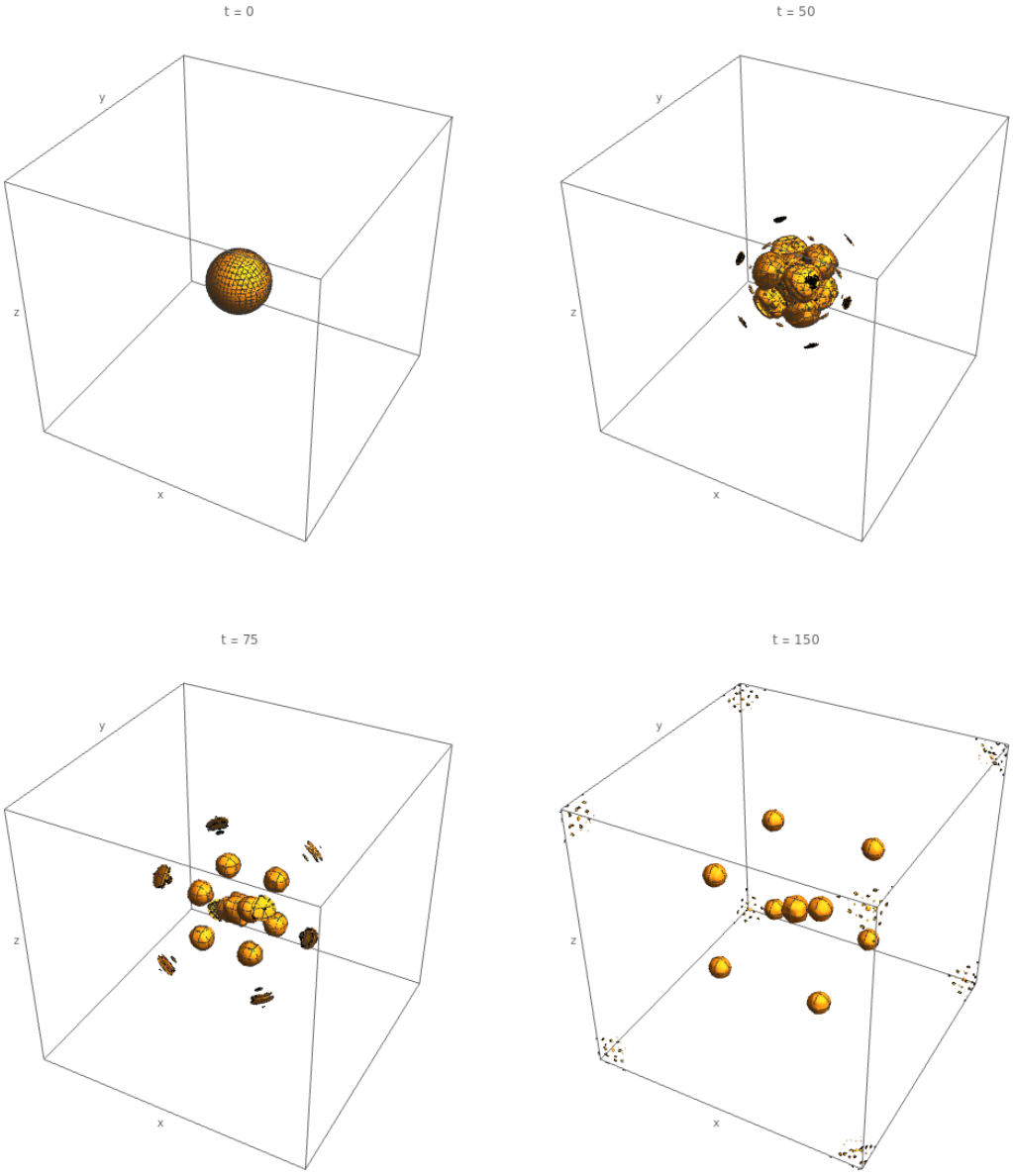

Figure 16. Snapshots of the lattice simulations starting with the oscillon state with one spatial node and frequency $\omega \sim 0.56$. Due to the fact that numerical perturbations get amplified, the state breaks up into 9 nodeless oscillons (one with $\omega \sim 0.58$ at the center and eight groundstates with $\omega \sim 0.92$, all oscillating out-of-phase with the central oscillon, moving outwards along the diagonals of the simulation box). The timescale of decay is about one order of magnitude shorter than those predicted by the spherical simulations. Contours are drawn around volumes that have energy density 20 times the average density in the box ($\rho = 20\bar{\rho}$).

a large harmonic composition. At the center we can approximate $\cos(\phi_{osc}(t,0)) \simeq \cos(\Phi_0 \cos(\omega t))$, which contains frequencies up to $\sim \Phi_0 \omega$. It seems feasible that high k modes can be resonantly

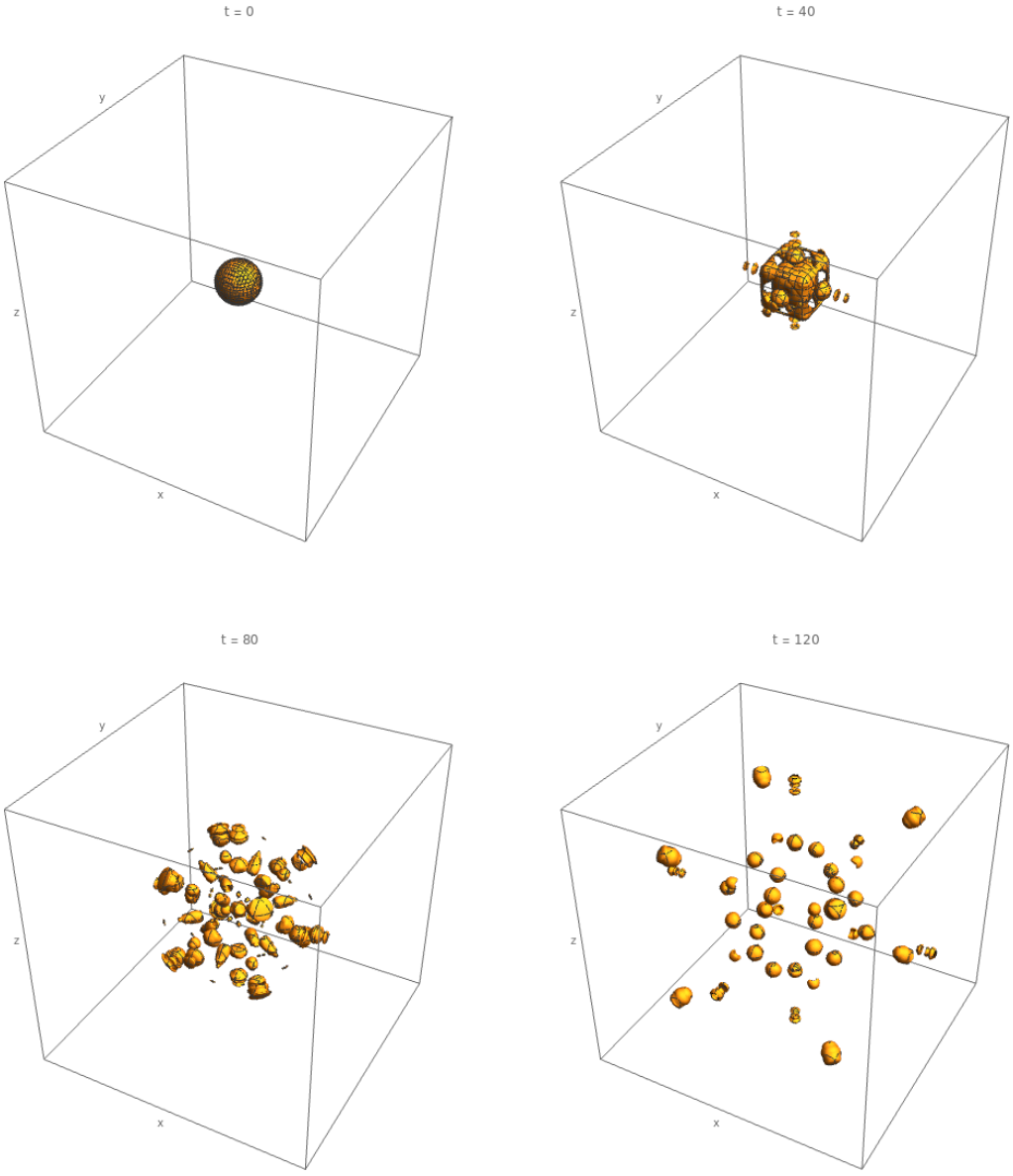

Figure 17. Snapshots of the lattice simulations starting with the oscillon state with three spatial nodes and frequency $\omega \sim 0.84$. Similar to Fig. 16, we see a breakup into nodeless oscillons, but due to the large amount of energy in the initial conditions we end up with many more final oscillons: a spectroscopic signature of oscillon states with several nodes. Contours are drawn around volumes with $\rho = 50\bar{\rho}$.

excited.

Let us assume that in the large Φ_0 limit the oscillon width R_{osc} is fixed, as Figs. 12, 13, 14 suggest. Then, a separation of scales appears $\Phi_0\omega \gg 1/R_{osc}$, and one can to see whether modes

with $k \gg 1/R_{osc}$ are resonant by switching to the homogeneous problem

$$\delta\ddot{\phi}_k + \left(k^2 + \cos(\Phi_0 \cos(\omega t))\right) \delta\phi_k = 0 \tag{16}$$

of which the instability bands can be found using Floquet theory. Indeed, Eq. (16) leads to unstable bands at large values of k, up to a maximal value that scales approximately as $k_{max} \propto \omega\Phi_0$.

The conclusion of this is that we can expect instabilities for modes in the range $R_{osc}^{-1} \lesssim k \lesssim \Phi_0 m$. On the other hand, the disctrete lattice inevitably introduces "noise" with the lattice symmetry that sources these unstable modes with same symmetry.

This gives a qualitative picture of the observed fragmentation effect. States with the amplitude $\Phi_0 \sim 8\pi$ can be expected to have a number of unstable modes. Indeed, the states shown in Fig. 16 and Fig. 17 both have an initial amplitude $\sim 8\pi$ and develop several lobes which then evolve into oscillons (accordingly to energy conservation of course). For states with lower amplitude the argument loses validity. Indeed, we find that of the two states with $\Phi_0 \sim 4\pi$, (the heavy $n = 0$ state and the light $n = 1$) only the $n = 1$ state (the heavier of the two) fragments.

Following this argument, and using the hints obtained from the lattice simulations we performed, it seems that the true lifetimes of many of the states found in previous sections are in reality significantly shorter, by about 1 order of magnitude. These considerations also highlight the incredible properties of the nodeless state living around $\omega \sim 0.58$. It is the longest lived state that we found, reaches a field amplitude comparable to some of the states with nodes, is highly relativistic as a bound state with $\omega \approx 0.58m$, and finally, is stable against aspherical decay even though it has about four times the mass of the groundstate.

Our lattice simulations reveal new interesting features that emerge in three dimensions. Namely, the different states should decay through a rich spectrum of transitions to the more stable states. This is a different type of "spectroscopic" feature which can be used to characterize the states. This is a topic we plan to address in future work. Furthermore, although we observe aspherical decay of the oscillon states with nodes in the sine-Gordon equation, following our reasoning in the previous paragraph there is no reason to think this is bound to happen in other models. There should in principle exist systems where states with nodes are just as stable as nodeless states; a question we will tackle in the future.

V. CONCLUSIONS

We found radically new spherically symmetric oscillon solutions in the three dimensional sine-Gordon equation. Their characteristic is the existence of nodes in their spatial profile, which they keep throughout their lifetime. They have significantly larger energy than their fundamental (nodeless) counterparts, in particular solutions with just one node exhibit one order of magnitude larger energy. We provided a semi-analytic construction by using the quasi-breather formalism, taking into account the non-perturbative presence of higher harmonics. This construction leads to a two-parameter family of solutions, discrete in the number of nodes and continuous in the frequency. However, the radiating tails of the quasi-breathers lead to the existence of long-lived oscillons, only around certain frequencies, with lifetimes reaching $\mathcal{O}(10^3)\, m^{-1}$.

Despite the vast difference in the mass (rest energy), the lifetime of excited oscillons is similar to their zero node counterparts, when computed under spherical symmetry. It is interesting that the lifetime is not monotonic; oscillons with three nodes exhibit longer lifetimes than their two-node or even fundamental counterparts. By considering oscillons as resonances in the particle spectrum of the theory, we can define their narrowness of as the product of the mass and lifetime. Surprisingly, this grows mildly with the number of nodes, being $\mathcal{O}(1)$ for nodeless oscillons and $\mathcal{O}(10)$ for oscillons with three nodes.

When perturbed outside the spherical ansatz, using a full three-dimensional simulation, the excited oscillons exhibit a significantly smaller lifetime of $\mathcal{O}(30)\, m^{-1}$. Interestingly, the decay does not lead to an incoherent bath of radiation, but instead leads to the formation of a number of fundamental oscillons. The possible existence of "selection rules" for the decay of excited multi-node oscillons is beyond the scope of the present work, but does present an intriguing challenge to which we will return in the future.

Our results add more remarkable properties to the heavy oscillon without nodes of the theory. Its low frequency indicates that it can be regarded as a relativistic bound state. Moreover, in our 3D lattice simulations we find it to be stable against fragmentation or anisotropic decay. This happens despite having about 4 times the mass of the lowest oscillon, and despite the field excursion being quite large, $\pm 4\pi f$, at the center.

Finally, we must note that the sine-Gordon model is certainly special. The potential has maxima, and with sizeable $V''_{\rm max} = -V''_{\rm min}$. It is natural to ask how many features (if any) of the current analysis carry on to more general potentials. We will explore the change in the oscillon spectrum from small or large deviations from the sine-Gordon model in a future publication.

ACKNOWLEDGEMENTS

We thank Mark Hertzberg, Alex Pomarol and Sergey Sibiryakov for useful discussions. The research leading to these results has received funding from the Spanish Ministry of Science and Innovation (PID2020-115845GB-I00/AEI/10.13039/501100011033). IFAE is partially funded by the CERCA program of the Generalitat de Catalunya. EIS acknowledges support of a fellowship from "la Caixa" Foundation (ID 100010434) and from the European Union's Horizon 2020 research and innovation programme under the Marie Skłodowska-Curie grant agreement No 847648. The fellowship code is LCF/BQ/PI20/11760021. The research leading to these results has received funding from the ESF under the program Ayudas predoctorales of the Ministerio de Ciencia e Innovación PRE2020-094420. This work is part of the doctoral thesis of F. D. within the framework of the Doctoral Program in Physics at the Autonomous University of Barcelona.

Appendix A: Multi-frequency oscillon solution

While the single frequency Ansatz is sufficient to describe the low-energy oscillon state(s), we need to go beyond it in order to better capture the structure of excited oscillons; meaning oscillons with nodes that have higher energy. We follow the method put forth in Ref. [51], which is tailored to the study of potentials that can be written in the form $V(\phi) \sim \sum_n \mathcal{V}_n \left[1 - \cos(n\phi)\right]$ (note that we have dropped the axion decay constant f for simplicity). The sine-Gordon model represents the simplest case of this family of potentials. We do not attempt to repeat the method of Ref. [51] in its full generality, but rather to present the basic steps, in order to make the current work self contained.

The first step in constructing a viable oscillon solution is extending the single frequency Ansatz to contain multiple frequencies. Due to the symmetry of the potential, the oscillon only contains odd multiples of the fundamental frequency (odd harmonics).

$$\phi_{sin}(r,t) = \sum_n \Phi_n(r,\omega)\sin(n\omega t)\,. \tag{A1}$$

However, we know that the oscillon is not a completely stable configuration and as such it contains small radiating tails, which explain both its longevity and its slow evolution and ultimate

decay. In order to capture the radiating tails, we need to add a cosine series to Eq. (A1), in particular

$$\phi_{cos}(r,t) = \sum_{n\omega>m} c_n(r,\omega)\cos(n\omega t)\,, \tag{A2}$$

where the cosine series only contains radiative modes with $n\omega > m$. Finally, our localized slowly radiating solution can be written as

$$\phi_{\rm full} \simeq \phi_{sin}(r,t) + \phi_{cos}(r,t)\,. \tag{A3}$$

We see that (e.g. Fig. 4), even for radiative modes with $n\omega > m$, the behavior close to the core of the oscillon and in the radiative tail can be very different. We insert the expansion of Eq. (A3) into the equation of motion (2) and use the Jacobi-Anger expansion

$$e^{i\alpha\,\sin b} = \sum_{k=-\infty}^{\infty} J_k(\alpha)e^{ikb} \tag{A4}$$

where J_k is the Bessel function of the first kind. If we assume that only the first and third harmonics are important $\phi_{\rm sin} \simeq \Phi_1\sin(\omega t) + \Phi_3\sin(3\omega t)$ the equation of motion is written as

$$\Phi_1\omega^2\sin(\omega t) + \Phi_3 9\omega^2\sin(3\omega t) + \frac{d^2\Phi_1}{dr^2} + \frac{2}{r}\frac{d\Phi_1}{dr} + \frac{d^2\Phi_3}{dr^2} + \frac{2}{r}\frac{d\Phi_3}{dr} + \sin\left[\Phi_1\sin(\omega t) + \Phi_3\cos(3\omega t)\right] = 0\,. \tag{A5}$$

The last term can be expanded using Eq. (A4)

$$\begin{aligned}\sin(\phi_{sin}) \simeq\; & 2\left[J_0(\Phi_3)J_1(\Phi_1) + J_1(\Phi_3)J_2(\Phi_1) + ...\right]\sin(t) \\ & + 2\left[J_0(\Phi_1)J_1(\Phi_3) + (J_0(\Phi_3) - J_2(\Phi_3))J_3(\Phi_1) + ...\right]\sin(3t)\,,\end{aligned} \tag{A6}$$

where we kept only a few terms in the Jacobi-Anger expansion for each of the two harmonics. We now see that the equation of motion naturally divides into separate parts, each oscillating with $\sin(t)$ and $\sin(3t)$

$$\frac{d^2\Phi_1}{dr^2} + \frac{2}{r}\frac{d\Phi_1}{dr} + \Phi_1\omega^2 - 2\left[J_0(\Phi_3)J_1(\Phi_1) + J_1(\Phi_3)J_2(\Phi_1) + ...\right] = 0\,, \tag{A7}$$

$$\frac{d^2\Phi_3}{dr^2} + \frac{2}{r}\frac{d\Phi_3}{dr} + 9\omega^2\Phi_3 - 2\left[J_0(\Phi_1)J_1(\Phi_3) + (J_0(\Phi_3) - J_2(\Phi_3))J_3(\Phi_1) + ...\right] = 0\,. \tag{A8}$$

For practical purposes, we kept a finite amount of Jacobi-Anger terms, making sure that we the truncation is enough to provide the desired accuracy. It is evident that the above equations do not include the cosine terms and thus cannot provide the proper radiative boundary conditions (outgoing waves) at spatial infinity. We assume that the cosine terms of the expansion in Eq. (A3) can be treated as a small quantity which does not back-react on the sinusoidal terms. Thus we

insert it into the equation of motion and use the Jacobi-Anger expansion, but linearize the resulting potential term, leading to

$$\frac{d^2c_3}{dr^2} + \frac{2}{r}\frac{dc_3}{dr} + 9\omega^2 c_3 - \left[J_0(\Phi_1)J_0(\Phi_3) - J_1(\Phi_3)J_3(\Phi_1) + ...\right] c_3 = 0\,. \tag{A9}$$

Since we require a solution with a confined first harmonic we set $\Phi_1(r \to \infty) = 0$ and set the other two functions to describe outgoing spherical waves at infinity $\Phi_3(r) - \sqrt{9\omega^2 - 1}\, rc_3(r) + r\Phi_3'(r) = 0$ and $\sqrt{9\omega^2 - 1}\, r\Phi_3(r) + r\Phi_3'(r) + rc_3'(r) = 0$. It is evident how this method can be generalized to include higher harmonics.

Appendix B: Basin of attraction

In this Appendix we examine the basin of attraction of the two different types of oscillons, with and without nodes. For this we must choose the initial conditions for the simulations to be different from the exact quasi-breather.

As stated in the beginning of Section III, the lattice simulations are initialized using the profiles derived from the single-frequency Ansatz. It can be seen in Figure 7, that in the quasi-breather formalism, ignoring the higher harmonics can induce a $\mathcal{O}(10)\%$ error.

In order to further explore the basin of attraction of the oscillon solutions in a controlled way, we distort the profile derived using the single-frequency Ansatz by amplifying the amplitude and stretching the spatial dependence by factors A and R as

$$\phi_{\rm in}(r) = A\,\phi_{\rm osc}(Br) \tag{B1}$$

and simulate the subsequent evolution. We perform this experiment for the lowest energy oscillons without nodes and with one node. An alternative choise of initial conditions comes from multiplying the single-freguency Ansatz by a Gaussian, thereby deforming its shape, as

$$\phi_{\rm in}(r) = A\,e^{-C^2r^2}\phi_{\rm osc}(r) \tag{B2}$$

where A and C are tunable parameters. We simulate the evolution using both prescriptions for the initial condition and define the lifetime, as the time required for the localized energy to fall below 80% of the quasi-breather energy corresponding to each configuration, as given in Figures 2 and 11. Fig. 18 shows the basin of attraction for these two oscillons. It is clear that, regardless of the choice of initial condition, the basin of attraction of the nodeless oscillon is larger than its one-node counterpart. However, the basin of attraction for the one-node oscillon is not negligible,

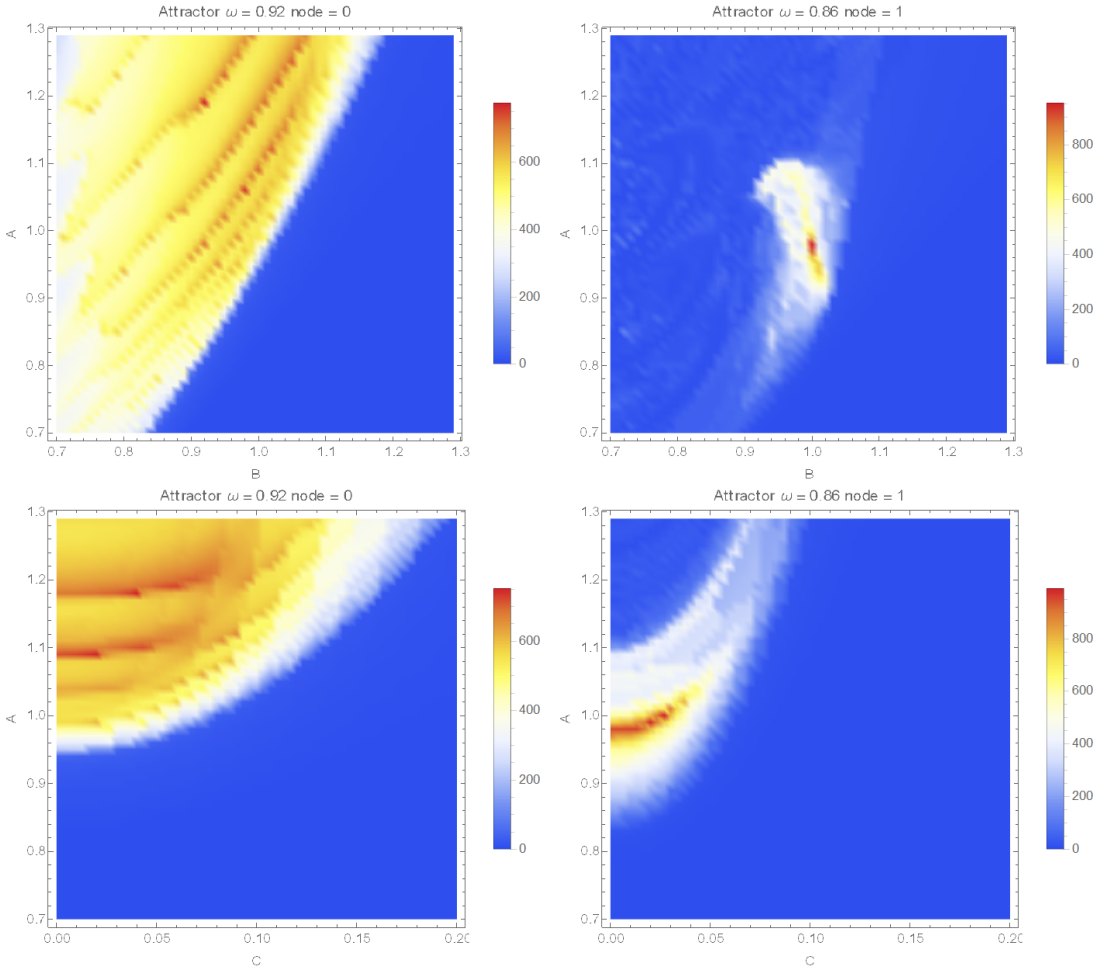

Figure 18. The lifetime of oscillons, starting from the initial conditions of Eqs. (B1) and (B2), upper and lower panels respectively, and oscillons with zero nodes (left) or one node (right).

showing that this configuration can be dynamically reached without resorting to fine-tuned initial conditions.

---

[1] I. L. Bogolyubsky and V. G. Makhankov, On the Pulsed Soliton Lifetime in Two Classical Relativistic Theory Models, JETP Lett. **24**, 12 (1976).

[2] I. L. Bogolyubsky and V. G. Makhankov, Dynamics of Heavy Spherically-Symmetric Pulsons, Pisma Zh. Eksp. Teor. Fiz. **25**, 120 (1977).

[3] M. Gleiser, Pseudostable bubbles, Phys. Rev. D **49**, 2978 (1994), arXiv:hep-ph/9308279.

[4] E. W. Kolb and I. I. Tkachev, Nonlinear axion dynamics and formation of cosmological pseudosolitons, Phys. Rev. D **49**, 5040 (1994), arXiv:astro-ph/9311037.

[5] E. J. Copeland, M. Gleiser, and H. R. Muller, Oscillons: Resonant configurations during bubble collapse, Phys. Rev. D **52**, 1920 (1995), arXiv:hep-ph/9503217.

[6] S. Kasuya, M. Kawasaki, and F. Takahashi, I-balls, Phys. Lett. B **559**, 99 (2003), arXiv:hep-ph/0209358.

[7] M. A. Amin and D. Shirokoff, Flat-top oscillons in an expanding universe, Phys. Rev. D **81**, 085045 (2010), arXiv:1002.3380 [astro-ph.CO].

[8] M. Kawasaki, F. Takahashi, and N. Takeda, Adiabatic Invariance of Oscillons/I-balls, Phys. Rev. D **92**, 105024 (2015), arXiv:1508.01028 [hep-th].

[9] M. A. Amin, K-oscillons: Oscillons with noncanonical kinetic terms, Phys. Rev. D **87**, 123505 (2013), arXiv:1303.1102 [astro-ph.CO].

[10] M. Ibe, M. Kawasaki, W. Nakano, and E. Sonomoto, Decay of I-ball/Oscillon in Classical Field Theory, JHEP **04**, 030, arXiv:1901.06130 [hep-ph].

[11] E. I. Sfakianakis, Analysis of Oscillons in the SU(2) Gauged Higgs Model, (2012), arXiv:1210.7568 [hep-ph].

[12] J. Olle, O. Pujolas, and F. Rompineve, Recipes for oscillon longevity, JCAP **09**, 015, arXiv:2012.13409 [hep-ph].

[13] M. P. Hertzberg, Quantum Radiation of Oscillons, Phys. Rev. D **82**, 045022 (2010), arXiv:1003.3459 [hep-th].

[14] N. Fonseca, E. Morgante, R. Sato, and G. Servant, Axion fragmentation, JHEP **04**, 010, arXiv:1911.08472 [hep-ph].

[15] D. G. Levkov, V. E. Maslov, E. Y. Nugaev, and A. G. Panin, An Effective Field Theory for large oscillons, JHEP **12**, 079, arXiv:2208.04334 [hep-th].

[16] G. Fodor, A review on radiation of oscillons and oscillatons, Ph.D. thesis, Wigner RCP, Budapest (2019), arXiv:1911.03340 [hep-th].

[17] M. A. Amin, R. Easther, H. Finkel, R. Flauger, and M. P. Hertzberg, Oscillons After Inflation, Phys. Rev. Lett. **108**, 241302 (2012), arXiv:1106.3335 [astro-ph.CO].

[18] M. Gleiser and D. Sicilia, A General Theory of Oscillon Dynamics, Phys. Rev. D **80**, 125037 (2009), arXiv:0910.5922 [hep-th].

[19] E. Farhi, N. Graham, V. Khemani, R. Markov, and R. Rosales, An Oscillon in the SU(2) gauged Higgs model, Phys. Rev. D **72**, 101701 (2005), arXiv:hep-th/0505273.

[20] N. Graham, An Electroweak oscillon, Phys. Rev. Lett. **98**, 101801 (2007), [Erratum: Phys.Rev.Lett. 98, 189904 (2007)], arXiv:hep-th/0610267.

[21] S.-Y. Zhou, E. J. Copeland, R. Easther, H. Finkel, Z.-G. Mou, and P. M. Saffin, Gravitational Waves from Oscillon Preheating, JHEP **10**, 026, arXiv:1304.6094 [astro-ph.CO].

[22] G. Fodor, P. Forgacs, Z. Horvath, and A. Lukacs, Small amplitude quasi-breathers and oscillons, Phys. Rev. D **78**, 025003 (2008), arXiv:0802.3525 [hep-th].

[23] T. Hiramatsu, E. I. Sfakianakis, and M. Yamaguchi, Gravitational wave spectra from oscillon formation after inflation, JHEP **03**, 021, arXiv:2011.12201 [hep-ph].

[24] F. Van Dissel and E. I. Sfakianakis, Symmetric multifield oscillons, Phys. Rev. D **106**, 096018 (2022), arXiv:2010.07789 [hep-th].

[25] H.-Y. Zhang, M. A. Amin, E. J. Copeland, P. M. Saffin, and K. D. Lozanov, Classical Decay Rates of Oscillons, JCAP **07**, 055, arXiv:2004.01202 [hep-th].

[26] H.-Y. Zhang, Gravitational effects on oscillon lifetimes, JCAP **03**, 102, arXiv:2011.11720 [hep-th].

[27] S. Antusch, F. Cefalà, and F. Torrentí, Properties of Oscillons in Hilltop Potentials: energies, shapes, and lifetimes, JCAP **10**, 002, arXiv:1907.00611 [hep-ph].

[28] S. Antusch, F. Cefala, S. Krippendorf, F. Muia, S. Orani, and F. Quevedo, Oscillons from String Moduli, JHEP **01**, 083, arXiv:1708.08922 [hep-th].

[29] M. A. Amin, J. Braden, E. J. Copeland, J. T. Giblin, C. Solorio, Z. J. Weiner, and S.-Y. Zhou, Gravitational waves from asymmetric oscillon dynamics?, Phys. Rev. D **98**, 024040 (2018), arXiv:1803.08047 [astro-ph.CO].

[30] S. Antusch, F. Cefala, and S. Orani, What can we learn from the stochastic gravitational wave background produced by oscillons?, JCAP **03**, 032, arXiv:1712.03231 [astro-ph.CO].

[31] J. Ollé, O. Pujolàs, and F. Rompineve, Oscillons and Dark Matter, JCAP **02**, 006, arXiv:1906.06352 [hep-ph].

[32] M. Kawasaki, W. Nakano, and E. Sonomoto, Oscillon of Ultra-Light Axion-like Particle, JCAP **01**, 047, arXiv:1909.10805 [astro-ph.CO].

[33] A. Arvanitaki, S. Dimopoulos, M. Galanis, L. Lehner, J. O. Thompson, and K. Van Tilburg, Large-misalignment mechanism for the formation of compact axion structures: Signatures from the QCD axion to fuzzy dark matter, Phys. Rev. D **101**, 083014 (2020), arXiv:1909.11665 [astro-ph.CO].

[34] E. Cotner, A. Kusenko, and V. Takhistov, Primordial Black Holes from Inflaton Fragmentation into Oscillons, Phys. Rev. D **98**, 083513 (2018), arXiv:1801.03321 [astro-ph.CO].

[35] N. Kitajima, J. Soda, and Y. Urakawa, Nano-Hz Gravitational-Wave Signature from Axion Dark Matter, Phys. Rev. Lett. **126**, 121301 (2021), arXiv:2010.10990 [astro-ph.CO].

[36] N. Kitajima, K. Kogai, and Y. Urakawa, New scenario of QCD axion clump formation. Part I. Linear analysis, JCAP **03** (03), 039, arXiv:2111.05785 [astro-ph.CO].

[37] M. Hindmarsh and P. Salmi, Oscillons and domain walls, Phys. Rev. D **77**, 105025 (2008), arXiv:0712.0614 [hep-th].

[38] J. Braden, J. R. Bond, and L. Mersini-Houghton, Cosmic bubble and domain wall instabilities II: Fracturing of colliding walls, JCAP **08**, 048, arXiv:1505.01857 [hep-th].

[39] J. R. Bond, J. Braden, and L. Mersini-Houghton, Cosmic bubble and domain wall instabilities III: The role of oscillons in three-dimensional bubble collisions, JCAP **09**, 004, arXiv:1505.02162 [astro-ph.CO].

[40] A. Vaquero, J. Redondo, and J. Stadler, Early seeds of axion miniclusters, JCAP **04**, 012, arXiv:1809.09241 [astro-ph.CO].

[41] M. Gorghetto, E. Hardy, and G. Villadoro, More axions from strings, SciPost Phys. **10**, 050 (2021), arXiv:2007.04990 [hep-ph].

[42] N. Kitajima, F. Kozai, F. Takahashi, and W. Yin, Power spectrum of domain-wall network, and its implications for isotropic and anisotropic cosmic birefringence, JCAP **10**, 043, arXiv:2205.05083 [astro-ph.CO].

[43] J. J. Blanco-Pillado, D. Jiménez-Aguilar, and J. Urrestilla, Exciting the domain wall soliton, JCAP **01**, 027, arXiv:2006.13255 [hep-th].

[44] G. Dvali and C. Gomez, Black Hole's Quantum N-Portrait, Fortsch. Phys. **61**, 742 (2013), arXiv:1112.3359 [hep-th].

[45] G. Dvali and C. Gomez, Landau–Ginzburg limit of black hole's quantum portrait: Self-similarity and critical exponent, Phys. Lett. B **716**, 240 (2012), arXiv:1203.3372 [hep-th].

[46] G. Dvali and C. Gomez, Black Holes as Critical Point of Quantum Phase Transition, Eur. Phys. J. C **74**, 2752 (2014), arXiv:1207.4059 [hep-th].

[47] J. N. Hormuzdiar and S. D. H. Hsu, Pion breather states in QCD, Phys. Rev. C **59**, 889 (1999), arXiv:hep-ph/9805382.

[48] J. N. Hormuzdiar and S. D. H. Hsu, On spherically symmetric breathers in scalar theories, (1999), arXiv:hep-th/9906058.

[49] Y.-J. Wang, Q.-X. Xie, and S.-Y. Zhou, Excited oscillons: cascading levels and higher multipoles, (2022), arXiv:2210.04969 [hep-th].

[50] L. M. Widrow, Dynamics of Thick Domain Walls, Phys. Rev. D **40**, 1002 (1989).

[51] D. Cyncynates and T. Giurgica-Tiron, Structure of the oscillon: The dynamics of attractive self-interaction, Phys. Rev. D **103**, 116011 (2021), arXiv:2104.02069 [hep-ph].

[52] M. P. Kinach and M. W. Choptuik, Dynamical evolution of $U(1)$ gauged Q-balls in axisymmetry, (2022), arXiv:2211.11198 [hep-th].

9 Soft oscillons

Soft Oscillons

Fabio van Dissel and Oriol Pujolàs

Institut de Física d'Altes Energies (IFAE) and Barcelona Institute of Science and Technology (BIST), Campus UAB, 08193 Bellaterra, Barcelona, Spain

Abstract. We present a novel type of soliton dubbed soft oscillons. In contrast with conventional oscillons the soft counterparts come in a continuum of unboundedly large sizes. They are peculiar also in that the oscillation frequency is set by their size and in their high harmonic content, that leads to a peculiar core structure and pulsating emission of radiation. Soft oscillons appear in a broad class of scalar field theories with plateau potentials and owe their existence to a simple confinement mechanism: a large field perturbation automatically acts as a cavity that traps massless modes. We study the classical evaporation rate, lifetime and stability under anisotropic deformations. Soft oscillons are longer lived in gapless models, where lifetimes can reach 100 times the initial radius or more.

Contents

1 Introduction **206**

2 Minimal models **209**
2.1 Shooting around 212

3 Bag model **215**
3.1 Spherical cavity 215
3.2 Quantum fingerprint 218
3.3 Cavity skin profile 219

4 The soft oscillon branch **221**
4.1 Numerical solutions 223
4.2 Radiation and global evolution 225
4.3 Clean and dirty regimes 229
4.4 Attractiveness 234

5 Evaporation **236**
5.1 Analytics 238
5.1.1 Clean regime 238
5.1.2 Critical radius and the dirty regime 241
5.2 Comparison to numerics 247

6 Anisotropies **250**

7 Conclusion **253**

1 Introduction

Oscillons are non-topological defects that arise quite generically in many massive bosonic theories due to attractive self-interactions [1–5]. Indeed a wide variety of models exhibit the formation of long-lived, localised states oscillating at frequencies below the mass threshold in the semi-classical limit [6–21]. See also Refs. [3–5, 22–28, 28–30, 30–41] for applications to early universe cosmology, dark matter [42–48] and topological defects [4, 5, 49–55].

While the oscillon lifetime is substantially model dependent, their size is typically set by the boson Compton radius,

$$R_o \simeq (\text{few}) \cdot m^{-1} \ . \tag{1.1}$$

This can be understood as resulting from the competition between gradient and potential terms that takes place in the oscillon core. Alternatively, from the QFT perspective, oscillons correspond to many particle bound states [56–60], see also [14, 18, 61, 62]. Since the theory is bosonic, particles can be in the same single-particle state. For moderately small binding energies the typical spread of this state is not far from the Compton wavelength, which reproduces (1.1).

In this work, we aim to challenge the 'universal' relation for the oscillon size (1.1). We will show that under some conditions, a new type of oscillon state emerges, with remarkably different properties. In particular, we will show that well defined oscillons with a continuum of sizes

$$R_o \gg m^{-1}$$

actually exist in a rather broad class of models. This is a new oscillon branch, mainly characterized by its size R_o (and low oscillation frequency $w \sim 1/R_o \ll m$), which is why we dub them *soft* oscillons.

We focus the discussion on the simplest conceivable theory of a single real scalar field with only self-interactions. (Gravity is unimportant for oscillons, so we 'set' $G_N = 0$) The key property for a theory to contain soft oscillons is that the scalar potential $V(\phi)$ flattens out to a plateau at large field. A simple example is

$$V(\phi) = \frac{1}{2}\frac{m^2\,\phi^2}{1+\phi^2/\Lambda^2} \ . \tag{1.2}$$

This potential is basically flat for $\phi \gg \Lambda$ and massive for $\phi \lesssim \Lambda$. This clearly leads to a confining effect: a localized configuration (or 'lump') with large field displacement $\phi_0 \gg \Lambda$ in this theory inevitably becomes equivalent to a cavity, the field being effectively massless inside and massive outside, see Fig. 1. The radius R of the cavity, corresponding to the region where $\phi \sim \Lambda$, is naturally expected to increase with the field amplitude ϕ_0. Balancing the (constant) potential and gradient terms one quickly sees that the amplitude and radius are linked as $\phi_0 \sim \Lambda m R$, so indeed large radii

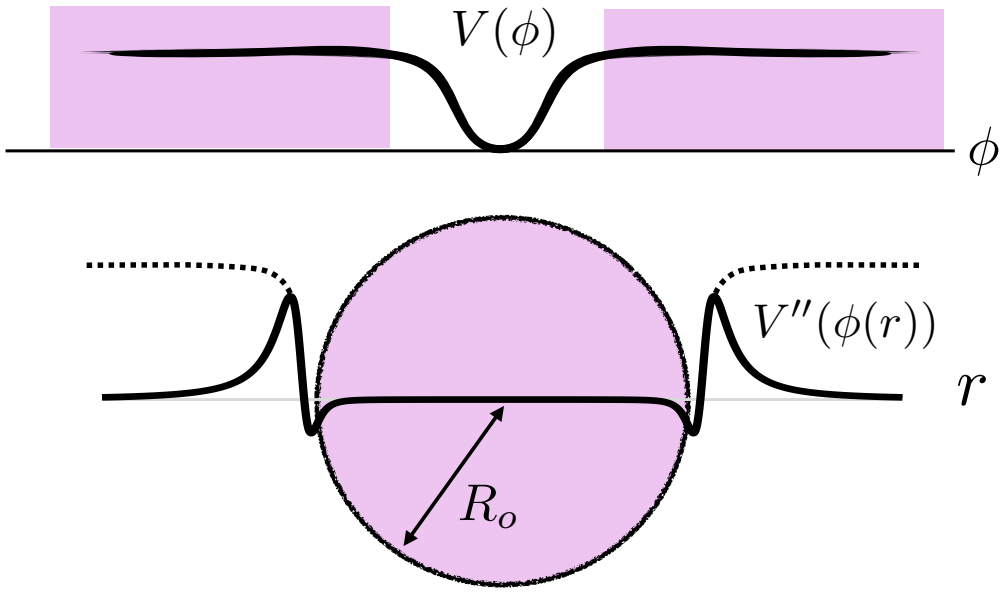

Figure 1. Illustration of the *cavity effect* arising in scalar theories with a plateau potential $V(\phi)$ (upper panel). Given a 'background' lump $\phi_o(r)$ with large field excursion, high field values correspond to the interior of the lump. The effective mass-squared of the field fluctuations (lower panel) is given by $V''(\phi_o(r))$ and it vanishes inside the lump. For massive theories such as (1.2) (dotted line) it approaches m^2 outside, resulting in a strong confining cavity effect. In quartic+plateau potentials such as (1.3), the effective mass vanishes away from the lump, but a localized effective mass term is induced on the surface. This still results in a confining cavity for large radii R_o and a more stable evolution.

$R \gg 1/m$ can be obtained with large amplitudes $\phi_0 \gg \Lambda$.

At such high field amplitudes the oscillons must be dramatically different than the conventional oscillons. The characteristic oscillation frequency can only be set by the object size

$$\omega \sim \frac{1}{R_o} \ll m \ ,$$

which can be much smaller than the mass threshold. This is in principle the perfect condition for tiny evaporation and so for a long-lived oscillon-like state.

The 'bad news' for massive models like (1.2) is that the confining effect of the mass term is actually too strong. For the cavity effect to lead to oscillons, maintaining the coherence of the field is crucial. An excessive confinement of modes tends to spoil coherence and these oscillons end up having short lifetimes in massive theories.

Our main finding is that the cavity effect is instead viable for oscillons in gapless

models, by which we mean that the field has a potential but the effective mass vanishes at the minimum. Generically the form of these potentials reduces to a quartic coupling (near $\phi = 0$) that continues to a plateau at large field. A prototypical example is

$$V(\phi) = \frac{M^2}{\Lambda^2} \frac{\phi^4}{(1 + \phi^2/\Lambda^2)^2} \ , \tag{1.3}$$

but the precise form is not important. At large field $\phi \gg \Lambda$ the potential plateaus as before but now the field is massless near $\phi = 0$, that is outside the cavity. The mass parameter M does not correspond to the mass of asymptotic states. Instead it sets the maximal effective mass that occurs at the cavity surface, where $\phi \sim \Lambda$, see Fig. 1.

Thus, a large amplitude oscillon also dynamically realizes a cavity, now with the field massless both inside and outside. The field being massless outside facilitates the emission of radiation – a welcome feature because the cavity can possibly shed the coherence-spoiling part of the field. As we will see, in contrast with the gapped case (1.2), a clear attractor with self-similar evolution indeed emerges in gapless models.

Our soft oscillons are different from the oscillons that have recently been found in gapless theories [19], see also [63, 64]. Those oscillons have a fixed size (set by the equivalent of $1/M$). This might have lead to the conclusion that a generic relation between the size and the mass scale of the theory would also be present for gapless models. Our soft oscillons show that this is not necessarily the case. Their radius is parametrically larger than $1/M$, in fact almost unboundedly so.

As we will show in detail, the soft oscillon structure is quite rich: they have a large number of harmonics (up to $n_{max} \sim MR_o/\pi$), with a precise relative harmonic content, that corresponds to a neat space-time evolution in the core. The attractor solution develops spherical front waves (one outgoing and one ingoing) traveling through the interior of the cavity. This configuration has the virtue that near the cavity surface the field is static most of the time, which of course implies that the emission of radiation is minimized.

Many of the properties of this new soft oscillon attractor can be understood with a bag model that exploits the cavity effect. In fact, our bag model is remarkably close to the MIT bag model of hadrons [65], so much so that it seems appropriate to say that oscillons in plateau potentials *realize* MIT bags.

The evaporation of soft oscillons is also quite interesting. Two clearly separated regimes can be identified depending on how the oscillon size compares with a certain critical radius R_c. Below R_c the dominant attractor is *clean*, it is maintained with fewer modes. Correspondingly the evaporation rate is low and characterized with the total emitted power scaling linearly with R_o. For $R_o > R_c$ instead, a *dirty* regime appears, with many more modes excited and emitted power scaling like R_o^2. We offer

both numerical and analytic evidence of this below.

The rest of this article is structured as follows. In Section 2 we discuss general aspects of the theories under study. We also show the oscillons that are obtained using 'random' initial conditions, far from the actual attractor, but which delivers sufficient hints to reveal the attractor. In Sec. 3 we give a simple bag model description of the attractor exploiting the cavity picture. In Sec. 4 we show the soft oscillons found numerically. In Sec. 5 we discuss evaporation, including both a theoretical estimate and the numerical results in the two regimes, above and below R_c. In Sec. 6 we show the effect of anisotropic perturbations using 3D lattice simulation, and we conclude in Sec. 7.

2 Minimal models

We start by specifying the requirements on a model to harbor soft oscillons. We shall restrict the discussion to the simplest model consisting in a single real scalar field ϕ, and with a standard kinetic term. The theory is then specified by the form of the scalar potential $V(\phi)$. In full generality, this can be written in terms of a generic function $\mathcal{V}$ as

$$V(\phi) = M^2\,\Lambda^2\,\mathcal{V}\left(\frac{\phi}{\Lambda}\right) \tag{2.1}$$

with M and Λ two mass scales. To ensure that the theory is weakly coupled, we assume that they are well separated as

$$M \ll \Lambda\ . \tag{2.2}$$

This regime is a small deformation of the shift invariant theory ($V = 0$). The choice $\mathcal{V}(x) = 1 - \cos x$ corresponds to an axion (or sine-Gordon), M plays the role of the axion mass and Λ the decay constant.

We write the potential in more general form because we are interested in the important case of massless ϕ. This is of course not incompatible with a nonzero potential $V(\phi)$. Rather it only requires a vanishing mass, that is, no quadratic term in the expansion near the vacuum. Assuming a Z_2 symmetry for simplicity $V(-\phi) = V(\phi)$, the gapless case is obtained by a generic function $\mathcal{V}$ of the form

$$\mathcal{V}(x) = \sum_{n=2}^{\infty} g_{2n}\,x^{2n} \tag{2.3}$$

where the coefficients g_{2n} being generically $O(1)$. This leads to

$$V(\phi) = \lambda\,\phi^4\,\left(1 + c_6\,\frac{\phi^2}{\Lambda^2} + \cdots\right) \tag{2.4}$$

with the quartic coupling identified as

$$\lambda = g_4\frac{M^2}{\Lambda^2}\ \ll 1\ . \tag{2.5}$$

At the same time, all of the coefficients $c_{2n} = g_{2n}/g_4$ are $O(1)$ pure numbers. Of course, we restrict to $\lambda > 0$ (otherwise $\phi = 0$ is not even a minimum). Notice that this implies that the lowest term, the quartic coupling, is of repulsive nature. Hence, the terms responsible for sustaining oscillons must be ϕ^6 and/or higher. That is, the coefficients c_6 and higher must be sufficiently negative, something that indeed happens in plateau potentials. We will refer to these potentials as having a *quartic+plateau* form.

The absence of a ϕ^2 term is certainly a fine-tuning, however this is a secondary concern since our main goal here is to show the new phenomenon that arises in gapless theories. Moreover, it is easy to envisage simple extensions of the minimal theory where masslessness is natural (see below). Importantly, the new degrees of freedom in these extensions do not affect the soft oscillons. For these reasons, we will proceed with the analysis of the gapless theory as the case for which the potential 'starts' with the quartic term.

The general form (2.1) makes manifest that we are dealing with an effective field theory (EFT) for the possibly massless scalar ϕ with an EFT cutoff determined by Λ (barring factors of 4π). We are going to look for semiclassical configurations in this EFT and we need to make sure that they are within the validity of the EFT. The separation of scales (2.2), or equivalently the smallness of the quartic coupling λ enforces that the solutions are within the EFT regime. Indeed, introducing

$$\varphi \equiv \frac{\phi}{\Lambda} \,, \tag{2.6}$$

the equation of motion reads

$$\Box\varphi - M^2\,\mathcal{V}'(\varphi) = 0 \tag{2.7}$$

so the nonlinear solutions (amplitude of order $\varphi \gtrsim 1$) are going to be characterized with gradients of order $M \ll \Lambda$. Recently [19] has given explicit examples of oscillons in a gapless model. The shape of the potential assumed in [19] is a double well and differs from our main focus, but the size of their oscillons is defined by the (inverse) mass scale analogous to our M, which is present in the model in spite of being gapless.

The situation is actually qualitatively similar to massive theories: near $\phi = 0$ a field 'lump' tends to expand, both because of radiation pressure and from repulsion from $\lambda > 0$. Formally this is parallel to what happens for oscillons in massive theories, where the mass term induces a repulsive-like effect. At large field, V is attractive if (sufficiently negative) self interactions can compensate the repulsion, and a localized object can be form. Naively, one expects that the condition on the set of g_n for this to happen is that V is smaller than either $m^2\phi^2/2$ or $\lambda\phi^4$ at $\phi \gtrsim \Lambda$ for the massive and massless theory respectively.

In this work we shall mainly discuss theories with plateau potentials

$$V(\phi) \simeq \text{const} \quad \text{for} \quad \phi \gtrsim \Lambda. \tag{2.8}$$

This type of potential admits especially interesting solutions with parametrically large size $R_o \gg 1/M$, to which we will refer as 'soft' oscillons. We anticipate that these solutions contain large field 'excursions' $\Delta\phi \gg \Lambda$, significantly larger than the scale Λ where the plateau starts. From the EFT perspective this is not *per se* an obstruction. In the case of axionic models, large field excursions have been studied at length [66]. The presence of large field-variations in the initial state is also quite clearly not a problem. (In axion models one could compare this to the initial state of a large number of domain walls, a configuration that is certainly captured by the low energy EFT.) A more non-trivial condition (that we impose on ourselves) is that the time evolution of such initial state remains within the applicability range of the EFT. As we shall see, this is indeed the case for our soft oscillons. At all points in the evolution the maximum space- and time- gradients everywhere on the solutions are near the soft scale M, well below the cutoff Λ.

For the sake of simplicity, we shall also impose that gravitational effects are small. This can be expressed in 4 different ways: i) small Newtonian potential at the oscillon surface, ii) small expansion rate inside the oscillon iii) being far from a black hole (R_o much larger than the Schwarzchild radius), and iv) requiring sub-Planckian field excursions. Interestingly enough, all these requirements reduce to a unique condition, setting an upper limit to the oscillon radius $MR_o \gg M_P/\Lambda$, with M_P the Planck mass. Having in mind sub-Planckian values of Λ this still gives room for large oscillons as we defined them $MR_o \gg 1$.

We now return to the issue of naturalness of the gapless potentials. Setting a vanishing mass ($g_2 = 0$ in the language of (2.1)) is of course a fine tuning. This is not a big concern for the purpose of this work because it does not affect the consistency of the theory. Let us add, though, that the model can certainly be augmented with a mechanism that preserves $m_\phi = 0$ naturally. For example, supersymmetry. The minimal SUSY extension of the real scalar consists in a chiral multiplet, that is an additional scalar χ and chiral fermion ψ. The resulting theory has a total of 4 massless degrees of freedom and the full lagrangian can be obtained from a superpotential $\mathcal{W}$, which leads to a potential $V = |d\mathcal{W}/d\Phi|^2$ with $\Phi = \phi + i\chi$ the complex scalar. To fix ideas, one can think of $\mathcal{W} = \Phi^3/(1+\Phi^2)$, which does not correspond precisely to (1.3) but is structurally of quartic+plateau form. It is easy to check that a nontrivial background for the real part ϕ is consistent classically with all the other fields set to 0, hence the classical analysis is unaffected. At quantum mechanical level, radiation of superpartners is expected, of course. Quantum radiation is also emitted by the real part ϕ, that provides the oscillon background. Since the oscillon emits classical radiation, though, one expects that the quantum evaporation is subleading. (A nontrivial effect from quantum radiation is the appearance of a quantum break time [59, 60], but we leave this for future work [67].) In practice, then, we can ignore the effects from any partners that may be responsible for keeping $m_\phi = 0$ naturally.

Let us point out an additional interesting property of the quartic+plateau poten-

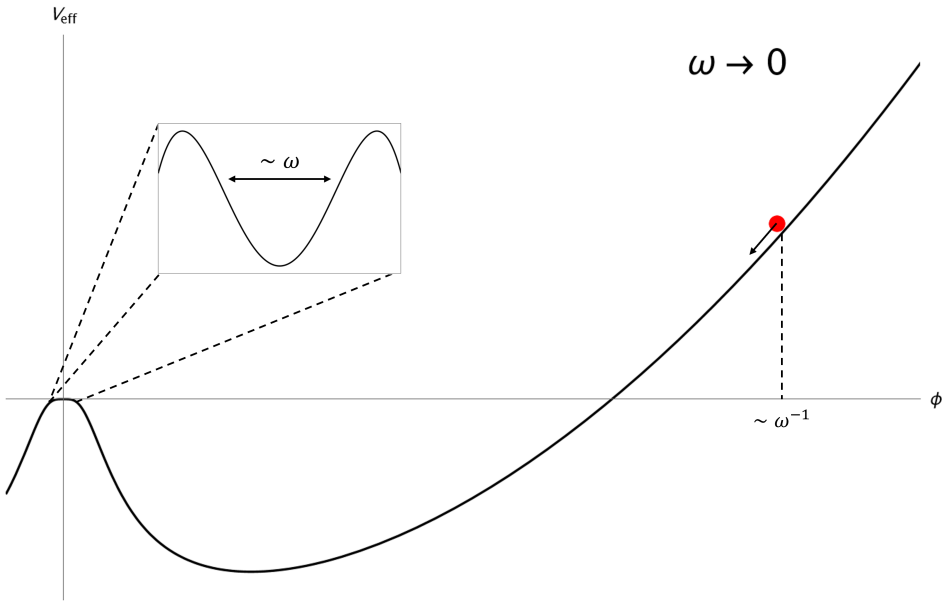

Figure 2. Although there are strictly speaking no bound breather modes in a gapless theory, there is a well-defined shooting problem to try and construct large amplitude and large radius oscillons. There are large, breather-like objects, whose radiation-tail can be asymptotically small.

tial $V(\phi)$. At high field, $V(\phi)$ is approximately shift-invariant. On the other hand, at small ϕ, the theory is invariant under dilatations. The quartic+plateau potential then represents a renormalization group flow from a shift symmetric to a conformal theory in the infrared. This suggests an embedding in a 5D model with a geometry that interpolates from 5D Anti-de Sitter to 5D Minkowski spacetime. Notice also that the quartic+plateau potential arises (in the Enstein frame) for a scale-invariant field nonminimally coupled to gravity [68, 69].

2.1 Shooting around

In massive theories, the scalar potential provides a natural frequency below which one can search for single-frequency breather modes that are bounded at spatial infinity, namely the mass m. In standard oscillon literature one then identifies each breather profile of frequency ω with the fundamental mode of the oscillon that exists at that frequency. To find localized breathers one looks for the unique solution of the ODE

$$\nabla^2\phi_{br} + (\omega^2 - m^2)\phi_{br} - V'_{eff}(\phi_{br}) = 0, \tag{2.9}$$

that satisfies the boundary condition $\phi_{br} \to e^{-\sqrt{m^2-\omega^2}\,r}$ as $r \to 0$. The effective potential is given by

$$V_{eff}(\phi) = \frac{1}{\pi}\int_0^{2\pi} dt'\, V_{nl}(\phi\cos(t')), \tag{2.10}$$

where $V_{nl}(\phi)$ is the nonlinear part of the scalar potential of the theory under consideration. This framework for understanding oscillons is well established in the literature.

However, in gapless theories, where $m^2 = 0$, a similar procedure leads to the conclusion that one can only find breather modes that have a radiative boundary condition $\phi_{br} \to e^{i\omega r}$ at spatial infinity. Furthermore, there is no unique solution that one can tentatively identify with an oscillon state. This situation seems somewhat dire to try and apply the standard toolkit to search for oscillons in massless theories. For certain potentials, in particular plateau potentials, something interesting happens to the breather equation (2.9) when $m^2 = 0$. Although there is no exponentially decaying solution that asymptotes to 0 (the true vacuum), there is now a unique solution that obeys $\phi_{br} \to e^{-r} + A\omega$ as $r \to \infty$. Here A should be interpreted as some $O(1)$ number. In the limit $\omega \to 0$, there exists a breather solution that is exponentially trapped and asymptotes to the true vacuum of the theory. Note that that solution will also have infinite size R_o.

We can look for the approximately localized solution of Eq. (2.9) through a numerical shooting problem, common in the oscillon literature. One solves the ODE with boundary conditions $\phi_{br}(0) = \phi_0$ and $\phi'_{br}(0) = 0$, and adjusts ϕ_0 until the solution obeys the appropriate boundary condition at $r \to \infty$. The procedure is analogous to the classical mechanics problem of releasing a ball in a potential landscape and searching for the correct initial release point so that the ball halts exactly at a local maximum of the potential (a hilltop). A schematic representation of the problem is shown in Fig. 2.

Since we are only interested in breather solutions that asymptote to something that is close to the true vacuum of the theory, we are necessarily interested in small frequencies $\omega \to 0$. Unlike standard oscillons where the size of the object is set by the mass, $R_o \sim m^{-1}$, these breather states can be arbitrarily large. In particular one has the relation $R_o \approx \pi/\omega$, so that $R_o \to \infty$ as $\omega \to 0$. It is interesting to see whether these ansatzes obtained through the shooting problem, remain localized when evolved with the full equations of motion. In Figs. 3 and 4, we show the result of numerically evolving a field configuration in a typical massless plateau potential, starting from the initial conditions $\phi(t = 0, r) = \phi_{br}(r)$ and $\dot{\phi}(t = 0, r) = 0$. We are intentionally vague concerning the exact shape of the potential, as this work will show that the type of soft oscillons that we describe can exist in any plateau potential.

Although the spatial-temporal profiles shown in Figs. 3 and 4 still show an oscillatory envelope, typical for oscillons, it is abundantly clear that the standard picture in which the oscillon is described by a bounded breather mode sourcing a small radiative tail, is no longer a sufficient description of the oscillatory solutions we find. In particular, higher harmonics can become of the same order as the fundamental mode as $R_o \to \infty$. To make progress in understanding these solutions, we will have to find a better ansatz that describes these oscillons with large radius R_o and amplitude ϕ_0, and small frequency ω. We will proceed to construct such an ansatz in Sec. 3, inspired by the results of Figs. 3 and 4. Note in particular that in Fig. 4, that as $R_o \to \infty$, the breather solution dynamically settles into a constant interior, connected to the vacuum

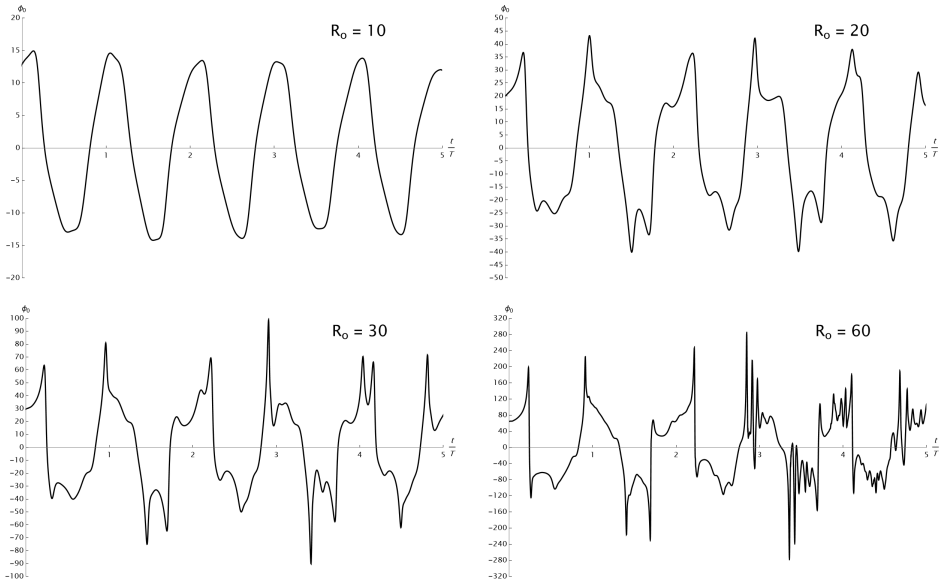

Figure 3. The amplitudes of the solutions at the origin $r = 0$ vs time in units of the period of the background. There is an approximate relation between the principal frequency and radius as $R_0 = \pi/\omega$. It is clear that as the solution becomes larger, the frequency content of the solution becomes larger as well. The classic oscillon described by a single harmonic is no longer a sufficient description as $R_0 \to \infty$.

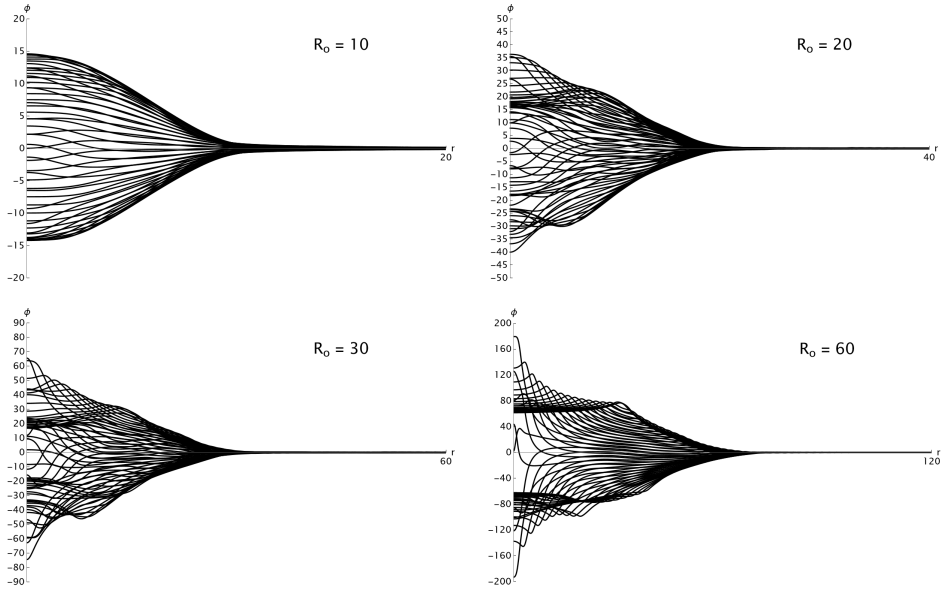

Figure 4. The spatial profiles of the solutions, where each line corresponds to a different time. The suggestion of a different type of ansatz emerges.

at $r \to \infty$ by a static envelope.

3 Bag model

From the arguments of Sec. 2 and the numerical time evolution of a 'random' initial condition, it is clear that the oscillons for plateau potentials in the soft limit $MR_o \gg 1$ have completely different characteristics compared to any oscillon discussed previously in the literature. The purpose of this Section is to get some first glimpse of this new regime. Inspired by the *cavity effect* inherent to plateau potentials, the first toy model consists in ignoring the radiation from the oscillon and view it simply as a perfect cavity populated with a massless field. We shall refer to this as a *bag model*. In fact, this approximation is very reminiscent of the MIT bag model for hadrons [65].

As we will see, even at zero-th order in the leakage of radiation a special configuration emerges in this bag model. Moreover, this sets the language to compute the evaporation rate. To that end, a closer look at the cavity surface (which we also refer to as *skin*) will be needed. We do so in Sec. 3.3.

3.1 Spherical cavity

Let us now bring some light into why the peculiar oscillon announced in the Introduction should exist. The key observation is that a configuration $\phi(t, r)$ with a large field displacement living in a plateau potential, has an effective mass that is a localized surface mass term

$$V''(\phi(r,t)) \simeq v(t)\delta(r - R_o)$$

In the $MR_o \gg 1$ limit, $v(t)$ stays constant during most of the oscillation period, so it can be approximated by a constant. Its value is set by the characteristic mass in the theory, M. Therefore, the first order approximation (accurate up to $1/MR_o$ corrections) reduces to that of a massless free field in a cavity[1] with a large surface mass term (compared to the cavity characteristic frequencies, of order $1/R_o$). This motivates the approximation of simply ignoring the exterior region and switching to the problem of a massless field inside a perfect cavity with a Dirichlet boundary condition $\phi(r = R_o) = 0$. This is of course the equivalent of working at zero-th order in the emitted radiation. Notice that this picture is the same as [65] only with the field satisfying Dirichlet instead of Neumann boundary condition on the bag.

In this approximation an accidental superposition principle emerges even though the theory is nonlinear. Among the infinitely many available solutions, we must seek a special configuration that minimizes the energy loss of the oscillon. The existence and longevity of oscillons is always connected to a reduced time-dependence in the oscillon core. The most special solution in the cavity then is one where the field is actually *constant* near the cavity surface during most of the oscillation period. Clearly the only static near-surface solution that vanishes at the surface must be proportional

[1] Ref. [70] has recently discussed a somewhat similar setup with the nonlinear field equation restricted to a 'ball' or cavity of fixed radius, intended to capture the small amplitude regime. The main difference with our case is that we consider large amplitude and, more importantly, the cavity arises dynamically in our setup.

to $1 - R_o/r$. This must be matched to some other exact solution of $\Box\phi = 0$ to avoid a singularity at $r = 0$. This is certainly possible thanks to the following property of the massless wave equation. Any pair of solutions of $\Box\phi = 0$, say $\phi_{1,2}$ (say, with different values of $X \equiv \partial_\mu\phi\partial^\mu\phi = \dot\phi^2 - \phi'^2$) that match continuously on a light-like region (a radiation front) delivers a new piece-wise defined solution that coincides with ϕ_1 or ϕ_2 on either side of the front. This allows to extend the near-surface static solution inwards easily by looking for solutions that overlap well on radiation fronts. It is easy to see that in each quarter of a cycle the 3 solutions involved are: $1 - R_o/r$ (with $X < 0$), t/r ($X > 0$) and a constant ($X = 0$), and we need two spherical fronts, one out-going and the other in-going.

The full solution can be written piece-wise[2] in spacetime regions separated by the exterior and interior concentrical fronts $r_{ext,\,int}(t)$,

$$\phi_{bag}(t,r) = \phi_0 \begin{cases} \mathrm{sq}\left(\dfrac{t}{2R_o}\right) & r < r_{int}(t) \\ \mathrm{tr}\left(\dfrac{t}{2R_o}\right)\dfrac{R_o}{2r} & r_{int}(t) < r < r_{ext}(t) \\ \mathrm{sq}\left(\dfrac{t}{2R_o}\right)\left(\dfrac{R_o}{r} - 1\right) & r_{ext}(t) < r < R_o \\ 0 & r \geq R_o\ , \end{cases} \tag{3.1}$$

with $\mathrm{sq}(x) = \mathrm{sign}(\cos x)$ and $\mathrm{tr}(x) = \frac{2}{\pi}\arcsin\cos\pi\,x$ the unit period square and triangular waves, and

$$\begin{aligned} r_{int}(t) &= \frac{R_o}{2}\,\frac{\mathrm{tr}(t/2R_o)}{\mathrm{sq}(t/2R_o)} = \frac{R_o}{2}\,\frac{\mathrm{tr}(t/R_o)+1}{2} \\ r_{ext}(t) &= R_o - r_{int}(t)\ . \end{aligned} \tag{3.2}$$

A sketch of the profile and motion of this field configuration is shown in Fig. 5. Notice the peculiar structure of (3.1), consisting in 3 layers: constant field profile near the center, time-like gradient in between the fronts and the static outer profile. These layers are separated by an inward and an outward front traveling at the speed of light, that cross each other at $r = R_o/2$.

It is clear from (3.1) and Fig. 5 that the field evolution is coherent in the cavity in the sense that it changes sign and reaches maximum values globally. It is also clear that the configuration has a well defined and constant radius – where $\phi = 0$ in this approximation. (In the full numerical solutions this is replaced by where ϕ is of order Λ, and it coincides with where most of the energy is concentrated.) Interestingly, this constant overall radius coexists with the bouncing motion within the cavity due to the spherical fronts. Notice also that twice per cycle the inner front focuses at the origin,

[2]We thank A. Wereszczyński for pointing out that potentials of the form $V(\phi) = |\phi|$ admit exact oscillon solutions in piece-wise form [71].

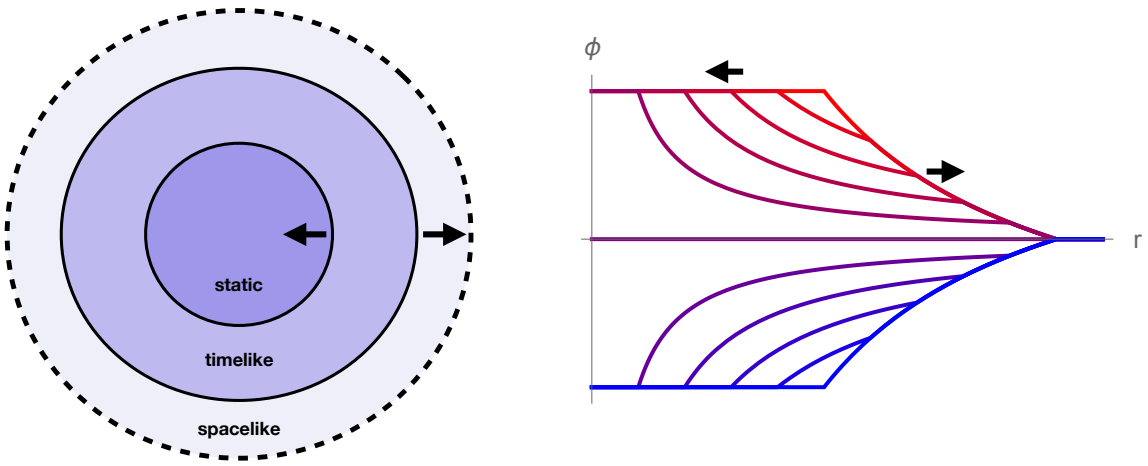

Figure 5. Sketch of the bag configuration (3.1), consisting in two concentric spherical fronts that bounce off the cavity surface. Snapshots of the field profile separated by equal times and for half a cycle are shown on the right. The fronts correspond to the points with discontinuous first derivative.

at which event also the field at the center abruptly changes sign. The large focusing is not a problem in the bag approximation because the field is effectively free while the amplitude is large. The sign flip (taking place in all the cavity) instead is not under control in this approximation since it implies probing small values of ϕ where the potential is noticeable. This leads to a physical effect, the 'dirty' regime of evaporation discussed in Sec. 5. However, since the sign flip is fast this is still a small effect and the idealized bag picture is still useful.

It is straightforward to compute the energy of the bag configuration (3.1),

$$E_{bag} = 4\pi \int r^2 \left(\frac{\phi'^2}{2} + V_0\right)\Big|_{\text{bounce}} = 8\pi\,\phi_0^2\,R + \frac{4\pi}{3} V_0\,R^3 \tag{3.3}$$

where $V_0 = \Lambda^2\,M^2$ is the value of the potential (everywhere in the cavity interior we are on the plateau) and the moment of the bounce refers to when the fronts meet, which is also when $\dot\phi = 0$ everywhere in the bag approximation. For reasons that will become clear in Sec. 3.3, the least radiating field configuration satisfies that the field gradient at the cavity surface relates to the value of the potential V_0 as

$$\frac{\phi'^2(R_o)}{2} = V_0. \tag{3.4}$$

(Notice that this is recognized as one of the two boundary conditions in the MIT bag model [65] for a static bag.) One reads from (3.1) that $\phi'(R) = \phi_0/R_0$ which leads to

$$\phi_0 = \sqrt{2}\,\Lambda\, M\, R_o \tag{3.5}$$

and

$$E_{bag} = \frac{16\pi}{3}\, M^2 \Lambda^2 R_o^3\ . \tag{3.6}$$

3.2 Quantum fingerprint

With this clear notion of the soft oscillon, we can move to a quantum mechanical language in the spirit of [56–58, 60, 72–76]. Thanks to the emergence of the cavity/bag the obvious natural procedure is to express the general state of the quantum field in a spherical cavity of radius R_o by the occupation numbers of each cavity mode

$$N_{nlm}\ . \tag{3.7}$$

The total energy is

$$E = \sum_{nlm} N_{nlm} w_{nlm} \tag{3.8}$$

For a perfect (non-leaking) cavity,

$$w_{nlm} = \frac{u_{n\,l}}{R_o} \tag{3.9}$$

with $u_{n\,l}$ the zeros of the spherical Bessel function $j_l(u)$. For large n, l, $u_{n\,l} \simeq \pi n + \pi l/2$. In a leaking cavity approximation where the field propagates outside, these modes would acquire a small imaginary part. Implicitly we are neglegting this, but it is clear that these are really resonant quasi-normal modes. For $l = 0$, the eigenfrequencies are

$$w_n = \frac{n\,\pi}{R_o} \tag{3.10}$$

and the $l = 0$ modes take the form

$$\phi_n = \frac{A}{\sqrt{n}} \frac{\sin \frac{n\pi r}{R_o}}{r} \tag{3.11}$$

with A an $n-$independent normalization constant.

In the bag approximation (3.1), the field at the origin $\phi(r = 0)$ evolves in time as a square wave, whose Fourier transform goes like $1/n$ (odd n's only). Thus the field is a sum of eigenmodes of the form $\phi(0) \sim \sum \phi_n(0)/n^{3/2}$, and we can read off the occupation numbers (recalling that we are dealing with a free field so the occupation

numbers are quadratic in ϕ_n). Putting it all together, the bag model (3.1) corresponds to a large occupation number of s-wave modes with a power law distribution

$$N_{n00} = \frac{128}{3\pi^2}\,\frac{\Lambda^2 M^2\,R_o^4}{n^3}\,\delta_{n,\,\rm odd}\ . \tag{3.12}$$

The overall amplitude follows by matched by requiring that the total energy matches (3.6) and using $\sum_{n\,odd} n^{-2} = \pi^2/8$.

The occupation numbers (3.12) exhibit some interesting properties: they follow a power-law distribution as expected by the absence of scales in the idealized bag model. The spectrum is very 'red', strongly dominated by the fundamental mode. For comparison, having the same amount of energy stored only in the fundamental mode leads to $N_{100} = \frac{16\pi^2}{3}\,\Lambda^2 M^2\,R_o^4$, which is larger than N_{100} in (3.12) by a factor $\simeq 12$. Notice also that (3.12) scales inversely with the coupling constant $\frac{1}{\lambda} \sim \frac{\Lambda^2}{M^2}$ as is common for oscillons in massive theories. In the soft limit $MR_o \gg 1$, it also scales with R_o, and with quite a strong dependence.

Recall that in the gapless theory the cavity effect arises from the large surface mass term, of order $M\delta(r-R_o)$, and the width of the delta function also of order $1/M$. Therefore the expressions are approximate, with corrections suppressed by $1/(MR_o)$ in the soft end of the spectrum. A finite skin mass term also implies that the total number of modes trapped in the cavity is finite. One expects that modes with frequencies

$$w_n \lesssim M$$

are 'confined' efficiently because M is the mass scale that characterizes the effective mass from the skin. Therefore one expects the highest harmonic have

$$n_{max} \simeq \frac{MR_o}{\pi}\ . \tag{3.13}$$

For this reason, a better picture of the background mode composition of the background is to cut it off beyond $n > n_{max}$,

$$N_{n00}^{(bag)} = \begin{cases} \dfrac{128\,\pi^2}{3}\,\dfrac{\Lambda^2}{M^2}\,\dfrac{n_{max}^4}{n^3} & n < n_{max} \ \text{ and odd} \\ 0 & n > n_{max} \end{cases} \tag{3.14}$$

An adiabatic evolution where the soft oscillon slowly evaporates and decreases its radius $R_o(t)$ translates in occupation number language in that the modes become depleated adiabatically by the time dependence implicit in $n_{max} = MR_o(t)/\pi$.

3.3 Cavity skin profile

Let us now move one step beyond the idealized bag model and look at the structure of the field near the edge of the effective cavity in the nonlinear theory. Namely, we are now aiming at solving the full equation of motion (2.7), and finding the static

near-surface profile. In the $MR_o \gg 1$ limit, zooming in on a narrow angular region the field profile near $r \simeq R_o$ is well approximated by a planar form where ϕ depends only on one cartesian coordinate, which we call z. Plugging the static ansatz $\phi(z)$ into the field equation leads to

$$\frac{\phi'(z)^2}{2} = V(\phi(z)) \ . \tag{3.15}$$

One immediately notices that in the interior region where ϕ has climbed the plateau $V(\phi) = V_0$ =const the field gradient is fixed. This justifies (3.4). In hindsight, it follows from staticity near the surface.

The solution to (3.15) can be viewed in a sense as 'half' a domain wall (DW), since it interpolates from the vacuum $\phi = 0$ at infinity to a large field value (analogous to the maximum in the potential for a theory with domain walls). This solution plays an important role, we will refer to it as the *half-DW* and will denote its profile as ϕ_{hDW}.

For quartic+plateau potentials, $\phi_{hDW}(z)$ generically approaches the vacuum asymptotically like $1/z$ for $z \to +\infty$, and grows linearly in z towards $z \to -\infty$. In between the two regimes $\phi_{hDW} \sim \Lambda$, which corresponds to the cavity skin. The precise form of the potential is not important. For the sake of illustration it is convenient to consider the particular choice

$$V(\phi) = 2\frac{M^2}{\Lambda^2}\frac{\phi^4}{(1+\phi^2/\Lambda^2)^2} \ , \tag{3.16}$$

for which the half-DW solution admits a simple closed form expression,

$$\phi_{hDW}(z) = \Lambda\left(\sqrt{1+(M\,z)^2} - M\,z\right) \ , \tag{3.17}$$

which we show in Fig. 6. As for regular DWs, the stress tensor has the form

$$T^{hDW}_{\mu\nu} = \rho(z)\ \mathrm{diag}\,(1,\,0,\,-1,\,-1\,) \tag{3.18}$$

implying equation of state parameter $w = -1$ and 0 in the transverse and longitudinal directions respectively. We denote by $\rho(z) = (\phi'^2/2 + V)|_{hDW}$ the energy density profile, which interpolates from 0 at $z \to +\infty$ to a constant in the interior region, see Fig. 6. (These equations of state are realized only in the near-surface region. The innermost region of (3.1) has constant field, so $w = -1$ in all directions.)

The half-DW profile is also useful to have a finer view of the confining mechanism. Having such large occupation numbers, the oscillon can be treated as a large semiclassical background. As usual, it is convenient to split the field ϕ into background and perturbations $\delta\phi$. Near the surface, the oscillon is well approximated by the half-DW so we write

$$\phi = \phi_{hDW}(z) + \delta\phi(t,z) \tag{3.19}$$

and the equation of motion leads to the Schrödinger-like equation for $\delta\phi$,

$$(\Box + V''(\phi_{hDW}(z)))\,\delta\phi = 0 \tag{3.20}$$

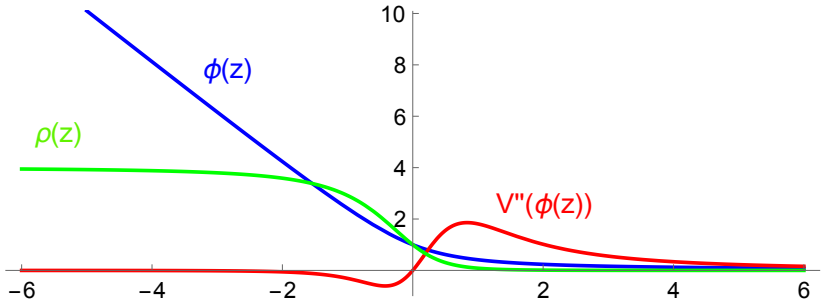

Figure 6. Field profile in units of Λ (blue), energy density $\rho(z) = \phi'^2/2 + V(\phi)$ in units of $M^2\Lambda^2$ (green) and effective mass-squared in units of M^2, for the half-DW $\phi_{hDW}(z)$ (3.17) in the example theory (3.16). This captures behaviour near the surface of the cavity/oscillon. The horizontal axis is $z\,M$.

with the Schrödinger potential equal to the effective mass-squared evaluated on the half-DW profile, which is shown in Fig. 6 for the potential (3.16). It is clear from the Figure that the Schrödinger potential is more positive than negative, and should lead to bound states in the volume of the cavity.

With Eq. (3.20) we compute the transmission and reflection coefficients for an incident wave that approaches the cavity surface from within and which of course is related to the oscillon evaporation. We analyse this in more detail in Sec. 5. It may suffice to say now that from the form of the Schrödinger potential one expects that low frequency waves ($w \ll M$) are reflected while high frequency modes ($w \gtrsim M$) are transmitted through the skin.

4 The soft oscillon branch

Based on the considerations outlined in the previous sections, we have a general recipe to construct potentially long-lived oscillons of arbitrary size R_o (and equivalently large amplitude ϕ_0) in real scalar field theories with a plateau potential. Schematically, this novel ansatz can be understood and constructed based on the following steps:

1. Construct the half-DW of the theory explicitly by looking for static solutions of the equations of motion (this can be done using the Bogomolny equations typically used when looking for Domain Wall solutions). The half-DW asymptotes to $\phi_{hDW}(z) \propto z$ as $z \to \infty$. The half-DW will serve as the confining skin of the bag model, cavity solution.

2. Match the bag model solution, given in Eq. 3.1, to the half-DW, shifted so that $\phi_{hDW}(R_o) \approx \mathcal{O}(1)$, where $r = R_o$ is the size of the oscillon. This can be done by varying the amplitude ϕ_0 in Eq. 3.1, which is a free parameter of the bag model ansatz.

3. By performing this matching we obtain a piecewise ansatz for the field $\phi(t, r)$

$$\phi(t,r) = \begin{cases} \phi_{bag}(t,r) & r < R_o \\ \phi_{hDW}\left(-(r-R_o)\right) & r \geq R_o \end{cases} \tag{4.1}$$

Since close to $r = R_o$ the bag model solution stays static (like the half-DW solution), this ansatz is almost exact until $t \sim R_o/2$, at which point the outgoing front of the bag model reaches the static skin. A sketch of the setup is shown in Fig. 7. A short

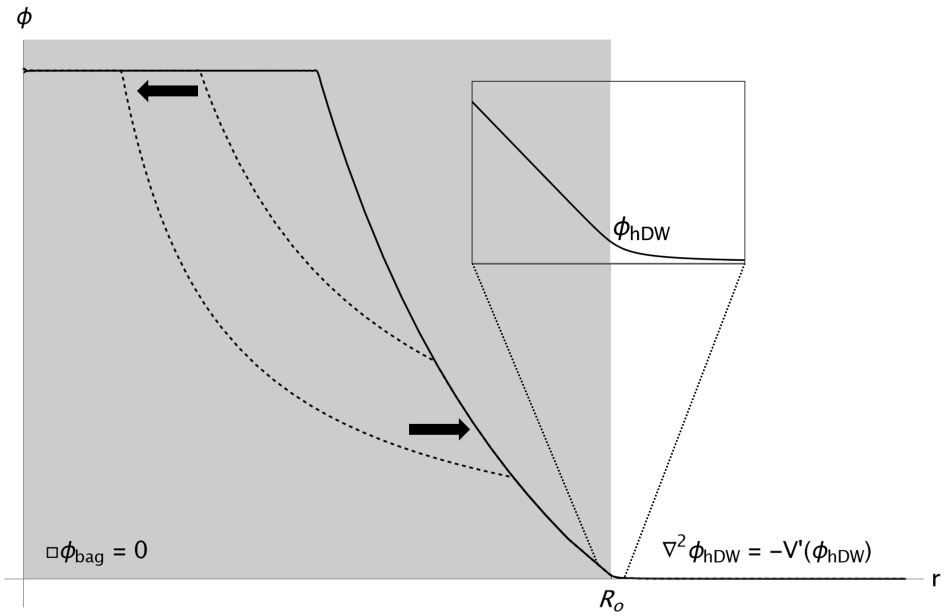

Figure 7. The soft oscillons can be thought of as a matching of two solutions of the equations of motion. At large field amplitudes $\phi \gg \Lambda$, the field is approximately free and the bag-model solution is exact (grey region). The bag-model configurations asymptotes to the half-DW solution that acts as a confining static 'skin' that matches the $\phi \gg \Lambda$ domain (grey) to the vacuum $\phi \approx 0$ domain (white). What's unique about the bag-model is the fact that the boundary region remains static as the outgoing front travels to R_o (dashed lines). This ansatz thus solves the equations of motion exactly until $t < R_o/2$.

remark concerning nomenclature is in order. In this work we use the following terms to refer to various concepts

1. *Cavity* or *bulk*: the inner region of the field, with $r < R_o$. This is the region where the field is effectively free for most of its evolution.

2. *Skin* or *half-DW*: the outer region, with $r \geq R_o$. The field in this region acts as a confining potential for the free inner region.

3. *Cycle*: A cycle is defined by the time in which the ingoing and outgoing fronts of the bag model travel a distance of $\Delta r = R_o$, flipping the overall sign of the field in the process. An entire period thus contains two cycles.

For notational convenience, we also define:

$$\mu \equiv \sqrt{V''_{max}(\phi)} \tag{4.2}$$

Where $V''_{max}(\phi)$ is the maximum value of the effective mass-squared for the potential under consideration. This sets the scale of the highest frequency mode trapped in the cavity. The cavity and skin correspond to the gray and white regions in Fig. 7 respectively. As we'll see this way of thinking about soft oscillons is an adequate representation of the physics at play.

Whenever $t \mod R_o/2 = odd$, the field value of this ansatz is $O(\Lambda)$ everywhere. The free cavity and hDW skin picture are no longer adequate descriptions of the configuration as nonlinearities of the potential are felt in the cavity. To understand what the effects of those nonlinearities are, one needs to understand how the outgoing front scatters off the static boundary, and the whole configuration flips sign. This process is best studied using numerical simulation. We will offer an analytic understanding of the decay processes of these soft oscillons in Sec. 5. In this section we will show what happens when we dynamically evolve our soft oscillon ansatz in a typical plateau potential.

4.1 Numerical solutions

We will focus the study of the dynamical evolution of the soft oscillon ansatz on a massless scalar field with plateau potential of the explicit form:

$$V(\phi) = M^2\Lambda^2 \frac{(\phi/\Lambda)^4}{1+(\phi/\Lambda)^4}, \tag{4.3}$$

leaving discussion concerning other potentials to Sec. 5.2. To obtain our results we solve the equation of motion of the scalar field

$$\ddot{\phi} - \nabla^2\phi + V'(\phi) = 0, \tag{4.4}$$

using finite difference methods. Additionally we impose spherical symmetry, so that $\nabla^2 \to \frac{1}{r^2}\partial_r r^2 \partial_r$. The importance of aspherical modes will be discussed in Sec. 6. Finally, we impose a Neumann boundary condition at $r = 0$, namely $\partial_r\phi(t,0) = 0$, and a radiative boundary condition at $r \to \infty$, namely $\dot{\phi}(t,r) = \frac{1}{r}\phi(t,r) + \partial_r\phi(t,r)$. We initialize the field as in eq. (4.1) at $t = 0$ (so at maximum amplitude with zero velocity).[3] In Figs. 8 and 9, we show the spatio-temporal evolution of a configuration of initial size $MR_o = 60$. Initializing at this size, the oscillon is able to adiabatically transition through *soft* configurations of ever smaller sizes. The profiles of different colors in Figs. 8 and 9 are thus obtained from the same initialization.

It is interesting to investigate whether the spectrum of the signal at $r = 0$, namely $\phi_0 \equiv \phi(t,0)$ in Fig. 8, follows the power law scaling of the bag model. Performing a Fourier transform of the signals shown in Fig. 8, one obtains the results shown in Fig. 10.

[3]Note that initializing with just the bag model ansatz, setting $\phi(0,r) = 0$ for $r \geq R_o$ does not make a big difference for our results.

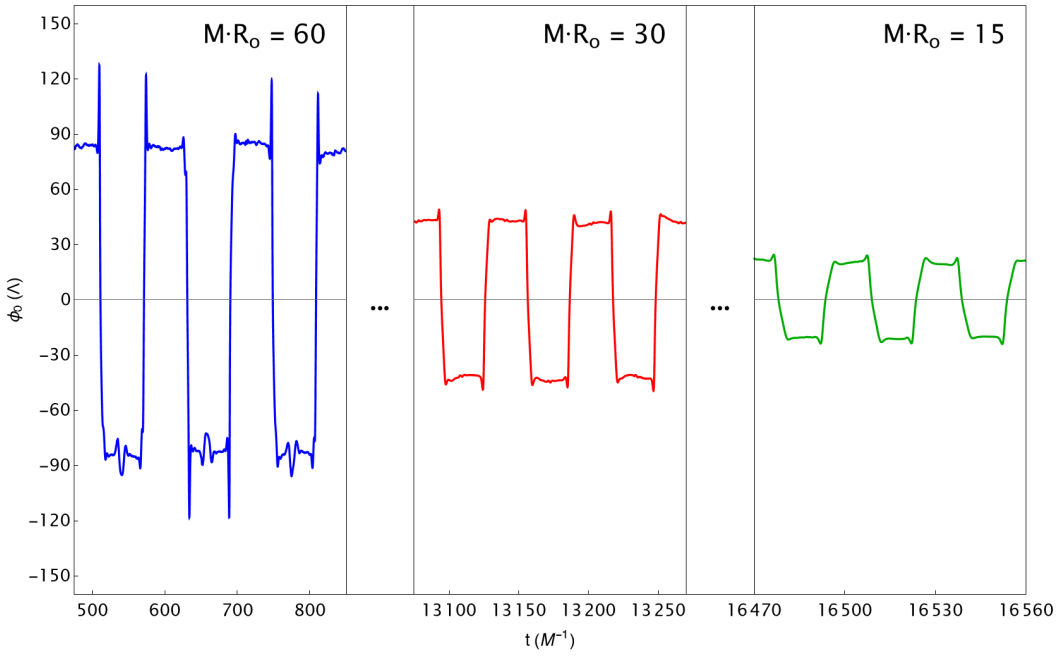

Figure 8. The evolution of the field at the origin $r = 0$, written as $\phi_0 = \phi(t, 0)$. The field shows a clear oscillatory pattern, similar to standard oscillons, but with a much higher harmonic content. The pattern is shown for a configuration of size $MR_o = 60$ (blue), $MR_o = 30$ (red) and $MR_o = 15$ (green). The triple dots are show to indicate that these configuration adiabatically transitions through different sizes. As the oscillon shrinks, its amplitude and period of oscillation shrink as well.

Fig. 10 shows that the frequency modes at the origin follow a broken power law. This type of spectrum can be understood within the cavity and skin picture of Sec. 3. Namely, modes that have frequency below the height of the cavity μ, with here $\mu \approx 1.5M$, are trapped. Their amplitude follows a power law $\phi_\omega \propto 1/\omega$, shown by the black dashed line in Fig. 10. This agrees with the scaling of the bag model. Moreover, the spectrum should be peaked at the cavity eigenmodes, given by $\omega_n = n\pi/R_o$, with $n = 1, 3, 5, 7....$ These eigen frequencies are clearly visible in the spectrum, shown by vertical gridlines. High frequency modes, with $\omega > \mu$, are able to tunnel through the hDW skin. The region with $\omega > \mu$ is shown in gray in Fig. 10. These modes are certainly transmitted through the cavity skin, and the relatively fast decay beyond $\omega > \mu$ confirms (and refines) the expectations drawn in Sec. 3.

Our numerics confirm that the ansatz of Eq. 4.1 has considerable longevity. In particular, the solution survives past the nonlinear scattering event that takes place at $t = R_o/2$. Also, our understanding of these soft oscillons as a collection of spherical modes within a free cavity, trapped by the hDW skin is adequate. The field transitions through soft oscillons of different sizes as it loses energy. Equation (4.1) does not explain how the configurations loses energy through nonlinear interactions, nor how the global evolution of the parameters (such as its size R_o) proceeds. We focus on

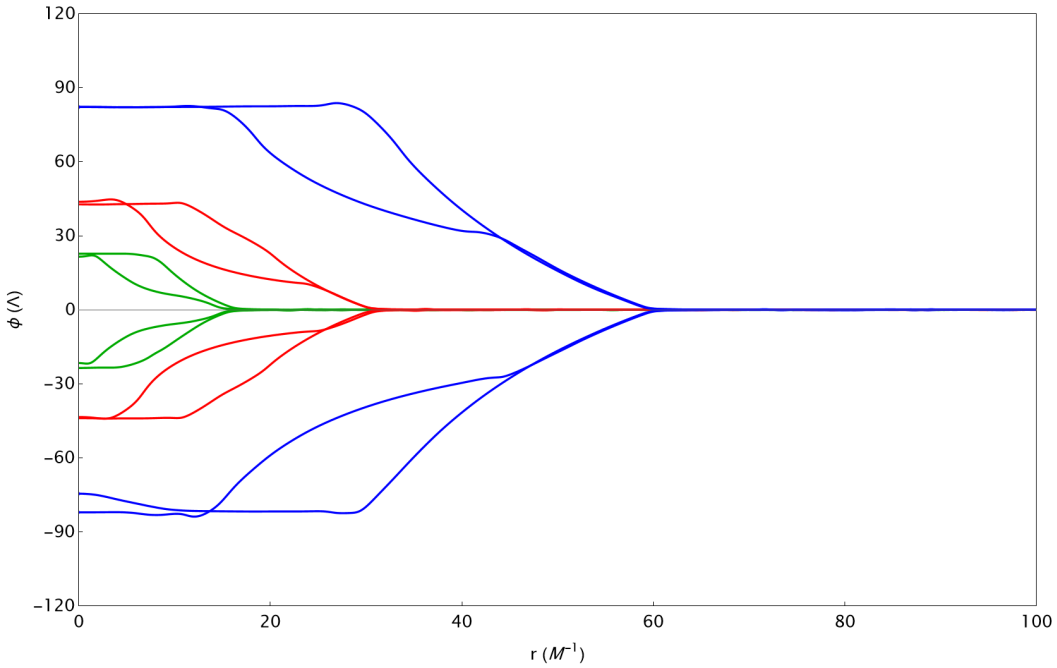

Figure 9. The spatial profiles of soft oscillons of three distinct sizes, (the same color coding as in Fig. 8), taken at different fraction of each respective period $T = 2R_o$; namely, $t \approx 0$, $t \approx R_o/4$, $t \approx 3R_o/4$ and $t \approx R_o$. Even as the soft oscillon shrinks in size, it's oscillation retains remarkable regularity.

these questions next.

4.2 Radiation and global evolution

As discussed, the cavity and skin picture breaks down when $t \mod R_o/2 \approx m$, where m is an odd integer. On the one hand because $V'(\phi) \neq 0$ within the bulk, resulting in an extra source term within the cavity. Moreover, the boundary of the bag model solution (see Fig. 7) is no longer static at this point in time, as the skin flips sign. We call this the nonlinear scattering event, where part of the outgoing wave is transmitted through the hDW, losing a percentage of its energy and flipping the overall sign of the solution. The soft oscillons thus lose energy in bursts of radiation, separated by $\Delta t = R_o$. These bursts are clearly visible at large distances $r > R_o$. Notice that oscillons emitting radiation bursts have also been found in $1+1$ dimensions [77, 78]. We will provide a better understanding of this evaporation mechanism in Sec. 5. Since the solution pulsates energy at a rate proportional to R_o^{-1}, and the energy of the soft oscillon scales with $E \propto R_o^3$, the configuration necessarily has to readjust its size and therefore its amplitude in order to conserve energy. In Fig. 11, we plot the temporal evolution of the size R_o and bulk average amplitude $\bar{\phi}$, the global parameters that characterize the soft oscillon. We define the size R_o of the oscillon as the radius r where the energy density $\rho(t,r) = \frac{1}{2}\dot{\phi}^2 + \frac{1}{2}(\nabla\phi)^2 + V(\phi)$ is equal to $\rho(t,R_o) \equiv 0.1\Lambda^2 M^2$. The bulk average amplitude $\bar{\phi}$ is then computed by averaging the field amplitude within the region $r \leq R_o/2$. Fig. 11 confirms that the oscillon is able to adiabatically change its

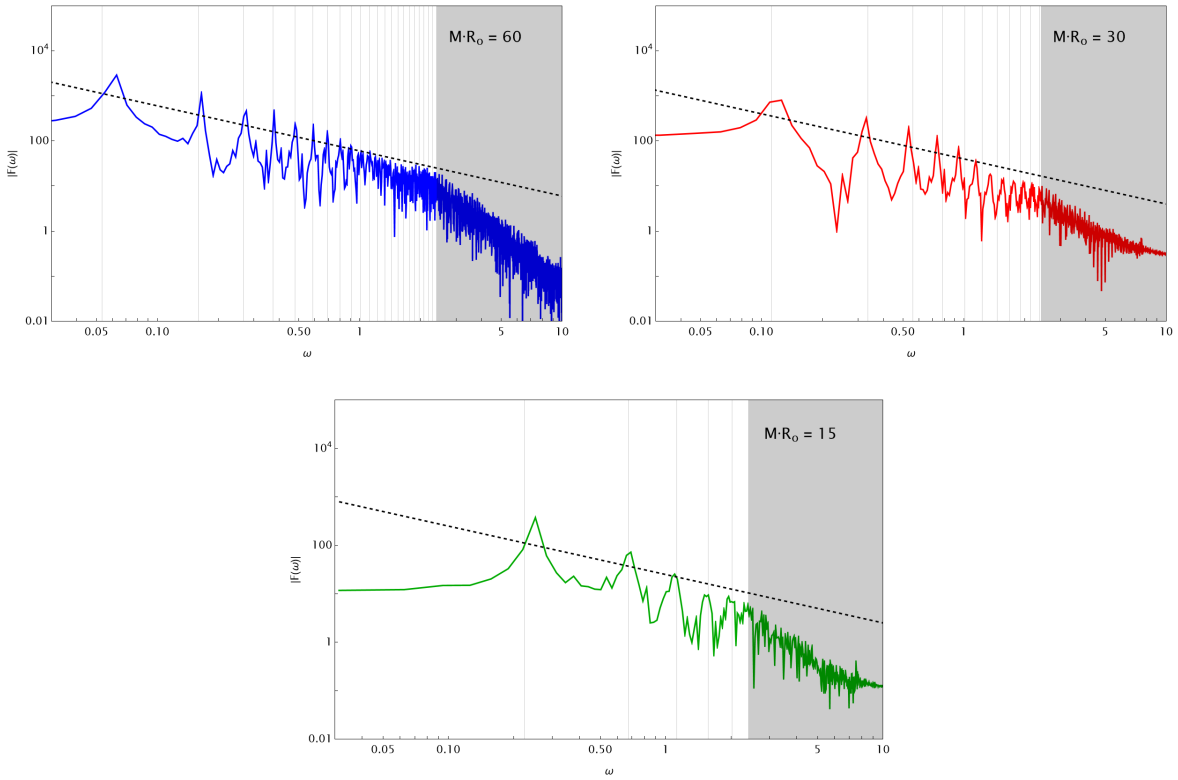

Figure 10. The Fourier decomposition of the time series ϕ_0, of the field oscillation at the origin, for an oscillon of different sizes (color coding as in Fig. 8). The peaks corresponding to the fundamental cavity mode $\omega_0 = \pi/R_0$ and its overtones $\omega_n = n\pi/R_0$ are clearly visible and shown by the vertical gridlines. They follow the power law $\propto 1/\omega$ predicted by the bag model (dashed lines). When $\omega \gtrsim \mu$, the half-DW 'skin' of the soft oscillon, no longer traps any of the modes, resulting in the broken power law that is observed.

size and amplitude as it pulsates away energy. The configuration transitions through a set of soft oscillons of different sizes and amplitude. The size of the solution is a perfect envelope of the oscillating bulk amplitude, confirming the understanding that there is a linear relation between R_o and the field amplitude ϕ_0 in the bag model picture. We measure $\bar{\phi} \approx \sqrt{2}(MR_o)\Lambda$, which agrees with our analytic expectation of Eq. (3.5). It is remarkable that an initial configuration of size $R_o = 60M^{-1}$ is able to survive for times that are much larger than its light crossing time $t_c = 2R_o$. In fact, the decay around $t = 1.7 \cdot 10^4 M^{-1}$ happens after about $140t_c$. Note that the evolution of the size of the oscillon $R_o(t)$ is approximately given by $R_o(t) = \sqrt{R_o(0)^2 - Ct}$, with $C \approx 0.22$.

We can obtain an estimate for the decay rate of these objects by simultaneously measuring how the energy of the object depends on R_o. Note that eq. 3.6, suggests a volume scaling between the two. In Fig. 12 we confirm this scaling. Only when the amount of modes trapped within the cavity becomes $\mathcal{O}(1)$, the approximation breaks down. As expected, the energy scales with the volume of the configuration, $E \propto R_o^3$, until the number of modes in the cavity becomes $\mathcal{O}(1)$.

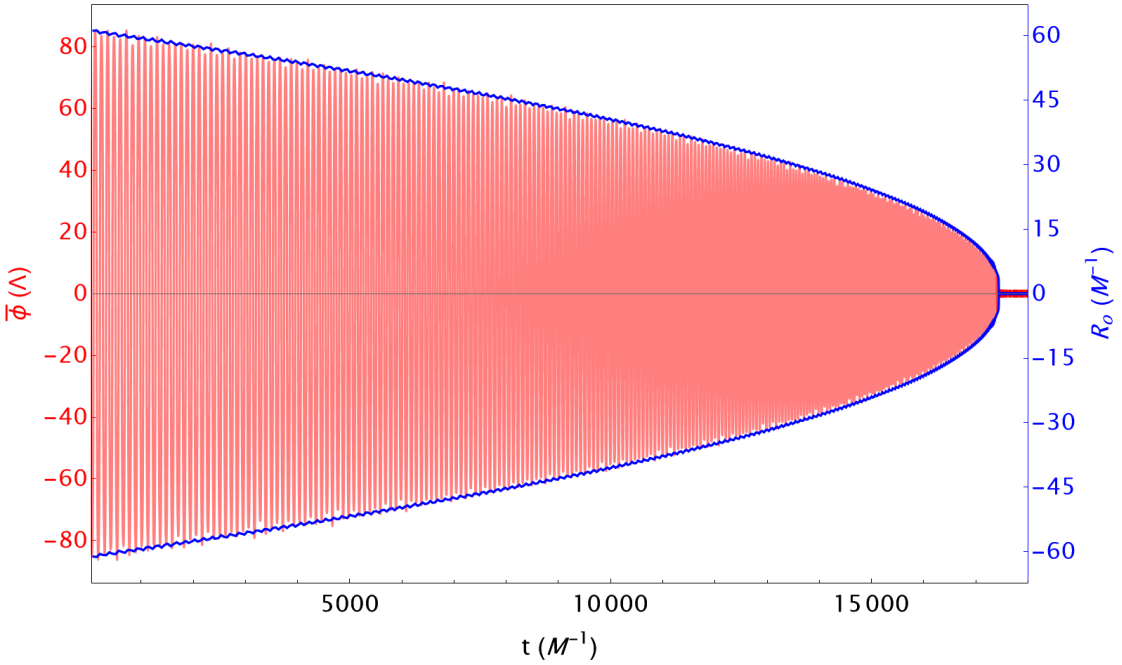

Figure 11. The evolution of the average bulk amplitude of the field $\bar{\phi}$ (red, left axis) and the size of the configuration (blue, right axis) over time. $\bar{\phi}$ oscillates rapidly and becomes almost indiscernible as the soft oscillon (and its period) shrinks. The size of the oscillon acts as a perfect envelope of the amplitude, as the bag model predicts $\phi_0 \propto R_o$. The proportionality factor here is $\approx \sqrt{2}$. Note that the $R_o < 0$ line here is just a visual guide and is simply obtained by mirroring the physical $R_o > 0$ measurements.

The evolution of the soft oscillon thus proceeds by a pulsating ejection of energy through wavepackets that travel to $r \to \infty$. The shape of the ejected wavepacket depends on the size of the oscillon at the time of ejection. As the configuration adiabatically changes size, different shapes of pulses can be found at various distances from the bulk. A schematic representation of this situation is shown in Fig. 13, where the exact waveforms are taken from our numerics. Note that the distance between the packets is not to scale, as much more time is spent in the larger configurations. The separation between each wavepacket is equal to $r = R_o$, as the time between pulses is given by $\Delta t_{pulse} = R_o$, and the wavepackets move at the speed of light which we have set to $c \equiv 1$.

These waveforms carry information about the properties of the soft oscillon to spatial infinity. The time delay between the pulses is a direct measure of the size R_o of the oscillon. Moreover, each emitted packet has a unique frequency composition.

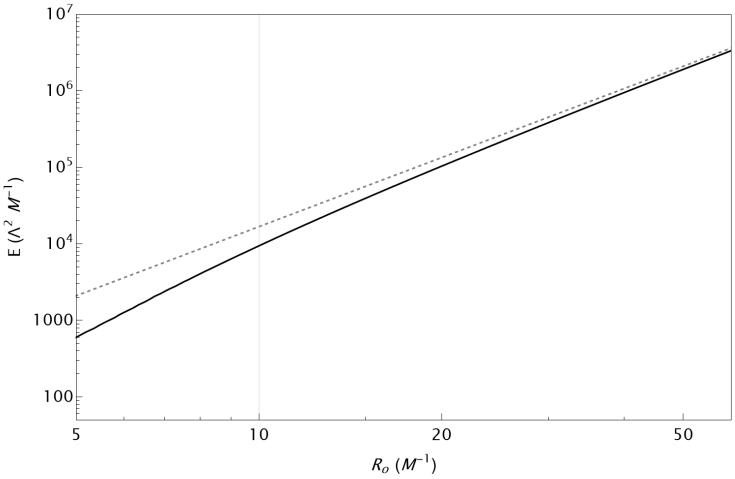

Figure 12. The energy contained within the soft oscillon configuration versus its size. The scaling of Eq. 3.6 (shown with the dashed line) is accurate until only a few modes are trapped by the half-DW skin, when $(MR_o)/\pi \sim \mathcal{O}(1)$, indicated by the vertical gridline. Here the bag model approximation is expected to break down.

The spectrum of the three waveforms, shown in Fig. 13, are shown in Fig. 14. To be precise, the spectra are computed by Fourier transforming five subsequent pulses of the type shown in Fig. 13. This gives a cleaner result.

Contrary to the bulk modes that follow the $1/n$ spectrum of the bag model, the spectrum of emitted pulses is nearly flat. The spikes of the bulk modes are still clearly visible. However, as high frequency modes are transmitted more easily through the skin at $r = R_o$, the result is a flat overall spectrum in the emitted wave. Again, for $\omega \geq \mu$, the spectrum decays, as happens in the bulk. This indicates that the adiabatic evolution of the soft oscillon does not lead to a significant hardening of the cavity modes.

As the size R_o increases (see upper left panel of Fig. 14), the radiation spectrum becomes less flat, and the spikes associated to the bulk modes are less visible. For soft oscillons whose size R_o is larger than some critical value R_c, we observe an instability that causes a change in the way the soft oscillon evolves. In sec. 5 we will argue that this instability is tied to a 'dirtying' of the spectrum of bulk modes and therefore the radiated waveforms, which starts to become visible in Fig. 14. The evolution we have described thus far is tied to a 'clean' spectrum in the bulk, associated to the bag model. At large size, the spectrum in the bulk becomes 'dirty' and we enter a different regime of evolution.

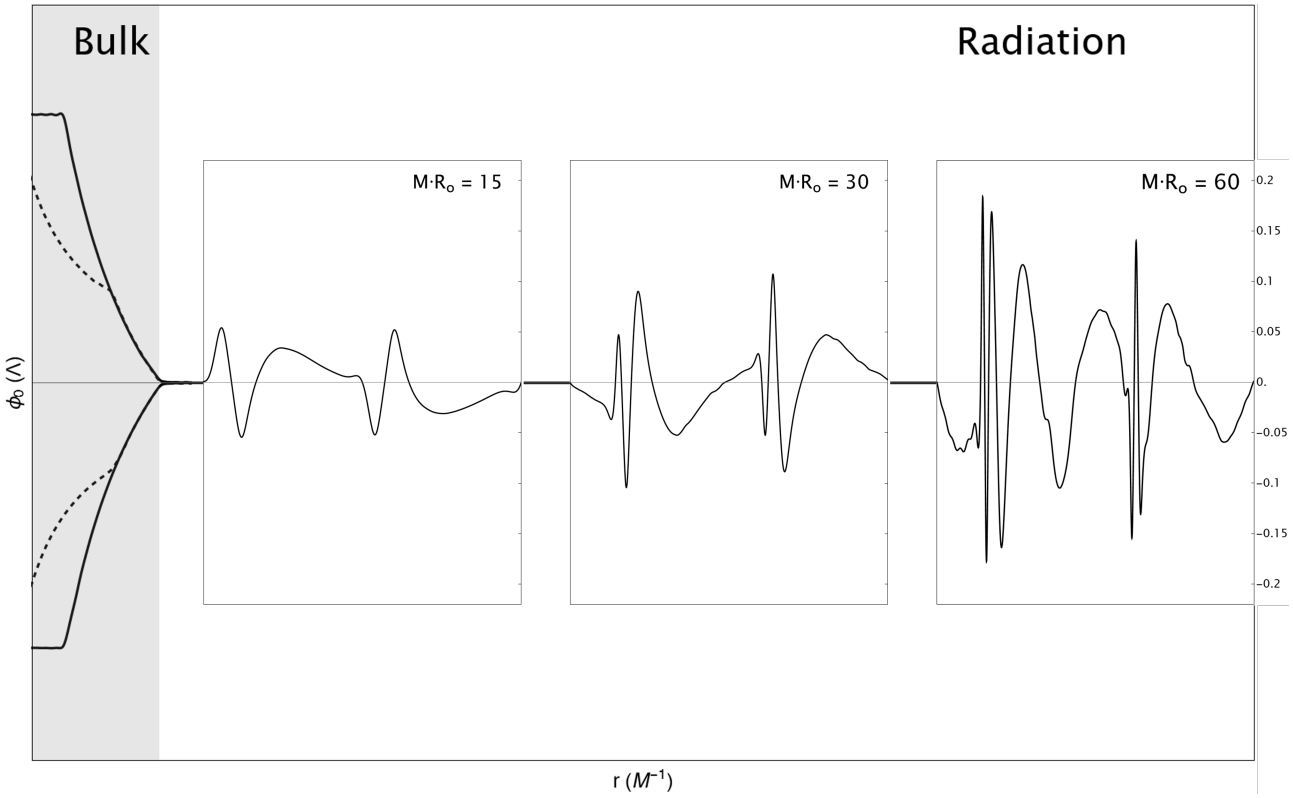

Figure 13. A schematic representation of how the soft oscillon loses energy. The oscillating bulk (right) emits pulses at regular intervals depending on the size of the configuration, $\Delta t = R_o$. The wavepackets travel to spatial infinity $r \to \infty$, where they can be measured by an observer. As the bulk shrinks the waveforms of the packets change as well, changing their frequency content. We show here the numerical wavepackets emitted by an oscillon of three different sizes. As the oscillon shrinks, the packets originating from the largest configurations have travelled the farthest.

4.3 Clean and dirty regimes

The results of the previous section show that at least some soft oscillons are able to pulsate away energy without significantly changing the relative amplitude of modes contained within the cavity. These oscillons simply transition through bag model solutions of ever decreasing size within the bulk. If we choose to initialize a soft oscillon with a smaller size, the global evolution of parameters as shown in Fig. 11 is simply shifted accordingly. We characterize this regime of evolution as the 'clean regime'.

As mentioned previously the clean regime does not persist to arbitrary size R_o. In fact, there seems to be a critical radius, which we call R_c, above which a soft oscillon is unable to sustain the particular cavity mode composition required for the clean regime. Starting with the ansatz of eq. (4.1) with $R_o > R_c$, the global evolution of parameters initially follows that of the clean regime. However, after a number of periods of the configuration, nonlinearities result in a significant deviation in the bulk with respect to the bag model. We colloquially call this moment in time the classical breaktime t_{br}

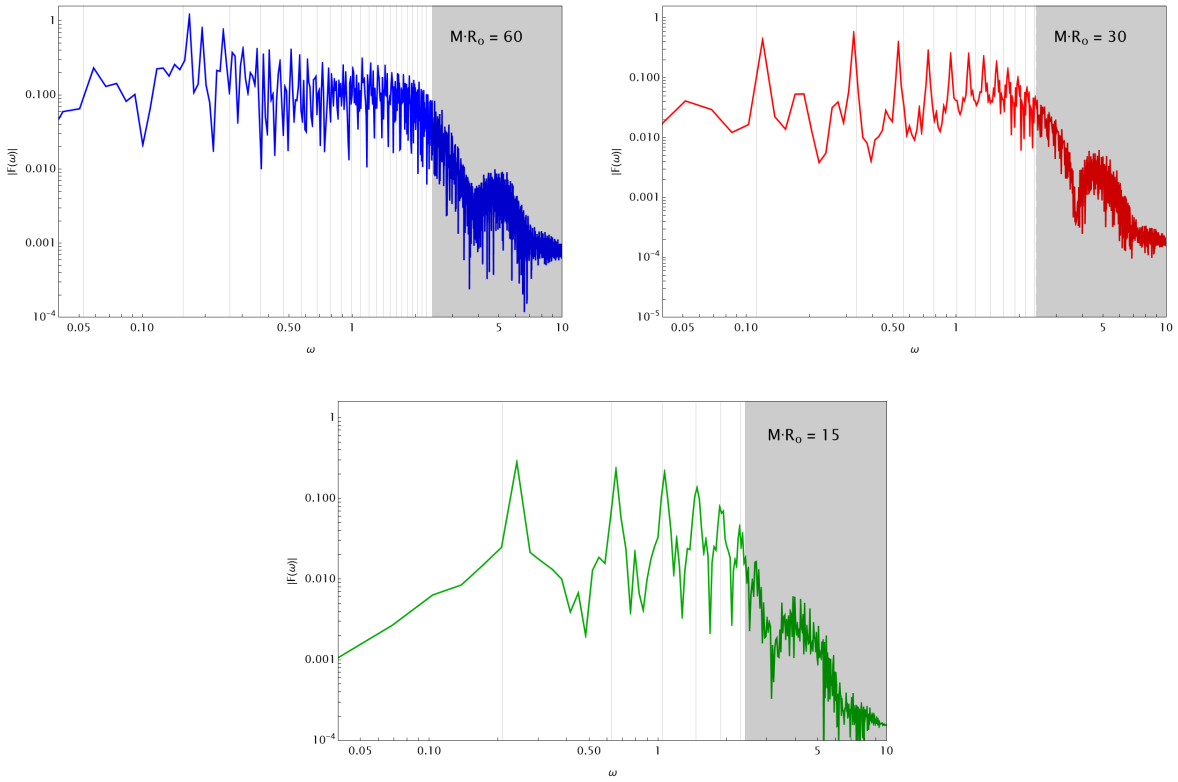

Figure 14. The Fourier transforms of the waveforms shown in Fig. 13. As for the bulk, the spectrum clearly shows the spikes associated to the cavity modes. However, the spectrum is now approximately flat. This can be understood intuitively by noting that, although the lower frequency modes have a higher occupancy in the cavity, they are also transmitted to a lesser degree by the 'skin'.

of the soft oscillon ansatz. This deviation from the bag model in the bulk results in a different evolution of the global parameters of the solution. We refer to this altered behavior as the dirty regime. The critical radius R_c can be understood as the maximum radius for which a soft oscillon is able to stay in the clean regime despite the nonlinear scattering event taking place twice every period. In sec. 5.1.2 we will show why R_c must necessarily exist for any potential although its precise value is model dependent.

The 'dirtying' of the configuration is visible at a qualitative level in the field profile. In Fig. 15 we show the difference in the bulk and radiated pulses, before and after the classical breaktime. The field shows clear wobbles with respect to the bag model solution. Moreover, the radiated pulses are less regular and more erratic.

Beside the qualitative differences in the field profile, it is interesting to check how the spectra of cavity and radiation modes change in the dirty regime. In Fig. 16 we show how breaking can be interpreted as a deviation from the bag model ansatz in the bulk (top row). In particular, we observe a hardening towards high frequency modes,

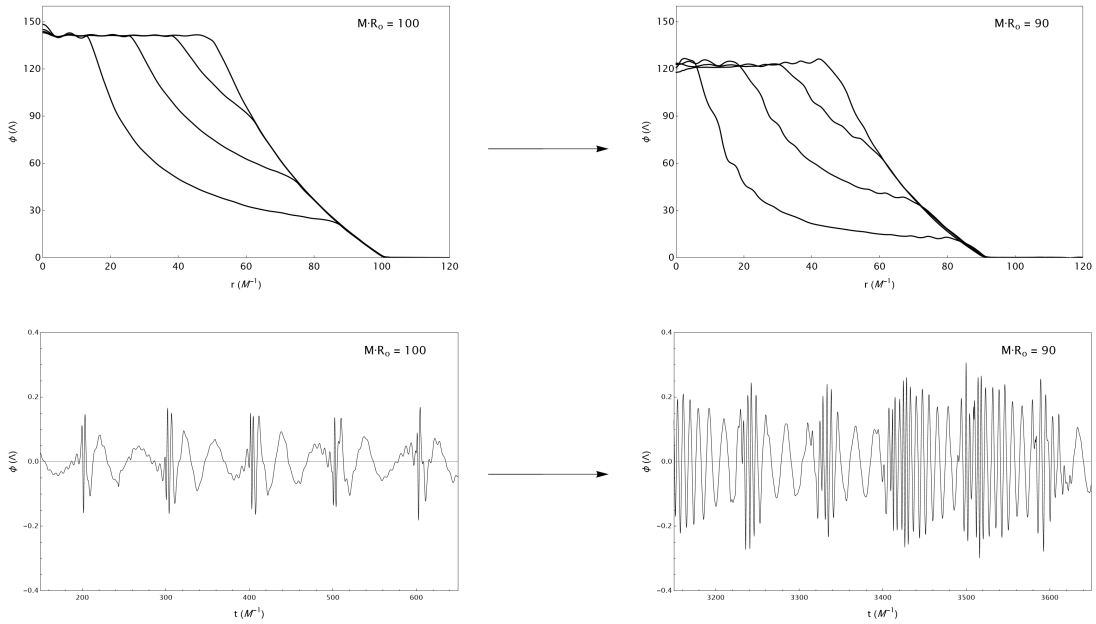

Figure 15. Above the critical radius, a soft oscillon only evolves in an ordered manner for a limited amount of time. This classical 'breaking' of the solution is visible at a qualitative level in the spatial profile (top row) and the radiated pulses (bottom row). Schematically, the evolution proceeds in a more perturbed and disorganized manner. The spatial profile becomes more 'wobbly', the radiated pulses are less periodic and localized, and the peaks in the spectrum characteristic of the bag model become less visible.

where the deviation from the $1/n$ dependence is clearly visible. The spectrum of radiation in turn loses the peaks associated to the bag model and shows no clear structure (bottom row).

The deviation from the bag model associated to the dirty regime results in a different evolution of the global parameters characterizing the soft oscillon. This is captured by the evolution of its size $R_o(t)$. Although initially $R_o(t) = \sqrt{R_o(0)^2 - Ct}$ the dirtying of the bulk eventually results in an increase of the evaporation rate after the classical breaktime. The size $R_o(t)$ therefore reduces more rapidly after t_{br}. In Fig. 17 we show $R_o(t)$ for oscillons initialized below and above R_c respectively. The blue line that respects $R_o(0) < R_c$ evolves as expected for the clean regime, until its eventual decay. The red line, which has $R_o(0) > R_c$, undergoes classical breaking, indicated by the cross, after which its size decays at an increased rate. When the size of the configuration has reduced below R_c, the oscillon is able to reenter the clean regime showing the attractive nature of the soft oscillon ansatz below R_c. In sec. 5 we will provide an analytic understanding of how and why this happens.

Inspecting Fig. 17, the evolution of $R_o(t)$ in the dirty regime seems unpredictable, lacking a clear power law description. We confirm that in the dirty regime, the evo-

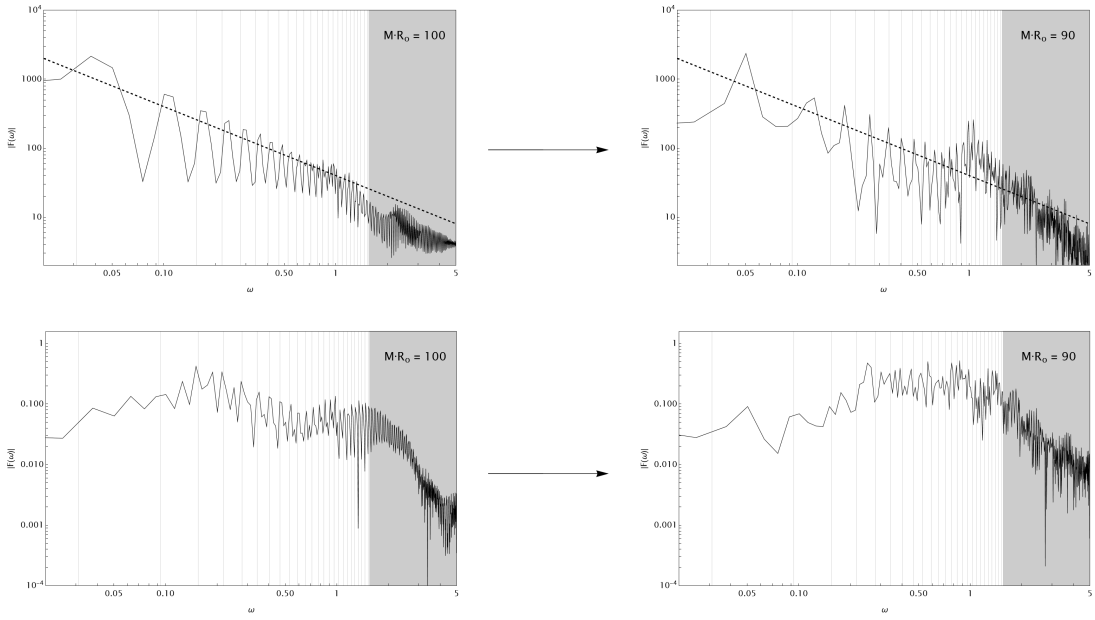

Figure 16. The breaking of the solution is also clearly visible in the spectrum of the field at the origin ϕ_0 (top row) and the spectrum of outgoing radiation (bottom row). The modes contained in the bulk get blue shifted with respect to the $1/n$ dependence associated to the bag model. Moreover, the spectrum of radiation is less regular.

lution of $R_o(t)$ is highly dependent on the exact distribution of bulk modes. In other words, a small difference in the way in which the cavity deviates from the bag model ansatz, can result in a very different evolution of $R_o(t)$ in the dirty regime. Note that Fig. 17 is produced by starting from the 'prefect' soft oscillon ansatz of (4.1). We can study the evolution of $R_o(t)$ by slightly perturbing this initial condition. In Fig. 18 we show the stochastic nature of the dirty regime. Each light gray line corresponds to a different initialization of a soft oscillon. We randomly perturb a finite number of the bulk modes by $\mathcal{O}(5\%)$ with respect to the bag model to obtain distinct evolutions of $R_o(t)$. After the classical breaktime, each configuration evolves independently until it is attracted to a soft oscillon smaller than the critical radius. The result is a considerable spread in the evolution of $R_o(t)$ (gray region), showing that the dirty regime is quite sensitive to small differences in the bulk mode population. This large spread is not visible if we perform the same procedure for a soft oscillon below the critical radius, as it never exits the clean regime.

Although Fig. 18 seems to suggest that it is impossible to predict the evolution of a particular configuration in the dirty regime, the average over all the different initializations (black line) is approximately linear for a long time. In particular, this is true when most of the configurations are in the dirty regime, indicated by the two gridlines. So although we can not make any predictions about a particular initialization, we can say something about the stochastic ensemble. The average global evolution in this

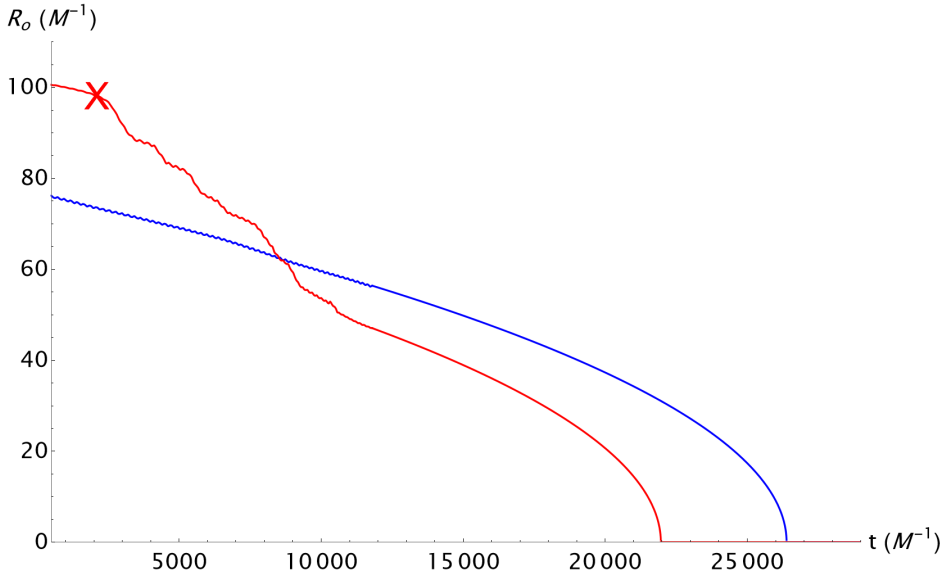

Figure 17. There exists a critical value of the soft oscillon R_c, above which the evolution of the size $R_o(t)$, deviates from the previously observed $R_o(t) \approx \sqrt{R_o(0)^2 - Ct}$, after a certain amount of cycles. After that the evolution of the size of the oscillon is less predictable, and almost chaotic. This is illustrated by the red curve, representing a soft oscillon with initial size $MR_o(0) = 100$. The classical break time is marked with the red cross and arises after about ten cycles. After some time the configuration is attracted to a smaller soft oscillon which isn't sensitive to breaking. If however, the initial oscillon is smaller, no breaking occurs whatsoever (blue curve).

regime can be summarized as following a very simple rule, namely that the overall radius decreases at a constant velocity

$$\dot{R}_o = -v\,t \qquad \text{with} \quad v \simeq 0.6 \cdot 10^{-2}\ . \tag{4.5}$$

Since the energy still scales as $E \propto R_o^3$, we conclude that in the dirty regime the average evaporation rate of the soft oscillon scales with its surface $\dot{E} \propto R_o^2$. We provide an analytic understanding of this rate in sec. 5.

A sketch of this evolution (4.5) together with the two radiation fronts in the oscillon core is given in Fig. 19. Oscillons deep in this regime, that is with initial $R_o \gg R_c$, are expected to have a lifetime

$$\Delta T \sim \frac{R_o}{v}\ ,$$

still significantly larger than the initial light-crossing time. Moreover, Fig. 19 is useful to visualize the large number of self-similar bounces that the oscillon goes through in this time. It's easy to see that the overall radius reduces in each cycle by a fixed multiplicative factor $(1-v)/(1+v)$. The total number of cycles in going from an initial

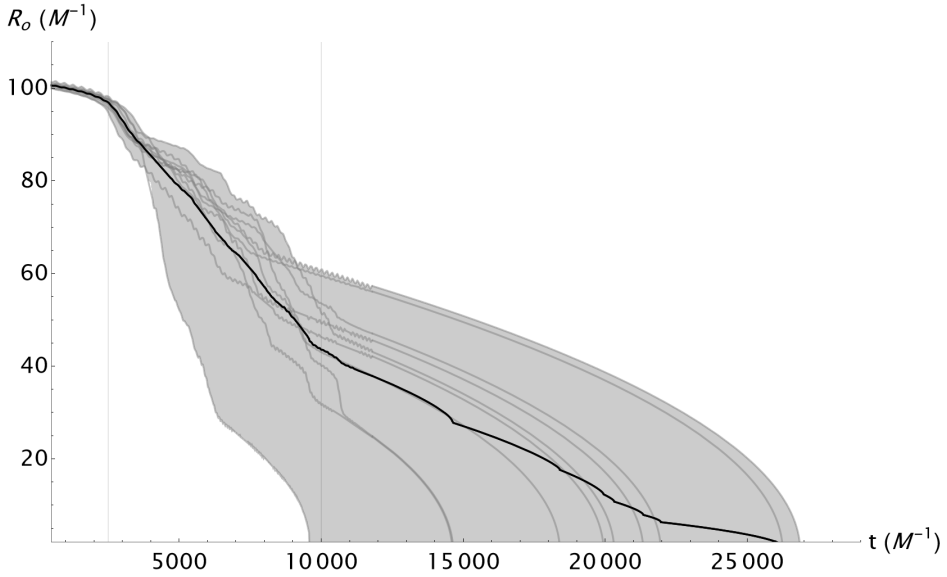

Figure 18. We show the stochastic nature of the classical breaking of the soft oscillons. Each light gray curve represents a different initialization of the soft oscillon with initial size $MR_o(t_0) = 100$, where each initialization is perturbed by a small fluctuation of order 5% of the background soft oscillon ansatz. The black curve represents the mean of each of the individual curves, while the gray region simply demarcates the maximum and minimum values of the simulated curves. After breaking after approximately ten cycles of the soft oscillon, each curve follows its own unique path, until it finds a smaller soft oscillon that is not sensitive to breaking. The mean of all the curves follows an approximate linear decay $R_o(t) \approx R_o(t_{br}) - vt$ for some time after breaking, until most curves are attracted to a 'non-breaking' smaller oscillon. The period where the evolution is approximately linear is indicated as the region between the two gridlines.

radius R_i to a final radius of order $1/M$ is

$$N_{bounces} \sim \frac{1}{2v} \log\left(M\, R_i\right) \ . \tag{4.6}$$

In other words, while the lifetime ΔT in units of the initial radius R_i is basically a constant, the number of cycles over which the evolution is approximately self-similar increases unboundedly with R_o.

To conclude this section we would like to address questions concerning the general attractiveness of soft oscillons in spherical symmetry.

4.4 Attractiveness

So far, we have described the properties of soft oscillons in detail. The dynamics of these oscillons can be split into two distinct forms of evolution, which we called the clean and dirty regimes respectively. Our discussion has focused on the properties of configurations initialized with the 'perfect' ansatz of eq. (4.1), or a slightly perturbed

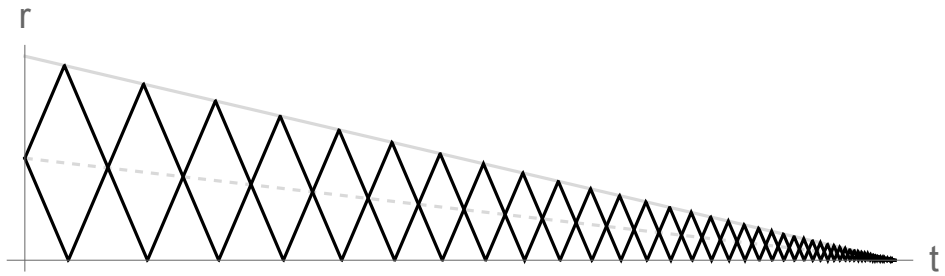

Figure 19. Sketch of the evolution, taking place at a constant slow decrease in radius, $\dot{R} = v \ll 1$. Solid black lines represent the in- and out-going fronts in the oscillon core (with fixed slopes). With an evolving oscillon radius $R_o(t)$ the structure of fronts that meet at $R_o(t)/2$ is preserved at all times.

version of it. This is sufficient to describe the general properties of soft oscillons, which we understand to be the configuration of size R_o that minimizes the evaporation rate of a localized wavepacket of that size. However, it remains unclear to what extent the decay rate of a generic spherical wavepacket of radius R and amplitude A is reduced due to the continuous set of soft oscillons characterized by their size R_o. We already showed that a soft oscillon in the dirty regime can reenter the clean regime below the critical radius, hinting at some form of attractor properties below the critical radius.

To study this question we analyze the decay rate of a localized field configuration of size R and amplitude A. We do this for two different parametrizations of the field:

1. The bag model initialization of size $R_o = R$ where we now allow $\phi_0 \equiv A$ to be a free parameter so that formally $\phi(0, r) = \frac{A}{\sqrt{2}R}\phi_{bag}(0, r/R)$;

2. A gaussian packet so that $\phi(0, r) = Ae^{-(r/R)^2}$.

For these initializations, we perform a scan over the free parameters A and R and measure the time it takes for the 20% of the initially localized energy to dissipate, a measure of the lifetime of the configuration. We show the results of this scan in Fig. 20. The red colors correspond to a longer lifetime.

There is a large region of parameter space where the existence of the soft oscillon solutions increases the lifetime of localized configurations. The fact that soft oscillons have attractive properties can be seen explicitly by looking at the evolution of the field, starting from away from the soft oscillon ansatz. We show an example of this in Fig. 21. The initialization (red line) is a solution of the breather profile equation (2.9) in the limit of $\omega \to 0$ and $m = 0$. It differs significantly from a soft oscillon as the breather contains only a single cavity mode. We can schematically describe the dynamics in Fig. 21 as follows. The breather is quickly attracted to a soft oscillon of some size R_o. Since we started far away from the exact mode distribution necessary in the cavity, we are initially in the dirty regime where the size of the object decays linearly

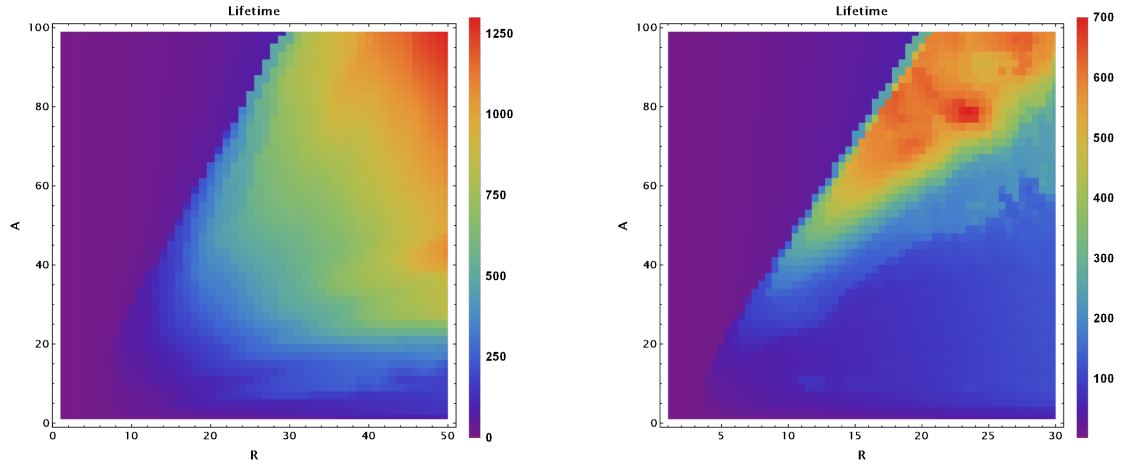

Figure 20. The lifetime defined as the time after which a general wavepacket loses 20 percent of its initial mass. On the left we show the bag model initialization while on the right we use a Gaussian packet, see text for the definitions of A and R. The scan clearly shows an island of attractiveness in both cases.

(blue profile). After some time, and below the critical radius we enter the clean regime after which the evolution proceeds exactly as if we started with the soft oscillon ansatz.

Figs. 20 and 21 are convincing evidence for the attractive properties of soft oscillons in spherical symmetry, both in the clean and dirty regimes. Although we mostly focus on studying their properties in this work, this fact is promising in light of potential applications. We now move on to understanding their decay rate in the different regimes of evolution.

5 Evaporation

In the previous section we have described our numerical observations regarding the behavior of the novel soft oscillon ansatz of Eq. 4.1. It is remarkable that, as the oscillon radiates away energy through what we called the nonlinear scattering event taking place at the hDW skin of the configuration, the bulk modes are able to arrange themselves in such a way that the configuration transitions through oscillons of ever smaller sizes. The size of the soft oscillons R_o is at the same time a measure of its overall amplitude $\phi_0 \propto R_o$, the amount of trapped modes $n_{max} \approx MR_o/\pi$ and its energy $E \propto R_o^3$. Its adiabatic evolution $R_o(t)$ therefore gives information about all the important properties of the oscillon itself. In this section we will therefore offer an analytic understanding of the adiabatic evolution of $R_o(t)$. In Sec. 4 we highlighted two distinct ways in which the oscillon evolves, namely:

1. The clean regime: a deterministic evolution with little to no noise, given by

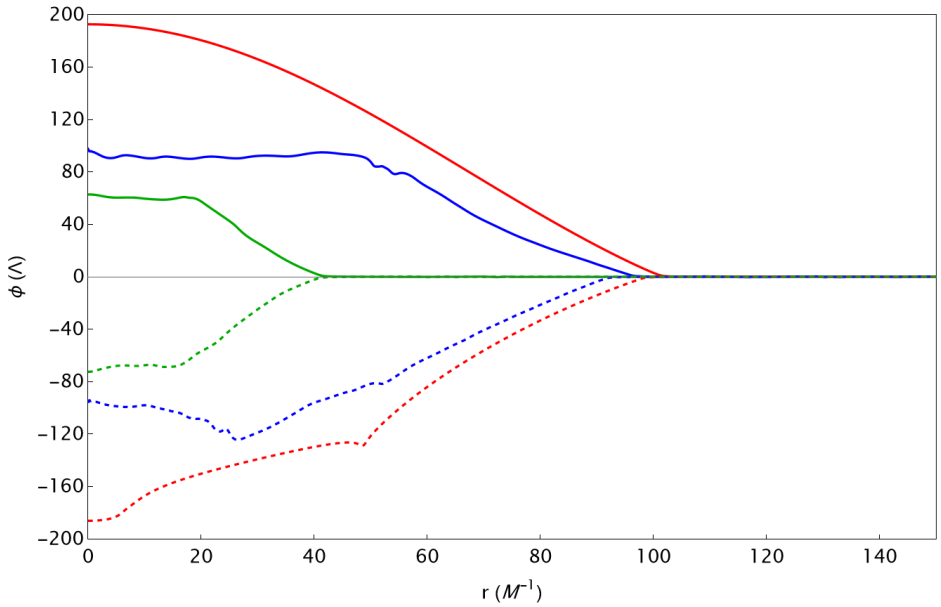

Figure 21. The evolution of the field after initializing with a configuration that is differs significantly from the ansatz of eq. (4.1). We show the field after one period (red), 10 periods (blue) and 50 periods (green). The field naturally moves from a soft oscillon in the dirty regime (blue regime) to one in the clean regime (green profile). This is not surprising since soft oscillons are the unique configurations of size R_o that have a static boundary, and thus don't radiate.

the analytic form $R_o(t) = \sqrt{R_o(t_0)^2 - Ct}$, where C is some constant which can depend on the exact shape of the potential.

2. The dirty regime: a stochastic decay, relevant after what we call the classical breaking time of the configuration t_{br}, where the exact way the configuration reduces its size depends on the exact deviation from the bag model. After taking the mean of multiple different evolutions, we concluded that the size decayed approximately linearly with $R_o(t) = R_o(t_{br}) - vt$. Here, again v is some constant which can be model dependent.

Given these two distinct ways in which the configuration evolves in these regimes, and the fact that $E \propto R_o^3$, it is simple to guess how the energy loss of the oscillon depends on its size. Since $\dot{E} \propto 3\dot{R}_o R_o^2$, it must be that for the two cases:

1. Clean: $\dot{E} \propto R_o$, so that $\dot{R}_o \propto R_o^{-1}$;

2. Dirty: $\dot{E} \propto R_o^2$, so that $\dot{R}_o \propto v$, with v again a constant.

In this section we offer an analytic understanding of both of these regimes using the cavity and skin picture.

5.1 Analytics

To obtain an analytic understanding of the evaporation of soft oscillons, we will make use of the notion that the field behaves as a set of free waves trapped in a cavity, confined by the hDW skin. This perspective provides accurate quantitative predictions for the rate of evaporation for soft oscillons in gapless plateau potentials, regardless of the exact shape of the potential. We remind the reader of the following definition:

$$\mu \equiv \sqrt{V''_{max}(\phi)} \tag{5.1}$$

Where $V''_{max}(\phi)$ is the maximum value of the potential under consideration. We use this as the height of the confining potential trapping modes within the cavity.

One can write a general solution of the field, confined to the cavity, as

$$\phi_{cavity}(r,t) = \begin{cases} \sum_n^{n_{max}} \frac{4\sqrt{2}R_o}{n\pi} \sin(n\pi/2) \cdot A_n \frac{\sin(k_n r)}{k_n r} \cos(k_n t + \delta_n) & r < R_o \\ 0 & r \geq R_o \end{cases} \tag{5.2}$$

Where $k_n = n\pi/R_o$ $(n = 1, 2, 3...)$ and n_{max} is the largest value of n for which $n\pi/R_o < \mu$. Note that we are working in this section (and will continue to do so) with rescaled dimensionless variables, meaning that spatio-temporal variables are always understood in terms of M^{-1} and field variables in terms of Λ. For the bag model solution one has $A_n = 1$ and $\delta_n = 0$. We could also have a different distribution of amplitudes and phases, which we will use to interpret the classical breaking of the solution and the dirty regime. First, we will focus on the bag model ansatz. Our numerics suggest that $\dot{E} \propto R_o$ in that case, corresponding to the clean regime.

5.1.1 Clean regime

It is convenient to think of Eq. 5.2 as the sum of an incoming wavepacket traveling towards the origin at $r = 0$ and and an outgoing wavepacket traveling to $r = R_o$. One cycle is completed when the two waves reach their respective destinations and the overall envelope of the solution switches sign. Part of the energy contained in the outgoing wave will be transmitted to infinity, leading to the evaporation of the solution. To calculate the transmission coefficient of the wavepacket, we are required to solve a nonlinear scattering problem, since the scattering potential is generated by the waves themselves. To make progress, it is useful to write the cavity field as the sum of a static background and a traveling front

$$\phi_{bag}(r,t) = \phi_{bag}(r,0) + \phi_{front}(r,t) \tag{5.3}$$

Note that this separation is somewhat trivial as $\phi_{front}(r,t) = \phi_{cavity}(r,t) - \phi_{bag}(r,0)$, in the clean regime where we assume $A_n = 1$ and $\delta_n = 0$. It is important conceptually however. The equation of motion for the front is then given by

$$\ddot{\phi}_{front} - \nabla^2\phi_{front} + V'(\phi_{front} + \phi_{bag}(r,0)) = \nabla^2\phi_{bag}(r,0) \tag{5.4}$$

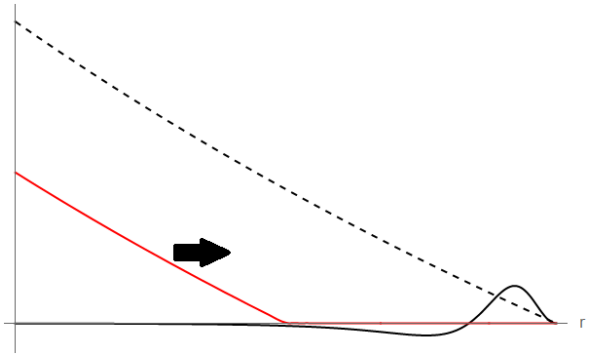

Figure 22. The Bag model can be understood as an outgoing front $|\phi_{front}|$ (red) traveling across a static background $\phi_{bag}(r,0)$ (dashed). The outgoing wave is free until it reaches the boundary at $r = R_o$. There it will scatter off the potential sourced by the background $V''(\phi_{bag}(r,0))$ (black) after which some of the energy in the wave is transmitted and lost. The typical height of the scattering barrier is set by μ and is independent of R_o.

To make progress, we approximate ϕ_{front} as a small perturbation of the static background, which should be valid at the edges of the traveling front. This sets up the linear scattering problem

$$\ddot{\phi}_{front} - \nabla^2\phi_{front} + V''(\phi_{bag}(r,0))\phi_{front} = \nabla^2\phi_{bag}(r,0) - V'(\phi_{bag}(r,0)) \tag{5.5}$$

The r.h.s. of this equation is identically zero if the skin of the cavity is in fact the static hDW. We can thus focus on the l.h.s. of Eq. (5.5). The flux emitted by the soft oscillons in the clean regime can be estimated as the transmission of ϕ_{front} through the static potential barrier $V''(\phi_{bag}(r,0))$. A schematic setup of the scattering problem is shown in Fig. 22. We need to compute the energy in the wavepacket that is transmitted through the barrier in this simple linear scattering setup. This will provide an estimate for the energy lost by the oscillon every cycle (half a period) since the process each time the front reaches the skin. Note that this way of estimating fluxes is merely an analogue of the full nonlinear system. However, as we'll see the results are accurate enough to confirm this interpretation of the physics at play.

We approximate the scattering potential $V''(\phi_{bag}(r,0)) \equiv V(r)$ as,

$$V(r) = 2\sqrt{V''_{max}(\phi)}\delta(r - R_o) = 2\mu\delta(r - R_o), \tag{5.6}$$

The transmission coefficient of this potential is well known. The ratio of the amplitudes of an incoming wave I and an outgoing wave T, depends on its wavenumber k and is given by

$$t(k) = |T/I|^2 = \frac{1}{1 + (\mu/k)^2} \tag{5.7}$$

Waves with $k \gg \mu$ get transmitted completely and won't be confined by the potential. The transmitted part of the outgoing front of the bag model can thus be written as

$$\phi_{rad}(r,t) = 2\sqrt{2}\sum_{n}^{n_{max}} \left(\frac{R_o}{n\pi}\right)^2 \frac{\sin\left(k_n(r-t)\right)}{r} \sin(n\pi/2) \frac{1}{\sqrt{1+\left(\mu/k_n\right)^2}} \tag{5.8}$$

We can estimate the energy loss per cycle by computing the total energy flux of the radiation field through the hDW-skin at $r = R_o$. This is given by

$$\Delta E = 4\pi R_o^2 \int_0^{R_o} dt' T_{0r}|_{r=R_o} = 4\pi R_o^2 \int_0^{R_o} dt' \dot{\phi}_{rad}(t', R_o)\phi'_{rad}(t', R_o) \tag{5.9}$$

Plugging (5.8) into (5.9), ignoring terms of $\mathcal{O}(1/R_o)$ and performing the integration over one cycle, one obtains the rather simple expression

$$\Delta E = 16\pi R_o^3 \sum_{n,odd}^{n_{max}} \frac{1}{(n\pi)^2} \frac{1}{1+\left(\frac{\mu R_o}{n\pi}\right)^2} \tag{5.10}$$

The sum of eq. 5.10, with $n_{max} = \mu R_o/\pi$ converges in the limit of $R_o \to \infty$. Namely, in that limit

$$\sum_{n,odd}^{n_{max}} \frac{1}{(n\pi)^2} \frac{1}{1+\left(\frac{\mu R_o}{n\pi}\right)^2} \simeq \frac{\tanh \mu R_o/2}{4\mu R_o} \approx \frac{1}{4\mu R_o} \tag{5.11}$$

In the large R_o limit the total energy loss per cycle of the soft oscillon can thus be estimated to be

$$\Delta E \approx 4\pi R_o^2/\mu \tag{5.12}$$

Eq. (5.12) can be understood as the total energy that the soft oscillon emits per cycle. The average energy loss $\dot{E}$ is given by averaging over the duration of the cycle $\Delta t = R_o$. We finally obtain

$$\dot{E} = \frac{\Delta E}{\Delta t} \approx 4\pi R_o/\mu \tag{5.13}$$

This linear dependence of $\dot{E}$ on the size of the soft oscillon R_o predicts that its size R_o decays as $\dot{R}_o \propto R_o^{-1}$, as we observed in sec. 4 during the clean regime.

Note that this computation was performed using an explicit form of the cavity field of eq. (5.2). In particular we chose the various A_n and δ_n as to reproduce the bag model ansatz in the cavity, which we associate to the clean regime of evolution. In the linear picture, the various modes of the field do not couple, and the distribution of amplitudes and phases do not change over time. However, in reality the scattering event taking place every cycle is nonlinear. It is clear that nonlinearities can in principle lead to a redistribution and dephasing of the modes contained in the cavity (so different values of A_n and δ_n). In what follows we will argue why this happens above a critical size of the oscillon. Then we'll show that this redistribution on average leads to an energy loss that scales with the surface of the oscillon $\dot{E} \propto R_o^2$.

5.1.2 Critical radius and the dirty regime

The derivation given in the previous section, which provides an understanding of the linear evaporation rate of the soft oscillon $\dot{E} \propto R_o$ in the clean regime. A crucial prerequisite for the validity of this derivation is that the relative amplitudes of the modes trapped within the oscillon follow the $1/n$ dependence associated to the bag model. There is no guarantee that, starting from the 'perfect' soft oscillon ansatz of Eq. (4.1), the modes trapped within the confining skin of the configuration still obey this scaling after the oscillon has completed one cycle. It even seems somewhat surprising that we found soft oscillons that are capable of adiabatically changing their size R_o, while retaining the appropriate mode composition in the bulk. In fact, the scattering event coincides with the overall sign flip of the field. Near that time (t mod $R_o \sim 1/2$ assuming $\dot{\phi} = 0$ initialization at $t = 0$), $V'(\phi) \approx \mathcal{O}(1)$ everywhere in the bulk and the soft oscillon is not an approximate solution of the equations of motion. In addition to an overall energy loss through the transmission of a wavepacket to spatial infinity, this will also result in a perturbation of the field within the bulk. This perturbation can in part be interpreted as the reflected part of the nonlinear scattering event taking place near $r = R_o$. After one cycle, the oscillon field profile should be written as a soft oscillon with an additional perturbation

$$\phi(t, r) = \phi_{soft}(t, r) + \delta(t, r) \tag{5.14}$$

Where the perturbation $\delta(t, r)$ obeys the equation of motion

$$\ddot{\delta} - \nabla^2\delta + V''(\phi_{soft})\delta = -V'(\phi_{soft}) \tag{5.15}$$

From Eq. (5.15) it is evident that perturbations are sourced whenever $V'(\phi_{soft}) \sim \mathcal{O}(1)$, namely during the nonlinear scattering event. A heuristic way to interpret the sourcing of $\delta(t, r)$ once per cycle is to understand its presence as an effective reshuffling of the relative amplitudes of the bulk modes. Schematically, one expects that multiple low frequency modes of the background ϕ_{soft} combine in $V'(\phi_{soft})$ to source a perturbation of higher frequency, leading to a general hardening of the relative amplitudes of the bulk modes. In Sec. 5.1.2 we will show that (in the linear approximation), this leads to an increase in the evaporation rate of the oscillon, something that we called the classical breaking of the solution.

In Sect. 4, we observed that classical breaking of the solution typically only occurs when the size of the oscillon lies above a certain threshold, which we called the critical size R_c. It is beyond the scope of this work to obtain an accurate prediction of R_c. The exact value of R_c is weakly dependent on the initial conditions taken (as long as we're close to a soft oscillon), and will strongly depend on the model under consideration. However, we can intuitively understand why the sourcing of perturbations by soft oscillons of large size necessarily has to lead to a significant reshuffling of the bulk modes.

Suppose we want to compute the perturbation sourced by a soft oscillon of size R_1. By solving eq. (5.15) we can obtain $\delta_1(t, r)$. This is the perturbation living atop

of the soft oscillon background after one cycle. This perturbation $\delta_1(t,r)$ should be is a wavepacket of typical wavenumber k_δ travelling across the bulk. Now, importantly, if $k_\delta \gg \mu$ (the height of the confining potential) the wavepacket will be transmitted perfectly through the skin layer at $r = R_1$. In this scenario, the sourced perturbation is shed in a time $t \sim R_o$. So we conclude there is no significant build-up of perturbations in the bulk as they are shed within one cycle. This is why soft oscillons are able to evolve adiabatically with a linear evaporation rate $\dot{E} \propto R_o$ in the clean regime: the cavity literally remains 'clean'. Next, we can try to compute the sourced perturbation for some oscillon of larger size R_2. In particular we would like to obtain a solution of the equation

$$\ddot{\delta_2} - \nabla^2\delta_2 + V''(\phi_{soft,2})\delta_2 = -V'(\phi_{soft,2}) \tag{5.16}$$

It is important to note that in the limit of large size R_o, the effective source and mass terms evaluated on the soft oscillon ansatz, are for any plateau potential, approximately given by

$$V_S(t,r) \equiv V'(\phi_{soft}(t,r)) \approx \begin{cases} V'_{max}(\phi)\delta'(1/2 - t \mod R_o) & r < R_o \\ 0 & r \geq R_o \end{cases} \tag{5.17}$$

$$V_M(t,r) \equiv V''(\phi_{soft}(t,r)) \approx \begin{cases} V''_{max}(\phi)\delta(1/2 - t \mod R_o) & r < R_o \\ 0 & r \geq R_o \end{cases} \tag{5.18}$$

Where $\delta(x)$ is the Dirac-delta function. There is now an explicit scaling transformation relating the source and mass terms in eq. (5.15) for background oscillons of different sizes. Namely,

$$V^2_M(t,r) = V^1_M(t\cdot(R_1/R_2), r\cdot(R_1/R_2)); \quad V^2_S(t,r) = V^1_S(t\cdot(R_1/R_2), r\cdot(R_1/R_2)) \tag{5.19}$$

Where the superscripts $V^1_{M,S}$ and $V^2_{M,S}$ refer to the effective source and mass functions of the two background oscillons of different sizes R_1 and R_2. Using this scaling we can rewrite (5.16),

$$\ddot{\delta_2} - \nabla^2\delta_2 + V^1_M(t\cdot(R_1/R_2), r\cdot(R_1/R_2))\delta_2 = -V^1_S(t\cdot(R_1/R_2), r\cdot(R_1/R_2)) \tag{5.20}$$

Which, after changing variables $\tilde{t} = t\cdot(R_1/R_2)$, $\tilde{r} = r\cdot(R_1/R_2)$ and $\tilde{\delta}_2 = \delta_2\cdot(R_1/R_2)^2$, becomes

$$\ddot{\tilde{\delta}}_2 - \tilde{\nabla}^2\tilde{\delta}_2 + (R_2/R_1)^2 V^1_M(\tilde{t},\tilde{r})\tilde{\delta}_2 = -V^1_S(\tilde{t},\tilde{r}) \tag{5.21}$$

The crux of our argument is that $\delta_1(\tilde{t},\tilde{r})$ is almost a solution of this equation, up to a correction originating from the shift in the effective mass term.

The approximate form of the perturbation δ_2 sourced by the soft oscillon of size R_2 can be guessed

$$\delta_2(t,r) \approx A\cdot(R_2/R_1)^2\delta_1\left(t\cdot(R_1/R_2), r\cdot(R_1/R_2)\right) \tag{5.22}$$

Where we allow a free parameter A to accommodate for the shift in the effective mass term in (5.21). To make sure our reasoning is correct, we explicitely solved the linearized equations numerically and checked that the approximate scaling relation (5.22) holds. In Fig. 23 we show the effect of the nonlinear scattering event schematically. Each cycle, the outgoing front (in red) scatters nonlinearly off the hDW. The whole configuration flips sign and the front travels again towards the origin (in blue). However, the scattering event results in a transmitted wavepacket ϕ_{rad} and an extra perturbation in the bulk δ.

We thus conclude that the wavepacket associated to δ_2 has a similar form as δ_1, albeit with a shifted wavenumber $k_\delta \to (R_1/R_2)k_\delta$. Moreover the prefactor in eq. (5.22) suggests that its amplitude is also larger. Each cycle of the soft oscillon of size R_2 such a wavepacket is created. However there necessarily exists a threshold value of R_2 where the typical wavenumber $k_\delta \sim \mu$. At that size, a significant portion of the perturbation does not get transmitted through the hDW skin. The bulk modes are thus unable to relax to the soft oscillon ansatz within one cycle, leading to a build-up of perturbations in the cavity. The fact that the amplitude of the perturbations also grows with R_o also contributes to this fact. It is to be expected that above some value R_2 the perturbations in the bulk grow large in $O(1)$ cycles. This threshold value of R_2 is what we previously referred to as the critical size R_c. Above this size the dynamics of the soft oscillon lead to a significant reshuffling of the relative amplitude of trapped bulk modes, away from the $1/n$ dependence of the bag model. This leads to a larger evaporation rate $\dot{E}$, the classical breaking of the soft oscillon solution.

Evaporation estimate

Based on the qualitative considerations of the previous section, we will use our understanding of the soft oscillon after classical breaking to get a quantitative understanding of how evaporation proceeds in such a phase. Again, it is useful to start from the general solution of a scalar field contained in a cavity, which we repeat here for clarity,

$$\phi_{cavity}(r,t) = \begin{cases} \sum_n^{n_{max}} \frac{4\sqrt{2}R_o}{n\pi} \sin(n\pi/2) \cdot A_n \frac{\sin(k_n r)}{k_n r} \cos(k_n t + \delta_n) & r < R_o \\ 0 & r \geq R_o \end{cases} \tag{5.23}$$

As outlined in sec. 5.1.2, we interpret the classical breaktime of the soft oscillon solution as the time after which the relative amplitudes and phases of the various modes deviate significantly from the bag model solution that has $A_n = 1$ and $\delta_n = 0$. This type of deviation from the bag model ansatz is generally expected due to the nonlinear nature of the scattering event. However, the key observation we made in the previous section is that, above the critical size R_c, the timescale of relaxation to the bag model solution is larger than the time it takes for a cycle of the solution to complete (and thus larger than the time until the next nonlinear scattering event). This will evidently lead to a significant redistribution of the amplitudes and phases of the various cavity modes. We thus interpret the soft oscillon after classical breaking

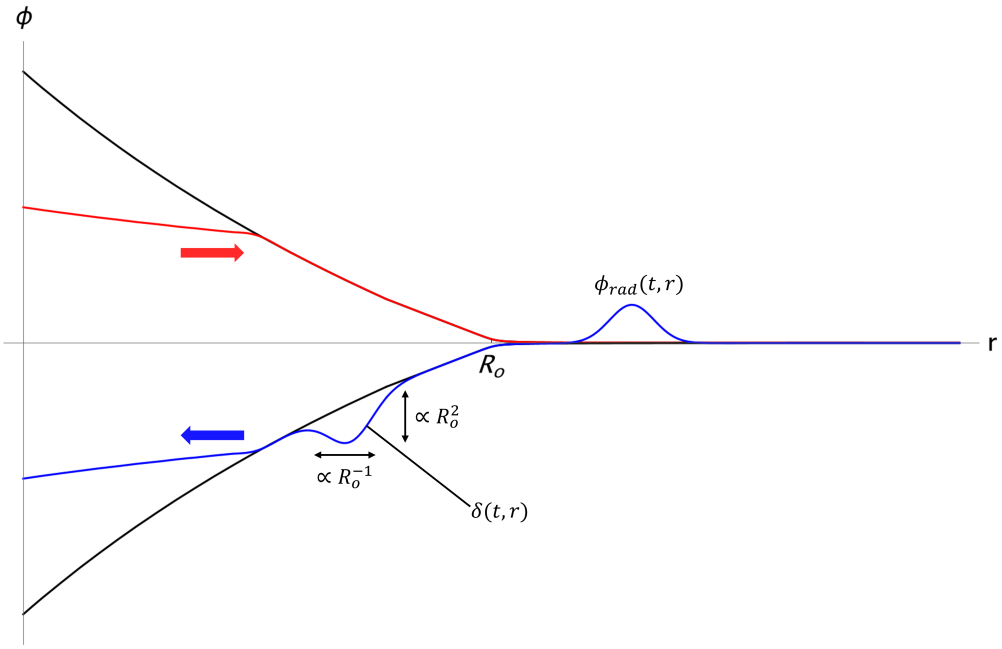

Figure 23. A schematic representation of the nonlinear scattering event. The outgoing front of the bag model travels towards the skin at R_o where it scatters nonlinearly as the whole bulk field switches sign. After the sign flip an ingoing front (in blue) travels towards the origin. However the scattering event has created a transmitted wavepacket ϕ_{rad} and a peturbation in the bulk δ. The size and width of δ depends on the size of the soft oscillon, causing an increased evaporation rate above the critical radius. In black we show the static bag model at $t = 0$ and $t = R_o$, across which the outgoing and ingoing front travel respectively.

as a field configuration trapped in a cavity as in Eq. 5.23, but differing significantly from $A_n = 1$ and $\delta_n = 0$. We can try to predict the rate of evaporation $\dot{E}$ for this more generic configuration.

First note that the total energy in the free cavity is readily computed and equals,

$$E_{cavity} = \frac{32}{\pi} R_o^3 \sum_{n,odd}^{n_{max}} \frac{A_n^2}{n^2}, \tag{5.24}$$

independent of the relative phases δ_n. For $A_n = 1$, the sum (for large size R_o and therefore n_{max}), converges to $\pi^2/8$, which gives the energy associated to the bag model. We will use this fact later.

We are interested in computing the energy loss of a configuration with some generic distribution of A_n and δ_n. Analogously to what was done in Sec. 5.1.1, we will approximate the radiation field of the cavity modes as the transmitted part of the

outgoing field modes. As before,

$$\phi_{rad}(r,t) = 2\sqrt{2}\sum_{n}^{n_{max}} A_n \left(\frac{R_o}{n\pi}\right)^2 \frac{\sin\left(k_n(r-t)+\delta_n\right)}{r}\sin(n\pi/2)\frac{1}{\sqrt{1+\left(\mu/k_n\right)^2}} \tag{5.25}$$

The energy loss per cycle of this configuration can be computed in a similar manner,

$$\Delta E = 4\pi R_o^2 \int_0^{R_o} dt T_{0r}|_{r=R_o} = 16\pi R_o^3 \sum_{n,odd}^{n_{max}} \frac{A_n^2}{(n\pi)^2}\frac{1}{1+\left(\frac{\mu R_o}{n\pi}\right)^2} \tag{5.26}$$

To get a quantitative prediction for the evaporation rat $\dot{E}$ we need to assume a particular distribution of the modes A_n. As observed numerically the process of breaking leads to an unpredictable and somewhat chaotic global evolution of the soft oscillon[4]. It was observed that a slight perturbation in the initial conditions of order $\mathcal{O}(5\%)$ can lead to substantial differences in the evolution of $R_o(t)$ and thus $\dot{E}$. This can be understood by realizing that a perturbation on the initial condition is equivalent to a particular distribution of A_n, differing from $A_n = 1$ by $\mathcal{O}(5\%)$. It seems reasonable that the redistribution of relative amplitudes, caused by the nonlinear scattering event proceeds differently for each individual initialization. Using Eq. (5.26) it is not surprising that we observe a different global evolution for each instantiation.

To make predictions about the ensemble of distributions we will assume the following form for the average distribution of amplitudes

$$\langle A_n^2 \rangle = Bn^p \tag{5.27}$$

Where $\langle\cdot\rangle$ should be interpreted as an average over many initializations, and B is some constant. The constant B can be fixed by requiring that the total energy in the cavity is equal to the equivalent bag model configuration. Using Eq. (5.24),

$$B = \pi^2/8\left(\sum_{n,odd}^{n_{max}} n^{p-2}\right)^{-1} \tag{5.28}$$

Next, we will assume that classical breaking translates into a deposition of low frequency modes into high frequency modes, so that $p > 0$. This is generally what happens when low frequency modes interact nonlinearly. Moreover, we seem to explicitly observe such a hardening in our numerics (see e.g. Fig. 15). Finally, we will assume that $p < 2$, so that the low frequency remain dominant in the cavity. These modes are associated with the static hDW skin and are required to be dominant in order for the cavity picture to be valid. The average energy loss per cycle is then given by

$$\langle \Delta E \rangle = 2\pi R_o^3 \frac{\sum_{n,odd}^{n_{max}} n^{p-2}\frac{1}{1+\left(\frac{\mu R_o}{n\pi}\right)^2}}{\sum_{n,odd}^{n_{max}} n^{p-2}} \tag{5.29}$$

[4]See [79, 80] for recent discussions of chaotic behaviour in other oscillon models.

Now, the sum in this expression converges for $n_{max} = \mu R_o/\pi$, taking the limit of $R_o \to \infty$. Although the sum has no closed form analytic expression, we checked numerically that in this limit the sum converges to, depending on the value of p

$$\frac{\sum_{n,odd}^{n_{max}} n^{p-2} \frac{1}{1+\left(\frac{\mu R_o}{n\pi}\right)^2}}{\sum_{n,odd}^{n_{max}} n^{p-2}} \propto \begin{cases} K(\mu R_o)^{p-1} & 0 < p < 1 \\ K \log(\mu R_o)^{-1} & p = 1 \\ K & p > 1 \end{cases} \tag{5.30}$$

With K some constant that depends on the value of p. We see that for a generic value of p between 0 and 2, the sum on the r.h.s. of eq. (5.29) is constant for a large range of sizes R_o. In what follows, we take it to be exactly K, which should be accurate for the range of sizes we have considered in this work. The average evaporation rate is then,

$$\langle \dot{E} \rangle = \frac{\langle \Delta E \rangle}{\Delta t} = 2\pi K R_o^2 \tag{5.31}$$

consistent with the surface evaporation observed for soft oscillons in the dirty regime. This prediction is completely generic: hardening of the cavity modes will typically lead to an evaporation rate that is proportional to the surface of the oscillon. Moreover we expect that, in the large R_o limit, the proportionality constant K is only mildly dependent on the exact shape of the potential. We can get an order of magnitude estimate of its value by evaluating the sum in Eq. (5.30) explicitly at $\mu R_o = 200$, for the range of $0 < p < 2$, and averaging the result. We obtain

$$K \sim 8 \cdot 10^{-2} \tag{5.32}$$

The average of the evolution of the size of the soft oscillon $R_o(t)$ is then,

$$R_o(t) = R_o(t_{br}) - \frac{K}{18} t = R_o(t_{br}) - vt \tag{5.33}$$

Where $K/18 \equiv v$ to make connection to our previous notation. This matches our expectation of oscillons in the dirty regime.

Note that our analysis assumes that the reshuffling of cavity modes is not too severe with respect to the bag model. If for some reason the hardening of the cavity modes is more extreme (e.g. $p > 2$) our estimate for K can be quite far off the true value. Even in those cases our analysis predicts an evaporation rate proportional to the surface of the object, although it will be larger. We expect this to be the case for a generic object of size R whose mode decomposition is not close to any soft oscillon. See sec. 4.4 for a discussion concerning this point.

To conclude, we will test our analytic understanding of the evaporation rate of soft oscillons against numerical results.

5.2 Comparison to numerics

Now that we have built a solid understanding of the mechanisms driving the evaporation of soft oscillons in gapless potentials, it is interesting to see how accurately the naive cavity picture can reproduce the full nonlinear evolution of the system. To do this we simulate soft oscillons of different sizes, for various gapless plateau potentials. In principle, soft oscillons are a valid ansatz for any plateau potential. Based on the considerations outlined in this section, we expect the influence of the potential to be visible through three phenomenological effects

1. In the clean regime, the rate of evaporation depends on the height of the scattering potential μ, which will be model dependent.

2. The critical size R_c, above which we expect classical breaking to occur and the soft oscillon enters the dirty regime, can differ for different potentials. This is obvious as the nonlinear scattering event and ensuing redistribution of particles in the bulk depend on the microscopic details of the interactions in the model.

3. Interestingly the evaporation rate in the dirty regime is only mildly dependent on the microscopic details of the potential. This assumes that the way in which the cavity modes reshuffle is not strongly dependent on the model under consideration (the value of p in the previous section).

In our comparison we will focus on four distinct gapless potentials to test our understanding,

$$V_1(\phi) = \frac{\phi^4}{1+\phi^4}; \quad V_2(\phi) = \frac{\phi^4}{(1+\phi^2)^2}; \quad V_3(\phi) = \frac{\phi^6}{1+\phi^6}; \quad V_4(\phi) = \frac{\phi^4}{1+10\phi^2+\phi^4} \tag{5.34}$$

Each of these potentials has a different critical size R_c and value of μ. We are interested in measuring the evaporation rates of soft oscillons at various sizes R_o, both below and above the critical radius. Since above the critical radius, we expect the evaporation rate to be stochastic, we average $\dot{E}(R_o)$ over multiple different instantiations of the field. We perform measurements as follows

1. Initialize a soft oscillon at $t = 0$ as in Eq.(4.1). To get distinct evolutions of the system we randomly perturb a fixed number of the bulk modes by $\mathcal{O}(5\%)$ with respect to the bag model.

2. Numerically time evolve the system. At each point in time we measure the size and evaporation rate of the oscillon.

3. After each cycle (defined as the moment that the bulk average amplitude $\bar{\phi}$ crosses 0), we average the size and evaporation rate over the duration of that cycle. We then save that data.

4. We gather data for $\mathcal{O}(10)$ different instantiations of the soft oscillon, each with random initial perturbations.

5. By binning over the sizes of the measured data, and averaging the evaporation rate within each bin, we obtain a measurement of $\langle \dot{E} \rangle$ at each size R_o.

By a process of trial and error, we first determine the approximate value of R_c for each potential. Based on our previous discussion, we expect that a soft oscillon initialized with a size smaller than this, will evolve similarly, regardless of the exact way in which we initially perturb it. The procedure outlined above should therefore give a value of $\langle \dot{E} \rangle$ with small error bars. The opposite is true above R_c, where the evolution is stochastic, and we are only able to understand the average $\langle \dot{E} \rangle$. In Fig. 24, we show results for the four potentials under consideration. The blue dots correspond to a background oscillon initially smaller than R_c, while the opposite is true for the red dots.

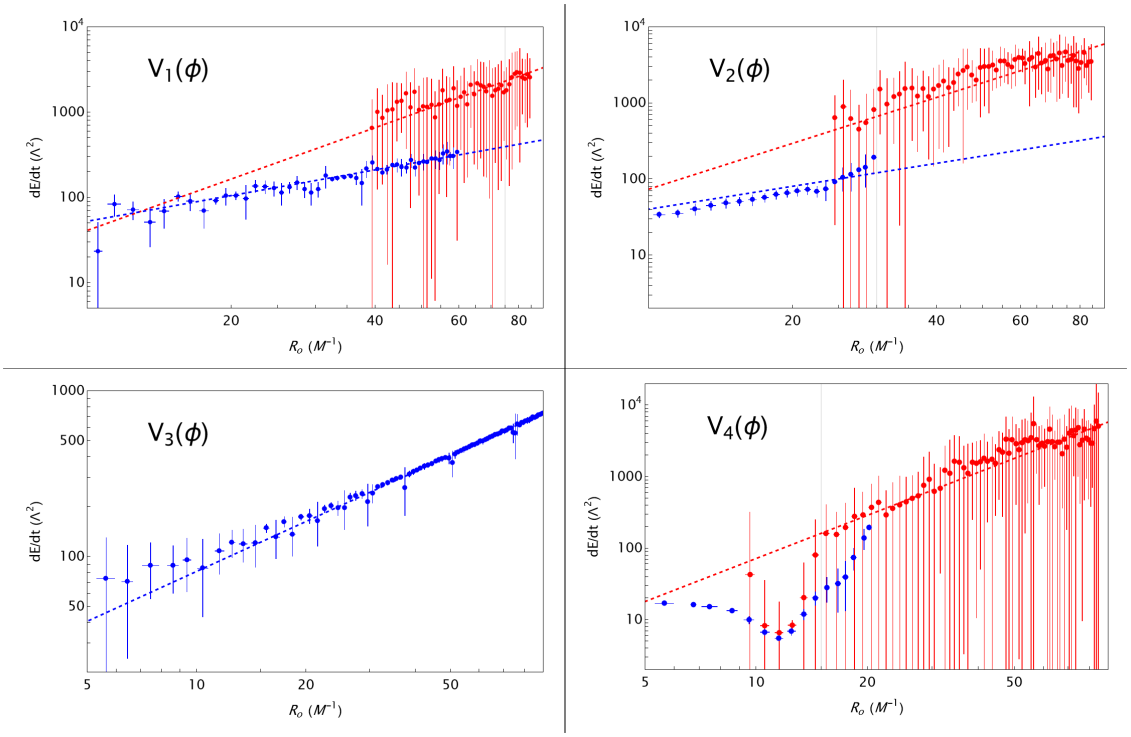

Figure 24. The average evaporation rate soft oscillons of various sizes R_o for the four potentials given in (5.34). The blue dots correspond to a background oscillon that is initialized with a size below R_c (indicated by the gridline in each plot). In that case $\dot{E} \propto R_o$ (blue dotted line). This is true for all potentials except $V_4(\phi)$ for which the soft oscillon ansatz is not a good solution at small $R_o < R_c$ (see text). The red dots on the other hand correspond to large background oscillons that undergo classical breaking. Each initialization evolves differently in that scenario resulting in large variances of the measurements. On average the evaporation rate scales as $\dot{E} \propto R_o^2$ (red dotted line). Note that the critical radius of V_3 is larger than the numerical domain, which is why we have no red dots in that plot.

The two distinct scaling behaviors of $\dot{E}$ are clearly visible in Fig. 24. For the potential $V_4(\phi)$ however, we don't observe the linear $\dot{E} \propto R_o$ associated to the clean

regime. This can be understood by noting that $\mu_4 \approx 0.5$. This means that even at moderately large $MR_o \sim 20$, the number of modes trapped by the hDW skin within the bulk is small. This means that the soft oscillon ansatz must necessarily break down. Instead, the configuration is attracted into a different type of solution, which behaves more like a typical single-frequency oscillon. This attractor is similar to the oscillons found in [19]. Strictly speaking the critical size of $V_4(\phi)$ therefore doesn't exist. but we interpret it here as the size for which a soft oscillon is quickly attracted to this type of single-frequency solution.

The reason that there are no red dots in the bottom left plot is because the critical radius for V_3 is very large. For computational reasons didn't perform a dedicated analysis of soft oscillons in the dirty regime for this potential. However, we did check that classical breaking and the ensuing dirty regime still occur for $R_o > R_c \approx 170M^{-1}$.

The red and blue dotted lines in Fig. 24 are obtained by searching for the best fit parameters of the data in the two scaling regimes $\dot{E} = CR_o$ and $\dot{E} = KR_o^2$ respectively. We previously obtained an estimate of the fit parameters using a linear analysis of the scattering problem. It is interesting to see how close our linear predictions are to the actual data obtained here. We summarize this along with some other characteristics in Table 1. Our analytic estimates are remarkably close to the numerical best fit parameters, only differing by an $\mathcal{O}(1)$ factor. This is quite remarkable since the scattering process is highly nonlinear in reality. Also note that the relative difference between the proportionality factor K in the dirty regime is less model dependent than C in the clean regime. However we would need more data to confirm this.

Potential	μ/M	MR_c	C	K	$\lvert\frac{C-C_{theory}}{C}\rvert$	$\lvert\frac{K-K_{theory}}{K}\rvert$
$V_1(\phi)$	1.54	80	5.24	0.41	0.2	0.23
$V_2(\phi)$	0.96	30	4.01	0.74	0.66	0.32
$V_3(\phi)$	2.1	170	8.12	N.A.	0.62	N.A.
$V_4(\phi)$	0.49	15	N.A.	0.72	N.A.	0.31

Table 1. The summary of the main results of this section. It is remarkable that the proportionality constants obtained using an entirely linear analysis, K_{theory} and C_{theory} are so close to the best fit values obtained from our simulations.

We want to close this section with a short discussion around massive plateau potentials. A priori, it seems that there is no reason to make a distinction between plateau potentials that are and aren't gapped in the vacuum of the theory. In fact, the cavity picture is even more appropriate in massive theories, since there the skin confines modes that have $\omega < m$ perfectly. Following the linear analysis of Sec. 5.1.1, we'd expect that the soft oscillons in these models radiate very little as no 'leakage' of cavity modes is taking place. To check this we also performed numerical simulations of soft oscillons in massive potentials. As the cavity picture suggests, the soft oscillons initially radiate very little and the radius of the configuration stays almost constant for $\mathcal{O}(10)$ cycles. However, after this initial period, the solution typically undergoes

a severe type of classical breaking, where we even observed situations for which the cavity picture breaks down significantly, meaning that the fundamental $n = 1$ mode of the bag model bacomes of the same order as the higher overtones ($p > 2$ in eq. (5.27)). After this breaking evaporation proceeds through the typical $\langle \dot{E} \rangle \propto R_o^2$, with the proportionality constant K larger than that found for the gapless potentials of this section. This type of severe breaking can be understood heuristically by considering the framework of sec. 5.1.2. As for the gapless potentials, the soft oscillons produce a perturbation every cycle that needs to be shed before the next nonlinear scattering event. It is quite intuitive that this relaxation is made impossible if the cavity is perfect as is the case for massive potentials. Since the perturbations produced during the nonlinear scattering event can not be removed from the bulk we expect a large buildup of perturbations causing the breaking of the solution. We have looked into a few different massive potentials and always see this type of breaking occuring. For this reason we don't expect soft oscillons of large size R_o to be a general attractor in gapped theories. Interestingly, the fact that the confining skin of the cavity isn't perfect in gapless theories, increases the lifetime of large objects in spherical symmetry.

Having obtained a solid understanding of soft oscillons enforcing spherical symmetry, both in this section and in section 4, it is interesting how these results are modified if we perturb the system with aspherical perturbations. We will do this in what follows.

6 Anisotropies

So far, we have analyzed the soft oscillons, enforcing exact spherical symmetry on the system. It can be worthwhile to understand how some of their properties are altered when allowing for asphericity. This is important for two distinct reasons. First, although we saw that soft oscillons in spherical symmetry have a moderate to large island of attractiveness, this is not guaranteed to translate to the full three dimensional situation. It'd be interesting to see how asphericity in the initial conditions affects this property. This can tell us whether the soft oscillons as we described them are the generic end products of classical large aspherical wavepackets in plateau potentials, with potential applications in cosmology. Second, even if one preparess a classical spherical field configuration following the soft oscillon ansatz of Eq. (4.1), there will always be an unavoidable aspherical component due to the quantum nature of the field. One typically expects that the spectrum of quantum fluctuations scales with $\langle \hat{\phi}^2_{nlm} \rangle \sim \mathcal{O}(\lambda)$, where $\hat{\phi}_{nlm}$ can be understood as the quantized cavity modes. The presence of these fluctuations has two effects. On the one hand, if there is an aspherical exponential instability of the background soft oscillon, these modes will rapidly become populated and cause a significant deviation from the semiclassical evolution of the system. This type of instability was observed in [18], causing a rapid aspherical breakup of certain types of oscillons. On the other hand, even when this doesn't happen, the aspherical quantum modes can become of the same order as the lowest occupied cavity modes (see Eq. (5.23)) as the oscillon shrinks. It might thus be expected

that the interaction between small aspherical modes and these lowest occupied bag model modes can have an impact on the overall evolution of the configuration. In this section we will mainly be interested in studying the second of these two issues, namely the effect of small aspherical perturbations on the soft oscillon ansatz. We leave the general attractiveness of these solutions for future work.

To investigate this question we simulate soft oscillons on a three dimensional cartesian lattice using a VV2-integrator and implement an absorbing boundary layer at spatial infinity by adding an artificial dissipative term to the equations of motion. Here, we limit ourselves to a few examples of soft oscillons in the potential,

$$V(\phi) = \frac{\phi^4}{1+\phi^4}, \tag{6.1}$$

which we called $V_1(\phi)$ in Sec. 5. The setup of the simulations is as follows. First, we initialize a soft oscillon with some size R_o. Next, we add perturbations with an amplitude of $\mathcal{O}(10\%)$ of the background. We do this by adding a random variable to the field in Fourier space (drawn from a Gaussian distribution) and transform back to real space to obtain the perturbed initial field configurations. We then evolve the system and take measurements every cycle.

Even with perturbations that are considerable with respect to the background, we report that the asphericity of the initial conditions does not cause a rapid breakup of the configuration as was observed in [18]. This is remarkable and shows that spherically symmetric soft oscillons can exist for a large number of periods in three dimensions.

There is a different type of effect that can decrease the lifetime of the soft oscillons with respect to the spherically symmetric solutions. Aspherical modes seem to cause an effective lowering of the critical radius of the soft oscillon. We thus enter the dirty regime of evolution more easily. The evolution of the system proceeds as follows:

1. Initially, the oscillon evolves as in spherical symmetry.
2. After a certain number of cycles the hDW skin of the oscillon starts to deform.
3. The deformation leads to an increased evaporation rate which is again proportional to the surface of the object $\dot{E} \propto R_o^2$. This is similar to the dirty regime described in earlier sections.

We show an example in Fig. 25 for $MR_o = 50$ (initially). The figures show $\rho(\vec{x}, t)$ in the $z = 0$ plane.

It seems that the small aspherical perturbations in the initial conditions eventually start to interact with the spherical modes, causing significant deformation of the hDW skin, speeding up the decay process by emitting surface radiation as in the dirty regime. This is not entirely surprising, since the perturbation δ created in the bulk

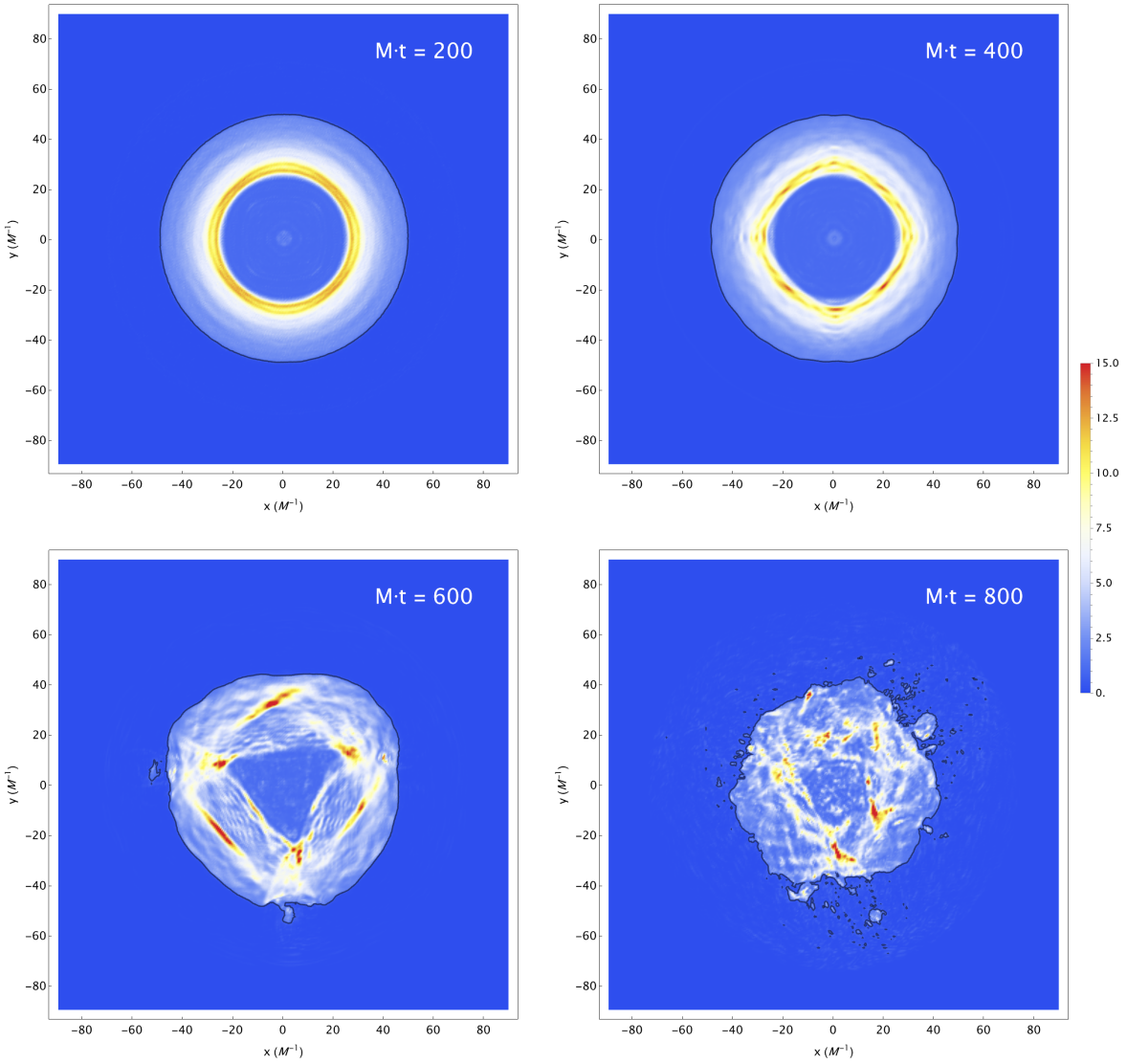

Figure 25. Showing a typical aspherical breaking of the soft oscillon solution. After the hDW skin deform considerably, the evaporation proceeds as we have seen in the case of spherical symmetry above the critical radius, with a rate proportional to the surface of the object $\dot{E} \propto R_o^2$. We put the contour line of $\rho = M^2\Lambda^2$ in black around the configuration. This broadly delimits the location of the cavity skin.

during each cycle during the nonlinear scattering event, has a larger phase space to populate in three dimensions.

What's interesting about this new type of breaking is that the microscopic initial conditions of the aspherical modes eventually lead to different shapes of the oscillon, similarly to how the evolution of $R_o(t)$ is stochastic in the dirty regime. In Fig. 26 we show two examples of initially equal macroscopic configurations. The macroscopic object thus retains some type of memory of the initial microstate of the system. This

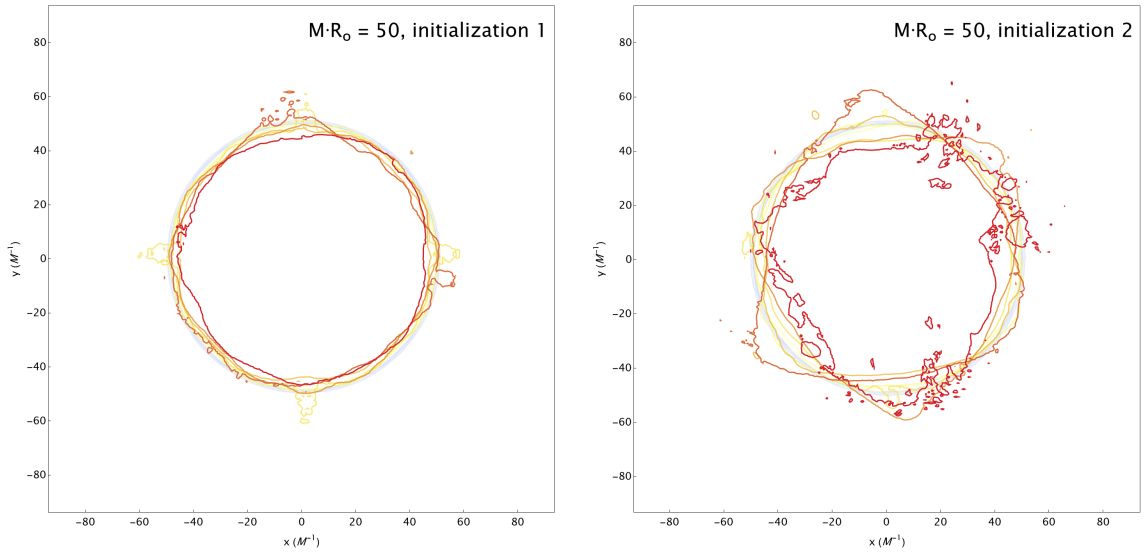

Figure 26. Contours of $\rho(\vec{x}, t) = M^2\Lambda^2$ separated by different cycles of the oscillon. Blue contours correspond to earlier times while red contours correspond to later times. Both cases correspond to an initial soft oscillon of size $MR_o = 50$, but both are initialized with distinct randomized perturbations. Although the initial spherical shapes of the solutions are identical, the randomized initial conditions result in widely different shapes.

property should translate to the quantum treatment of the cavity modes as well.

It's plausible that aspherical perturbations reduce the lifetime of soft oscillons by causing a significant deformation of the cavity skin. Analyzing how this novel type of breaking differs from the spherically symmetric case, and how it depends on the size of the initial perturbation, is beyond the scope of the current work. This is in part because soft oscillons require a large resolution to resolve accurately (simply because of the amount of modes that are contained in them), which is computationally expensive and difficult to attain in larger dimension. We therefore cannot at this point answer exact quantitative questions about soft oscillons with aspherical modes. One important goal for future work will be to understand their effect in more detail.

7 Conclusion

In this work we have presented a new soliton type, termed *soft oscillons*, similar to oscillons but with a number of quite distinctive features:

- Soft oscillons come in a continuum of sizes R_o (and masses, that scale like $\propto R_o^3$).
- Their size R_o is unbounded from above (up to gravitational effects), and unrelated to the parameters in the Lagrangian.
- The oscillation frequency is governed by the size $\omega \sim 1/R_o$.

- They have a high harmonic content, with Fourier modes with frequencies $n\pi/R_o$ (with n odd integers) scaling like $1/n$. This translates into two coherent radiation fronts in the bulk and a pulsating emission of scalar radiation to spatial infinity.

These oscillons appear in a broad class of scalar field theories with plateau potentials $V(\phi)$, in the the large amplitude regime where the field probes the plateau. They are longer-lived in 'gapless' models where $V(\phi)$ has a quartic+plateau form. Two parameters characterize these potentials: the quartic coupling λ and the scale Λ where the potential changes shape. The maximum typical gradient and frequency in the solution is set by a $M = \sqrt{\lambda}\,\Lambda$. Hence at weak coupling $\lambda \ll 1$ our oscillons involve only soft modes, from $1/R \ll M$ to $M \ll \Lambda$.

We have further studied the evolution and the scalar radiation of these novel oscillons and found that: i) there are two regimes of evaporation, dubbed clean and dirty, characterized by an emitted power scaling like R_o and R_o^2 respectively; ii) the clean (dirty) regimes also correspond to sizes R_o smaller (larger) than a critical radius whose value is model dependent; iii) the lifetime scales with the initial radius R_i typically like $\sim 100R_i$ in the dirty regime and $\sim R_i^2$ in the clean regime; iv) soft oscillons exhibit a clear attractor nature to spherical perturbations. They are also stable under small anisotropic deformations, however the lifetime can be reduced.

Let us now give a few remarks.

The natural interpretation of oscillons in quantum field theory is that they are simply many-particle quasi-bound states of scalar quanta [14, 56, 57, 72]. Remarkably, then, oscillons in gapless models correspond to bound states of *massless* quanta. This is also the case for potentials without a plateau such as those in [19, 63, 64] (the only difference is that the radius is fixed). Notice that bound states of massless constituent particles are particularly challenging as they are profoundly relativistic. Similar objects in other theories include glueballs in pure Yang Mills and black holes in pure GR [56, 57, 72]. Oscillons in gapless scalar models represent the equivalent of these interesting objects in a much simpler, spin 0, theory. This seems an analogy worth exploiting [67].

Another byproduct of our work that could be useful to the general understanding of oscillons is the mechanism behind soft oscillons. The peculiar core motion (Fourier mode composition) is understood at once due to the dynamical cavity effect that operates in plateau potentials: large field excursions lead to a cavity inside which the field is effectively massless. This singles out a special solution, the attractor, that i) is static near the surface during most of the evolution (implying small radiation and therefore long lifetime) and ii) acts as a confining cavity capable of trapping many soft modes.

This cavity picture emerges (and allows for a controlled understanding) in the asymptotic limit of large field excursion. The perturbative understanding of oscillons

in general starting from the operators in the Lagrangian is a challenging task, especially in the large-field and relativistic regime. For perturbative treatments in the (unstable) small amplitude approximation see [7, 29, 81]. For a recent improvement to large fields in the nonrelativistic limit see [17]. In the QFT language [14, 18, 56, 58–61, 82], large field oscillons correspond to large occupation number $N \gtrsim 1/\lambda$ with the dimensionless microscopic coupling. For soft oscillons, the occupation number is even higher as it scales with R_o. In other words they correspond to large collective coupling. The fact that a simple controllable picture emerges in terms of weakly coupled ('asymptotically free') modes in a cavity is quite welcome and remarkable.

This perhaps opens the door to a new aproximation scheme to understand oscillons in more general models without a plateau or with a mass gap. In the well-studied sine-Gordon case in 3+1 dimensions, for example, there is a well known oscillon of amplitude 4π that has been seen to confine the first harmonic at $3w_o$, see [16, 18, 83]. This oscillon has a remarkably low oscillation frequency, $w_o \simeq 0.55m$, which also renders it close to a relativistic regime, much like the soft oscillons in the gapless models.

Another derivative of the confining cavity effect is the close similarity with the MIT bag model of hadrons [65], especially manifest in our bag model discussion in Sec. 3. At least in the spherical case studied here, it seems fair to say that the soft oscillons arising in plateau potentials realize MIT bags, filled with certain coherent radiation. Inspired by the movable bag of the MIT bag model, it is also natural to ask whether soft oscillons with a moving cavity or with angular momentum exist in our model.

There are yet even more questions that we must leave for the future. A proper account of the impact of anisotropic perturbations, the emission of quantum radiation, the dependence on the shape of the potential, the effects of gravity, or possible formation mechanisms. We hope to return to these topics soon.

Acknowledgments

We thank Mark Hertzberg, Fabrizio Rompineve, Juan Sebastian Valbuena Bermúdez and Andrzej Wereszczyński for useful discussions and comments. We acknowledges the support from the Departament de Recerca i Universitats from Generalitat de Catalunya to the Grup de Recerca 'Grup de Fisica Teorica UAB/IFAE' (2021 SGR 00649). This work is part of the grant PID2023-146686NB-C31 funded by MICIU/AEI/10.13039/501100011033/ and by FEDER, UE. IFAE is partially funded by the CERCA program of the Generalitat de Catalunya. F. D. acknowledges funding from the ESF under the program Ayudas predoctorales of the Ministerio de Ciencia e Innovación PRE2020-094420. This work is part of the doctoral thesis of F.D. within the framework of the Doctoral Program in Physics at the Autonomous University of Barcelona.

References

[1] I. L. Bogolyubsky and V. G. Makhankov, *On the Pulsed Soliton Lifetime in Two Classical Relativistic Theory Models*, *JETP Lett.* **24** (1976) 12.

[2] I. L. Bogolyubsky and V. G. Makhankov, *Dynamics of Heavy Spherically-Symmetric Pulsons*, *Pisma Zh. Eksp. Teor. Fiz.* **25** (1977) 120–123.

[3] M. Gleiser, *Pseudostable bubbles*, *Phys. Rev. D* **49** (1994) 2978–2981, [hep-ph/9308279].

[4] E. W. Kolb and I. I. Tkachev, *Nonlinear axion dynamics and formation of cosmological pseudosolitons*, *Phys. Rev. D* **49** (1994) 5040–5051, [astro-ph/9311037].

[5] E. J. Copeland, M. Gleiser and H. R. Muller, *Oscillons: Resonant configurations during bubble collapse*, *Phys. Rev. D* **52** (1995) 1920–1933, [hep-ph/9503217].

[6] S. Kasuya, M. Kawasaki and F. Takahashi, *I-balls*, *Phys. Lett. B* **559** (2003) 99–106, [hep-ph/0209358].

[7] M. P. Hertzberg, *Quantum Radiation of Oscillons*, *Phys. Rev. D* **82** (2010) 045022, [1003.3459].

[8] M. A. Amin and D. Shirokoff, *Flat-top oscillons in an expanding universe*, *Phys. Rev. D* **81** (2010) 085045, [1002.3380].

[9] E. I. Sfakianakis, *Analysis of Oscillons in the SU(2) Gauged Higgs Model*, 1210.7568.

[10] M. A. Amin, *K-oscillons: Oscillons with noncanonical kinetic terms*, *Phys. Rev. D* **87** (2013) 123505, [1303.1102].

[11] M. Kawasaki, F. Takahashi and N. Takeda, *Adiabatic Invariance of Oscillons/I-balls*, *Phys. Rev. D* **92** (2015) 105024, [1508.01028].

[12] M. Ibe, M. Kawasaki, W. Nakano and E. Sonomoto, *Decay of I-ball/Oscillon in Classical Field Theory*, *JHEP* **04** (2019) 030, [1901.06130].

[13] G. Fodor, *A review on radiation of oscillons and oscillatons*. PhD thesis, Wigner RCP, Budapest, 2019. 1911.03340.

[14] J. Olle, O. Pujolas and F. Rompineve, *Recipes for oscillon longevity*, *JCAP* **09** (2021) 015, [2012.13409].

[15] H.-Y. Zhang, M. A. Amin, E. J. Copeland, P. M. Saffin and K. D. Lozanov, *Classical Decay Rates of Oscillons*, *JCAP* **07** (2020) 055, [2004.01202].

[16] D. Cyncynates and T. Giurgica-Tiron, *Structure of the oscillon: The dynamics of attractive self-interaction*, *Phys. Rev. D* **103** (2021) 116011, [2104.02069].

[17] D. G. Levkov, V. E. Maslov, E. Y. Nugaev and A. G. Panin, *An Effective Field Theory for large oscillons*, *JHEP* **12** (2022) 079, [2208.04334].

[18] F. van Dissel, O. Pujolas and E. I. Sfakianakis, *Oscillon spectroscopy*, *JHEP* **07** (2023) 194, [2303.16072].

[19] P. Dorey, T. Romanczukiewicz, Y. Shnir and A. Wereszczynski, *Oscillons in gapless theories*, *Phys. Rev. D* **109** (2024) 085017, [2312.05308].

[20] F. Blaschke, T. Romańczukiewicz, K. Sławińska and A. Wereszczyński, *Oscillons from Q-Balls through Renormalization*, *Phys. Rev. Lett.* **134** (2025) 081601, [2410.24109].

[21] S.-Y. Zhou, *Non-topological solitons and quasi-solitons*, *Rept. Prog. Phys.* **88** (2025) 046901, [2411.16604].

[22] M. A. Amin, R. Easther and H. Finkel, *Inflaton Fragmentation and Oscillon Formation in Three Dimensions*, *JCAP* **12** (2010) 001, [1009.2505].

[23] M. A. Amin, R. Easther, H. Finkel, R. Flauger and M. P. Hertzberg, *Oscillons After Inflation*, *Phys. Rev. Lett.* **108** (2012) 241302, [1106.3335].

[24] N. Fonseca, E. Morgante, R. Sato and G. Servant, *Axion fragmentation*, *JHEP* **04** (2020) 010, [1911.08472].

[25] M. Gleiser and D. Sicilia, *A General Theory of Oscillon Dynamics*, *Phys. Rev. D* **80** (2009) 125037, [0910.5922].

[26] E. Farhi, N. Graham, V. Khemani, R. Markov and R. Rosales, *An Oscillon in the SU(2) gauged Higgs model*, *Phys. Rev. D* **72** (2005) 101701, [hep-th/0505273].

[27] N. Graham, *An Electroweak oscillon*, *Phys. Rev. Lett.* **98** (2007) 101801, [hep-th/0610267].

[28] S.-Y. Zhou, E. J. Copeland, R. Easther, H. Finkel, Z.-G. Mou and P. M. Saffin, *Gravitational Waves from Oscillon Preheating*, *JHEP* **10** (2013) 026, [1304.6094].

[29] G. Fodor, P. Forgacs, Z. Horvath and A. Lukacs, *Small amplitude quasi-breathers and oscillons*, *Phys. Rev. D* **78** (2008) 025003, [0802.3525].

[30] T. Hiramatsu, E. I. Sfakianakis and M. Yamaguchi, *Gravitational wave spectra from oscillon formation after inflation*, *JHEP* **03** (2021) 021, [2011.12201].

[31] F. Van Dissel and E. I. Sfakianakis, *Symmetric multifield oscillons*, *Phys. Rev. D* **106** (2022) 096018, [2010.07789].

[32] H.-Y. Zhang, *Gravitational effects on oscillon lifetimes*, *JCAP* **03** (2021) 102, [2011.11720].

[33] S. Antusch, F. Cefalà and F. Torrentí, *Properties of Oscillons in Hilltop Potentials: energies, shapes, and lifetimes*, *JCAP* **10** (2019) 002, [1907.00611].

[34] S. Antusch, F. Cefala, S. Krippendorf, F. Muia, S. Orani and F. Quevedo, *Oscillons from String Moduli*, *JHEP* **01** (2018) 083, [1708.08922].

[35] M. A. Amin, J. Braden, E. J. Copeland, J. T. Giblin, C. Solorio, Z. J. Weiner et al., *Gravitational waves from asymmetric oscillon dynamics?*, *Phys. Rev. D* **98** (2018) 024040, [1803.08047].

[36] S. Antusch, F. Cefala and S. Orani, *What can we learn from the stochastic gravitational wave background produced by oscillons?*, *JCAP* **03** (2018) 032, [1712.03231].

[37] K. D. Lozanov and V. Takhistov, *Enhanced Gravitational Waves from Inflaton Oscillons*, *Phys. Rev. Lett.* **130** (2023) 181002, [2204.07152].

[38] D. G. Levkov and V. E. Maslov, *Analytic description of monodromy oscillons*, *Phys. Rev. D* **108** (2023) 063514, [2306.06171].

[39] K. D. Lozanov, M. Sasaki and V. Takhistov, *Universal gravitational waves from interacting and clustered solitons*, *Phys. Lett. B* **848** (2024) 138392, [2309.14193].

[40] K. D. Lozanov, M. Sasaki and V. Takhistov, *Universal gravitational wave signatures of cosmological solitons*, *JCAP* **01** (2025) 094, [2304.06709].

[41] D. Pîrvu, M. C. Johnson and S. Sibiryakov, *Bubble velocities and oscillon precursors in first-order phase transitions*, *JHEP* **11** (2024) 064, [2312.13364].

[42] E. Cotner, A. Kusenko and V. Takhistov, *Primordial Black Holes from Inflaton Fragmentation into Oscillons*, *Phys. Rev. D* **98** (2018) 083513, [1801.03321].

[43] J. Ollé, O. Pujolàs and F. Rompineve, *Oscillons and Dark Matter*, *JCAP* **02** (2020) 006, [1906.06352].

[44] M. Kawasaki, W. Nakano and E. Sonomoto, *Oscillon of Ultra-Light Axion-like Particle*, *JCAP* **01** (2020) 047, [1909.10805].

[45] A. Arvanitaki, S. Dimopoulos, M. Galanis, L. Lehner, J. O. Thompson and K. Van Tilburg, *Large-misalignment mechanism for the formation of compact axion structures: Signatures from the QCD axion to fuzzy dark matter*, *Phys. Rev. D* **101** (2020) 083014, [1909.11665].

[46] N. Kitajima, J. Soda and Y. Urakawa, *Nano-Hz Gravitational-Wave Signature from Axion Dark Matter*, *Phys. Rev. Lett.* **126** (2021) 121301, [2010.10990].

[47] N. Kitajima, K. Kogai and Y. Urakawa, *New scenario of QCD axion clump formation. Part I. Linear analysis*, *JCAP* **03** (2022) 039, [2111.05785].

[48] G. Dvali, *Saturon Dark Matter*, 2302.08353.

[49] M. Hindmarsh and P. Salmi, *Oscillons and domain walls*, *Phys. Rev. D* **77** (2008) 105025, [0712.0614].

[50] J. Braden, J. R. Bond and L. Mersini-Houghton, *Cosmic bubble and domain wall instabilities II: Fracturing of colliding walls*, *JCAP* **08** (2015) 048, [1505.01857].

[51] J. R. Bond, J. Braden and L. Mersini-Houghton, *Cosmic bubble and domain wall instabilities III: The role of oscillons in three-dimensional bubble collisions*, *JCAP* **09** (2015) 004, [1505.02162].

[52] A. Vaquero, J. Redondo and J. Stadler, *Early seeds of axion miniclusters*, *JCAP* **04** (2019) 012, [1809.09241].

[53] M. Gorghetto, E. Hardy and G. Villadoro, *More axions from strings*, *SciPost Phys.* **10** (2021) 050, [2007.04990].

[54] J. J. Blanco-Pillado, D. Jiménez-Aguilar and J. Urrestilla, *Exciting the domain wall soliton*, *JCAP* **01** (2021) 027, [2006.13255].

[55] N. Kitajima, F. Kozai, F. Takahashi and W. Yin, *Power spectrum of domain-wall network, and its implications for isotropic and anisotropic cosmic birefringence*, *JCAP* **10** (2022) 043, [2205.05083].

[56] G. Dvali and C. Gomez, *Black Hole's Quantum N-Portrait*, *Fortsch. Phys.* **61** (2013) 742–767, [1112.3359].

[57] G. Dvali and C. Gomez, *Black Holes as Critical Point of Quantum Phase Transition*, *Eur. Phys. J. C* **74** (2014) 2752, [1207.4059].

[58] G. Dvali and C. Gomez, *Landau–Ginzburg limit of black hole's quantum portrait: Self-similarity and critical exponent*, *Phys. Lett. B* **716** (2012) 240–242, [1203.3372].

[59] G. Dvali and S. Zell, *Classicality and Quantum Break-Time for Cosmic Axions*, *JCAP* **07** (2018) 064, [1710.00835].

[60] G. Dvali, C. Gomez and S. Zell, *Quantum Break-Time of de Sitter*, *JCAP* **06** (2017) 028, [1701.08776].

[61] J. Eby, P. Suranyi, C. Vaz and L. C. R. Wijewardhana, *Axion Stars in the Infrared Limit*, *JHEP* **03** (2015) 080, [1412.3430].

[62] A. H. Guth, M. P. Hertzberg and C. Prescod-Weinstein, *Do Dark Matter Axions Form a Condensate with Long-Range Correlation?*, *Phys. Rev. D* **92** (2015) 103513, [1412.5930].

[63] K. D. Lozanov and M. A. Amin, *Self-resonance after inflation: oscillons, transients and radiation domination*, *Phys. Rev. D* **97** (2018) 023533, [1710.06851].

[64] M. Piani, J. Rubio and F. Torrenti, *Ephemeral Oscillons in Scalar-Tensor Theories: The Higgs-like case*, 2501.14869.

[65] A. Chodos, R. L. Jaffe, K. Johnson, C. B. Thorn and V. F. Weisskopf, *A New Extended Model of Hadrons*, *Phys. Rev. D* **9** (1974) 3471–3495.

[66] D. E. Kaplan and R. Rattazzi, *Large field excursions and approximate discrete symmetries from a clockwork axion*, *Phys. Rev. D* **93** (2016) 085007, [1511.01827].

[67] F. van Dissel and O. Pujolàs, *in preparation*, .

[68] F. L. Bezrukov and M. Shaposhnikov, *The Standard Model Higgs boson as the inflaton*, *Phys. Lett. B* **659** (2008) 703–706, [0710.3755].

[69] A. De Simone, M. P. Hertzberg and F. Wilczek, *Running Inflation in the Standard Model*, *Phys. Lett. B* **678** (2009) 1–8, [0812.4946].

[70] N. V. Alexeeva, I. V. Barashenkov, A. A. Bogolubskaya and E. V. Zemlyanaya, *Understanding oscillons: Standing waves in a ball*, *Phys. Rev. D* **107** (2023) 076023, [2304.05911].

[71] H. Arodz, P. Klimas and T. Tyranowski, *Compact oscillons in the signum-Gordon model*, *Phys. Rev. D* **77** (2008) 047701, [0710.2244].

[72] G. Dvali, M. Michel and S. Zell, *Finding Critical States of Enhanced Memory Capacity in Attractive Cold Bosons*, *EPJ Quant. Technol.* **6** (2019) 1, [1805.10292].

[73] G. Dvali, *Entropy Bound and Unitarity of Scattering Amplitudes*, *JHEP* **03** (2021) 126, [2003.05546].

[74] G. Dvali, O. Kaikov and J. S. V. Bermúdez, *How special are black holes? Correspondence with objects saturating unitarity bounds in generic theories*, *Phys. Rev. D* **105** (2022) 056013, [2112.00551].

[75] G. Dvali and O. Sakhelashvili, *Black-hole-like saturons in Gross-Neveu*, *Phys. Rev. D* **105** (2022) 065014, [2111.03620].

[76] G. Dvali, O. Kaikov, F. Kühnel, J. S. Valbuena-Bermudez and M. Zantedeschi, *Vortex Effects in Merging Black Holes and Saturons*, *Phys. Rev. Lett.* **132** (2024) 151402, [2310.02288].

[77] C. Adam, K. Oles, T. Romanczukiewicz and A. Wereszczynski, *Kink-antikink scattering in the ϕ^4 model without static intersoliton forces*, *Phys. Rev. D* **101** (2020) 105021, [1909.06901].

[78] A. García Martín-Caro, J. Queiruga and A. Wereszczynski, *Feshbach resonances and dynamics of BPS solitons*, *Phys. Rev. D* **111** (2025) 096002, [2501.02589].

[79] C. Adam, K. Oles, T. Romanczukiewicz and A. Wereszczynski, *Spectral Walls in Soliton Collisions*, *Phys. Rev. Lett.* **122** (2019) 241601, [1903.12100].

[80] F. Blaschke, T. Romańczukiewicz, K. Sławińska and A. Wereszczyński, *Amplitude modulations and resonant decay of excited oscillons*, *Phys. Rev. E* **110** (2024) 014203, [2403.00443].

[81] H. Segur and M. D. Kruskal, *Nonexistence of Small Amplitude Breather Solutions in ϕ^4 Theory*, *Phys. Rev. Lett.* **58** (1987) 747–750.

[82] M. P. Hertzberg, *Quantum and Classical Behavior in Interacting Bosonic Systems*, *JCAP* **11** (2016) 037, [1609.01342].

[83] J. N. Hormuzdiar and S. D. H. Hsu, *Pion breather states in QCD*, *Phys. Rev. C* **59** (1999) 889–893, [hep-ph/9805382].

10 Semiclassical backreaction: a qualitative assessment

Semiclassical Backreaction: A Qualitative Assessment

Fabio van Dissel*

Institut de Física d'Altes Energies (IFAE)

The Barcelona Institute of Science and Technology (BIST)

Campus UAB, 08193 Bellaterra (Barcelona) Spain

George Zahariade†

Instytut Fizyki Teoretycznej, Uniwersytet Jagielloński,

Lojasiewicza 11, 30-348 Kraków, Poland

The backreaction of quantum degrees of freedom on classical backgrounds is a poorly understood topic in theoretical physics. Most often it is treated within the *semiclassical approximation* with the help of various *ad hoc* prescriptions accounting for the effect of quantum excitations on the dynamics of the background. We focus on two popular ones: (i) the *mean-field* approximation whereby quantum degrees of freedom couple to the classical background via their quantum expectation values; (ii) the (stochastic) *Truncated Wigner* method whereby the fully coupled system is evolved using classical equations of motion for various randomly sampled initial conditions of the quantum degree of freedom, and a statistical average is performed *a posteriori*. We evaluate the performance of each method in a simple toy model against a fully quantum mechanical treatment, and identify its regime of validity. We interpret the results in terms of quantum entanglement and loss of classicality of the background.

* fvdissel@ifae.es

† george.zahariade@uj.edu.pl

CONTENTS

I. Introduction 264

II. Motivation 266

III. Model 268

A. Numerical methods 270

1. Quantum Mechanics 271

2. Semiclassical approximations 271

3. Measure of correctness and semiclassical break time 274

IV. Results 274

V. Summary and Discussion 282

Acknowledgments 286

A. Analytical Results for Small Collective Coupling 286

1. Quantum Mechanics 286

2. Mean-Field 289

3. Trunctated Wigner 290

B. Systems with more degrees of freedom 291

C. Numerics and performance tests 292

References 294

I. INTRODUCTION

Since the dawn of quantum mechanics, understanding the dynamics of quantum variables evolving in classical background fields has played a central role in the development of fundamental physics. In fact some of the foundational experiments of quantum mechanics, such as the Stern-Gerlach experiment [1] for instance, rely on the existence of a classical external electromagnetic field which interacts with the quantum system. This *semiclassical* point of view, where part of the system is treated classically while another part is treated quantum mechanically, is well-suited for situations where either (i) the external field is actively maintained by an operator, or (ii) the field is so strong (in a sense that can be made precise) that any fluctuations due to its interactions with the quantum degrees of freedom are negligible. In both of these cases, the dynamics of the background is unaffected by the presence of the quantum degrees of freedom, and the external field obeys classical equations of motion.

This approach has been tremendously successful in explaining the splitting of atomic energy levels in the presence of external electromagnetic fields [2, 3] (Zeeman and Stark effects), and is routinely used in quantum optics [4, 5], where it allows for the accurate description of laser-matter interaction, and of many features of the photoelectric effect.[1] Within the framework of quantum field theory, it also predicts the creation of electron positron pairs in a strong enough electric field, phenomenon known as *Schwinger pair production* [6].

The exact same paradigm applies to situations where the external field is no longer electromagnetic in nature. This is for instance the case in condensed matter when studying quantum fluctuations on top of Bose-Einstein condensates [7], and more generally in field theory where the quantum stability of long-lived non-perturbative classical solutions such as solitons and topological defects [8], oscillons, and q-balls [9] has been studied [10–14]. But the external field can also be gravitational in nature. This is covered in detail within the framework of quantum field theory in curved spacetime [15] and leads to important phenomena such as cosmological particle production [16, 17] or Hawking radiation [18, 19].

The latter example is particularly important, since it suggests that black holes radiate thermally and thus, by energy conservation, lose mass and evaporate. Such a situation lies precisely outside the regime of validity of the semiclassical regime of quantum mechanics described above since the classical background (the metric around a Schwarzschild black hole for instance) must be sensitive

[1] Historically, the photoelectric effect was understood as a *smoking gun* for the quantization of the electromagnetic field and the existence of the photon, however it turns out that its most salient features can be understood as arising from the interaction of quantum matter with a classical electromagnetic field (see e.g. Chapter 9 or Ref. [4] or Chapter 2E of Ref. [5]).

to the production of Hawking quanta. This *backreaction* of quantum radiation on the classical background that has generated it, lacks a satisfying description since a full theory of quantum gravity is unavailable for the time being. One possible way of taking quantum backreaction into account is to replace the energy-momentum tensor on the right hand side of the Einstein equations with its quantum expectation value taken in a properly chosen quantum state. This of course comes with its own difficulties because surely such a *mean field* approximation would only be valid as long as the quantum state stays sufficiently regular and doesn't develop a spatially multi-modal character (the analog of a double-humped spatial probability density in quantum mechanics).[2]

While the mean-field approximation can be applied in any context (and not just to semiclassical gravity) by replacing any ocurrences of the quantum degrees of freedom in the classical equation of motion for the background with their quantum expectation values, it is just one of the possibilities. Another is to treat the fully coupled system classically but to sample the initial conditions for the quantum degree of freedom from a properly chosen probability distribution (usually specified by the relevant quantum state). Of course the initial condition for the background would be uniquely defined since it is supposed to be classical. Each initial condition will yield a particular realization of the dynamics and one could expect that averaging over a large number of realizations would produce the quantum backreacted dynamics of the classical background. This *stochastic* method has been used in the context of early universe cosmology and (p)reheating in particular [20, 21]

Of course there are various other ways of taking backreaction into account, with the help of Langevin or Fokker-Planck equations [22–24], by integrating out quantum fluctuations and using an effective action to determine the background dynamics [25, 26], or by using open quantum field theory methods akin to the so-called *in-in* or Schwinger-Kheldysh formalism [23, 27, 28]. However all of these methods are quite unwieldy and often times lead to computations that, although in principle doable to arbitrary precision (see for instance Ref. [29] where the reflection coefficient on a so-called reflectionless kink is computed in a fully quantum field theoretic manner and backreaction is included), are difficult to perform in practice. Moreover, to our knowledge none of the above semiclassical backreaction methods has been checked against a fully quantum mechanical treatment of the coupled system (either because of the intrinsic complexity of the task or because such a treatment is unavailable as in the case of gravity).

In this work we will be focusing on the above mean field and stochastic methods only. The goal is to gauge their performance in a physically motivated toy model where a fully quantum mechanical

[2] Not to mention the many subtleties relating to the renormalization of the usual quantum field theoretic divergences accompanying correlation functions in the coincident limit [15].

numerical treatment is within reach. In Section II we will give some background and motivate our approach in the context of previous work on the so-called *quantum break time* of a system [30–35]. In Section III we will introduce the cosmologically inspired toy model that we will be considering (two simple harmonic oscillators coupled via a bi-quadratic interaction) and set up the two semiclassical backreaction methods whose performance will be assessed. In Section IV we will showcase our results, outlining the regions of parameter space where they should be trusted and for how long. Finally, we will end in Section V with a broad discussion of the role that classical instabilities of the background and quantum entanglement play in the breakdown of the semiclassical approximations used widely in the literature.

II. MOTIVATION

The standard way of performing computations in quantum field theories is to look for an extremum of the classical action, the classical background, and expand the path integral around it, using perturbation theory in the coupling parameter (or equivalently in $\hbar$). If the background is static, this procedure is well defined to any order and is particularly well suited for analyzing scattering problems. However, if it has some nontrivial time dependence, there is only an adiabatic notion of vacuum for the quantum fluctuations living on top of it. This means that the time-varying background will generically create particles "out of nothing." Since energy conservation holds, it is expected that the creation of these particles will affect the classical background, entangling it with the first-order perturbations appearing in the saddle point approximation. There is at this point no clear consensus in the literature on how to deal with the question of backreaction in such situations and the present work aims to shed some light on the issue.

To highlight some of the important ideas we will take the following Lagrangian describing the dynamics of two real scalar fields, ϕ and χ, in flat 4 dimensional spacetime, and interacting via a so-called *portal* interaction, as a starting point,[3]

$$\mathcal{L} = \frac{1}{2}\partial_\mu\phi\partial^\mu\phi + \frac{1}{2}\partial_\mu\chi\partial^\mu\chi - \frac{1}{2}\omega^2\phi^2 - \frac{1}{2}\nu^2\chi^2 - \frac{\lambda}{2}\phi^2\chi^2, \tag{1}$$

where we work in units where $c = 1$ (but keep explicit factors of $\hbar$ for the time being), ω, ν are two angular frequencies (corresponding to the mass parameters or inverse Compton wavelengths of the two fields), and λ is the coupling constant.

[3] We use the mostly minus signature for the Minkowski metric.

This type of lagrangian is of particular interest in early universe cosmology as it represents a popular toy model to study (p)reheating after inflation, although here we will neglect the effects of expansion and work in Minkowski spacetime. To study this model, standard lore tells us to start from an extremum of the classical action. In the context of reheating, one often considers one of the fields (by convention ϕ) to play the role of the inflaton, while the other field (χ) is simply a spectator. In particular, a natural solution for the physics at the end of inflation is given by

$$\phi(t,\vec{x}) = \phi(t) = \phi_0 \cos(\omega t) \quad \text{and} \quad \chi(t,\vec{x}) = 0. \tag{2}$$

Equation (2) represents an analytic solution of the classical equations of motion, valid for all times. As mentioned above, this is only true in the classical limit of $\hbar \to 0$, and the quantum mechanical fluctuations of the fields will alter these dynamics. To understand how, and to make the connection between classical and quantum physics, we then ask the question of whether there exists a quantum mechanical state (in the Heisenberg picture) for which the 1-point functions $\langle\hat{\phi}(t,\vec{x})\rangle$ and $\langle\hat{\chi}(t,\vec{x})\rangle$ obey Eqs. (2), and which is, at least approximately, Gaussian and "well localized" in field phase space. In other words we require (i) that the higher order correlation functions can be related to the 2-point ones via Wick's formula, and (ii) that these 2-point functions approximately factorize up to vacuum contributions [36] e.g. $\langle\hat{\phi}(x)\hat{\phi}(x')\rangle \approx \langle\hat{\phi}(x)\rangle\langle\hat{\phi}(x')\rangle + \langle 0|\hat{\phi}(x)\hat{\phi}(x')|0\rangle$. In other words, are there states in quantum mechanics that can (almost) be described by classical physics?

Of course, such states exist and are the well-known coherent states of quantum mechanics [37]. Formally, a coherent state for the mode $\vec{k}$ is an eigenstate of the corresponding annihilation operator $\hat{a}_{\vec{k}}$. It is a state $|\mathcal{N}_{\vec{k}}\rangle$, populated by an on average constant number of particles $\langle\hat{N}_{\vec{k}}\rangle = \langle\mathcal{N}_{\vec{k}}|\,\hat{a}^\dagger_{\vec{k}}\hat{a}_{\vec{k}}\,|\mathcal{N}_{\vec{k}}\rangle = \mathcal{N}_{\vec{k}}$. (In particular, the state with no particles in the mode $\vec{k}$, $|0_{\vec{k}}\rangle$, is a coherent state.) A field coherent state is obtained by taking the tensor product of mode coherent states. The coherent state corresponding to Eqs. (2) is obtained by populating the homogeneous mode of the ϕ field with $\mathcal{N} = \dfrac{\phi_0^2}{2\omega^2\hbar}$ particles per (Compton) volume ω^{-3} while keeping all other modes (including those of the field χ) empty. Although we can formally construct this state in the Heisenberg picture, there is no guarantee that the desirable properties mentioned above survive during time evolution. In fact, for $\lambda \neq 0$, the particles in the coherent state will scatter, get entangled[4] with each other, and lose their original coherence. After some time the 1-point function will no longer correspond to the solution of the classical equations of motion. At that time a full quantum treatment is required to compute observables, as higher order correlation functions cease to be computable from

[4] By this we simply mean that the quantum state of the coupled system will no longer be *separable* i.e. factorizable as a tensor product of individual mode states.

the classically obtained solutions. This time has been referred to as the *quantum break time* in the literature [30]. Interestingly, the classical limit of $\hbar \to 0$ is equivalent to the double scaling of the dimensionless coupling $\alpha = \hbar\lambda \to 0$ and the average occupancy of the coherent state $\mathcal{N} \to \infty$, with the so-called *collective coupling* $\alpha\mathcal{N}$ kept finite (which is possible since it just contains classical variables). It is therefore good to keep in mind that many coherent particles correspond to weak coupling, which in turn corresponds to the classical limit.

For any finite value of $\hbar$ we expect a finite value of the quantum break time, which was argued to scale as $t_q \sim 1/(\omega\alpha^2\mathcal{N})$ in [30]. Since a full quantum treatment is usually difficult,[5] simply because of the dimensionality of the problem, various semiclassical approximations have been proposed to study quantum corrections in the limit of large occupation number $\mathcal{N}$ and be able to evolve the problem beyond the quantum break time. Generically, all of these methods assume ϕ to be classical and χ to be quantum, and prescribe the way in which these two fundamentally different degrees of freedom interact with one another. However, since in most cases we don't have an exact quantum field theoretic computation to compare to, the validity of these approximations is untested. As mentioned in the introduction, we are interested in comparing two such popular methods to a full quantum mechanical calculation. We are thus forced to limit ourselves to a toy model of two coupled quantum harmonic oscillators. This can be thought of as the field theory model of Eq. (1) restricted to the homogeneous mode of the field ϕ and just one of the *real* modes of the field χ. We are thus interested in computing the effect that the production of quanta in a χ field mode has on the dynamics of the homogeneous mode of the classical field ϕ. In other words we are interested in the semiclassical backreaction of χ on ϕ in a minisuperspace approximation. In the next section, we introduce the toy model that we will consider as well as the two semiclassical approximation schemes. From now on we will focus exclusively on this simplified system but we will also be touching upon concepts that are important to the more general case outlined here in this section.

III. MODEL

In what follows we will be working with a quantum mechanical system consisting of two simple harmonic oscillators coupled via a bi-quadratic interaction term. The dynamics of the model will thus be described by the Hamiltonian

$$H = -\frac{\hbar^2}{2m}\partial_x^2 - \frac{\hbar^2}{2M}\partial_y^2 + \frac{1}{2}m\omega^2 x^2 + \frac{1}{2}M\Omega^2 y^2 + \frac{\lambda}{2}x^2 y^2, \tag{3}$$

[5] Although some attempts have been made to study this problem by explicitly constructing high occupancy coherent states in an *interacting* quantum field theoretic setting [35, 38–41].

where m, M, ω, Ω are the masses and angular frequencies of the oscillators, and λ is the coupling strength.

In analogy with the model of Sec. II, the (Heisenberg picture) state of the system, defined at the initial time $t = 0$ and denoted by $|x_0, 0\rangle$, should be prepared in such a way that the x variable is in a coherent state with large occupation number (or in other words $\langle x_0, 0| \hat{x}(t = 0) |x_0, 0\rangle = x_0 \gg \sqrt{\hbar/2m\omega}$), thus playing the role of the classical homogeneous background ϕ, while y is in its ground state, thus playing the role of one of the $\chi_{\vec{k}}$. This can be achieved in the following way: (i) we start with the free Hamiltonian and both x and y in their respective ground states; (ii) we then adiabatically displace the potential for x to a position x_0, which has the effect of changing the ground state for x into a coherent state; (iii) we adiabatically turn on the interaction term which mildly entangles the two degrees of freedom with one another. At this point the system is in the interacting vacuum of the potential $\frac{1}{2}m\omega^2(x - x_0)^2 + \frac{1}{2}M\Omega^2 y^2 + \frac{\lambda}{2}x^2 y^2$ and thus has no dynamics. The sudden recentering $\frac{1}{2}m\omega^2(x - x_0)^2 \to \frac{1}{2}m\omega^2 x^2$ at $t = 0$ starts the evolution of the system with dynamics given by (3).

We will be concerned with various ways of numerically finding the dynamics of $\langle \hat{x}(t) \rangle = \langle x_0, 0| \hat{x}(t) |x_0, 0\rangle$ in this setup. On the one hand, because our toy model is simple enough, it is feasible to solve the full Schrödinger equation numerically, thus obtaining a reliable benchmark that we can compare other methods to. On the other hand, we can treat $\langle \hat{x}(t) \rangle$ as a classical variable whose classical dynamics incorporate the semiclassical backreaction of the quantum variable y. As mentioned before, this can be achieved in various ways but we will focus on two specific ones. As we will show, the quantum coupling will in some cases cause large entanglement of the variables, making any attempt at understanding the dynamics of $\langle \hat{x}(t) \rangle$ semiclassically, fruitless.

Let us pause for a moment to define what we mean by entanglement here and more generally throughout this paper. Generally, an entangled quantum state is defined in opposition to a product (or separable) state. Thus, in the case of our toy model, an entangled state will be a state $|\psi\rangle$ that cannot be written as a tensor product $|\rho\rangle_x \otimes |\sigma\rangle_y$ of an x state and a y state. There are many measures of entanglement including *purity*, *entanglement entropy*, and more generally *Renyi entropies* [42], but here we will mostly adopt a less sophisticated approach. We will call a state that is separable up to terms of order λ a *weakly entangled* state, and conversely, a state that does not satisfy this property will be called *strongly entangled*. At the end of Sec. IV we will check that this naive approach agrees with more quantitative measures of quantum entanglement.

Before going any further it is useful to rescale the variables and parameters so that we are strictly working with dimensionless quantities. This will also help in making the connection with

the general quantum field theoretic case. We start by defining $\tilde{x} = x\sqrt{m\omega/\hbar}$ and $\tilde{y} = y\sqrt{M\Omega/\hbar}$. The Hamiltonian of Eq. (3) can then be recast as

$$\tilde{H} = -\frac{1}{2}\partial_{\tilde{x}}^2 + \frac{1}{2}\tilde{x}^2 + \frac{\Omega}{\omega}\left[-\frac{1}{2}\partial_{\tilde{y}}^2 + \frac{1}{2}\left(1 + \tilde{\lambda}\tilde{x}^2\right)\tilde{y}^2\right], \tag{4}$$

where we have introduced the dimensionless Hamiltonian $\tilde{H} = H/\hbar\omega$ and dimensionless coupling $\tilde{\lambda} = \dfrac{\hbar\lambda}{m\omega M\Omega^2}$. Since the average occupation number in the x degree of freedom for the state $|x_0, 0\rangle$ is given by $N = \dfrac{m\omega x_0^2}{2\hbar} = \dfrac{\tilde{x}_0^2}{2}$, we can estimate the relative importance of the different terms in the above expression. The term outside the parentheses is of order N (in the limit of large occupation number that we are interested in), while the other term is of order $\dfrac{\Omega}{\omega}(1 + \tilde{\lambda}N)^{1/2}$. From this observation, it becomes clear that the limit $N\omega/\Omega \to \infty$ with $N\tilde{\lambda} = \dfrac{\lambda x_0^2}{2M\Omega^2}$ kept fixed corresponds to a classical decoupling limit where the x variable's dynamics are those of a pure coherent state and are not influenced by the presence of y. In a semiclassical treatment, where the full quantum dynamics of x are reduced to those of its average expectation value, this will correspond to the *vanishing quantum backreaction limit*. Notice that for a given ratio ω/Ω, this can be thought of as the limit $N \to \infty$, $\tilde{\lambda} \to 0$, keeping the *collective coupling* $\tilde{\lambda}N$ fixed, which is manifestly the direct analog of the double scaling we already encountered in Sec. II. This double scaling behavior is automatically satisfied in the limit $\hbar \to 0$.

For numerical convenience, we rescale y one last time by defining $\tilde{\tilde{y}} = \tilde{y}\sqrt{\omega/\Omega} = y\sqrt{M\omega/\hbar}$, and $\tilde{\tilde{\lambda}} = \tilde{\lambda}\,(\Omega/\omega)^2 = \dfrac{\hbar\lambda}{mM\omega^3}$, and, getting rid of the tildes and double tildes, we obtain the form of the Hamiltonian we will be working with in the rest of the paper,

$$H = -\frac{1}{2}\partial_x^2 + \frac{1}{2}x^2 - \frac{1}{2}\partial_y^2 + \frac{1}{2}\left[(\Omega/\omega)^2 + \lambda x^2\right]y^2. \tag{5}$$

We now turn to the numerical study of the dynamics given by this quantum Hamiltonian.

A. Numerical methods

In what follows we will compare the fully quantum mechanical evolution of $\langle\hat{x}(t)\rangle$ obtained from a numerical solution of the Schrödinger equation with Hamiltonian (5), to the one predicted by two semiclassical approximation schemes for including the effects of the quantum backreaction of y on the (classical) dynamics of $\langle\hat{x}(t)\rangle$. We will refer to these two methods as the *Mean Field* (MF) and *Truncated Wigner* (TW) methods.[6]

[6] Note that what we call MF method is known in the literature by many names: Hartree, Hartree-Fock or simply *semiclassical approximation* (especially in a semiclassical gravity context). Likewise the TW method is sometimes known as the *stochastic* or *statistical* method.

1. Quantum Mechanics

As discussed at the beginning of the section, the Schrödinger picture state at $t = 0$ is prepared in such a way that its wavefunction can be written (to first-order in λ) as

$$\psi_0(x, y) = \mathcal{N}_0 e^{-(x-x_0)^2/2} e^{-\left((\Omega/\omega)^2+\lambda x_0^2\right)^{1/2} y^2/2}, \tag{6}$$

where $\mathcal{N}_0$ is a normalization factor. This corresponds to the tensor product of a coherent state with a large occupation number, $N = x_0^2/2$, for the x degree of freedom, with the zeroth order adiabatic vacuum of the y degree of freedom (whose width is corrected by the interaction term). We stress that this is an approximate expression valid up to order λ in perturbation theory. In particular higher order corrections may reveal non-Gaussianity and entanglement.

Starting from these initial conditions we will solve the Schrödinger equation numerically using a second-order symplectic integrator (see Appendix C). At any point in time we can then output $\langle \hat{x}(t) \rangle$ and use this to assess the performance of the semiclassical approximation schemes. We outline these schemes next.

2. Semiclassical approximations

The starting point of any semiclassical method is the classical equations of motion stemming from Hamiltonian (5),

$$\ddot{x} + \left(1 + \lambda y^2\right) x = 0, \tag{7}$$

$$\ddot{y} + \left[(\Omega/\omega)^2 + \lambda x^2\right] y = 0. \tag{8}$$

As mentioned in Sec. II and at the beginning of Sec. III, we have prepared our quantum system in such a way that its dynamics yield $\langle \hat{x}(t) \rangle = x_0 \cos t$ and $\langle \hat{y}(t) \rangle = 0$ i.e. such that the 1-point functions obey the above classical equations of motion with initial conditions $x(0) = x_0$ and $y(0) = \dot{x}(0) = \dot{y}(0) = 0$. Of course this is only strictly true in the limit $\lambda \to 0$, $x_0 \to \infty$ (with λx_0^2 constant), or $\hbar \to 0$ in standard units. In fact for large but finite x_0 (or small but finite λ) the full quantum dynamics of the expectation values is expected to agree with the corresponding classical dynamics only until the quantum break time of the system.

The aim of any semiclassical approximation is to continue treating the x degree of freedom classically while relaxing the assumption of classicality for the y degree of freedom. To do this one would need to consistently incorporate the effect of the quantum fluctuations of y on the classical dynamics of x i.e. the quantum backreaction of y on x. Without much computational cost, one

should thus be able to extend the validity of the resulting, semiclassical, dynamics for x beyond the quantum break time. We will be focusing on two methods implementing this strategy.

1. *Mean Field approximation*

   While keeping x classical we promote y to a quantum operator $\hat{y}$. Working in the Heisenberg picture we can expand it as $\hat{y}(t) = z(t)\hat{a}^\dagger + z^*(t)\hat{a}$, where the creation and annihilation operators are defined with respect to the initial adiabatic ground state such that $\hat{a}\,|0\rangle = 0$ (see Refs. [43, 44] for details). The dynamics of the complex function $z(t)$ results from the Heisenberg equations of motion and follows a complexified version of Eq. (8),

   $$\ddot{z} + \left[(\Omega/\omega)^2 + \lambda x(t)^2\right] z = 0. \tag{9}$$

   At this point $x(t)$ can be chosen to be $x_0 \cos t$ but in fact it can be any arbitrary background function of time such that $x(0) = x_0$. The appropriate initial conditions for $z(t)$, corresponding to the choice of the adiabatic ground state for y, are $z(0) = -i\left((\Omega/\omega)^2 + \lambda x_0^2\right)^{-1/4}$ and $\dot{z}(0) = \left((\Omega/\omega)^2 + \lambda x_0^2\right)^{1/4}$. As long as the function $x(t)$ is fixed, the solution $z(t)$ of Eq. (9) is enough to specify the exact quantum dynamics of y i.e. to exactly compute all of its correlation functions. For instance $\langle \hat{y}(t)^2 \rangle = |z(t)|^2$. However, in this case we are precisely interested in how the background x is corrected, or backreacted upon, by the quantum excitations of y. Within the MF approximation, we include this correction in the classical equation of motion for x, Eq. (7), by replacing y^2 with $\langle \hat{y}^2 \rangle = |z|^2$. The solution, $x(t)$, of the resulting coupled system of equations will thus deviate from the purely classical harmonic and will also appear in Eq. (9). In summary, the set of equations to be solved for in the MF approximation will be

   $$\ddot{x} + \left(1 + \lambda |z|^2\right) x = 0, \tag{10}$$

   $$\ddot{z} + \left[(\Omega/\omega)^2 + \lambda x^2\right] z = 0, \tag{11}$$

   with the adiabatic initial conditions for z and the classical initial conditions for $x(0) = x_0$, $\dot{x}(0) = 0$. For some practical applications of this technique, including in field theory, see Refs. [43–46].

2. *Truncated Wigner method*:

The Wigner function of our initial state (6) is given by

$$W_0(x,y,p_x,p_y) = \frac{1}{\pi}\int dx'dy'\psi_0^*(x+x',y+y')\psi_0(x-x',y-y')e^{2i(p_xx'+p_yy')}$$
$$= \mathcal{N}_0^2 e^{-(x-x_0)^2}e^{-p_x^2}e^{-\left((\Omega/\omega)^2+\lambda x_0^2\right)^{1/2}y^2}e^{-\left((\Omega/\omega)^2+\lambda x_0^2\right)^{-1/2}p_y^2}, \qquad (12)$$

and can be interpreted as a joint probability distribution for the initial phase space variables of our system of interest. The idea of the TW method is to approximate the time-evolved Wigner function by a truncated sum of δ functions,

$$W_t(x,y,p_x,p_y) \approx \frac{1}{N_s}\sum_{i=1}^{N_s}\delta(x-x_i(t))\delta(p_x-p_{x,i}(t))\delta(y-y_i(t))\delta(p_y-p_{y,i}(t)), \qquad (13)$$

where $N_s \gg 1$ and different $x_i(t)$, $p_{x,i}(t) = \dot{x}_i(t)$, $y_i(t)$, $p_{y,i}(t) = \dot{y}_i(t)$ are solutions to the classical equations of motion (7) and (8), with initial conditions $x_i(0)$, $p_{x,i}(0)$, $y_i(0)$, $p_{y,i}(0)$ sampled randomly from the joint probability distribution[7] of Eq. (12) [47]. A nice review of the method is given in [48]. In the following we shall use a variant of this method where all $x_i(t)$, $p_{x,i}(t)$ have definite initial conditions $x_i(0) = x_0$, $p_{x,i}(0) = 0$. This corresponds to the assumption of classicality for the x degree of freedom. Likewise the randomness in the initial conditions of the y degree of freedom is supposed to mimic its quantum nature.

The expectation value of any (Weyl ordered) Heisenberg picture observable $\hat{O}(\hat{x},\hat{p}_x,\hat{y},\hat{p}_y)$ can then be estimated via

$$\langle\hat{O}(t)\rangle \approx \frac{1}{N_s}\sum_{i=1}^{N_s} O\left(x_i(t),p_{x,i}(t),y_i(t),p_{y,i}(t)\right), \qquad (14)$$

or in other words by averaging over the different classical paths. We will be interested in the case $\hat{O} = \hat{x}$ for which we obtain the backreacted dynamics of the classical background

$$x(t) = \langle\hat{x}(t)\rangle = \frac{1}{N_s}\sum_{i=1}^{N_s} x_i(t). \qquad (15)$$

In summary, this method is implemented by drawing a large number N_s of random initial conditions for y and p_y from the Wigner function (12) while constraining the initial conditions for x and p_x to be x_0 and 0 respectively. Each initial condition is then evolved classically using Eqs. (7) and (8), yielding a particular classical realization of the coupled dynamics. Finally, an average over all N_s realizations $x_i(t)$ is performed to obtain a uniquely defined $x(t)$ (see Eq. (15)).

[7] Although the Wigner function does not generically satisfy all the properties required of a *bonna fide* probability distribution, in particular positivity, it does satisfy them in the Gaussian case considered here.

Notice that this method is more computationally intensive that the Mean Field approximation, since N_s usually has to be a large number in order to bring the statistical variance to negligible levels. In this work we typically take $N_s \sim 10^4$.

We will need to compare the results of these two methods to the full quantum mechanical evolution of $\langle \hat{x}(t) \rangle$. Indeed, while we expect the above semiclassical solutions to agree with the exact one for a time longer than the quantum break time, they will eventually deviate from it. We will thus need a measure of "correctness" allowing us to decide until what time a given semiclassical method is to be trusted.

3. Measure of correctness and semiclassical break time

Each of the two semiclassical methods described above gives a value for $x(t)$. We would like to know at what point in time this value deviates significantly from the true value, $\langle \hat{x}(t) \rangle$, obtained by evolving the wavefunction with the Schrödinger equation. For this purpose, we first need to introduce an appropriate error function $\delta(t)$. A straightforward way to do this is to use the so-called L^1 norm to compute the (relative) integrated difference between semiclassical and full quantum solutions. We thus define

$$\delta(t) = \frac{\int_0^t |x(t') - \langle \hat{x}(t') \rangle| dt'}{\int_0^t \left(|x(t')| + |\langle \hat{x}(t') \rangle| \right) dt'}, \tag{16}$$

where $x(t)$ is computed semiclassically either in the MF or TW approximations. The denominator in this definition is simply a normalization factor and is required if we want to use this error function to compare the accuracy of different semiclassical methods across a large region of parameter space.

We can then define the *semiclassical break time* of a specific method to be the time t for which the monotonous function $\delta(t)$ rises above a certain threshold. For most of our results, we shall choose a threshold of 0.05, but any qualitative conclusions are quite insensitive to this value. In the next section we will estimate the semiclassical break times of the MF and TW methods, referred to as t_{MF} and t_{TW}, and compare them to the quantum break time t_q obtained by replacing $x(t)$ in Eq. (16) with the classical solution $x_{cl}(t) = x_0 \cos t$. We now move on to discussing our results.

IV. RESULTS

There are three different dimensionless parameters that we can vary in this problem: the coupling λ, the ratio of frequencies Ω/ω (or equivalently the ratio of energies in each mode), and finally x_0,

which is proportional to the square root of the average occupation number N in the coherent state. As we will see, each of these parameters has a profound effect on the different break times, and on the validity of the semiclassical approximation in general. To understand this point better, it is useful to linearize the classical equations of motion (7) and (8) around the solution $x_{cl}(t) = x_0 \cos t$ and $y_{cl}(t) = 0$. We obtain only one non-trivial equation

$$\ddot{\delta y} + \left[(\Omega/\omega)^2 + \lambda x_0^2 \cos^2 t\right] \delta y = 0, \tag{17}$$

which will seem familiar to many readers. It is the famous Mathieu equation, which finds many applications in various areas of physics. The solutions of Eq. (17) can be written as $\delta y(t) \propto p(t)e^{\mu t}$, where $p(t)$ is a periodic function and μ can in principle be complex (see e.g. [49]). Clearly, if μ has a positive real part, δy will grow exponentially signifying that the classical trajectory $(x_{cl}(t), y_{cl}(t))$ is unstable against classical fluctuations and the system becomes parametrically resonant. Whether μ indeed has a real part is entirely dependent on the three parameters of the problem, λ, Ω/ω and x_0. In fact, the three dimensional parameter space $(\lambda, \Omega/\omega, x_0)$ of the Mathieu equation (17) is characterized by the presence of instability bands, centered around the surfaces of equation

$$\lambda x_0^2 = 2\left(n^2 - (\Omega/\omega)^2\right), \tag{18}$$

where n is a positive integer. When the parameters lie sufficiently close to these surfaces, the system is classically unstable. At the quantum level, it has already been conjectured in the literature that the entanglement of the x and y degrees of freedom will grow quickly in the presence of parametric resonance at the classical level [50–52]. We may therefore reasonably expect that this will also lead to qualitatively different behaviors between semiclassical and full quantum dynamics (in other words to shorter semiclassical break times) as our semiclassical approximations struggle to capture purely quantum features such as entanglement. We will show that indeed the instability bands of the Mathieu equation, defined by Eq. (18), will have a profound effect on the semiclassical break times of the two approximation schemes under consideration.

To visualize the break times for the various methods under consideration, we performed a large number of numerical simulations for different combinations of parameters within the two semiclassical approximation schemes as well as within a full quantum treatment. We obtained independent predictions for the dynamics of the classical x degree of freedom: $x_{MF}(t)$ for the MF method, $x_{TW}(t)$ for the TW method, and $\langle \hat{x}(t) \rangle$ for the exact quantum benchmark. For completeness we also included the classical solution $x_{cl}(t) = x_0 \cos t$.

In Fig. 1 we show some typical results obtained from our simulations for a range of parameters. Already at the qualitative level, the influence of the instability bands is apparent. Parameters have

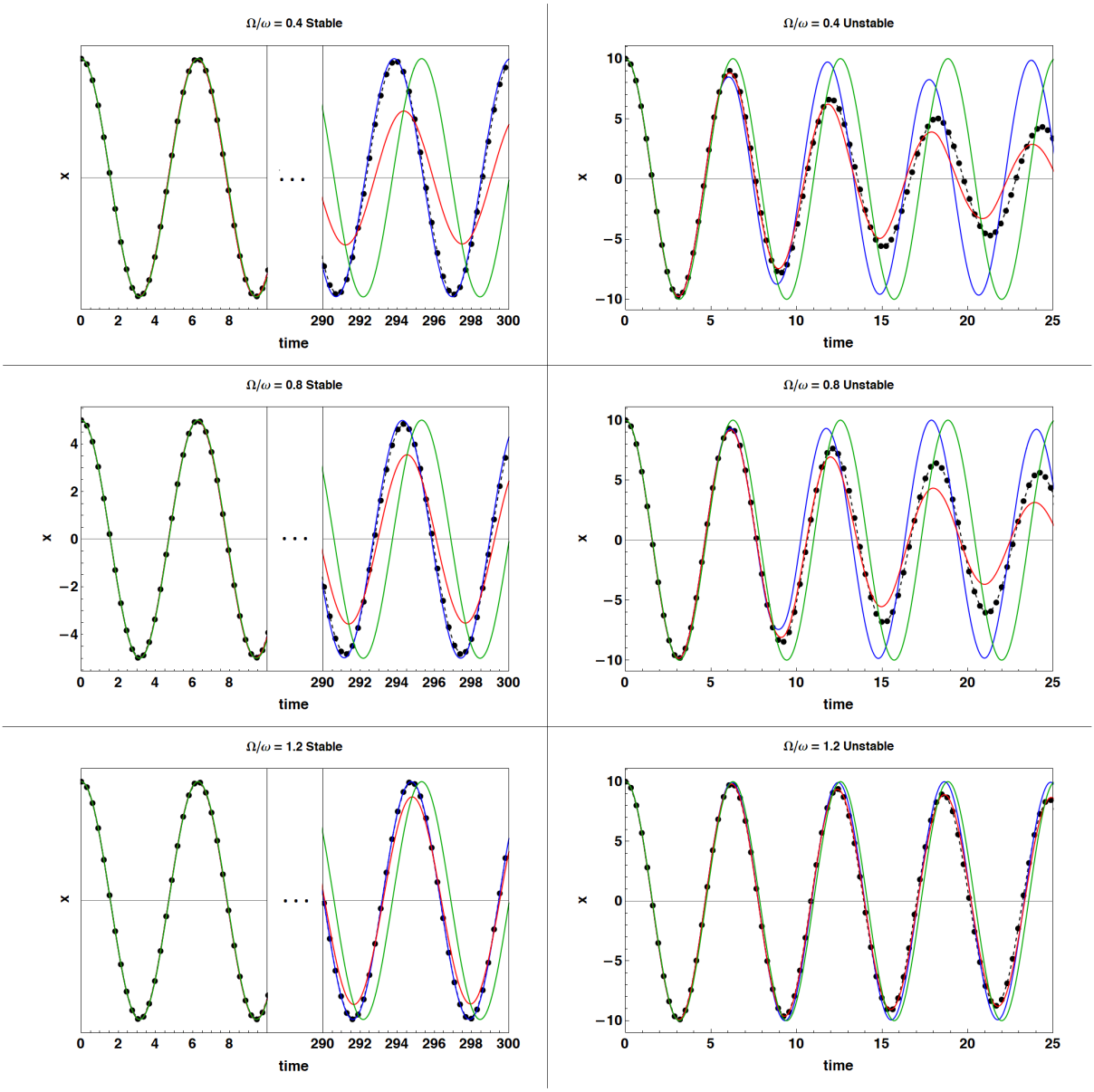

Figure 1. Some typical evolutions of $\langle \hat{x}(t) \rangle$ (black dotted line), $x_{MF}(t)$ (blue line), $x_{TW}(t)$ (red line) and $x_{cl}(t)$ (green line). We illustrate the importance of classical instability by choosing parameters in such a way that we are either in a completely stable regime (left panels, $\lambda = 0.01$, $x_0 = 5$) or in a regime where the dynamics (at least intermittently) move through an instability band (right panels, $\lambda = 0.1$, $x_0 = 10$). The qualitative difference is visible. In the stable region, we mostly see a small change in the frequency of oscillation (the disagreement between the plots is only visible after some time), whereas in the unstable situation, we see a rapid decay of the amplitude on top of the frequency shift. The different rows correspond to the different choices of Ω/ω: 0.4 (upper row), 0.8 (middle row), and 1.2 (lower row).

been chosen such that the left panel plots correspond to a stable system while those on the right

panel correspond to an unstable, parametrically resonant one, at the classical level. Focusing on the time evolution of $\langle \hat{x}(t) \rangle$, we first notice that its frequency of oscillation gets a small additive correction equal to $\lambda\omega/4\Omega$ (see Appendix A for details). This has the net effect of slightly shifting the instability bands upwards, their new position still given by Eq. (18) but with the substitution $n^2 \to n^2 \left(1 + \lambda\omega/4\Omega\right)^2$. From now on we will only be referring to these, shifted, instability bands. Notice that, the shift being small, this change in definition has no impact on the classical stability properties of the solutions represented in Fig. 1.

Besides this correction to the oscillation frequency, we also observe a qualitative difference between the stable and unstable cases: while in the stable case the amplitude of oscillation remains more or less constant, the unstable case features a dissipative-like dampening. This can be understood heuristically, in a field theoretic language, as follows. In a classically unstable region of parameter space, the particles making up the x mode coherent state rapidly scatter and get entangled with the particles produced in the y mode. The state then "decoheres"[8] quickly and ceases to mimic a classically oscillating system, thus leading to significant deviations from classical motion. In particular this triggers a dissipative behavior whereby higher and higher moments of the joint probability distribution of x and y are excited and Gaussianity is completely lost [53–58]. By contrast, in a stable region of parameter space entanglement still occurs but in a more controlled manner, only leading to the above mentioned multiplicative correction to the oscillation frequency of the x mode coherent state while preserving its Gaussianity. Note that in the stable case where entanglement is expected to be small and controlled, the full quantum dynamics seems to be better described by the MF method. The opposite seems to be true in the unstable situation where entanglement grows and only the TW method is able to capture dissipative-like effects, although both semiclassical methods fare quite poorly in this case. We will come back to this interesting fact later.

The importance of the instability bands is qualitatively clear at the level of the individual simulations, but how does it influence the break times of the various methods for a broad range of parameters? In Figs. 2, 3, and 4 we show the results of a parameter scan of the break times t_{MF}, t_{TW}, and t_q. Recall that these are defined as the times when $\delta(t)$, given by Eq. (16) with $x(t)$ replaced by $x_{MF}(t)$, $x_{TW}(t)$, and $x_{cl}(t)$ respectively, crosses a predefined threshold value in the simulation. Here we chose 0.05 as this critical threshold. Inspecting Figs. 2, 3 and 4, we see the effect of the classical instability band structure of the Mathieu equation. Around

[8] Here we simply mean that the state is becoming less like a coherent state. This has nothing to do with the decoherence phenomenon used to explain the classical to quantum transition.

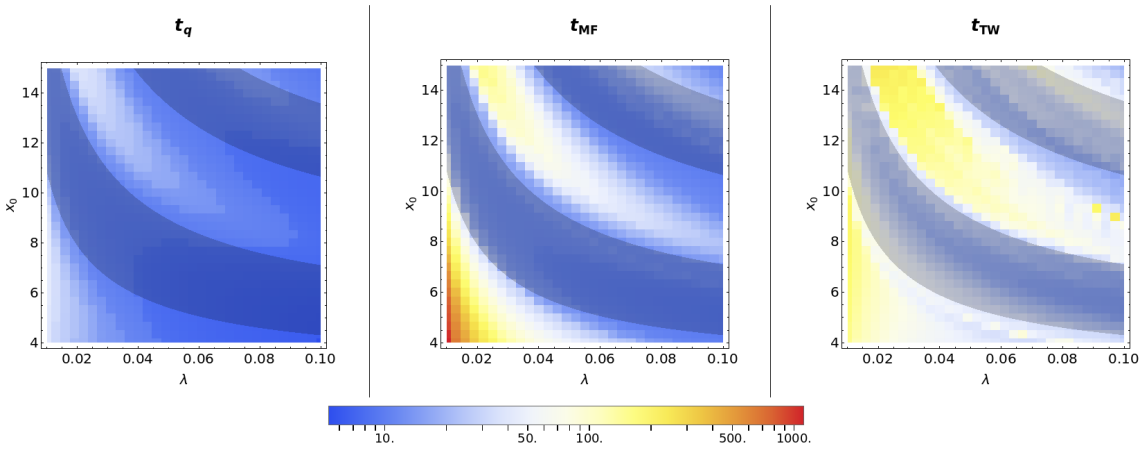

Figure 2. Quantum, and semiclassical break times for the MF and TW methods (as defined via Eq. (16) and a threshold value of 0.05) for a region of the $(\lambda, x_0, \Omega/\omega = 0.4)$ parameter plane. Redder (bluer) regions correspond to larger (shorter) break times and thus a more (less) accurate approximation of $\langle \hat{x} \rangle$. The shaded regions represent the instability bands of the Mathieu equation (see Eq. (18)). Their influence is clear: when the parameters of the system lie in their vicinity, there is a considerable enhancement of quantum entanglement between x and y, leading to a breakdown of classicality for x.

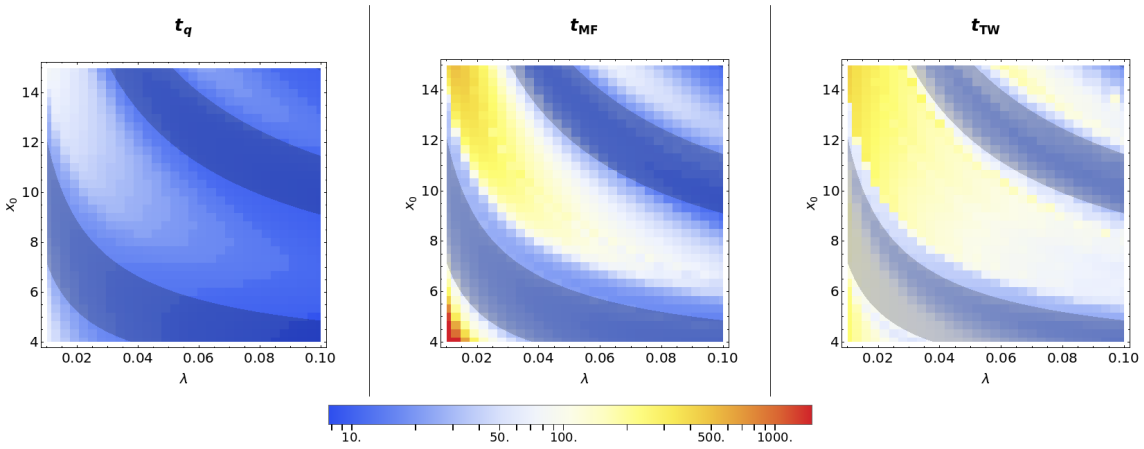

Figure 3. Same plot as Fig. 2 with $\Omega/\omega = 0.8$.

the bands, indicated by the shaded regions, the quantum and semiclassical break times decrease considerably. This supports the understanding that entanglement is at the root of the breakdown of (semi)classicality. The MF and TW methods prolong the agreement between the full quantum dynamics and a semiclassical description of the quantum backreacted dynamics of the x degree of freedom, in certain regions of parameter space considerably. Indeed, generically t_{MF}, $t_{TW} > t_q$ with a larger time gain far from the classical instability bands. However, both methods perform poorly within the instability bands, even though TW performs marginally better there. Notice also, that

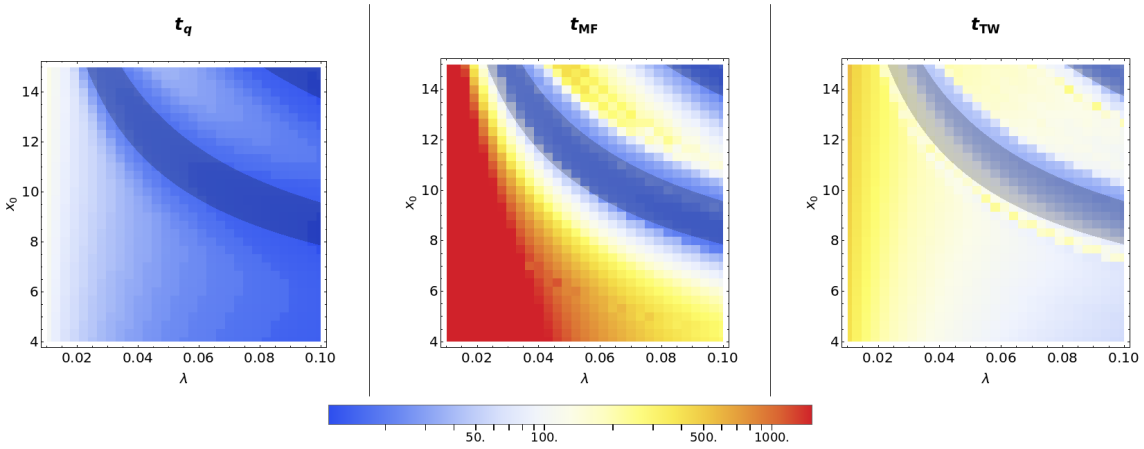

Figure 4. Same plot as Fig. 2 with $\Omega/\omega = 1.2$.

because the amplitude of $x(t)$ decreases in the parametrically unstable case, the system dynamically moves out of the instability band in the direction of decreasing x_0, which presumably brings the resonant phase to its natural conclusion. Finally, it is noteworthy that break times generally decrease substantially when moving upwards and to the right in parameter space, even outside any instability band, which is correlated with an increase in the collective coupling $\lambda x_0^2/2 = \lambda N$. In appendix A we show perturbatively that this can be understood as an increase in quantum entanglement between x and y.

It is natural to ask which of the two highlighted semiclassical methods, MF or TW, does a better job at extending the validity of a classical treatment for the background degree of freedom x in the presence of interactions with the quantum degree of freedom y. As seen in Figs. 2, 3, and 4, the answer depends on the parameters of the problem. In Fig. 5 we give a representation of the performance of the MF method relative to the TW method, identifying the regions in parameter space where $t_{MF} > t_{TW}$ and vice versa. Fig. 5 suggests that the MF method generally performs better whenever parameters are such that the system is far from any instability band. This highlights the importance of entanglement between the x and y degrees of freedom in evaluating which method to apply: it seems that whenever we are in a situation where entanglement remains under control, the MF method is more adequate in describing the exact quantum dynamics of $\langle \hat{x}(t) \rangle$. However, in situations where x and y become highly entangled, the TW method seems to perform better (although only marginally as seen in Figs. 1, 2, 3, and 4). In Fig. 6 we give a sense of the absolute difference in the break times of the two methods by plotting the difference $t_{TW} - t_{MF}$ as a function of λ and x_0 (for different values of the ratio Ω/ω).

To summarize our results and to make the connection with quantum entanglement a bit more

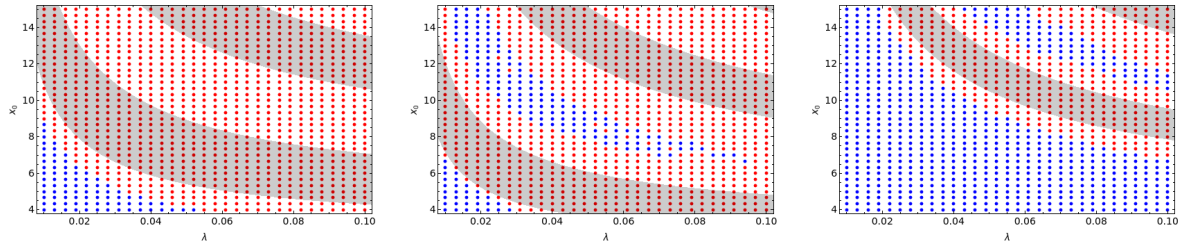

Figure 5. Plot showing the regions in the (λ, x_0) parameter plane where $t_{MF} > t_{TW}$ (blue dots) and $t_{MF} < t_{TW}$ (red dots) for different values of the ratio Ω/ω: 0.4 (left), 0.8 center, and 1.2 (right). The shaded region represent the instability bands. A heuristic picture emerges: far away from the instability bands, the MF method outperforms the TW method.

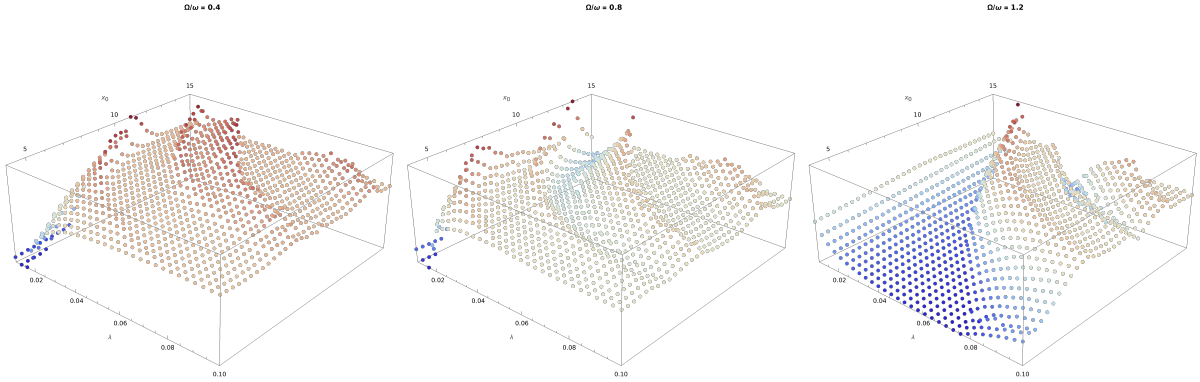

Figure 6. The three dimensional version of Fig. 5. We plot the difference in break times $t_{TW} - t_{MF}$ as a function of λ and x_0 for different values of the ratio Ω/ω: 0.4 (left), 0.8 (center), and 1.2 (right). Again, the influence of the instability bands is clear.

precise, in Table I we give the break times as well as the entanglement entropy (at some fiducial time) for a few prototypical values of the parameters. The entanglement entropy of the system is computed as the Von Neumann entropy of the reduced density matrix, $\hat{\rho}_x$,

$$\hat{\rho}_x = \sum_m \langle m| \hat{\rho} |m\rangle \,, \tag{19}$$

where $|m\rangle$ are the eigenstates of the y quantum harmonic oscillator and $\hat{\rho}$ is the full density matrix of the coupled system. As the Hilbert space has infinite dimension we limit the computation to a maximum quantum number $m_{max} = 28$, making sure that the state is contained up to a few parts in 10^2 in this reduced space. Then the entanglement entropy is given by

$$S_e = -\sum_i \lambda_i \log(\lambda_i), \tag{20}$$

where λ_i are the eigenvalues of $\hat{\rho}_x$. Heuristically, S_e measures the uncertainty in the "classical" x degree of freedom due to the interaction with the "quantum" y degree of freedom. Its maximum value is related to the dimensionality of the Hilbert space: in our case $S_{e,max} = \ln(m_{max}) = 3.33$. If and only if there is no entanglement (so that the state is separable) is it exactly 0. Note that this way of estimating quantum entanglement is just one of many possibilities [42].

λ	x_0	Ω/ω	Stability	t_q	t_{MF}	t_{TW}	S_e at $t = 25$
0.1	5	0.4	Unstable	6	9	17	1.86
0.05	8	0.4	Unstable	9	12	22	1.64
0.03	5	0.4	Stable	14	83	73	0.31
0.1	5	0.8	Unstable	10	16	25	1.21
0.04	6	0.8	Unstable	13	20	32	1.47
0.05	8	0.8	Stable	20	127	105	0.70
0.03	5	1.2	Stable	40	3304	164	0.026
0.04	6	1.2	Stable	31	1385	140	0.068
0.08	10	1.2	Unstable	14	22	34	0.13

Table I. A summary of some prototypical results from our numerical computations. The influence of stability on entanglement, and in turn the influence of entanglement on the break times, is evident.

The results in Table I contain the most salient features of our results. Namely, unstable modes result in larger entanglement, which in turn reduces the break times of the various methods. As suggested earlier, when entanglement is small, one typically has $t_{MF} > t_{TW}$. The quantum break time t_q is always smaller than both t_{MF} and t_{TW}, showing that the methods give at least some improvement with respect to a purely classical treatment. Note in particular that for the stable cases of $\Omega/\omega = 1.2$, quantum entanglement is extremely small and t_{MF} is orders of magnitude larger than both t_q and t_{TW}.

Interestingly, and on a slightly different note, we can also use the data from the previous plots to investigate the classical limit. As alluded to in Sec. II, this corresponds to the limit $\hbar \to 0$, for which $\lambda \to 0$ and $N \sim x_0^2 \to \infty$ (while the collective coupling $\lambda N = \lambda x_0^2/2$ is kept constant). For fixed λx_0^2, we therefore intuitively expect that the different break times should increase as x_0 increases (and consequently λ decreases). In fact, Ref. [30] uses heuristic arguments to predict break times that scale like N. In Fig. 7 we plot t_q, t_{MF}, and t_{TW} as a function of x_0 for various values of the collective coupling λN. We observe that although the heuristic linear scaling is sometimes correct, the influence of classical instabilities can be considerable, spoiling this prediction. In particular, as has been noted before, classically unstable systems have break times that scale with $\log N$ instead

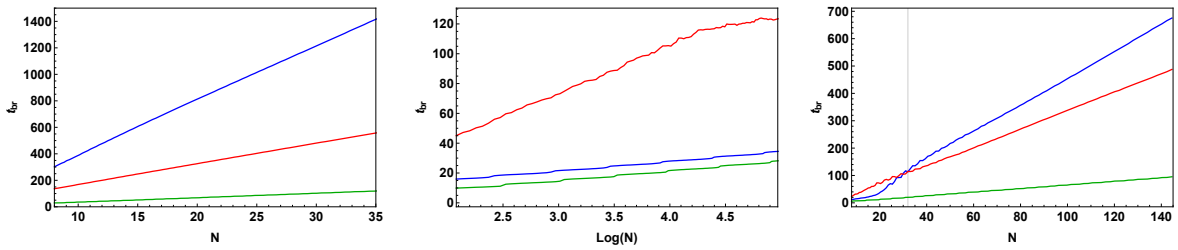

Figure 7. The break times t_q (green), t_{MF} (blue) and t_{TW} (red) plotted against $N = x_0^2/2$ (a proxy for $\hbar^{-1}$) for different values of the collective coupling λN and for $\Omega/\omega = 0.8$. The leftmost plot corresponds to $\lambda N = 0.15$, and to systems that remain stable all the way through the quantum to classical transition. The middle plot corresponds to $\lambda N = 0.6$, and to systems that are unstable. The rightmost plot corresponds to $\lambda N = 1.5$, a situation where the system transitions from unstable to stable during the double scaling $\lambda \to 0$ and $N \to \infty$. The approximate point of transition is represented by a vertical line on the plot. The expected N and $\log N$ scalings are evident in the stable and unstable situations respectively.

[34, 50]. For certain values of the collective coupling, one can have a situation where the system exits an instability band during the double scaling limit. There, we observe a transition between the two types of dependence ($\propto N$ and $\propto \log N$), e.g. the rightmost plot of Fig. 7.

V. SUMMARY AND DISCUSSION

In this work we tried to broach the topic of the regimes of validity of different semiclassical approximations. Indeed when classical degrees of freedom are coupled to quantum ones, there is no entirely consistent theory that one can use to make predictions. We therefore only have two options: either (i) find a way of describing the classical degrees of freedom by an appropriate set of quantum degrees of freedom and thus reduce the initial classical-quantum system to purely quantum one; or (ii) come up with approximate methods to evolve the initial system semiclassically i.e. by prescribing how the quantum degrees of freedom should backreact on the dynamics of the classical ones. Since option (i) generically comes with its own set of daunting problems (ambiguities in the quantum description of classical systems, computational complexity, inapplicability to gravitational systems...), progress has mostly relied on the use of various semiclassical approximations. Unfortunately the limitations of such methods have rarely been studied, an important blind spot that we have tried to partially cover. By focusing on a simple toy model involving two quantum, bi-quadratically coupled, harmonic oscillators, whose full quantum dynamics we were able to numerically compute, and taking an appropriate semiclassical limit whereby one (and only one) of

the two oscillators becomes effectively classical, we were able to assess the accuracy of two popular semiclassical approximation methods: the Mean Field and Truncated Wigner methods.

We found that the two methods are not nearly equivalent and that their regime of applicability depends on the parameters of the problem. By computing the duration for which a particular semiclassical evolution stays true to the exact quantum evolution (i.e. the semiclassical break time) we noticed that the parametric stability or instability of the associated classical system plays an important role.

Both semiclassical methods improve upon the purely classical description of the coupled system for all values of the parameters. This is to be expected since they do capture at least some of the quantum backreaction effects that the classical description cannot possibly describe. More interestingly though, for parameters such that the system is not classically parametrically unstable, the MF method outperforms the TW method. This gain in performance seems to be larger for weak collective coupling (product between the coupling and the average occupation number of the coherent state describing the "classical" oscillator). On the contrary, for parameters such that the system exhibits classical parametric resonance, the TW method fares better than the MF method. Although the break times are much lower than in the stable case, the TW method is able to capture the dissipative behavior of the system and to track the decay in the amplitude of the classical oscillator. We hypothesize that this behavior is a consequence of the rapid growth of the quantum entanglement between the two oscillators that was pointed out in particular in Ref. [52]. There the entanglement entropy was conjectured to grow linearly in time with a coefficient proportional to the sum of the positive Lyapunov exponents of the system.

Based on these observations we can venture a heuristic interpretation of our results. The fact that both methods fare worse in regions of classical instability and large collective coupling highlights the importance of entanglement between the two degrees of freedom. (In appendix A we point out that entanglement is indeed controlled by the magnitude of the collective coupling in the perturbative regime, when the system is classically stable.) It is not entirely surprising then that the TW method is able to track the system better in unstable regions, since the method evolves many more degrees of freedom over its different initializations, and is thus better able to capture the higher order moments of the wavefunction for y that are excited as quantum entanglement grows. Although this improves the ability of the method to capture the effects entanglement, the slow diffusion of the classical paths through phase space always leads to a finite break time. The MF method does not suffer from this problem and can track the evolution of the quantum state for all times, as long as the collective coupling is small and the system is classically stable. Based on these considerations

we can write down a heuristic formula for the break times of the two methods:

$$t_{MF} \propto (\alpha \cdot Entanglement)^{-1}\,, \tag{21}$$

$$t_{TW} \propto (\beta \cdot Entanglement + Diffusion)^{-1}\,. \tag{22}$$

Note that this should only be taken as a schematic equation, summarizing our results. The break time of the MF method is generally a function of the amount of entanglement between the two systems. While this is also true for TW, its break time also depends on a general diffusive drift between the various classical paths, due to the random nature of the initial conditions. The dependence on entanglement is stronger for MF however and we generally expect $\alpha > \beta$. Thus in unstable regions where entanglement is high, $t_{TW} > t_{MF}$ although both are relatively short, whereas in stable regions, entanglement is suppressed and the presence of the diffusion term forces $t_{TW} < t_{MF}$.

The previous observations have important consequences for some of the major domains of application of these two semiclassical methods. Taking the example of (p)reheating with which we started our discussion in Sec. II, we are now able to reinterpret the standard methodology in terms of our analysis. In fact, what is typically done in the literature of preheating, is to compute particle production from parametric resonance of classical fluctuations (typically obtained through cosmological lattice simulations), averaged over a variety of initializations [21]. In essence this is an application of the Truncated Wigner method to cosmological quantum fluctuations. We now understand why this is the correct choice as parametric resonance and classical instability are central to preheating, and one can expect a fair amount of entanglement between the inflaton and the resonant vacuum modes. The stable analogue of preheating is reheating [59]. Our expectation is that a mean-field approach should be appropriate in this scenario. Note that the period of reheating has traditionally been studied by assuming cubic couplings $\propto \phi\chi^2$, instead of the quartic coupling under consideration here. It is an interesting question to understand how reheating calculations would be altered by using the MF approach. We leave this interesting question for future work.

Other scenarios that have been treated using either of the approaches in this paper include the quantum decay of breather states (MF method) [46], kink-antikink scatterings in a quantum vacuum (MF method) [45], and false vacuum decay (TW method) [20]. It would be interesting to revisit some of these cases and assess their validity given the results in this work.[9] It is also important to mention that the quantum stability of soliton, oscillon, and breather backgrounds has been thoroughly investigated in the literature using perturbative methods as for instance in

[9] Many breather states under consideration in the literature have nonperturbative collective couplings where $\lambda N = \mathcal{O}(1)$. It has been suggested that the threshold $\lambda N = \mathcal{O}(1)$ characterizes a class of macroscopic objects that saturate the entropy bound coming from $2 \to N$ scattering amplitudes of the theory under consideration [60].

Ref. [61], and more recently in Refs. [62, 63] where it was argued that semiclassical methods may obscure important details about the quantum state of the background. For instance it was found that the quantum breather decay discussed using semiclassical MF methods in Ref. [46], resulted from an implicitly non-coherent choice of state for the background, rather than from an intrinsic quantum instability of the breather.

One of the main limitations of this work is its reliance on the assumption that $\langle \hat{x}(t) \rangle$ computed in a full quantum treatment, should always be a good benchmark against which to compare the performance of different semiclassical approximation methods. This is in fact only true as long the wavefunction $\psi(x, y)$ for the coupled system is well localized and more or less monomodal in the x direction. When this ceases to be true, it is clear that the average expectation value cannot possibly represent the dynamics of a classical variable. This introduces a more fundamental upper limit for the duration of validity of *any* semiclassical approximation, irrespectively of the associated value of $\delta(t)$ (see Eq. (16)). While we have checked that the wavefunction remains approximately Gaussian in the x direction for the duration of our simulation for some parameter choices, we leave a more exhaustive and rigorous study of this issue for future work. Another important limitation is the fact that it is unclear how to extend our results to the many-mode case and eventually to field theory. Appendix B gives some partial answers in the case where the "classical" mode is coupled to not one but two "quantum" modes. Again the presence of unstable modes seems to shorten the validity of the semiclassical methods under consideration but more work is needed in order to really understand the net effect of stable and unstable modes on the background in a many mode scenario. We also plan to tackle this problem in the near future. The results of Appendix B do provide some indication that classical instability and entanglement continue to play an important role in field theory, as it does in the quantum mechanical system under consideration here.

The investigations presented in this article do not claim to be the definitive answer to the question: "Given a specific classical system interacting with a quantum one, which semiclassical method is the most accurate?" They do however point out some of the subtleties that are often overlooked in the literature and that could in principle have important consequences. In particular the relation between classical parametric resonance and the rapid breakdown of semiclassical treatments may be relevant for early universe cosmology predictions. In future work, we aim to extend the above analysis to systems with different couplings, exhibiting different forms of instabilities (not just parametric resonance) that may be good toy models for gravitational collapse scenarios for instance. This is central to understanding which semiclassical method (if any) is most suitable for the study of black hole evaporation. In particular it might well be that all semiclassical methods

break down before a meaningful fraction of the black hole mass has evaporated, thus rendering black hole abundance estimates moot [64]. We also plan on assessing the performance of other semiclassical methods, and extending the MF method via the so-called quasi-classical formalism [53–58]. Lastly, an amusing side project would be to turn the logic of this paper on its head and explore the possibility of devising an interaction that classicalizes a quantum state, taking for instance a highly excited harmonic oscillator state $|n\rangle$ and naturally evolving it into a coherent state $|\alpha\rangle$ with average occupation number $|\alpha|^2 = n$.

ACKNOWLEDGMENTS

We would like to thank Eugenio Bianchi, Martin Bojowald, Tanmay Vachaspati, and Juan Sebastien Valbuena for useful discussions. F. D. acknowledges the support from the Departament de Recerca i Universitats from Generalitat de Catalunya to the Grup de Recerca 00649 (Codi: 2021 SGR 00649) and funding from the ESF under the program Ayudas predoctorales of the Ministerio de Ciencia e Innovación PRE2020-094420. G. Z. is supported by SONATA BIS Grant No. 2023/50/E/ST2/00231 from the Polish National Science Centre. This work is part of the doctoral thesis of F. D. within the framework of the Doctoral Program in Physics at the Autonomous University of Barcelona. The data used to produce the figures in this work are available at [65].

Appendix A: Analytical Results for Small Collective Coupling

It is instructive to understand how our toy model behaves when the coupling between the two degrees of freedom is weak. When this is the case, it can generally be expected that the "classical" x variable is weakly entangled with the "quantum" y variable. The first part of this appendix aims to show this explicitly. Then we will show that the MF method can exactly reproduce the average expectation value $\langle \hat{x}(t) \rangle$ for this weakly entangled state, while the Truncated Wigner method will never be able to achieve this, supporting our observations in Sec. IV.

1. Quantum Mechanics

In this derivation, we closely follow Ref. [66]. We start by writing the quantum state of the coupled system as

$$|\psi\rangle = \sum_{n,m=0}^{\infty} c_{n,m}(t) f_n(t) \, |n\rangle_x \, |m\rangle_y \,, \tag{A1}$$

where $|n\rangle_x$ and $|m\rangle_y$ are eigenstates of the free Hamiltonians for x and y in Eq. (5) respectively. The functions $f_n(t)$ are introduced for future convenience and correspond to the expansion coefficients of the initial coherent state for x,

$$f_n(t) = e^{-it/2} e^{-|z_0|^2} \frac{z_0^n e^{-int}}{\sqrt{n!}}, \tag{A2}$$

where z_0 is related to the initial displacement x_0 through $z_0 = x_0/\sqrt{2}$, since we assume 0 initial momentum. All the nontrivial time dependence is thus included in the undetermined $c_{n,m}(t)$ terms. It is useful to express the position and momentum operators in terms of creation and annihilation operators via

$$x = \frac{1}{\sqrt{2}}\left(a + a^\dagger\right), \qquad p_x = \frac{i}{\sqrt{2}}\left(a^\dagger - a\right), \tag{A3}$$

$$y = \sqrt{\frac{\omega}{2\Omega}}\left(b + b^\dagger\right), \qquad p_y = i\sqrt{\frac{\Omega}{2\omega}}\left(b^\dagger - b\right). \tag{A4}$$

Then the Hamiltonian (5) reads

$$H = \left(a^\dagger a + \frac{1}{2}\right) + \frac{\Omega}{\omega}\left(b^\dagger b + \frac{1}{2}\right) + \frac{\lambda\omega}{2\Omega}\frac{(a+a^\dagger)^2}{2}\frac{(b+b^\dagger)^2}{2}. \tag{A5}$$

Note that the effective coupling now appears to be $\lambda\omega/\Omega$, however in what follows we will assume $\Omega/\omega \sim \mathcal{O}(1)$. Plugging the ansatz (A1) into the Schrödinger equation with Hamiltonian (A5), we obtain a coupled set of equations for the different $c_{n,m}(t)$. Until now, the steps are completely general and the set of equations we obtain in this way have no closed form. As shown in [66], one can make progress by using the perturbative expansion

$$c_{n,m}(t) = \delta_{m0} e^{-i\frac{\Omega}{2\omega}t} + \mathcal{O}(\lambda). \tag{A6}$$

This expansion implicitly assumes weak collective coupling $\lambda z_0^2 = \lambda N \ll 1$ in order to match with the setup of our problem on the one hand, and to be consistent perturbatively on the other. Without showing all the details of the computation (we refer the reader to [66] for the complete version) it turns out that only the $m = 0$ and $m = 2$ terms get non-trivial corrections at leading order in λ, and the result can be elegantly written, in a form valid for all times, as

$$c_{n,0}(t) = e^{-i\frac{\Omega}{2\omega}t}\left[e^{-i\frac{\lambda\omega}{8\Omega}(2n+1)t} - i\frac{\lambda\omega}{8\Omega}\left(z_0^2 e^{-it} + \frac{n(n-1)}{z_0^2}e^{it}\right)\sin t\right], \tag{A7}$$

$$c_{n,2}(t) = -i\frac{\lambda\omega}{4\sqrt{2}\Omega}e^{-i\frac{3\Omega}{2\omega}t}\left[e^{-it}z_0^2\frac{\sin((\Omega/\omega-1)t)}{\Omega/\omega-1} + (2n+1)\frac{\sin((\Omega/\omega)t)}{\Omega/\omega} + e^{it}\frac{n(n-1)}{z_0^2}\frac{\sin((\Omega/\omega+1)t)}{\Omega/\omega+1}\right]. \tag{A8}$$

The requirement of small collective coupling now becomes evident since terms of order λz_0^2 make their appearance. Also note that the terms inversely proportional to z_0 become unimportant as $N \to \infty$ but we will keep the discussion general. Of course, in this work we are not interested in the quantum mechanical state itself, but instead on observables such as $\langle \hat{x}(t) \rangle$. Using (A3) we find

$$\langle \hat{x}(t) \rangle = \frac{z_0}{\sqrt{2}} \sum_{n,m=0}^{\infty} \left(e^{-it} c_{n+1,m} c^*_{n,m} + e^{it} c^*_{n+1,m} c_{n,m} \right) |f_n|^2, \tag{A9}$$

and plugging in the solutions from Eqs. (A7) and (A8) we obtain to lowest order in the coupling [10]

$$\langle \hat{x}(t) \rangle \approx x_0 \cos\left[t \left(1 + \lambda \frac{\omega}{4\Omega} \right) \right]. \tag{A10}$$

The behavior of higher moments is also important in order to ascertain how classical the state looks. For instance we find

$$\langle \hat{x}^2(t) \rangle = \sum_{n,m=0}^{\infty} \left(\frac{1}{2} z_0^2 e^{-2it} c_{n+2,m} c^*_{n,m} + \frac{1}{2} z_0^2 e^{2it} c^*_{n+2,m} c_{n,m} + \left(n + \frac{1}{2} \right) |c_{n,m}|^2 \right) |f_n|^2, \tag{A11}$$

and plugging in the solutions (A7) and (A8) we obtain

$$\langle \hat{x}^2(t) \rangle \approx \frac{x_0^2}{2} \left(1 + \cos\left[2t \left(1 + \lambda \frac{\omega}{4\Omega} \right) \right] \right) + \frac{1}{2} = \langle \hat{x}(t) \rangle^2 + \frac{1}{2}. \tag{A12}$$

This result suggests that, to leading order in λz_0^2, time evolution preserves the approximately classical nature of the state (see Sec. II and Ref. [36]). In other words, all the information about the state of the x variable is encoded in $\langle \hat{x}(t) \rangle$ suggesting that the state remains coherent. It simply transitions to a coherent state with a different frequency. In the next subsection we show that this type of behavior is mimicked perfectly by the MF method in the weak collective coupling limit.

Finally, we make a brief comment regarding entanglement. In the main part of the text, we suggest that entanglement is intimately tied to the breakdown of semiclassicality and also plays a vital role in determining which method performs better between MF and TW. Using (A7) it is easy to see that the state $|\psi\rangle$ is a product state at leading order in λ,

$$|\psi\rangle = \sum_{n,m=0}^{\infty} \delta_{m0} e^{-i\frac{\Omega}{2\omega}t} e^{-i\frac{\lambda\omega}{8\Omega}(2n+1)t} f_n(t) \, |n\rangle_x \, |m\rangle_y + \mathcal{O}(\lambda), \tag{A13}$$

and that quantum entanglement only arises at higher order in the collective coupling. In this low entanglement limit quantum effects seem to mainly manifest as a correction to the oscillation frequency of the classical solution. In what follows we will show that this is well captured by the MF method.

[10] Note that in [66] the perturbative expansion was organized in such a way that corrections to the frequency and amplitude of the oscillations could be treated separately. In this way the perturbative expansion is under control for all times. The result given here is zeroth order in the amplitude and first order in the frequency.

2. Mean-Field

The MF equations of motion are Eqs. (10) and (11) and we wish to find a perturbative solution with the appropriate initial conditions. Previously, we saw that in the limit of small couplings, the main correction to the classical solution $x(t) = x_0 \cos t$ was a change in the frequency, proportional to λ. With this in mind, we perform a two-timing analysis in which we introduce an extra timescale $\tau = \dfrac{\lambda\omega}{\Omega} t$. Then the perturbative solution can be obtained via the replacement

$$\partial_t^2 \to \partial_t^2 + 2\frac{\lambda\omega}{\Omega}\partial_t\partial_\tau + \mathcal{O}(\lambda^2) \tag{A14}$$

as well as a standard expansion of the solutions,

$$x = x^{(0)} + \lambda x^{(1)} + \mathcal{O}(\lambda^2), \tag{A15}$$

$$z = z^{(0)} + \lambda z^{(1)} + \mathcal{O}(\lambda^2). \tag{A16}$$

Plugging this into Eqs. (10) and (11) it is straightforward to find the general solutions for $x^{(0)}$ and $z^{(0)}$. They are given by

$$x^{(0)} = x_0 \cos(t + \delta_x(\tau)), \tag{A17}$$

$$z^{(0)} = -i\sqrt{\frac{\omega}{2\Omega}} e^{i((\Omega/\omega)t + \delta_z(\tau))}, \tag{A18}$$

where we allow for a dependence on τ of the phases. Without loss of generality we may set $\delta_x(\tau)$ and $\delta_z(\tau)$ to 0 at $t = \tau = 0$. We can then use the first-order equations of motion to find the form of these phase corrections. Since we are mainly interested in the behavior of x we only write down the zeroth-order equation for $x^{(1)}$ and we again assume small collective coupling $\lambda x_0^2 \ll 1$. We find

$$\ddot{x}^{(1)} + x^{(1)} = -\frac{2\omega}{\Omega}\partial_t\partial_\tau x^{(0)} - |z^{(0)}|^2 x^{(0)}. \tag{A19}$$

After plugging in the zeroth order solutions we obtain

$$\ddot{x}^{(1)} + x^{(1)} = \left(\frac{2\omega}{\Omega}\partial_\tau\delta_x(\tau) - \frac{\omega}{2\Omega}\right) x_0 \cos(t + \delta_x(\tau)). \tag{A20}$$

If the right hand side of this equation is not 0, the solution for $x^{(1)}$ would resonate, resulting in an immediate breakdown of perturbation theory. This yields the condition

$$\delta_x(\tau) = \frac{1}{4}\tau = \frac{\lambda\omega}{4\Omega} t. \tag{A21}$$

In principle, we can continue this procedure to higher orders, but at this point we have perfect agreement between the MF solution,

$$x(t) \approx x^{(0)}(t) = x_0 \cos\left[\left(1 + \lambda\frac{\omega}{4\Omega}\right) t\right], \tag{A22}$$

and the quantum mechanical result (A10). It is remarkable that in the weak collective coupling regime the MF method can reproduce quantum mechanical results for very long times. What's more, since the average expectation value completely determines the quantum mechanical state in this regime (see (A12)), the MF method manages to reproduce the results of a full quantum mechanical simulation at just a fraction of the computational cost. We will now end by arguing that this desirable property is not shared by the TW method.

3. Trunctated Wigner

It is significantly more difficult to derive an analytic estimate for the results of the TW method. However, here we will argue that after some time it will necessarily deviate from the weak collective coupling behavior of quantum mechanics. The best way to see this is to inspect one of the many classical realizations obtained in the TW framework. Applying the two-timing perturbative expansion of the previous section to the classical equations of motion (7) and (8), it is straightforward to show that the solution for the "classical" x variable approximately reads

$$x(t) \approx x_0 \cos\left[\left(1 + \lambda\frac{\omega}{4\Omega}\left((\Omega/\omega)y_0^2 + (\omega/\Omega)p_{y,0}^2\right)\right)t\right], \tag{A23}$$

for a particular, randomly sampled, initial condition for the "quantum" y variable, $(y_0, p_{y,0})$. Looking at this expression we see that the phases of the various classical realizations become completely uncorrelated within a time of order $\lambda^{-1}\left(\langle y_0^2\rangle + (\omega/\Omega)^2\langle p_{y,0}^2\rangle\right)^{-1} \sim \lambda^{-1}(2\omega/\Omega)^{-1}$ (where the brackets denote a statistical average weighted by the distribution (12)). After this time it should be approximately equivalent to write each solution as

$$x(t) \approx x_0 \cos\left(t + \phi\right), \tag{A24}$$

where ϕ is some random phase. At large times, the TW method thus seems to predict that the x variable slowly dissipates, as averaging over an ensemble of solutions such as the ones in (A24) will inevitably lead to amplitude decay. This behavior is not the one predicted by quantum mechanics in a classically stable region of parameter space, where the system settles to a new equilibrium solution and there is no dissipation. These results explain why the MF method performs better than TW in regions where the collective coupling is small. The fact that the TW method seems to explore the full phase space of the theory, which helps the method in regions of classical instability, hurts it when quantum entanglement doesn't grow uncontrollably.

Appendix B: Systems with more degrees of freedom

This appendix constitutes a preliminary investigation of how our results extend to systems with more degrees of freedom. In field theory, there are many modes, of which some can be stable, while others can be unstable. To understand how our results extend to quantum field theory it is thus important to introduce more degrees of freedom in our analysis.

As a first step, we analyze a three mode system defined through the dimensionless Hamiltonian

$$H = -\frac{1}{2}\partial_x^2 + \frac{1}{2}x^2 - \frac{1}{2}\partial_y^2 + \frac{1}{2}\left[(\Omega_1/\omega)^2 + \lambda x^2\right] y^2 - \frac{1}{2}\partial_z^2 + \frac{1}{2}\left[(\Omega_2/\omega)^2 + \lambda x^2\right] z^2. \tag{B1}$$

Here both the y and z degree of freedom should be interpreted as quantum modes, while x still corresponds to the classical background. We perform the computations in the same way as for the two-mode system, focusing on the break times of the different methods as well as on the entanglement entropy of x (this time the density matrix is partially traced over both the y and z degrees of freedom whose Hilbert space has been restricted to a finite dimensional subspace). We are particularly interested in cases where: (i) both modes are classically stable, (ii) both modes are classically unstable, and (iii) one mode is unstable while the other is stable. Results are shown in Table II.

λ	x_0	Ω_1/ω	Ω_2/ω	Stability	t_q	t_{MF}	t_{TW}	S_e at $t = 25$
0.1	5	0.4	0.8	UU	4	9	17	2.93
0.05	8	0.4	0.8	US	7	12	25	2.37
0.04	6	0.8	1.2	US	11	19	31	1.62
0.03	5	0.4	1.2	SS	11	83	70	0.34

Table II. Some prototypical results for the three mode system. Three situations can be distinguished: UU, when both modes are unstable, US, when the first mode is unstable while the second one is stable, and SS when both modes are stable. We can readily compare these results to those of Table I, for the two mode system. Again the influence of the existence of unstable modes on the break times is evident.

Our conclusions about the influence of classical instability and entanglement on the break times seem to extend to the three mode system. Comparing the above results to the analogue ones for the two mode case (see Table I), we see that the "most entangling" mode ultimately determines the entanglement entropy and break times of the three mode system. However the amount of unstable modes also seems to play a role. It is in particular unclear to what extent the presence of more stable modes can wash out the effect of the instability and extend the validity of semiclassical methods.

Unfortunately incorporating more modes quickly becomes computationally expensive, and is thus beyond the scope of this work.

Appendix C: Numerics and performance tests

In this appendix, we expand on the numerical integration schemes that we employed in this work. We had to solve three different sets of equations corresponding to the various methods under investigation. To be precise, the Mean Field equations (11) and (10), the Truncated Wigner equations (which are just the classical equations of motion (7) and (8), evolved for a large number of different initial conditions), and the full Schrödinger equation of quantum mechanics. Since the Schrödinger equation is a wave equation requiring lattice discretization to solve, we will mostly focus on the latter. As for the MF and TW methods, we will just mention that we used a *VV8* integration scheme for most of the results shown in this paper [67]. For certain prototypical points in parameter space (in particular in the corners of Figs. 2, 3 and 4) we explicitly checked that our results were stable against decreasing the time increment Δt. It is also good to mention that numerical results in the TW method were obtained by averaging over $N_s = 8192$ different realizations. Again, we checked for some prototypical parameter values that a higher number of samples did not change the results.

Now we turn our attention to the integration scheme used for the Schrödinger equation

$$i\frac{\partial \psi}{\partial t} = H\psi, \tag{C1}$$

where the Hamiltonian is written in position space as in Eq. (5). The initial conditions given in Eq. (6) completely determine the time evolution of the system. Formally this is given by

$$\psi(t, x, y) = e^{-i\int_0^t H dt}\psi_0(x, y). \tag{C2}$$

To find a numerical approximation of this solution we need to discretize space on a grid, writing $x_j = j\Delta x$ and $y_j = j\Delta x$, and solve the equation in a finite domain defined to be a square box of size L (centered around the origin). The number N^2 of gridpoints we include determines the spatial resolution $\Delta x = L/N$. Finally, we also discretize time, by defining $t_j = j\Delta t$, and evolve the wavefunction by rewriting (C2) as

$$\psi(t_f, x_j, y_j) = \Pi_{s=0}^{f} e^{-i\frac{\Delta t}{2}H_k} e^{-i\Delta t H_p} e^{-i\frac{\Delta t}{2}H_k}\psi_0(t_0, x_j, y_j), \tag{C3}$$

where H_k denotes the kinetic part of the Hamiltonian (the spatial derivatives) and H_p, the potential part. In practice, we employ a pseudo-spectral method where we evolve with H_k in Fourier space

by rotating the discrete Fourier transform (DFT) of $\psi(x_i, y_i, t_i)$ twice at each timestep. Notice that this is simply a *VV2* integration scheme applied to the discretized Schrödinger equation [68]. It is a symplectic integrator, conserving the total probability and average energy to high precision. Our method implicitly assumes periodic boundary conditions due to the way the DFT is performed. We checked that the boundary has little effect on our numerical solution, as long as the initial coherent state is well separated from it. This is because we are always working with a confining potential. To check that our results are not too sensitive to the spatial and temporal resolutions (Δx and Δt), and to the finite size of the box (L) we have performed convergence tests of the code, and investigated the influence of each source of truncation error individually. We did this by defining benchmark simulation parameters, $N = 256$, $L = 40$, $\Delta x = L/N \approx 0.15$ and $\Delta t = 0.03$, and comparing the resulting numerical solution to the one obtained by changing either Δt, Δx, or L, keeping everything else constant. Note that the benchmark parameters are precisely the ones we used for most of the results that we present in the main body of the text.

For example, we can compare how the average value of some operator $\hat{O}$, $\langle \hat{O}(t) \rangle$, changes when varying one of the benchmark parameters, by plotting the quantity[11]

$$\delta(t) = \frac{|\langle \hat{O}(t) \rangle - \langle \hat{O}(t) \rangle_b|}{\langle \hat{O}(t=0) \rangle}, \tag{C4}$$

where the subscript b refers to the benchmark simulation and the normalization factor in the denominator is exactly computable in terms of the initial conditions. In Fig. 8, we show the result of this test for operators $\hat{x}$ and $\hat{x}^2$ for three representative points in physical parameter space.

We observe that the errors remain small for all times. In fact, the maximum error is obtained when varying Δt. For $\Omega/\omega = 0.8$, $\lambda = 0.1$ and $x_0 = 15$ it becomes of order 10^{-2}. These errors do not influence the conclusions of this work as they are too small to change the results in any meaningful way. Of course, we could have reduced the error of our numerics by increasing the resolution of our grid, but opted not to in order to keep the computational time within reasonable limits. We believe that the results of Fig. 8 warrant this decision.

As a final test of our numerics, we also explicitly show that the average energy is conserved (by plotting $\Delta H(t) = |1 - \langle H(t) \rangle / \langle H(t=0) \rangle|$)for our benchmark simulation parameters. This is shown in Fig. 9. As expected we see that our code conserves energy up to 1 part in 10^4.

[11] Note that the quantity δ introduced here has nothing to do with the one in in Eq. (16).

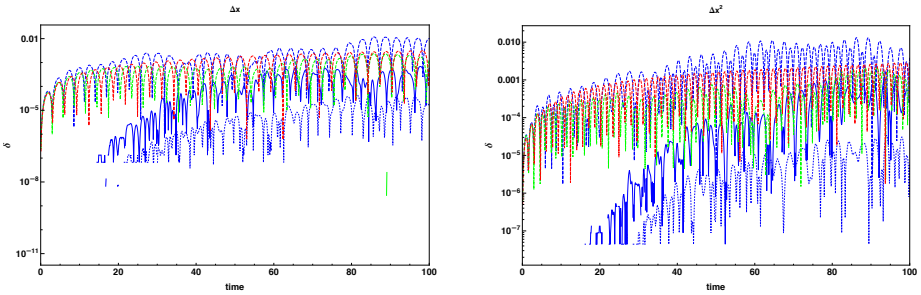

Figure 8. Plot of the convergence parameter as defined in Eq. (C4) as a function of time, for the operators $\hat{x}$ (left) and $\hat{x}^2$ (right). The results are shown for three representative points in our physical parameter space, namely $\Omega/\omega = 0.8, \lambda = 0.1, x_0 = 15$ (blue), $\Omega/\omega = 0.4, \lambda = 0.1, x_0 = 4$ (green) and $\Omega/\omega = 1.2, \lambda = 0.04, x_0 = 10$ (red). We vary the benchmark simulation parameters in three different ways: reducing Δt by a factor of two (dashed line), reducing Δx by a factor of two (dotted line), and increasing the box size L by a factor of two (continuous line). In some cases the differences were smaller than machine precision, which is why they were not plotted here. The influence of Δt is the most important although it is limited. Note that in the case where the error becomes $\mathcal{O}(10^{-2})$ (dashed blue line), the associated break times are much shorter (see Fig. 3) than the 100 time units that are shown here and therefore our results can still be trusted.

[1] W. Gerlach and O. Stern, Der experimentelle nachweis der richtungsquantelung im magnetfeld, Zeitschrift für Physik **9**, 349–352 (1922).

[2] P. ZEEMAN, The effect of magnetisation on the nature of light emitted by a substance, Nature **55**, 347–347 (1897).

[3] J. Stark, Beobachtungen über den effekt des elektrischen feldes auf spektrallinien. i. quereffekt, Annalen der Physik **348**, 965–982 (1914).

[4] L. Mandel and E. Wolf, *Optical Coherence and Quantum Optics* (Cambridge University Press, 1995).

[5] G. Grynberg, A. Aspect, and C. Fabre, *Introduction to Quantum Optics: From the Semi-classical Approach to Quantized Light* (Cambridge University Press, 2010).

[6] J. Schwinger, On gauge invariance and vacuum polarization, Phys. Rev. **82**, 664 (1951).

[7] C. J. Pethick and H. Smith, *Bose–Einstein Condensation in Dilute Gases*, 2nd ed. (Cambridge University Press, 2008).

[8] R. Rajaraman, *Solitons and Instantons: An Introduction to Solitons and Instantons in Quantum Field Theory*, North-Holland personal library (North-Holland Publishing Company, 1982).

[9] S. R. Coleman, Q-balls, Nucl. Phys. B **262**, 263 (1985), [Addendum: Nucl.Phys.B 269, 744 (1986)].

[10] R. F. Dashen, B. Hasslacher, and A. Neveu, Nonperturbative Methods and Extended Hadron Models

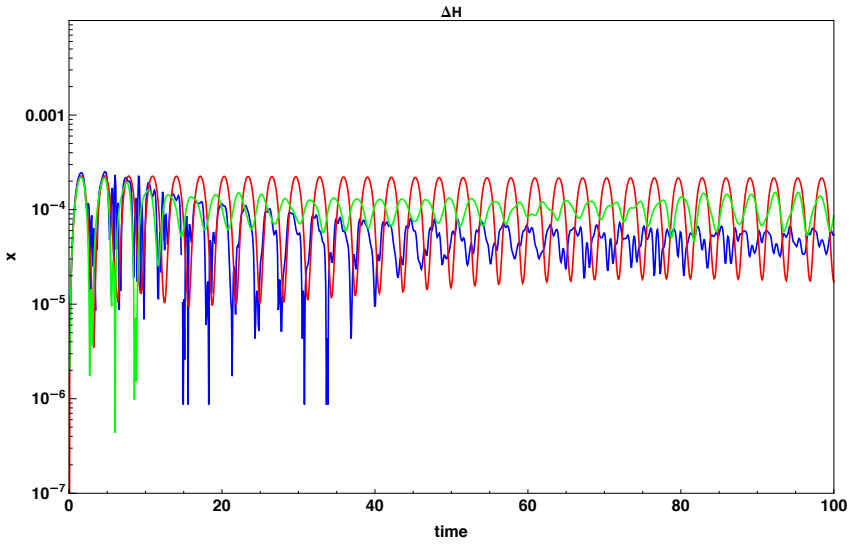

Figure 9. The degree of conservation of the expectation value of H for the benchmark simulations of the previous three choices of physical parameters. In all cases energy is conserved up to 1 part in 10^4.

in Field Theory 1. Semiclassical Functional Methods, Phys. Rev. D **10**, 4114 (1974).

[11] R. F. Dashen, B. Hasslacher, and A. Neveu, Nonperturbative Methods and Extended Hadron Models in Field Theory 2. Two-Dimensional Models and Extended Hadrons, Phys. Rev. D **10**, 4130 (1974).

[12] R. F. Dashen, B. Hasslacher, and A. Neveu, The Particle Spectrum in Model Field Theories from Semiclassical Functional Integral Techniques, Phys. Rev. D **11**, 3424 (1975).

[13] M. P. Hertzberg, Quantum radiation of oscillons, Physical Review D **82**, 10.1103/physrevd.82.045022 (2010).

[14] A. Tranberg and D. J. Weir, On the quantum stability of q-balls, Journal of High Energy Physics **2014**, 10.1007/jhep04(2014)184 (2014).

[15] N. D. Birrell and P. C. W. Davies, *Quantum Fields in Curved Space*, Cambridge Monographs on Mathematical Physics (Cambridge University Press, Cambridge, UK, 1982).

[16] L. H. Ford, Gravitational Particle Creation and Inflation, Phys. Rev. D **35**, 2955 (1987).

[17] L. H. Ford, Cosmological particle production: a review, Reports on Progress in Physics **84**, 116901 (2021).

[18] S. W. Hawking, Black hole explosions, Nature **248**, 30 (1974).

[19] S. W. Hawking, Particle Creation by Black Holes, Commun. Math. Phys. **43**, 199 (1975), [Erratum: Commun.Math.Phys. 46, 206 (1976)].

[20] J. Braden, M. C. Johnson, H. V. Peiris, A. Pontzen, and S. Weinfurtner, New semiclassical picture of vacuum decay, Physical Review Letters **123**, 10.1103/physrevlett.123.031601 (2019).

[21] D. G. Figueroa, A. Florio, F. Torrenti, and W. Valkenburg, The art of simulating the early universe. part i. integration techniques and canonical cases, Journal of Cosmology and Astroparticle Physics

2021 (04), 035.

[22] G. W. Ford, J. T. Lewis, and R. F. O'Connell, Quantum Langevin equation, Phys. Rev. A **37**, 4419 (1988).

[23] B. L. Hu and A. Matacz, Back reaction in semiclassical cosmology: The Einstein-Langevin equation, Phys. Rev. D **51**, 1577 (1995), arXiv:gr-qc/9403043.

[24] J. R. Klauder, Coherent State Langevin Equations for Canonical Quantum Systems With Applications to the Quantized Hall Effect, Phys. Rev. A **29**, 2036 (1984).

[25] J. Goldstone, A. Salam, and S. Weinberg, Broken symmetries, Phys. Rev. **127**, 965 (1962).

[26] J. F. Donoghue, General relativity as an effective field theory: The leading quantum corrections, Phys. Rev. D **50**, 3874 (1994), arXiv:gr-qc/9405057.

[27] E. Calzetta and B. L. Hu, Closed Time Path Functional Formalism in Curved Space-Time: Application to Cosmological Back Reaction Problems, Phys. Rev. D **35**, 495 (1987).

[28] B. L. Hu and E. Verdaguer, Stochastic Gravity: Theory and Applications, Living Rev. Rel. **11**, 3 (2008), arXiv:0802.0658 [gr-qc].

[29] J. Evslin and H. Liu, Reflection coefficient of a reflectionless kink, Phys. Rev. D **109**, 085019 (2024).

[30] G. Dvali, C. Gómez, and S. Zell, Quantum break-time of de sitter, Journal of Cosmology and Astroparticle Physics **2017** (06), 028–028.

[31] G. Dvali and S. Zell, Classicality and quantum break-time for cosmic axions, Journal of Cosmology and Astroparticle Physics **2018** (07), 064–064.

[32] G. Dvali, C. Gomez, and S. Zell, Quantum breaking bound on de sitter and swampland, Fortschritte der Physik **67**, 10.1002/prop.201800094 (2018).

[33] G. Dvali and L. Eisemann, Perturbative understanding of nonperturbative processes and quantumization versus classicalization, Physical Review D **106**, 10.1103/physrevd.106.125019 (2022).

[34] M. Michel and S. Zell, The timescales of quantum breaking (2023), arXiv:2306.09410 [quant-ph].

[35] L. Berezhiani, G. Cintia, and M. Zantedeschi, Background-field method and initial-time singularity for coherent states, Physical Review D **105**, 10.1103/physrevd.105.045003 (2022).

[36] R. J. Glauber, The quantum theory of optical coherence, Phys. Rev. **130**, 2529 (1963).

[37] R. J. Glauber, Coherent and incoherent states of the radiation field, Phys. Rev. **131**, 2766 (1963).

[38] L. Berezhiani and M. Zantedeschi, Evolution of coherent states as quantum counterpart of classical dynamics, Physical Review D **104**, 10.1103/physrevd.104.085007 (2021).

[39] A. Ilderton and D. Seipt, Backreaction on background fields: A coherent state approach, Physical Review D **97**, 10.1103/physrevd.97.016007 (2018).

[40] P. Copinger, J. P. Edwards, A. Ilderton, and K. Rajeev, Pair creation, backreaction, and resummation in strong fields (2024), arXiv:2411.06203 [hep-ph].

[41] L. Berezhiani, G. Cintia, and M. Zantedeschi, Perturbative construction of coherent states (2023), arXiv:2311.18650 [hep-th].

[42] R. Horodecki, P. Horodecki, M. Horodecki, and K. Horodecki, Quantum entanglement, Rev. Mod. Phys.

81, 865 (2009), arXiv:quant-ph/0702225.

[43] T. Vachaspati and G. Zahariade, Classical-quantum correspondence and backreaction, Physical Review D **98**, 10.1103/physrevd.98.065002 (2018).

[44] T. Vachaspati and G. Zahariade, Classical-quantum correspondence for fields, Journal of Cosmology and Astroparticle Physics **2019** (09), 015–015.

[45] M. Mukhopadhyay, E. I. Sfakianakis, T. Vachaspati, and G. Zahariade, Kink-antikink scattering in a quantum vacuum, Journal of High Energy Physics **2022**, 10.1007/jhep04(2022)118 (2022).

[46] J. Ollé, O. Pujolàs, T. Vachaspati, and G. Zahariade, Quantum evaporation of classical breathers, Physical Review D **100**, 10.1103/physrevd.100.045011 (2019).

[47] A. Sinatra, C. Lobo, and Y. Castin, The truncated wigner method for bose-condensed gases: limits of validity and applications, Journal of Physics B: Atomic, Molecular and Optical Physics **35**, 3599–3631 (2002).

[48] A. Eberhardt, A. Zamora, M. Kopp, and T. Abel, The classical field approximation of ultra light dark matter: quantum breaktimes, corrections, and decoherence (2023), arXiv:2310.07119 [astro-ph.CO].

[49] M. A. Amin, M. P. Hertzberg, D. I. Kaiser, and J. Karouby, Nonperturbative dynamics of reheating after inflation: A review, International Journal of Modern Physics D **24**, 1530003 (2014).

[50] G. Dvali, D. Flassig, C. Gomez, A. Pritzel, and N. Wintergerst, Scrambling in the black hole portrait, Physical Review D **88**, 10.1103/physrevd.88.124041 (2013).

[51] W. H. Zurek and J. P. Paz, Decoherence, chaos, and the second law, Physical Review Letters **72**, 2508–2511 (1994).

[52] E. Bianchi, L. Hackl, and N. Yokomizo, Linear growth of the entanglement entropy and the kolmogorov-sinai rate, Journal of High Energy Physics **2018**, 10.1007/jhep03(2018)025 (2018).

[53] M. Bojowald and A. Skirzewski, Effective equations of motion for quantum systems, Rev. Math. Phys. **18**, 713 (2006), arXiv:math-ph/0511043.

[54] M. Bojowald, D. Brizuela, H. H. Hernandez, M. J. Koop, and H. A. Morales-Tecotl, High-order quantum back-reaction and quantum cosmology with a positive cosmological constant, Phys. Rev. D **84**, 043514 (2011), arXiv:1011.3022 [gr-qc].

[55] B. Baytaş, M. Bojowald, and S. Crowe, Effective potentials from semiclassical truncations, Phys. Rev. A **99**, 042114 (2019), arXiv:1811.00505 [quant-ph].

[56] B. Baytas, M. Bojowald, and S. Crowe, Faithful realizations of semiclassical truncations, Annals Phys. **420**, 168247 (2020), arXiv:1810.12127 [math-ph].

[57] M. Bojowald and D. Ding, Canonical description of cosmological backreaction, Journal of Cosmology and Astroparticle Physics **2021** (03), 083.

[58] M. Bojowald, Canonical description of quantum dynamics*, Journal of Physics A: Mathematical and Theoretical **55**, 504006 (2022).

[59] L. Kofman, A. Linde, and A. A. Starobinsky, Towards the theory of reheating after inflation, Physical Review D **56**, 3258–3295 (1997).

[60] G. Dvali, Entropy bound and unitarity of scattering amplitudes, Journal of High Energy Physics **2021**, 10.1007/jhep03(2021)126 (2021).

[61] J. L. Gervais, A. Jevicki, and B. Sakita, Perturbation expansion around extended-particle states in quantum field theory, Phys. Rev. D **12**, 1038 (1975).

[62] J. Evslin, T. Romańczukiewicz, and A. Wereszczyński, Quantum oscillons may be long-lived, JHEP **08**, 182, arXiv:2305.18056 [hep-th].

[63] K. Ogundipe and J. Evslin, Perturbative approach to time-dependent quantum solitons, JHEP **06**, 174, arXiv:2403.13232 [hep-th].

[64] G. Dvali, J. S. Valbuena-Bermúdez, and M. Zantedeschi, Memory burden effect in black holes and solitons: Implications for pbh (2024), arXiv:2405.13117 [hep-th].

[65] G.-A. Zahariade and F. van Dissel, Semiclassical Backreaction: A Qualitative Assessment - replication data. (2025).

[66] T. Vachaspati, Quantum backreaction on classical dynamics, Physical Review D **95**, 10.1103/physrevd.95.125002 (2017).

[67] H. Yoshida, Construction of higher order symplectic integrators, Physics Letters A **150**, 262 (1990).

[68] D. Levkov, A. Panin, and I. Tkachev, Gravitational bose-einstein condensation in the kinetic regime, Physical Review Letters **121**, 10.1103/physrevlett.121.151301 (2018).